Non-destructive characterization of thermally sprayed cylinder coatings using laser-excited lock-in thermography

Zur Erlangung des akademischen Grades eines

DOKTORS DER INGENIEURSWISSENSCHAFTEN
(Dr.-Ing.)

von der KIT-Fakultät für Maschinenbau des
Karlsruher Instituts für Technologie (KIT)
angenommene

DISSERTATION

von

M.Sc. Jannik Marcel Arbogast

Tag der mündlichen Prüfung: 07.07.2021

Hauptreferent: Prof. Dr. Hans Jürgen Seifert
Korreferent: Prof. Dr. Marc Kreutzbruck

Danksagung

Die Verfassung und Durchführung dieser Arbeit wäre ohne eine Vielzahl an Personen nicht möglich gewesen. Mein großer Dank geht an diejenigen, die mich tatkräftig bei meiner Promotion unterstützt haben.

Da diese Promotion in enger Zusammenarbeit mit der Mercedes-Benz AG und dem Karlsruher Institut für Technologie (KIT) durchgeführt wurde, möchte ich mich recht herzlich bei allen Beteiligten dieser beiden Institutionen bedanken.

Besonders möchte ich mich bei Herrn Prof. Hans Jürgen Seifert für die Möglichkeit bedanken, meine Promotion am Institut für Angewandte Materialien - Angewandte Werkstoffphysik (IAM-AWP) des KIT durchführen zu können. Es ist nicht selbstverständlich, dass Sie es mir ermöglicht haben, in Zusammenarbeit mit der Mercedes-Benz AG bei Ihnen am Institut zu promovieren. Vielen Dank für die fachliche und methodische Unterstützung und die sehr lehrreiche Zeit.

Darüber hinaus geht mein tiefster Dank an Herr Dr. Magnus Rohde für die Betreuung meiner Arbeit am KIT. Vielen Dank für Ihre bedingungslose Unterstützung bei jeglichen Problemstellungen. Ohne Sie wäre die Kooperation mit dem KIT nicht so reibungslos und so erfolgreich verlaufen.

Des Weiteren bedanke ich mich herzlich bei Herrn Prof. Dr. rer. nat. habil. Marc Kreutzbruck vom IKT der Universität Stuttgart, der als Zweitgutachter für meine Arbeit einsteht. Ebenfalls möchte ich mich bei seinen Kollegen Dr. Wolfgang Essig und Johannes Rittmann für deren fachliche Expertise und Unterstützung meiner Arbeit bedanken.

Mein Dank geht weiterhin an Dr. Hermann Walter und die Mercedes-Benz AG, welche mir die Chance gegeben haben meine Promotion in Zusammenarbeit mit einem Unternehmen durchführen zu können. Ich habe vielfältige Einblicke erhalten und eine einmalige Zeit genossen. Zusätzlich bedanke ich mich bei allen aktuellen sowie ehemaligen Mitgliedern des Teams Physikalische Prüfverfahren, die mich sehr herzlich in die Gruppe aufgenommen und mich stets tatkräftig unterstützt haben. Es war eine wunderbare Zeit bei euch.

Mein besonderer Dank geht in diesem Zuge an Dr. Rolf Schaller, der die Betreuung meiner Promotion bei der Mercedes-Benz AG übernommen hat. Ohne deine bedingslose und unendliche Unterstützung wäre diese Arbeit nicht möglich gewesen. Ich danke dir aus tiefsten Herzen für die gemeinsame Zeit und all die Dinge, die ich von dir lernen durfte. Ich wünsche dir und deiner Familie für die Zukunft nur das Beste!

Zusätzlich möchte ich mich bei allen Doktorandenkollegen und dem Doktorandenkernteam

Abstract

Improving the efficiency of combustion engines and thus reducing CO_2 emissions of modern powertrains, thermally sprayed cylinder coatings replaced cast iron liners over the last decades. In order to guarantee the life-long functionality and durability of modern combustion engines, the bond strength of thermally sprayed cylinder coatings to the crankcase is one crucial property continuously monitored during the large-scale production of modern powertrains. However, since the bond strength between cylinder coating and crankcase substrate presently can only be measured by destructive "Pull-off adhesion testing" (PAT™), a fast and reliable non-destructive method characterizing the bonding behavior of cylinder coatings is highly desired. As the presence of defects in the microstructure lowers the bond strength of cylinder coatings, assessing the defect morphology by defect-sensitive non-destructive thermal diffusivity measurements shows promising correlation between thermal and mechanical behavior. The application of thermal diffusivity measurements as a non-destructive testing method to evaluate the bond strength of thermally sprayed cylinder coatings is discussed in this work. Laser-excited lock-in thermography is used to apply thermal wave interferometry (TWI) measurements on wire arc sprayed cylinder coatings of passenger car engines. Measured thermal diffusivity values of these coatings show significant variations within the crankcases especially along the investigated liners. Further, destructive bonding testing as well as microstructural analysis of the investigated cylinder coatings are acquired to evaluate mechanical and microstructural properties. Additional fracture analysis after PAT™ allows to quantify the amount of adhesive and cohesive failure of the coating systems. Investigations of the relationship between thermal diffusivity, bonding behavior and microstructure result in major correlations between the observed quantities.

Zusammenfassung

Zur Effizienzsteigerung von Verbrennungsmotoren und der daraus resultierenden Reduktion des CO_2-Ausstoßes moderner Antriebsstränge ersetzten thermisch gespritzte Zylinderlaufflächen gegossene Zylinderbuchsen in den vergangenen Jahrzehnten. Um eine langlebige Funktionalität und Haltbarkeit moderner Verbrennungsmotoren zu gewährleisten, wird die Haftung solcher thermisch gespritzter Zylinderlaufflächen an das Kurbelgehäuse laufend innerhalb der Großserienproduktion überwacht. Da die Haftung zwischen der Lauffläche und dem Kurbelgehäuse gegenwärtig nur mittels zerstörendem "Pull-off adhesion testing" (PAT™) gemessen werden kann, wird eine schnelle und zuverlässige zerstörungsfreie Prüfmethode benötigt, die das Bindungsverhalten der Zylinderlaufflächen bestimmen kann. Das Auftreten von Bindungsfehlern innerhalb der Mikrostruktur verringert die Haftung der Zylinderlaufflächen. Deshalb zeigen zerstörungsfreie Temperaturleitfähigkeitsmessungen, die sensitive auf diese Defektmorphologie reagieren, vielversprechende Korrelationen zwischen den thermischen und mechanischen Eigenschaften der Laufflächen. Die Anwendung solcher Temperaturleitfähigkeitsmessungen als zerstörungsfreies Prüfverfahren zur Bewertung der Haftfestigkeit thermisch gespritzter Zylinderlaufflächen ist Gegenstand dieser Arbeit. Hierzu wird die laserangeregte Lock-In Thermographie verwendet, um Interferenzmessungen thermischer Wellen innerhalb lichtbogendrahtgespritzter Zylinderlaufflächen von PKW-Motoren zu untersuchen. Die daraus gemessenen Temperaturleitfähigkeitswerte der untersuchten Schichten zeigen signifikante Veränderungen innerhalb der Kurbelgehäuse, insbesondere entlang der Laufflächen. Darüber hinaus werden zerstörende Haftzugsmessungen und Mikrostrukturanalysen der untersuchten Zylinderlaufflächen durchgeführt, um die mechanischen und mikrostrukturellen Eigenschaften zu beurteilen. Zusätzliche Bruchstellenanalysen nach den PAT™-Messungen ermöglichen die quantitative Beurteilung des adhäsiven und kohäsiven Versagens der Schicht. Die Untersuchungen der Zusammenhänge zwischen der Temperaturleitfähigkeit, des Haftzuges und der Mikrostruktur ergeben bedeutende Korrelationen zwischen diesen beobachteten Größen.

Contents

List of Abbreviations

ANOVA	Analysis of variance
CFRP	Carbon fiber reinforced polymers
Cont. ratio	Contribution ratio
(n)CT	(nano) Computed tomography
DF	Degrees of freedom
DFT	Discrete Fourier transformation
DoE	Design of Experiment
IA	Image analysis
LFA	Laser flash analysis
NMRP	Nissan Mechanical Roughening Profile
OLM	Optical light microscopy
PAT™	Pull-off adhesion testing
Pos	Position
ROI	Region of interest
SEM	Scanning electron microscopy
SoS	Sum of squares
TWI	Thermal wave interferometry
w/	with
w/o	without

List of Symbols

A	Amplitude of surface oscillation
α	Thermal diffusivity
c	Specific heat capacity
C	Offset correction
d	Layer thickness
$\boldsymbol{D}$	Electric displacement field
e	Thermal effusivity
$\boldsymbol{E}$	Electric field
ϵ	Dielectric constant
η	Fitting coefficient
f	Frequency
F	F-values of a Fisher distribution
Γ	Transmission coefficient
k, k'	Wave numbers
λ	Thermal conductivity
μ	Thermal diffusion length
ω	Angular frequency
P	Probability that the null hypothesis is correct
φ	Electric potential
ϕ	Phase of surface oscillation
$\dot{\boldsymbol{q}}$	Thermal heat flux
R	Reflection coefficient
ρ	Density
σ_x	Standard deviation of quantity x
t	Time
$t_{0.5}$	Measured time to the half maximum temperature rise
T	Temperature
T_0	Temperature at the sample surface

List of Figures

List of Tables

1. Introduction

Over the last decades, research and development of the automotive industry focused on increasing the efficiency of modern powertrains, as it became one of the most important objectives to reduce fuel consumption to fulfill the rising requirements and regulations concerning CO_2 emissions. Since the crankcase represents one of the core components of a combustion engine, efficiency increasing technologies have been applied to further improve this part of the powertrain. Modern cast crankcases consist of aluminum alloys combined with thermally sprayed cylinder coatings of low alloyed steel. These heterogeneous crankcases are light weight constructions showing the required mechanical properties and wear resistances of specific components within the crankcases. In this context, Mercedes-Benz developed the NANOSLIDE™ technology process chain to produce progressive cylinder liners. This process chain technology combines wire arc spraying with a surface-finish through honing. While the thermally sprayed coatings allow to reduce the friction losses between the pistons and the cylinder liner by up to 50 % compared to conventional cast liners [1, 2], also a significant reduction of weight can be achieved. The NANOSLIDE™ technology enables to reduce the material thickness of the effective cylinder coating to only a few $100\,\mu m$, resulting in a loss of weight of over $1\,kg$ per cylinder in contrast to cast cylinder liners. Therefore, combining all these advantages of the NANOSLIDE™ process, it allows to lower the overall CO_2 emissions of a modern powertrain by approximately 3 % [3, 4].

However, despite all known improvements towards the efficiency, life-long integrity and durability are two additional mandatory aspects concerning the functionality of a modern engine and depend among others on the coating's mechanical properties. Using wire arc spraying to coat the cylinder liners, molten particles hit the substrate and cool down consecutively building up a typical lamellar structure of partially separated splats and pores. Based on this characteristical microstructure, mechanical as well as other properties such as thermal diffusivity are mainly defined by decisive defects such as splat interfaces, bonding defects or pores. Besides coating thickness and surface quality, the bond strength between the aluminum crankcase and the thermally sprayed coating is one of the most important mechanical properties of the cylinder liner. The bond strength of thermally sprayed coatings is defined by the adhesive bond between coating and substrate as well as by the cohesive bond between the individual splats. While adhesion depends on clamping between the coating and the substrate as well as on metallurgical diffusion bond between the two materials, cohesive bond is mainly dominated by the coating's microstructure itself [5]. Hence, the morphology of the observed coating defects plays a key role in defining the bonding behavior of the coatings [6–8]. The coatings' microstructures show

distinct differences in amount, size and shape of the observed coating defects depending on the conditions during wire arc spraying. This results in a varying bonding behavior of the coating to the substrate correlated to the applied process parameters [9].

In order to ensure the functionality of such modern cylinder coatings, destructive "Pull-off adhesion testing" (PAT™) is used for quality assurance of such thermally sprayed cylinder coatings during the large-scale production at Mercedes-Benz. Therefore, a test element is glued directly onto the cylinder surface, while the bond strength is measured by pulling off the test elements hydraulically removing the thermally sprayed coating from the substrate. By increasing the wastage of the large-scale production due to the destructive nature of PAT™ and therefore decreasing the profitability, a non-destructive testing method to characterize the quality of cylinder coatings especially regarding their bonding properties is highly desired.

As shown in various publications and approved literature [8, 10–16], the microstructure of thermally sprayed coatings can be directly correlated to the thermal properties of such materials. Thermal transport properties such as the thermal diffusivity of coated systems reveal important knowledge of the underlying microstructure and hence open the ability to inversely access the morphology of coating defects non-destructively [17]. Further, due to the correlation of coating defects and bonding behavior [6–8], thermal diffusivity measurements are assumed to correlate thermal and mechanical properties. Due to their non-destructive character, this work focuses on the applicability of thermal diffusivity measurements on thermally sprayed cylinder coatings to assess the microstructures of the coatings and to gather information about their mechanical properties.

While optically and non-optically excited thermography opens a broad spectrum of possible applications [18], laser flash analysis (LFA) defines the standard method to measure thermal diffusivities [19]. However, since commercially available systems require planar samples with a standardized size and shape as well as access to both sides of the material, LFA is not feasible for the non-destructive investigation of rather thin and curved thermally sprayed cylinder bore coatings with only one-side access. An alternative method to investigate the thermal diffusivity of a coated substrate is called thermal wave interferometry (TWI) [20]. It has been established for a wide range of characterization and testing applications during the past decades [21–23]. The measuring principle is based on the propagation, the reflection and the interference of so-called "thermal waves", which are determined by the material's thermal diffusivity. Surface heating with a sinusoidal amplitude-modulated heat source can trigger such thermal waves in a layered structure [24]. While infrared sensors are capable of detecting the material's thermal response to the applied thermal waves, a discrete Fourier transformation of the obsereved surface temperature oscillations allows to discriminate between its amplitude and phase information. Laser-excited lock-in thermography is a specific form of TWI and provides access to the phase shift between surface temperature and sinusoidal heat excitation. This technique allows to estimate the material's thermal diffusivity and even gathers information about its local variations when combined with a fast, two-dimensional infrared detector.

The following chapters of this work focus on the applicability of TWI measurements to

reliably determine the thermal diffusivity of wire arc sprayed coatings. Further, thermal and mechanical properties are correlated to evaluate the applicability of TWI to determine the bonding behavior of such coatings non-destructively. Statistical analysis of the thermal and mechanical measurements helps to understand the major influencing factors on both characteristics. Metallographic analysis as well as X-ray computed tomography are further used to assess the microstructures and the related defect morphology. The study aims to connect the thermal diffusivity with the bond strength of the cylinder coatings via the underlying microstructure. In this context, further influencing factors of the large-scale production need to be investigated to gather reliable conclusions about the application of TWI in an industrial environment.

2. Fundamental descriptions

The following chapter introduces the topic of thermally sprayed coatings. First, a brief overview about the principle spraying technique is given. The chapter focuses on wire arc spraying, which is used in the large-scale production of Mercedes-Benz engines to produce essential components of the used crankcases. It is of great interest for the findings of this study to discuss the thermal and mechanical behavior of such sprayed coatings. A distinct literature review over the process of coating formation is given in Chapter 2.3. Since the process of coating formation has great impact on the thermal and mechanical properties, also thermal as well as bonding behavior of thermally sprayed coatings with respect to the coating formation process are presented in the following sections. Finally, the chapter introduces the theory of thermal waves and the application of thermal wave interferometry to measure the thermal transport properties of coating systems.

The following review over the topic of thermal spraying and different spraying techniques as well as the introduction of material characteristics of thermally sprayed coatings is based on the book of Fauchais, Heberlein and Boulos "Thermal Spray Fundamentals" [5]. This book reveals a broad overview over all necessary topics dealt with in the following. However, also further literature as cited in the text is used to describe the concepts and characteristics of thermal spraying.

2.1. Concept of thermal spraying

Continuously pushing the functionality, durability and economics of materials used for industrial applications to further limits, such performance improvements always require new techniques to achieve the desired outcome. Whereas geometrical design and choice of materials determine the performance and costs of components, an appropriate manufacturing technique is necessary to create these parts. Complex combinations of multiple requirements as allowing for e.g. high temperature exposure combined with abrasive wear or corrosion resistance and on the other hand reduction of the costs for component engineering and manufacturing processes are mostly not achievable with a single material. Costs of having an entire part made out of such materials is certainly beyond the limits. Therefore, coatings became really prominent since they allow to apply the desired functional surface locally at the necessary position of the parts, while the main volume of the component have not to show these special characteristics. Further, combining multiple materials opens the ability to produce heterogeneous parts showing composite characteristics which are not achievable with bulk materials. Therefore, thermal

spraying opened the ability to deposit metallic, non-metallic or even polymeric coatings on a wide range of substrate materials to obtain a big variety of different coating properties in all kinds of industries.

The principle of the thermal spraying concept can be defined as: "Thermal spraying comprises a group of coating processes in which finely divided metallic or nonmetallic materials are deposit in a molten or semi-molten condition to form a coating. The coating material may be in the form of powder, ceramic rod, wire, or molten materials" [5]. By this definition, a torch is used to form a high-temperature, high-velocity gas stream. The coating material is melted by a variety of techniques, while the molten material is accelerated by the gas stream towards a prepared substrate. The individual droplets hit the substrate, deform, flatten and cool down consecutively to form so-called splats (solidified individual particles). Multiple layered splats build up the final coating, which can reach material thicknesses between several tens of micrometer up to a few millimeters. The ability to produce such coating structures is one big advantage of thermal spraying. Due to mechanical and diffusive mechanisms, a bond between splats and substrate is formed.

The coating material can be introduced in different kind of forms such as powders, wires or rods. Because thermal spraying is mostly operated in open-air environment, in-flight oxidation of the accelerated droplets may lead to certain changes of the coating material properties. On the other hand, using a controlled, protective atmosphere, oxidation of the coating material may be suppressed or at least lowered to a minimum. However, using protective gases such as nitrogen, argon or other gases leads to higher costs of the applied thermal spraying technique. Another critical step in thermal spraying is the preparation of the substrate before coating. As substrates can be metals, ceramics, polymers, glasses, etc., activation and cleaning of the substrate is most important for the bond of the coating to the substrate. Roughening the substrate surface leads to a mechanical clamping of the droplets on the substrate and is among other mechanisms one important step for the adhesion of a coating. Cleaning the surface from oil or grease is necessary to allow for diffusive bonds between coating and substrate material. While some applications do not require further treatments of the coating after thermal spraying, surface finishing through mechanical, thermal or chemical methods may be desired to obtain the final surface for the application.

2.2. Wire arc spraying of cylinder bore coatings

In order to reduce the fuel consumption as well as to fulfill rising requirements and regulations concerning CO_2 emissions, the automotive industry intents to further increase the efficiency of modern combustion engines in passenger cars. Representing one of the core components of a combustion engine, major efficiency increasing technologies such as light weight construction also received entry to the design and construction of crankcases in modern engine types. As a result of research on lightweight design over the last decades, the automotive industry changed from cast iron to cast aluminum alloys as the main material of their crankcases. While this change drastically reduced the weight of the engine itself, it required further advanced technologies to solve upcoming tasks. Since the piston-liner group contributes approximately
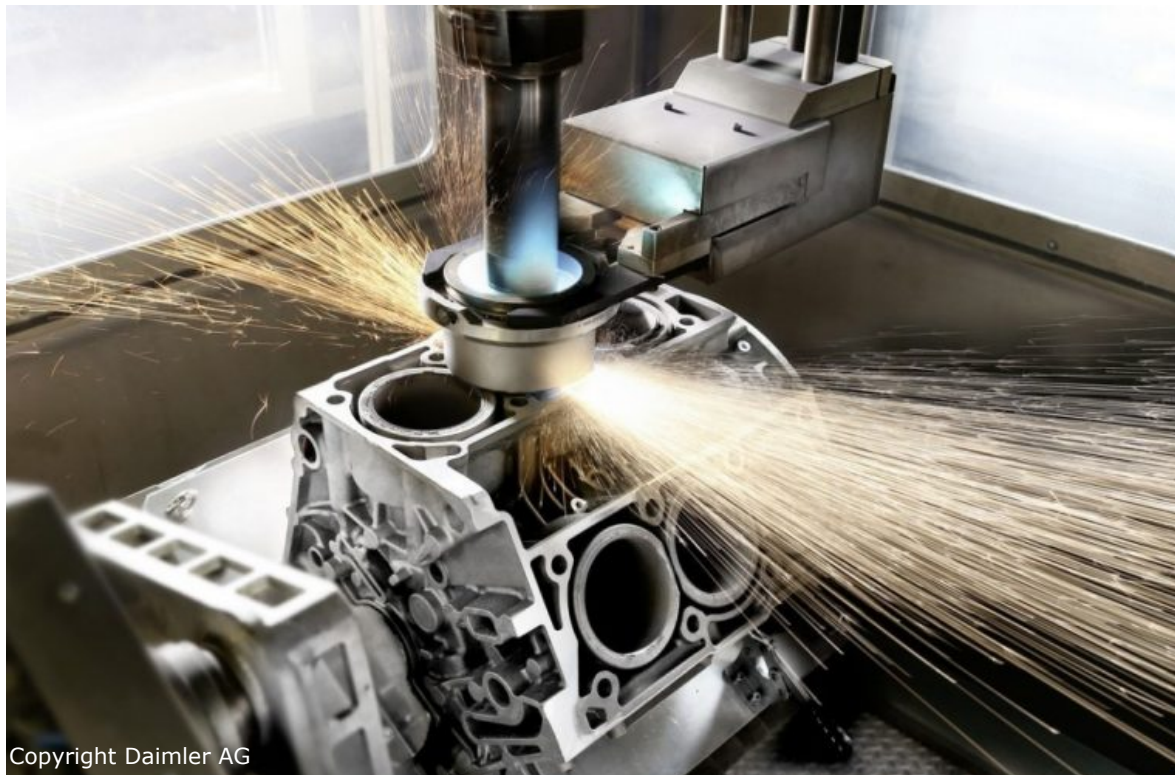
Copyright Daimler AG

Figure 2.1.: Wire arc spraying of a cylinder coating. Reference: Daimler AG, Stuttgart, Germany.

50 % to the friction losses in a combustion engine [1], further efficiency increasing can be achieved by reducing such losses using appropriate material combinations for the cylinder liner-piston group. However, whereas aluminum alloys are known to exhibit high friction with piston rings (mostly manufactured of Fe-C alloy) [25], a heterogeneous concept of the crankcase material and the cylinder liner surface is highly necessary to obtain reliable and efficient functionality of the powertrain. Applying thermal spraying to coat the cylinder bores, size and weight of the entire engine can be reduced significantly. Compared to the material thickness of cast liners of up to several millimeters, thermal spraying opened the ability to produce cylinder coatings showing thicknesses of only a few hundreds of micrometers. The change to thermally sprayed coatings resulted in a weight reduction of the crankcase of over 1 kg per cylinder bore as well as in a significant decrease of the size of the crankcase while maintaining its original functionality. Further, thermally sprayed cylinder coatings may not only reduce weight and size of the crankcases but also stand out reducing the friction of the piston-liner group. In this context, Mercedes-Benz developed the so-called NANOSLIDE™ process chain for the large-scale production, which combines wire arc spraying of the functional cylinder running surface with surface-finish through honing. The adaption of thermally sprayed cylinder coatings results in a significant reduction of the CO_2 emissions of modern combustion engines by approximately 3 % [3, 4].

2.2.1. Preparation of the crankcases

The large-scale process chain can be divided into three major steps. The first step includes casting as well as mechanical and other treatments of the aluminum alloy (AlSi8Cu3) crankcases. Secondly, wire arc spraying is applied to coat the prepared aluminum alloy bores with low-alloyed carbon steel (13Mn6). Finally, several mechanical machining and honing steps are required to obtain the desired, mirror-like surface of the cylinder liners.

The used aluminum alloy crankcases for combustion engines are manufactured using high pressure die casting or mold casting [26]. Since gasoline and diesel engines are loaded on different levels during operation, the respective cast crankcases must exhibit different levels of robustness. The type of casting technology may define the stability of the cast crankcase, while also economical aspects have a significant influence on choosing the applied casting method. The aluminum alloy AlSi8Cu3 is currently used for all mentioned types of cast crankcases in the large-scale production at Mercedes-Benz.

After casting and several follow-up steps, the crankcases need to be washed. Previous treatments such as preparation of the crankcase shaft or the cylinder head sealing surface are performed under oily conditions. Therefore, the aluminum-based crankcases run through a cleaning process to remove contaminants from the substrate such as oil and grease and get air-dried afterwards. Subsequent surface preparation of the cylinder bores is the first core step for thermal spraying of the cylinder coatings. Surface preparation defines one of the most essential steps in advance of thermal spraying. An optimized substrate surface is crucial to obtain the required properties of the coating, since adhesion quality is directly related to the cleanliness as well as roughness of the substrate [5]. Resistant bonding of the coating layer to the substrate defines one of the most important mechanical properties of the cylinder running surface to maintain the desired functionality and durability of the combustion engine. While multiple different types of techniques such as grit blasting, abrasive water jetting or even laser treatments are conceivable, also mechanical treatments can be used in order to achieve the desired roughening profile of the substrate. The so-called *Nissan Mechanical Roughening Process* (NMRP) uses tools with defined cutting edges to create a roughening profile. The roughened profiles show vertical extensions of up to $150\,\mu m$, while two neighboring peaks are separated by about $200 - 300\,\mu m$. The NMRP profile is shown in Figure 2.2. The NMRP allows to undercut the substrate target area creating a wave-shaped profile of the crankcase surface to achieve enhanced interlocking of the thermally sprayed splats and the roughened substrate. During thermal spraying of the cylinder coatings the torch moves upwards in the cylinder bore. The spray jet geometry possesses a gradient of particle size (Chapter 2.2.2 and Figure 2.4), while smaller droplets can be found in the lower part of the spraying jet. Therefore, the created wave peaks are orientated towards the cylinder head sealing surface to guarantee an appropriate backfilling of the roughened substrate by the layer material during the spraying process.

The used roughening tools have defined cutting edges that the highest peaks of the roughened substrate may not exceed a certain height. This step is crucial such that aluminum substrate may never protrude from the cylinder liners after final surface-finishing treatments. Due to
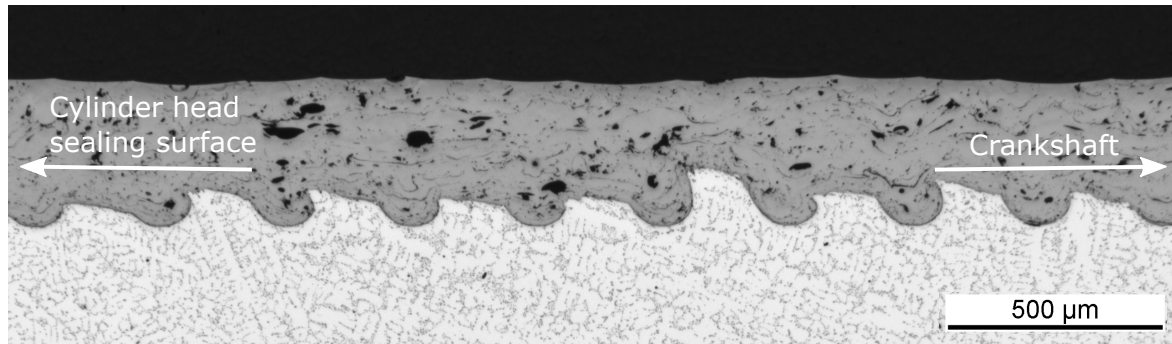
Figure 2.2.: Cross section image of a thermally sprayed cylinder coating (dark grey) on top of the roughened aluminum alloy substrate (light grey).

Table 2.1.: Elemental composition of the coating steel 13Mn6[1](1.0479)

Element	Mass fraction [%]	Element	Mass fraction [%]
C	$0.08 - 0.14$	Ni	≤ 0.12
Cr	≤ 0.12	P	0.025
Cu	≤ 0.17	S	0.025
Mn	$1.35 - 1.65$	Si	$0.3 - 0.45$

the enhanced friction of aluminum to piston rings [25], such failure of the cylinder coatings may lead to a collapse of the sprayed system and can cause a fatal break down of the entire engine. Therefore, non-destructive thickness measurements of the thermally sprayed cylinder coatings during the large-scale production has been applied to monitor and guarantee the required thicknesses of the functional coatings over the aluminum-based substrate. A detailed description of the applied measurement technique can be found in Chapter 3.6 or in [27]. Clean aluminum surfaces are necessary to achieve highest possible bond strength between coating and substrate. Reliable bond between cylinder coating and crankcase can only be achieved in the absence of any types of residuals such as oil, chips or grease [5]. Therefore, mechanical roughening is performed under dry conditions without any use of oil. The roughened interface needs to be protected against any sorts of residuals after the roughening process and remaining chips on the interface are removed by air blasting.

The final step of the crankcase preparation is achieved by a preheating procedure of the crankcases before wire arc spraying. The crankcases remain in an oven for 30 minutes up to 10 hours depending on the need of crankcases during the large-scale production. The oven temperature is set to about 140°. Preheating of the substrate plays a major role for the bond of the layered coating, since preheated crankcases tend to increase the formation of diffusion bonding between the cylinder coating and the substrate [5].

2.2.2. Spraying process

Wire arc spraying is used to produce the functional cylinder liner coatings in combustion engines due to its high economics, high deposition rate and its reliability [5]. A schematic

---

[1]Reference: Schweißdraht Luisenthal GmbH – Saarstahl AG, Völklingen, Germany

overview of the applied wire arc spraying principle is shown in Figure 2.3. In general, wire arc spraying is defined introducing the coating material in form of two wires continuously fed into the spray torch. An applied voltage to the two wires forms an electrical arc in the point of contact at the tip of the torch. The electrical arc melts the coating material (13Mn6; the elemental composition of the coating steel is shown in Table 2.1), while a high-velocity gas flow accelerates the molten particles, breaks down larger particles into smaller ones and propels them towards the substrate [5]. The injected gas flow mainly sputters the molten particles and accelerates them. This process gas flow may also be called primary gas flow. Further, a secondary gas flow is applied to lead and focus the spraying jet. The secondary gas flow is introduced surrounding the primary gas flow and can be controlled individually.

Depending on the application as well as on the economics of the process, different types of gases such as oxygen, nitrogen or inert gases can be used as the process gas for thermal spraying. In terms of wire arc spraying within the NANOSLIDE™ process chain, nitrogen is chosen as the primary and secondary gas. Due to its protective behavior against oxidation of the spraying droplets, nitrogen favors to build up coatings without enhanced oxide contents [28]. As the molten particles are sputtered by the primary gas flow, the spraying particles vary among others in temperature, velocity and size within the spray jet. While various process parameters influence the particle distribution in the spray jet, also the unique design of the spraying torch used for wire arc spraying in crankcases leads to certain variations of the particle properties. To apply wire arc spraying in crankcases, gas flow and material feeding must exhibit a 90° turn in the torch to achieve a vertical spray jet towards the substrate. A schematic illustration of the burner and the resulting spraying jet is shown in Figure 2.4. This characteristic design of the torch leads to strong turbulence of the gas flow at the tip, while these turbulence cause gradients of particle size, temperature and velocity [27, 29]. As the mean particle size of the spraying droplets increases from bottom to top of the spray jet, temperature and velocity of the particles decrease.

Wire arc spraying within the crankcases is realized by a rotating torch with a frequency of 300 rpm which is plunged into the cylinder bores. Coating of the individual cylinder bores is performed consecutively, starting with the cylinder bore nearest to the outer crankcase surface facing the gear box (cylinder number 4 or 6; depending on the size of the crankcase, see also Figure 3.1). Optimized filling of the substrate cavities is achieved by adapting the spray jet geometry and the particle distribution within the spray jet to the wave-shaped undercut roughening profile of the aluminum substrate. The cylinder liners are coated from the crankshaft towards the cylinder head sealing surface, while the spray jet is formed to have a cone-shape opened downwards. Thus, the droplets are sprayed into the cavities to backfill the roughening peaks and to obtain highest possible filling of the roughening structure. Improving the quality of the cylinder coatings, a circular mask on the cylinder head sealing surface as well as a mask in the crankshaft zone are mounted for each cylinder bore individually (The upper mask can be seen in Figure 2.1 on top of the cylinder head sealing surface). These masks seal and protect the inner atmosphere within the bore during the coating process against ambient atmosphere and exterior contamination. The masks also protect several crankcase parts from undesired coating overlay such as cavities for the con-rods near the crankshaft. Additionally, to
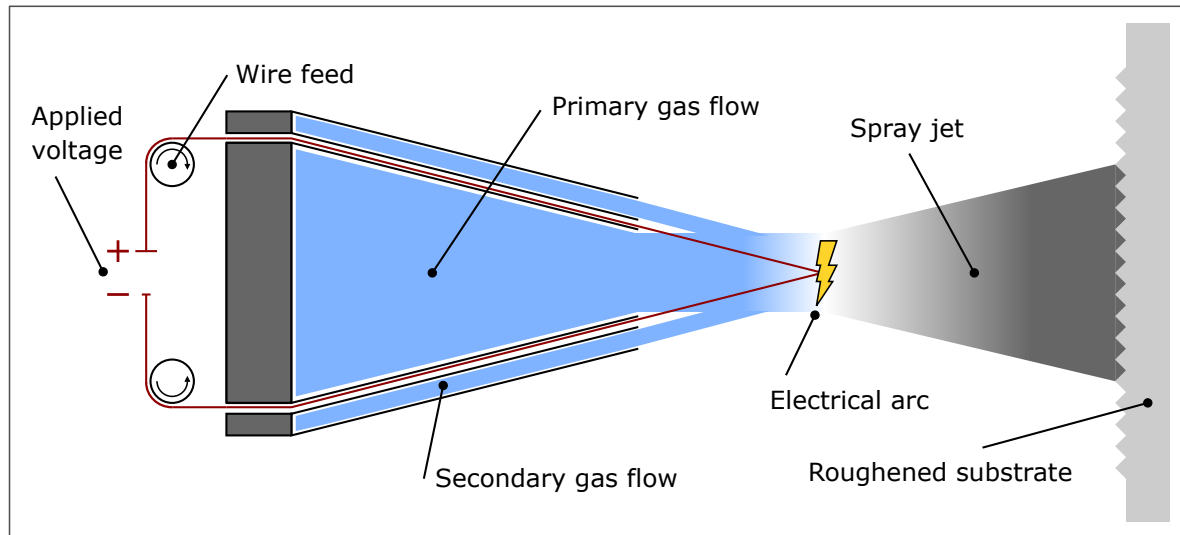
Figure 2.3.: Schematic of a wire arc spray setup
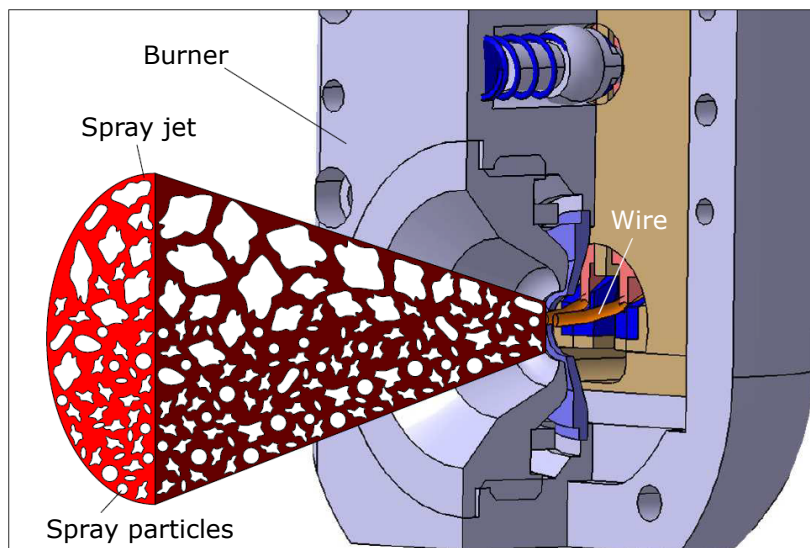
Figure 2.4.: Schematic of a wire arc burner including the spray jet and the resulting gradient of particle size. This figure was originally published in [27].

avoid impurities of the cylinder coatings due to excessive, non-adhesive particles and to lower the oxygen content within the spray jet, the atmosphere within the crankcase is extracted continuously during the coating process.

After the coating process the cylinder liners show rough surfaces, hence multiple machining steps are necessary to create the required surface structure of the cylinder coating for latter operation in the combustion engine. A mirror-like surface quality is finalized by precision turning followed by several honing steps, since finished-honed cylinder bore coatings exhibit material thicknesses of a few hundreds of micrometer. Finalizing honing steps reveal the typical pore structure of the cylinder coating by excavating sprayed particles. These craters exhibit the required oil detention volume at the liner surface, which is crucial to maintain the necessary

Copyright Daimler AG

Figure 2.5.: Image of a thermally sprayed cylinder liners. The coating is shown in its final condition after the honing process. The cylinder coatings show mirror-like surfaces. Reference: Daimler AG, Stuttgart, Germany.

lubrication between piston rings and cylinder liners [1]. Conventional cast liners required an additional machining step, providing necessary honing grooves to ensure this crucial oil volume on the liner surface during operation. The final thermally sprayed cylinder coatings are shown in Figure 2.5.

2.3. Formation of thermally sprayed coatings

Formation of thermally sprayed coatings is of particular interest, since it defines many characteristic properties of the coatings. For the following evaluation in this work, especially thermal and mechanical properties of sprayed coatings are investigated in detail. Due to the fundamental idea of thermal spraying, molten and finely distributed material is accelerated and deposit on the designated substrate to form a coating. Thus, the final coating builds up successively splat by splat [30, 31]. A schematic illustration of the formation for a typical sprayed coating can be found in Figure 2.6. Molten droplets undergo severe deformation and rapid solidification when they impinge on the substrate or already solidified coating material forming splats (also called lamellae) [28]. The impact, deformation and rapid solidification of individual droplets lead to a coating structure of overlapping bond splats [6, 7]. Depending on their temperature and velocity at the impact, different shapes and sizes of deformed splats or already solidified particles occur on the substrate. Using constant spraying parameters, globular flattening of the spray particles can be seen as reproducible, however individual deformation of each single splat can be observed thus causing a varying coating microstructure [5]. Due to the coating process, a typical lamellar structure builds up showing several types of defects such as partially separated splats, pores and embedded unmolten particles [6–8]. Thus, the coating formation process leads to a characteristic microstructure of thermally sprayed coatings exhibiting anisotropic behavior.

The coating microstructure is known to greatly influence effective properties based on their defect morphology [10]. Deformation and solidification of the particles as well as successive
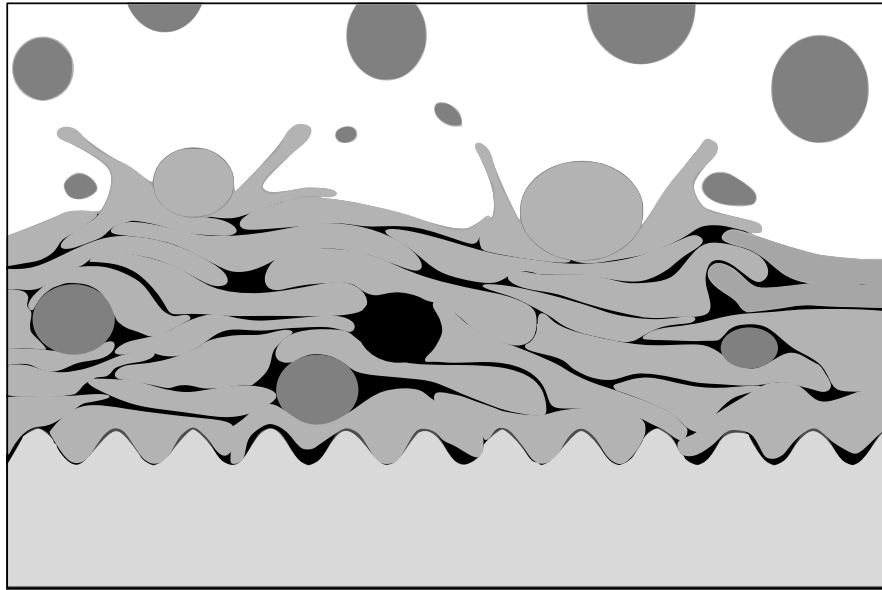
Figure 2.6.: Illustration of the formation for a sprayed coating (dark grey) on a roughened surface (light grey). The coating formation results in several coating defects such as laterally expanded splat interfaces, globular pores (both black) or embedded, solidified droplets (very dark grey). Also bonding defects at the roughened substrate interface are shown. Such bonding defects may occur due to residuals of oil, grease or remaining chips from mechanical activation of the substrate.
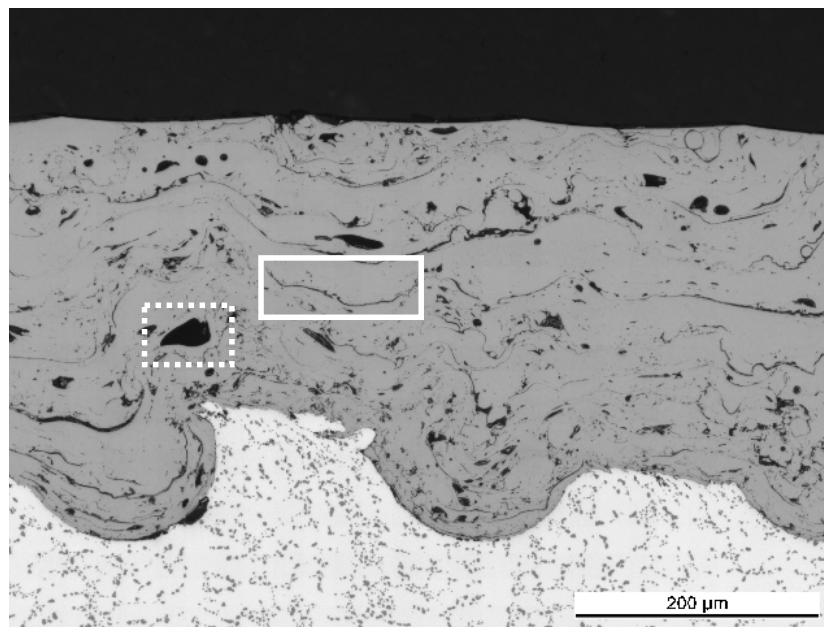
Figure 2.7.: Optical microscopy cross section image of a thermally sprayed cylinder bore coating. The steel-based cylinder coating is shown in dark grey, while the aluminum alloy substrate is depicted in light grey. A typical lamellar coating structure of lateral splat interfaces and globular porosity can be found in this cross section. Solid box: lateral splat interface; dotted box: globular pore

build up of the coating leads to a global coating made of individual spray particles. Therefore, bonding and interlocking between the solidified splats as well as between splats and substrate in thermally sprayed coatings is of major importance [32]. Literature reported that coating properties are mainly influenced by the bonding at the interface between individual splats, including such properties as thermal conductivity or cohesive strength [14,32–34]. Further, the way particles hit and deform on the coating strongly influences the bond between the splats and thus affecting the thermal and mechanical properties of the coating [15].

The defect morphology of the coatings is defined by the contact between individual splats, globular porosity as well as splashing and deformation of the spray particles at the impact. Figure 2.7 shows a cross section image of a thermally sprayed coating including the described coating defects. Two main defect types found in coating microstructures are highlighted by the boxes. A lateral splat interface is shown in the solid box, while a globular pore is surrounded by the dotted box. The contact area between splats is seen as the connected areas of splat-splat interfaces or splat-substrate interfaces, which reveal cohesive metallurgical bonds without any types of gaps or discontinuities within the coating [15]. At regions showing no contact between layered splats, interlamellar flat pores also called **lateral splat interfaces** can be found [35]. These defects describe flat, thin voids, orientated orthogonally to the spray direction building gaps between two successive splats. These types of defects are known to influence thermal and mechanical properties [5]. Further, **globular pores** describe another defect type of thermally sprayed coatings. Pores can occur when impacting particles cannot cover or fill the gaps left open by already solidified splats, which is also called the shadowing effect [5]. Globular pores can be caused by unmolten or partially molten particles, by trapping of process gases in the coating or by the shrinkage of solidifying splats. Finally, splashing and deformation of the spray particles especially on the roughened substrate but also on already deposit layers is of further important interest during the coating formation. Especially, adhesion effects between coating and substrate can be traced back to the size and shape of the splashed particles [36].

It is of further interest to characterize the influences of the introduced spraying techniques on the microstructures of the coatings to achieve the required properties of the designed coatings. While spraying techniques are distinguished by major conceptional differences resulting in a great variety of microstructures [7], even within one spraying principle the resulting coating microstructure depends strongly on more than 60 independent spray parameters [5]. Hence, properties of thermally sprayed coatings are not as predictable as those of conventional materials making it even more complicated to design the associated features of the coatings.

Besides particle temperature and velocity, the spraying atmosphere is one of the most important influences on the microstructures in thermally sprayed coatings. The relevance of the spraying atmosphere is the topic of many investigations, and additionally the oxygen content within the spraying atmosphere plays a significant role determining the coating properties [6,7,37–39]. Especially for spraying of metallic materials, the oxygen content in the spraying atmosphere is most important. Oxides are known to significantly influence the microstructure as well as the thermal and mechanical properties [6,7,40]. Oxygen within the gas flow can cause the spraying particles to experience in-flight oxidation as well as oxidation after impact during the

solidification [41]. Oxide shells form around the particles in the presence of oxygen during the flight, embedding the metallic, molten material. Due to the large difference between the melting points of oxides and metals, a solid crust can be formed around the particles [5]. After the impact of the oxidized droplet, the oxide shell builds up a boundary between the already solidified splats and the impacting ones forming horizontally orientated splat boundaries. Thus, the spraying atmosphere is found to strongly influence the interfacial contacts between the individual splats, while oxygen in the spraying atmosphere lowers the contact areas between successive splats significantly [15].

Since oxides have such a strong influence on the coating properties, process influences on the coating atmosphere regarding the oxygen content are widely described in the literature. One obvious approach to reduce oxidation of spraying particles is to replace oxygen as the main component of the gas stream by the use of alternative process gases. Hence, oxidation of the droplets can be drastically reduced if non-oxidizing gases are used such as nitrogen or inert gases [28]. Additionally, the gas velocity and the resulting particle velocity play an important role upon the oxidation of metal droplets. Since higher gas flow velocities lead to smaller droplet sizes, the reduced droplet sizes obtain an increased surface-to-volume ratio compared to slower particles. Therefore, smaller particles react more readily with the surrounding air forming oxides. This leads to a higher fraction of oxide shells around the particles and therefore to enhanced amount of splat boundaries within the coatings processed from higher gas velocities [6, 7]. However, increased particle velocity lowers the time of the particles in the oxygen atmosphere thus reducing the amount of deposited oxide material. Also, the particle temperatures can influence the degree of oxidation of spraying droplets since higher temperature favor the reactivity between metals and oxygen to form oxides [5]. Therefore, an optimized setup of process parameters especially regarding the particle velocity and temperature has to be obtained to reduce the influence of oxidation within a coating.

2.4. Bond mechanisms of thermally sprayed coatings

Mechanical properties such as the bond strength between deposit layers and substrates are of great interest for thermally sprayed coating systems. Bonding of a thermally sprayed coating to a substrate can be divided into two main mechanisms: **mechanical bond** and **diffusion bond** [9]. Further, bonding may also be divided into two types of bonds: **adhesion** and **cohesion**. Adhesion describes the bond between the layer and the substrate surface, while cohesion is the inner bond of the layer itself, mainly the bond between the individual splats of a coating. Hence, the coating bond is defined by the interaction between individual splats and between splats and the substrate [28]. Since failure occurs at the weakest part of a coating-substrate system, bond failure can appear to be adhesive (failure at the interface), cohesive (failure within the layer) or of mixed type.

Mechanical bonding describes the interlocking and anchoring of splats with the substrate as well as of splats with already deposited coating material. For adhesive effects, the design of the roughened substrate is of great importance. Fluid droplets are hitting and flattening on the roughened surface, while they adapt to the shape of the substrate. The deposited splats shrink during the cooling and adhere to the substrate or cohere to already deposited splats
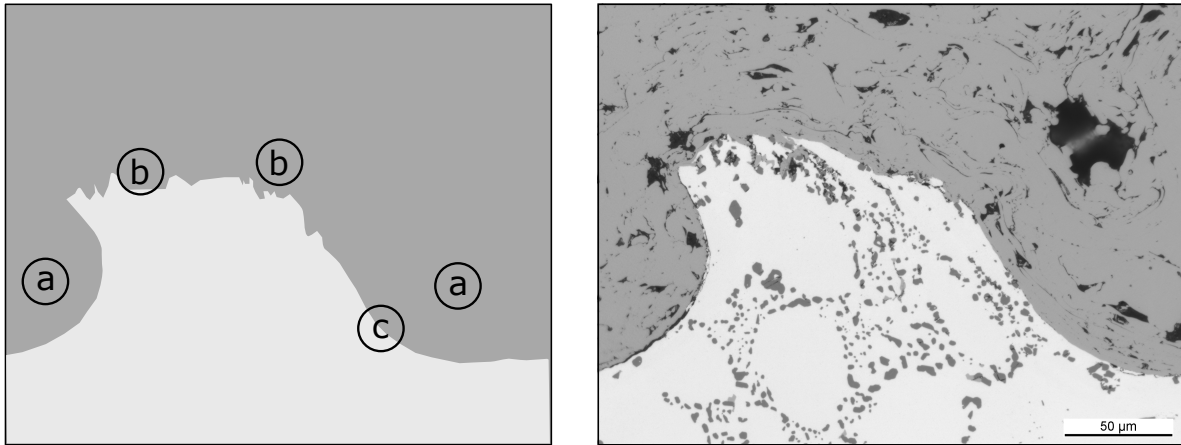
Figure 2.8.: Adhesion mechanisms of thermally sprayed coatings to roughened substrates. (a) Macroscopic mechanical interlocking, (b) Microscopic mechanical interlocking and (c) Diffusion bond

due to frictional forces [5, 28]. This mechanical interlocking is improved with higher velocity of the sprayed particles. The reduced size of the droplets increases the surface of possible interlocking splats as well as the ability of the flattening particles to fill gaps or to assume the shape of the target material [28]. High coating bond strength can only be achieved if the sprayed droplets are fully molten such that they can spread out and flow into the contours of the roughened profile as well as into gaps between overlapping layers. Further, the adhesion of the coating depends strongly on the elevation and the distance between profile peaks of the roughened surface. The mean size of the sprayed droplets has to be adapted to the peak height and the peak distance [5]. If the droplet size is too large compared to the roughening profile, appropriate filling and interlocking with the substrate cannot be achieved.

The second important bond mechanism is known as **diffusion** or **metallurgical bonding**. Diffusion bonds are found when the molten droplets hit a hot substrate such that the substrate also gets molten and a diffusion process between splat and substrate material appears. Thus, diffusion bond is detected, if coating material can be found in the substrate phase near the surface forming a diffusion zone. Such bonds are favored by preheating of the substrate using an external heat source before the coating process, since diffusion bond is only present for high substrate temperatures and if the substrate surface is free of oxides or other residuals [5]. Substrate oxides, oxide crusts around the droplets or oily residuals on the interface surface may all cause a barrier between the coating and the substrate such that diffusion of the two materials is prohibited [5]. Overall, the adhesion bond quality is directly related to the cleanliness, roughness and proper machining of the substrate interface [5]. Research on the bond strength of various different thermally sprayed coating types reveal common values between $10 - 70\,\text{MPa}$ [42–46]. The reported bond strengths depend among others on various influencing factors such as thermal spraying technology, roughening profile or layer material. However, results of destructive bond strength measurements of thermally sprayed cylinder coatings present bond strengths in the range between $30 - 60\,\text{MPa}$ [9, 25].

The adhesion bond of a thermally sprayed cylinder coating to a NMRP roughened substrate

material is illustrated in Figure 2.8. The adhesion bonding type may be further divided into macroscopic and microscopic mechanical interlocking. As the roughening profiles shows a wave-shaped profile, coating material fills the large contours of the substrate profile (macroscopic interlocking). However, the substrate surface additionally exhibits fine structures, allowing the individual spraying droplets to further interlock with the roughening profile on a different length scale than the macroscopic roughening structure (microscopic interlocking). Finally, also diffusion bond between substrate and coating material is highlighted as the third bonding mechanism.

Poor cohesion can be traced back to poor interfacial interlocking or to a low degree of metallurgical bond of the individual splats [28]. Defects in the microstructure can also reduce the overall bonding behavior of thermally sprayed coatings [6, 47]. Coating defects such as lateral splat interfaces lower the amount of contact areas between overlapping splats. Therefore, bond strength is reduced by such microstructural defects as the poor bond between splats and other imperfections in the form of pores cause mechanical properties of thermally sprayed coatings to be lower than those of respective monolithic materials [16, 47–49]. Mechanical testing revealed that in the presence of lateral splat interfaces only a limited area is in contact between overlapping splats reducing its cohesion strength and thus lowering the entire bonding behavior of the coating [35, 50, 51]. Hence, not only the adhesion of the coating layer to the substrate but also the cohesion lowered by inner coating defects plays a significant role in determining the overall bond strength. Both of these aspects has to be considered designing the spraying process and adapting the process parameters.

Additionally, the atmosphere during the coating process has a strong influence on the coating microstructures especially regarding the oxidation of spraying droplets and the resulting formation of coating defects. As discussed above, oxides within the coating microstructure are known to drastically reduce the contact area of overlapping splats and thus reduce the coating's cohesive bond strength [6, 40, 52]. Oxides along the splat boundaries can affect the interlamellar cohesion, while the bond strength of the coatings is reduced showing a high oxygen content [7, 30]. If molten particles with oxide layers on the outside impact on a substrate or on a splat, it flattens trapping the oxide layer in between and causing a strong coating defect, which is primarily extended horizontally [5]. Hence, by reducing the oxide content in the coating for instance increasing the particle velocity to reduce the time of the droplet in the oxidizing atmosphere, higher bond strengths of thermally sprayed layers can be found [38]. Oxides are also considered as coating defects since oxides are brittle and have different thermal expansion coefficients than the surrounding material thus causing high internal stresses and disturbing the mechanical behavior of the pure coating material [30, 53].

2.5. Thermal transport properties of thermally sprayed coatings

The information on the ability to transport heat within a material is of high interest, especially when it comes to choosing the thermal properties of a thermally sprayed coating for an industrial application [54]. The fundamental heat transfer process is defined by a continuum

equation as

$$\dot{\boldsymbol{q}} = -\lambda \nabla T \tag{2.1}$$

where $\dot{\boldsymbol{q}}$ is the thermal energy flux acting in the scalar temperature field T [55]. The proportionality factor λ is called thermal conductivity and is given in the units $\frac{\mathrm{W}}{m \cdot K}$. The thermal conductivity describes the transport of thermal energy in the investigated material within a temperature field over a specified distance and within a defined time interval. As the thermal conductivity λ connects the heat flow with a temperature gradient in the stationary heat conduction process, knowledge about this characteristic is strongly desired when choosing the right properties of a material which is exposed to great heat loads. However, due to time consuming and less productive measurements of the thermal conductivity, another thermal property comes into play [18, 54]. The thermal diffusivity α connects the spatial with the temporal gradient of a temperature field by

$$\triangle T - \frac{1}{\alpha}\frac{\partial T}{\partial t} = 0 \tag{2.2}$$

The thermal diffusivity is commonly given in the units of $\frac{\mathrm{m}^2}{\mathrm{s}}$ or $\frac{\mathrm{mm}^2}{\mathrm{s}}$. This quantity describes the ability of a material to equalize spatial temperature gradients over a defined time interval thus seeking for a thermal equilibrium. Table 2.2 presents an overview over selected thermal diffusivity values of pure metals, non-metals as well as alloys including the introduced AlSi8Cu3 and 13Mn6 alloys. Both, thermal conductivity and thermal diffusivity are closely related via the expression of

$$\alpha = \frac{\lambda}{\rho \cdot c} \tag{2.3}$$

where ρ is the density and c describes the specific heat capacity of the material. The description of thermal diffusivity measurements are further presented in Chapters 2.6, 3.1 and 3.2.

The thermal transport properties of metals and metal alloys are mainly defined by two mechanisms: **Electron thermal conduction** and **lattice conduction** (namely phonon conduction; lattice vibrations can be described by quasiparticles, showing bosonic behavior which are called "phonons") [56–58]. These two types of energy carriers contribute to the overall resulting thermal conductivity. However, depending on the investigated material, different energy carriers are dominant for the respective solid. The thermal conductivity via electrons is mainly dominant for all materials having free electrons (metals and alloys). Especially thermally high conductive metals such as gold, silver, copper or aluminum are majorly dominated by electron conduction [58]. However, for lower thermally conductive metals and alloys phonons contribute a significant part to the resulting heat conduction of such materials [58]. The effective thermal conductivity of a material is limited by scattering processes of the contributing energy carriers. Electrons can either be scattered by lattice impurities and imperfections, which dominate the scattering of the electrons at low temperatures. Electron-electron as well as electron-phonon interactions define further scattering processes limiting the contribution of these type of energy carriers to the total thermal conductivity. Further, also phonons can be scattered by other phonons or at lattice imperfections thus limiting their thermal conductivity.

Table 2.2.: Typical thermal diffusivity values taken from the Netzsch GmbH database of the LFA 467 *HyperFlash* system, if not stated otherwise.

Material	α [mm^2/s] at 25°	Material	α [mm^2/s] at 25°
Al	96.8	Fe	21.6
Al$_2$O$_3$	10.2	Stainl. Steel 310	3.4
AlSi8Cu3^2	66-69	Steel 13Mn6 (C < 0.2 %)^3	11.2
Cu	117.2	W	69.6

Thermally sprayed coatings mostly show a highly porous microstructure due to a lamellar coating formation (Chapter 2.3). Coating defects such as laterally orientated splat interfaces or globular pores (Figure 2.7) lower the resulting thermal transport properties of the solid material [8, 10, 12–15, 17, 37, 59]. To describe the influence of the porosity on the resulting thermal transport behavior, the heat transport through the material is described as a diffusion process based on Equation (2.1) [8, 12, 13, 15, 60]. While the mean free path of electrons or phonons in metals ranges in the scale of some nanometers [8], microstructure defects in thermally sprayed coatings mostly show extensions of several micrometers. Thus, the influence of coating porosity on the resulting thermal transport behavior of thermally sprayed coatings is generally described by the disturbance of this diffusion process of the thermal heat by the observed coating defects. Coating defects build up multiple thermal barriers lowering the heat flux, while generally neglecting heat transfer through interlamellar pores [13, 15]. While coating defects are either filled with gases or consist of oxides, both show thermal conductivities several orders lower than those of metals [15, 61]. The resulting thermal conductivity does not only strongly depend on the amount of porosity within the material but also on the shape of the pores and their orientation with respect to the heat flow [5, 14, 37]. It is reported that the most important parameter defining the thermal diffusivity of thermally sprayed coatings is the contact area of overlapping splats [5, 14, 15, 37, 62]. Due to the anisotropic layer formation as described previously, however thermal transport properties also show anisotropic behavior comparing the through-plane with the in-plane conductivity. While through-plane conductivity may be significantly reduced due to laterally oriented splats, in-plane conductivity can be comparable to those of bulk material [37]. The presence of oxide layers due to in-flight oxidation can cause void areas and lack of intersplat contacts between overlapping splats. In the presence of laterally orientated splat interfaces the through-plane thermal conductivity is mainly reduced due to the reduced effective contact area and the void morphology parallel to the substrate [7, 39]. Oxides in the microstructure act as thermal barriers for the heat transfer due to the fact that the thermal conductivity of oxides are much lower than those of metals [40, 61, 63]. It is shown in the literature that higher of oxide content in the coating material leads to reduced thermal conductivity [15, 39, 40].

---

[2]Thermal diffusivity values separately measured with a LFA 467 *HyperFlash* system (Netzsch Gerätebau GmbH, Selb, Germany)

[3]Reference: Schweißdraht Luisenthal GmbH – Saarstahl AG, Völklingen, Germany

In the following, various approaches are described which aim to explain the general influence of the microstructure on two-phase coating systems. The relevant references to the described approaches are discussed and cited in the following. Mathematical descriptions and models allow to modulate the perturbation of a defect morphology within a homogeneous material. Here, especially thermally sprayed coatings and their thermal behavior for both metallic and non-metallic materials are of high interest. While some research tries to calculate the influence of defects theoretically based on the perturbation of the continuum equation (2.1) and comparing it to experimental results, others use phenomenological approaches describing the influences of the microstructure qualitatively by using cross section images of the coatings and analyzing the defect structures.

Analytic descriptions of the thermal conductivity of a porous two-phase material aim to connect the thermal conductivity of the bulk material with a resulting term accounting for the influence of the defects on the overall thermal transport properties [64, 65]. On a macroscopic scale, the coating is seen as quasihomogeneous, as the size of the investigated sample is much larger than the size of the individual pores. Therefore, a measurement of the thermal transport properties acquires the thermal behavior of the two-phase system as an integral value. The measured thermophysical properties combine the thermal conductivity of the bulk material with the influence of the microstructure. Thus, the final measurement result does not simply allow to differentiate between the bulk material and the influence of the coating defects. In this context, the applied theoretical models describe the influence of the microstructure as an additional term added to the thermal transport properties of the ideal defect free bulk material.

Most theoretical descriptions base on the behavior of porous materials within an electrical field. It is a common approach to describe various physical phenomena with comparable theoretical models [66, 67]. The electric displacement field $\boldsymbol{D}$ within a dielectric medium arises from an applied electrical field $\boldsymbol{E}$ and is proportional to this field with the dielectric constant of the medium ϵ as

$$\boldsymbol{D} = \epsilon \boldsymbol{E} = -\epsilon \nabla \varphi. \tag{2.4}$$

Here, φ describes the electric potential. As the shape and size of defect structures affect the polarization behavior of two-phase materials, the resulting dielectric constant is varied due to the defect microstructure [16, 68–71]. The pioneering work of Maxwell in 1881 [68] and Rayleigh in 1892 [69] allowed to calculate the electrical behavior of a dispersion of spheres with fixed radius embedded in a continuous matrix theoretically. Further, Bruggeman in 1935 [70] and Niesel in 1952 [71] adapted Maxwell's approach by describing the electrical behavior of a dispersion of single spheres with varying radius, lamellar structures or spheroids. Here, the influence of the size and shape of the defects is accounted by the surface integral of such spheroids (also called shape factors [72]). However, the analogy of Equation (2.4) to Equation (2.1) allows to use the description of the electrical behavior for thermal properties of porous materials. Thus, in 1981 Schulz used the descriptions of Niesel's specific model of the influence of spheroids on the dielectric constant [71] to describe the thermal behavior of porous materials [12]. Expecting the obtained defects of a coating to be of spheroidal shape, a perturbation of the temperature field in Equation (2.1) is assumed. Based on the shape and the orientation of the spheroids, a theoretical correlation between the two-phase

material and the resulting thermal conductivity can be expressed showing promising results. The main focus of Schulz' work is to calculate the influence of the shape and orientation of the pores on the overall thermal conductivity of the coating [12]. Shape factors based on the surface of the spheroids as well as the orientation of the major axis of the spheroid to the incoming heat flux are taken to weight the porosity of the material and calculate the resulting thermal conductivity [65, 72, 73]. However, the expressed model function only accounts for one type of porosity concerning the shape and orientation of the spheroids. Therefore, if the microstructure of a solid material shows multiple types of defects, the entire defect morphology must be averaged to a final type of pores with fixed shape, size and orientation to estimate the resulting thermal conductivity based on this prediction.

While the presented theoretical model of Schulz [12] assumes the porosity of a coating only consisting of a single shape of pores having a specific orientation, in 2004 Cernuschi et al. [13] expanded the description from a single shape porosity to a spectrum of different porosity shapes and orientations. The model can be extended to a four-phase system by an iterative approach in order to describe three different classes of porosity within thermally sprayed coatings (non-flat spheroids, randomly orientated globular porosity and lateral splat interfaces). Based on the model function, thermal diffusivity measurements of thermally sprayed thermal barrier coatings are compared and show good agreement to the calculated values. The three different types of defects are extracted from cross section images of thermally sprayed coatings. Still, only three types of porosity are respected while an increase of the number of defect types results in a dramatic increase of number of terms and degrees of freedom thus lowering the accuracy of the model approach [13]. While this analytic approach is restricted to only a limited amount of shapes and orientations, it still reveals that a small amount of laterally orientated defects with its major axis orientated orthogonal to the heat flux produces a strong reduction of the thermal conductivity of the porous material [13]. The same authors tried to invert the previously described procedure, such that they used thermal diffusivity measurements on thermally sprayed coatings to calculate significant parameters of the underlying microstructure [17]. Using their model function described in [13], they fitted measured thermal conductivity values to this function to inversely assess the microstructure and obtain important parameters describing the defect morphology of porous thermal barrier coatings.

Parallel to the description of the electrical transport properties by Bruggemann [70] and thermal transport properties by Schulz [12], the "dethermalization theory" delivers a comparable description of the thermal diffusivity of two-phase materials [16, 60, 74]. Again, the behavior of the thermal heat flux can be well described by the conventional theory of the electrical displacement. In 2002, Ringermacher et al. use the same analogy of a dielectric medium within an electrical field and the resulting dielectric polarization density to the thermal diffusivity of such materials according to the thermal heat flux equation in (2.1) [74]. Thus, the description of the "dethermalization theory" founds on the same idea as discussed above by B. Schulz [12]. The defects cause a "depolarization" of the dielectric material acting against the resulting polarization due to the external applied electric field. As the "dethermalization theory" assumes the detected defects to be of spheroidal shape, also the defects have to be orientated perpendicular

to the incoming heat flux. This allows to use the descriptions of the electric displacement to explain the influence of size and shape of the defects on the resulting thermal conductivity represented by the introduced "dethermalization" [74]. While the theoretical descriptions of the thermal conductivity of two-phase materials by Maxwell-Bruggeman-Schulz as well as by the dethermalization theory of Ringermacher found on the same idea, unfortunately there are no cross references as well as comparisons available between these two theoretical approaches. However, Mayr et al. [59, 67] use this model to accurately predict the thermal behavior of carbon fiber reinforced polymers (CFRP) based on Computed Tomography porosity analysis and thermal diffusivity measurements by flash technique. Especially for such CFRP materials, the expected porosity is truly aligned along the surface of the samples showing spheroidal shape. However, applying this type of models on thermally sprayed coatings, the necessary boundary conditions must match the shape and orientation of the observed defect structures to accurately describe the thermal behavior.

In 1984, McPherson [14] proposed another analytic approach to calculate thermal transport properties of porous coatings. Based on the work from Bowden and Tabor [75] regarding the electrical resistance of metallic contacts, McPherson adapts this model to ceramic thermal barrier coatings of stacked layers with connected and non-connected splats. The resulting heat flux is only present at positions of contact between the individual splats thus determining the ratio between the thermal conductivity of pure bulk and porous material [14, 76]. Boire-Lavigne et al. [15] calculate the resulting thermal diffusivity of thermally sprayed tungsten coatings based on the assumptions of McPherson [14]. They also assume that the resulting heat flux can only be transferred over areas of real contact, while defects are seen as no-contact areas. A final model is shown where parameters such as splat thickness, splat distance, number of contact zones and the radius of the contact zones are considered to calculate the thermal diffusivity of the coating. Experimental results reveal that the quantity of contact zones is well correlated with the resulting thermal diffusivity of tungsten coatings. Further, it is also presented that the spraying atmosphere has a strong influence on the contact quality and quantity between splats and thus on the thermal diffusivity [15].

Aside from the theoretical and mathematical descriptions of the thermal transport properties of thermally sprayed coatings, another common approach to emphasize the influence of coating defects is to simulate the heat flux through the coating material based on a grid obtained from real cross section images. Wang et al. [10] use cross section images of thermal barrier coatings based on yttria-stabilized zirconia to create a realistic mesh of the coating microstructures. Cross section images are processed using a global threshold-based binarization algorithm to extract the defect information of the microstructure. This defect information is transferred into a simulation mesh and they further simulate the heat flux based on the continuum equation (2.1) with respect to the observed defects. Finally, the simulation results of the thermal diffusivity are compared with experimental measurement results of the coating samples [10]. Their simulations underline that laterally orientated splat interfaces result in a lack of contact areas thus clearly lowering the vertical heat flux from the coating surface
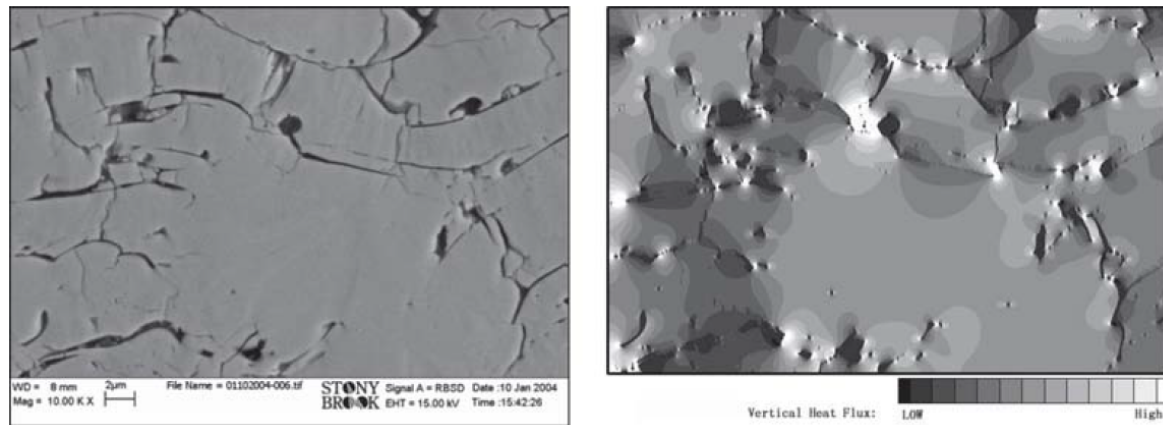
Figure 2.9.: (a) Original SEM image of yttria-stabilized zirconia coating, (b) vertical heat flux counter. Black and white represent the lowest and highest heat fluxes, respectively. This figure was originally published in [11].

to the substrate. Heat flux concentrations can be found between neighboring defects, while narrow spaces between such defects lead to even higher heat flux. Consequently, less heat flux can be found above and below of large defects [10, 11]. Such a simulation of the vertical heat flux within a thermally sprayed coating is presented in Figure 2.9. Finally, a great variation of heat flux caused by a broad variation of coating defects correspond to an overall lower effective thermal conductivity [10]. The comparison of simulations and experimental measurements confirmed the important role of interlamellar pores and splat interfaces on the reduction of the effective thermal conductivity [77].

2.6. Thermal wave interferometry (TWI)

As the thermal transport properties of a solid material are important characteristics, especially if exposed to great heat loads, measuring these properties is of high interest. Commonly, the laser flash analysis (LFA, see Chapter 3.2) is used as the standard technique to measure the thermal diffusivity of solids [78, 79]. This technique uses a pulsed heat flux (mostly from a halogen lamp or a laser) to heat up one side of a thin disk or square-shaped sample and records the surface temperature on the rear side of the sample by an infrared sensor. First described by Parker et al. [19] in 1961, the thermal diffusivity can be calculated from the temperature rise at the rear surface. However, the laser flash method has two main disadvantages with respect to non-destructive testing of components. First, this technique requires accurate and specified sample geometries. Even though the general method can be applied non-destructively, the necessary shape of the samples mostly requires destructive treatments. Further, the laser flash method generally operates as a transmissive measurement requiring access to both sides of the tested specimen. Especially for the application of thermal diffusivity measurements on coated systems, commonly only one side access can be ensured. Thus, in-situ measurements of thermally sprayed cylinder coatings are not possible with LFA. While measurements of coated samples are basically achievable, laser flash measurements are commonly applied for bulk materials. To measure the thermal properties of a coated system, additional thermal properties of the substrate must be known.

Alternatively, thermal wave interferometry (TWI) is well known to obtain reliable measurements of the thermal properties of thermally sprayed coating systems [20–24, 80–84]. TWI uses a sinusoidal modulated heat source to heat up a sample's surface generating so-called "thermal waves" in a layered structure. These thermal waves propagate through the material to the layer interface at which they are partially reflected due to an existing mismatch of the thermal transport properties of the materials involved at the interface. The reflected thermal waves propagate back to the surface and interfere with incoming thermal waves. The resulting temperature oscillation at the surface is related to the sub-surface layered structure and can be used to determine coating characteristics such as thickness or thermal properties [20]. Using a discrete Fourier transformation (DFT) of the surface temperature according to the excitation frequency, one can calculate the amplitude and the phase value of the oscillation. The obtained temperature oscillation is phase shifted with respect to the applied excitation, while this phase shift depends on the coating's thermal properties, on the layer thickness and on the mismatch of the thermal properties at the interface. An analytic expression of this phase shift is derived in the following chapter and can be found in Equation (2.42). The theoretical description of thermal waves was first published by Rosencwaig and Gerhso [85] in 1976 and later improved by Bennett and Patty [24] in 1982. Further, Almond and Patel [86, 87] discussed the method of thermal wave interferometry to detect sub-surface defects of thermally sprayed coatings non-destructively. A defect of the coating system may produce a different reflection of the thermal waves than the coating substrate interface, therefore coating defects may be observed by a change of the phase angle of the surface temperature [86, 87].

TWI measurements can be applied using different kinds of excitation sources. While halogen lamps or laser sources are quite common, also ultrasonic or eddy current excitation are valid approaches to introduce thermal waves in a solid material [18]. In the following, laser-excited lock-in thermography is described to measure the thermal diffusivity of thermally sprayed cylinder coatings. Such a thermography setup includes a high power diode laser source, a 2D infrared camera as well as a lock-in amplifier. Thus, the name *laser-excited lock-in thermography* is based on these three major components of the method. The laser diode introduces the thermal waves into the sample while the infrared camera detects the surface temperature oscillations and processes the individual thermography images. The lock-in amplifier is applied to filter only those frequencies fitting to the excitation frequency of the heat source. Therefore, disruptive signals are filtered out and the signal-to-noise ratio of this method is increased [88]. A detailed description of the used laser-excited lock-in thermography measurement setup can be found in Chapter 3.1.

TWI measurements have the main advantages that they can be applied non-destructively and contactless as well as with only one-side access to a sample. Further, to define the thermal transport properties of the layer, substrate properties are not necessary to be known. Hence, TWI provides the possibility for inline monitoring e.g. after the spraying process of the coating systems regarding to their thermal properties or coating thicknesses. As described above, thermal properties of thermally sprayed coatings depend on multiple microstructural defects as well as on the coating process parameters. Therefore, measuring the thermal properties of

a coating system may not only allow to determine the thermal behavior of the coatings but also enable to conclude information about the coatings microstructures or the applied coating process parameters [7, 77, 89, 90].

In this work, TWI measurements are performed within multiple crankcases to obtain the thermal characteristics of thermally sprayed cylinder coatings. Therefore, the method and the theory of thermal wave interferometry is explained in further detail. The following sections provide a theoretical description of thermal waves and their behavior in solid materials. A theoretical description of thermal waves is shown in Chapter 2.6.2. Thermal waves are building the base for latter application of TWI measurements of the thermal diffusivity for thermally sprayed cylinder coatings.

2.6.1. Introduction to thermal waves

The photoacoustic effect first described by Alexander Graham Bell in 1880 is known as the discovery of thermal waves [91]. Bell recognized an audible sound when a periodically interrupted beam of sunlight shined on a solid material entrapped in a closed cell. Based on Bell's discovery, Röntgen and Tyndall [92, 93] showed that also entrapped gases or liquids can produce such an audible sound when heated periodically. While the photoacoustic effect was a recognizable finding and Bell was convinced of his "best discovery" [94], however it soon became forgotten due to the lack of applications. In 1976, almost 100 years later, the photoacoustic effect came up again as this phenomena was used to measure the absorption coefficients of lighted solids. A solid is placed in a closed cylindrical cell, one side facing a backing material the other side facing entrapped gas. A sensitive microphone is placed in the center of the cell. Using chopped monochromatic light to illuminate the solid in the photoacoustic cell, the microphone detects sound waves as already described by Bell. It can be recognized that the amplitude of the recorded sound signal is proportional to the amount of heat emanating from the solid. This finding allows to correlate the recorded signal from the microphone with the heat absorption of the tested solid [85].

Rosencwaig and Gersho [85] first described thermal waves responsible for the photoacoustic effect theoretically in 1976. The photoacoustic effect is based on a periodic heating of a solid. The periodic heating causes heat oscillations by absorption of the light within the solid also called thermal waves. These thermal waves lead to a temperature oscillation on the surface of the solid. The source for the acoustic signal recorded by the microphone in the cell arises from the periodic heat flow from the solid surface to the surrounding gas [85]. This periodic heating of the gas results in an increase of the kinetic energy of the gas near the surface and thus causing pressure fluctuations in the cell. Such pressure fluctuations can be measured as audible sound by the microphone. Further, Rosencwaig and Gersho described a thin gas layer close to the surface of the solid as thermally responding to the heat flow from the solid to the surrounding air. This air layer can be seen as a vibrating piston expanding and contracting periodically due to the periodic heating of the sample surface and thus creating the acoustic signal. The periodic pressure fluctuations in the cell are proportional to the radiated heat of the solid material, hence there is a close correspondence between the strength of the acoustic

signal and the amount of absorbed light by the solid [85]. Rosencwaig and Gersho used and solved the thermal diffusion equation (2.2) with a wave approach and appropriate boundary conditions to describe the surface temperature of the solid material. These temperature oscillations show wave-like nature, however there are important differences since thermal waves arise from a differential equation that is of first order in time, while conventional waves such as electromagnetic waves are solutions of equations that are of second order in time [24]. Thermal waves are based on a diffusion process of the heat flux from regions with high temperature to regions with low temperature. This diffusion process can be described formally using a wave approach, however thermal waves cannot be seen as true conventional waves. Therefore, the description of thermal waves aims to characterize this heat diffusion process as accurate as possible, however deviations from the theory may arise as a result of the application of a wave description to a diffusive process.

As thermal waves show conventional wave-like character at some phenomena, reflection and transmission as well as interference effects can be detected for these type of oscillations [24,86,87]. While Rosencwaig and Gersho [85] implicitly described these behaviors in their theory, Bennett and Patty [24] explicitly showed the interference of thermal waves theoretically in 1982 based on the photoacoustic effect. They developed a one-dimensional theory to explain and calculate the reflection and interference of thermal waves within a thermally thin layer of solid material. The shown theory is still be used to describe the temperature oscillation on coated systems when heated periodically by a heat source.

2.6.2. Theoretical description of thermal waves

The following chapter presents the phenomena of thermal waves theoretically. The description is based on the findings of Bennett and Patty in 1982 [24]. Other detailed explanations about the formalism of thermal waves as well as their reflective and interference behavior can be found in [95, 96].

To describe thermal waves theoretically, one may start with the mathematical description of spatial and temporal resolved temperature fields by Fourier [55] in Equation (2.2) or even for a one-dimensional case

$$\frac{\partial^2 T(z,t)}{\partial z^2} - \frac{1}{\alpha}\frac{\partial T(z,t)}{\partial t} = 0. \tag{2.5}$$

Using an external heat source with a sinusoidal-modulated amplitude to heat up the surface of a sample periodically, thermal waves are introduced in the specimen. The one-dimensional thermal diffusion equation (2.5) can be solved by using a conventional wave approach

$$T(z,t) = T_0 \cdot \exp(i(\omega t + kz)) \qquad z \geq 0 \tag{2.6}$$

with

$$k^2 = -\frac{i\omega}{\alpha} \tag{2.7}$$

$$k = \frac{i}{\sqrt{2}} \cdot (1+i) \cdot \sqrt{\frac{\omega}{\alpha}}. \tag{2.8}$$

Defining the thermal diffusion length of such a thermal wave as

$$\mu = \sqrt{\frac{2\alpha}{\omega}}, \tag{2.9}$$

the wave number k can be reduced to

$$k = \frac{(i-1)}{\mu}. \tag{2.10}$$

Inserting the wave number k into the wave approach in Equation (2.6), one may find the solution of

$$T(z,t) = T_0 \cdot \exp\left(\frac{-z}{\mu}\right) \cdot \exp\left(i\left(\omega t - \frac{z}{\mu}\right)\right). \tag{2.11}$$

Describing the external heat flow $\dot{\boldsymbol{q}}$ with a sinusoidal amplitude shape and excitation frequency $\omega = 2\pi f$ as

$$\dot{\boldsymbol{q}} = \dot{\boldsymbol{q_0}} \cdot \exp(i\omega t), \tag{2.12}$$

we can use Equation (2.2) to express T_0 at the sample surface ($z = 0$) in Equation (2.11) to

$$T_0 = \frac{(1-i)\dot{q_0}}{\sqrt{2\lambda\rho c\omega}}. \tag{2.13}$$

Further, introducing the thermal effusivity

$$e = \sqrt{\lambda\rho c} \tag{2.14}$$

the thermal wave expression is written as

$$T(z,t) = \frac{(1-i)\dot{q_0}}{\sqrt{2\lambda\rho c\omega}} \cdot \exp\left(\frac{-z}{\mu}\right) \cdot \exp\left(i\left(\omega t - \frac{z}{\mu}\right)\right) \tag{2.15}$$

$$= \frac{\dot{q_0}}{e\sqrt{\omega}} \cdot \exp\left(\frac{-z}{\mu}\right) \cdot \exp\left(i\left(\omega t - \frac{z}{\mu} - \frac{\pi}{4}\right)\right). \tag{2.16}$$

To simplify the expression in (2.16), k' is introduced as

$$k' = \frac{1+i}{\mu} \tag{2.17}$$

to reduce the expression to

$$T(z,t) = T_0 \cdot \exp\left(i\omega t - k'z\right). \tag{2.18}$$

According to Equation (2.16) - (2.18), thermal waves are rapidly damped temperature oscillations with a thermal diffusion length μ. However, the penetration depth of thermal waves can be controlled by the excitation frequency f. Lower excitation frequencies cause deeper

penetration depth and vice versa. Therefore, varying the excitation frequency allows to obtain information about the sample from different depths [80]. Since the thermal diffusion length is also related to the thermal properties of the material, the applied frequencies have to be adapted to the investigated material as well as to the thickness of the sample. Further, the amplitude of a thermal wave depends on the external heat flow $\dot{q}_0$. However, the amplitude is also dependent on the applied frequency of the external heat source. Lower excitation frequencies result in higher amplitudes of the thermal waves and vice versa. The temperature oscillations described by (2.16) obtain a constant phase shift with respect to the incoming heat flux from the excitation source. On the sample surface ($z = 0$), the described phase shift is $-\frac{\pi}{4} = -45°$.

Showing wave-like character, thermal waves are reflected at material interfaces obtaining different thermal properties comparable to ultrasonic or electromagnetic waves [24, 86, 87]. However, reflections of thermal waves may only appear if the interface depth is in the same order as the thermal diffusion length μ.

To describe the reflection and transmission of thermal waves, we split up the thermal wave into three different parts, the intrinsic thermal wave $T_i(z, t)$ coming from the sample surface towards the interface, the reflected thermal wave $T_r(z, t)$ propagating backwards to the sample surface and the transmitted thermal wave $T_t(z, t)$ in the substrate material.

$$
\begin{align}
T_i(z,t) &= T_0 \cdot \exp\left(i\omega t - k_1' z\right) \tag{2.19}\\
T_r(z,t) &= T_0 \cdot R \cdot \exp\left(i\omega t + k_1' z\right) \tag{2.20}\\
T_t(z,t) &= T_0 \cdot \Gamma \cdot \exp\left(i\omega t - k_2' z\right) \tag{2.21}
\end{align}
$$

Here, R is the reflection coefficient and Γ is the transmission coefficient, while the indexes 1 and 2 describe the respective layer and substrate. To express the reflection of thermal waves at material interfaces, one may also need appropriate boundary conditions to describe the physical behavior of the thermal waves.

We assume a steady temperature at the interface such that

$$
T_i + T_r = T_t. \tag{2.22}
$$

Inserting the expressions of Equations (2.19) - (2.21) into Equation (2.22) leads to

$$
1 + R = \Gamma. \tag{2.23}
$$

Further, the heat flux at the interface must be conserved. Therefore, using the expression in Equation (2.1), the reflection and transmission coefficients can be written as

$$\dot{\boldsymbol{q}}_i + \dot{\boldsymbol{q}}_r \quad = \quad \dot{\boldsymbol{q}}_t \tag{2.24}$$

$$\lambda_1 k_1' - \lambda_1 k_1' R \quad = \quad \lambda_2 k_2' \Gamma = \lambda_2 k_2' + \lambda_2 k_2' R \tag{2.25}$$

$$\rightarrow \quad R \quad = \quad \frac{\lambda_1 k_1' - \lambda_2 k_2'}{\lambda_1 k_1' + \lambda_2 k_2'} = \frac{\sqrt{\lambda_1 \rho_1 c_1} - \sqrt{\lambda_2 \rho_2 c_2}}{\sqrt{\lambda_1 \rho_1 c_1} + \sqrt{\lambda_2 \rho_2 c_2}} \tag{2.26}$$

$$\text{and} \quad \Gamma \quad = \quad \frac{2\sqrt{\lambda_1 \rho_1 c_1}}{\sqrt{\lambda_1 \rho_1 c_1} + \sqrt{\lambda_2 \rho_2 c_2}}. \tag{2.27}$$

Using the definition of the thermal effusivity $e = \sqrt{\lambda \rho c}$, the reflection and transmission coefficients R and T are simplified to

$$R \quad = \quad \frac{e_1 - e_2}{e_1 + e_2}, \tag{2.28}$$

$$\Gamma \quad = \quad \frac{2e_1}{e_1 + e_2}. \tag{2.29}$$

As the reflected thermal waves travel back towards the sample surface, incoming and reflected waves show interference effects. To describe the interference of thermal waves, Bennett and Patty [24] use a one-dimensional description of the underlying physics. The described theory is only valid for certain boundary conditions. The substrate is assumed to be thermally thick. Hence, the thickness of the substrate must be much greater than the diffusion length of the thermal wave within the substrate. Also, the observed heat flux is only applied on the surface, additional heat sources are not considered. Further, the heat flows orthogonally into the layer. Lateral heat flow is not allowed for the description of a one-dimensional layer structure. Therefore, a homogeneous excitation over the entire surface is assumed.

The reflected thermal waves propagate back to the surface, while also reflections at the surface-air interface occur causing the waves propagating again towards the layer-substrate interface thus multiple reflections of the thermal wave within the layer must be considered. The reflection coefficient at the interface is written as R_i, while the reflection coefficient of the thermal wave at the layer-air interface is noted as R_a. To describe multiple reflections of the thermal waves within the layer, we may divide the thermal waves into the following parts [95]:

$$T_0(z, t) \quad = \quad T_0 \cdot \exp(-k'z) \cdot \exp(i\omega t) \tag{2.30}$$

$$T_1(z, t) \quad = \quad T_0 \cdot R_i \cdot \exp(-k'(2d - z)) \cdot \exp(i\omega t) \tag{2.31}$$

$$T_2(z, t) \quad = \quad T_0 \cdot R_i \cdot R_a \cdot \exp(-k'(2d + z)) \cdot \exp(i\omega t) \tag{2.32}$$

$$T_3(z, t) \quad = \quad T_0 \cdot R_i^2 \cdot R_a \cdot \exp(-k'(4d - z)) \cdot \exp(i\omega t) \tag{2.33}$$

$$... \quad = \quad ...$$

Here, d describes the thickness of the investigated layer. While the surface temperature of the sample is investigated, we can set $z = 0$. Since the surface temperature is the sum of all terms in Equation (2.30) to (2.33), we can show the expressions from above as rows divided by the

even and odd terms as

$$T_{even}(0,t) = T_0 \cdot \exp(i\omega t) \sum_{n=0}^{\infty} R_i^n \cdot R_a^n \cdot \exp(-2ndk') \tag{2.34}$$

$$T_{odd}(0,t) = T_0 \cdot R_i \cdot \exp(-2dk') \cdot \exp(i\omega t) \sum_{n=0}^{\infty} R_i^n \cdot R_a^n \cdot \exp(-2ndk'). \tag{2.35}$$

The surface temperature results from the sum of the even and odd term in Equations (2.34) and (2.35), which follows in the expression of

$$T(0,t) = T_0 \cdot \exp(i\omega t) \cdot (1 + R_i \cdot \exp(-2dk')) \sum_{n=0}^{\infty} (R_i \cdot R_a \cdot \exp(-2dk'))^n. \tag{2.36}$$

The expression in (2.36) is found to be a geometric series

$$\sum_{n=0}^{\infty} \chi^n = \frac{1}{1-\chi} \quad \text{for} \quad |\chi| < 1. \tag{2.37}$$

Since the reflection coefficients R_i and R_a always range between -1 to 1 as well as d and k' are truly positive values, the necessary condition of $|\chi| < 1$ is fulfilled and the geometric row converges. This leads to the expression of the function describing the surface temperature of a layered structure first derived by Bennett and Patty [24]:

$$T(0,t) = T_0 \cdot \exp(i\omega t) \cdot \frac{1 + R_i \cdot \exp(-2dk')}{1 - R_a \cdot R_i \cdot \exp(-2dk')} \tag{2.38}$$

Assuming a total reflection of the thermal wave at the layer-air interface, the reflection coefficient can be approximated to $R_a = 1$ and thus the equation simplifies to

$$T(0,t) = T_0 \cdot \exp(i\omega t) \cdot \frac{1 + R_i \cdot \exp(-2dk')}{1 - R_i \cdot \exp(-2dk')}. \tag{2.39}$$

Amplitude A and phase ϕ of the surface temperature oscillation are further calculated from Equation (2.39) by

$$A = |T(0,t)| \tag{2.40}$$

$$\phi = \arg(T(0,t)). \tag{2.41}$$

While especially the phase information of the surface temperature is of further interest, an analytical expression of the phase ϕ for the temperature oscillation on the surface of a layered structure caused by thermal waves can be found in [24]:

$$\phi(f) = \tan^{-1}\left(\frac{-2 \cdot R_i \cdot \exp(-2\eta\sqrt{f}) \cdot \sin(2\eta\sqrt{f})}{1 - (R_i \cdot \exp(-2\eta\sqrt{f}))^2}\right) - \frac{\pi}{4} \quad \text{with} \quad \eta = d\sqrt{\frac{\pi}{\alpha}}. \tag{2.42}$$

For any further consideration, the reflection coefficient R_i is simplified to R in the following.
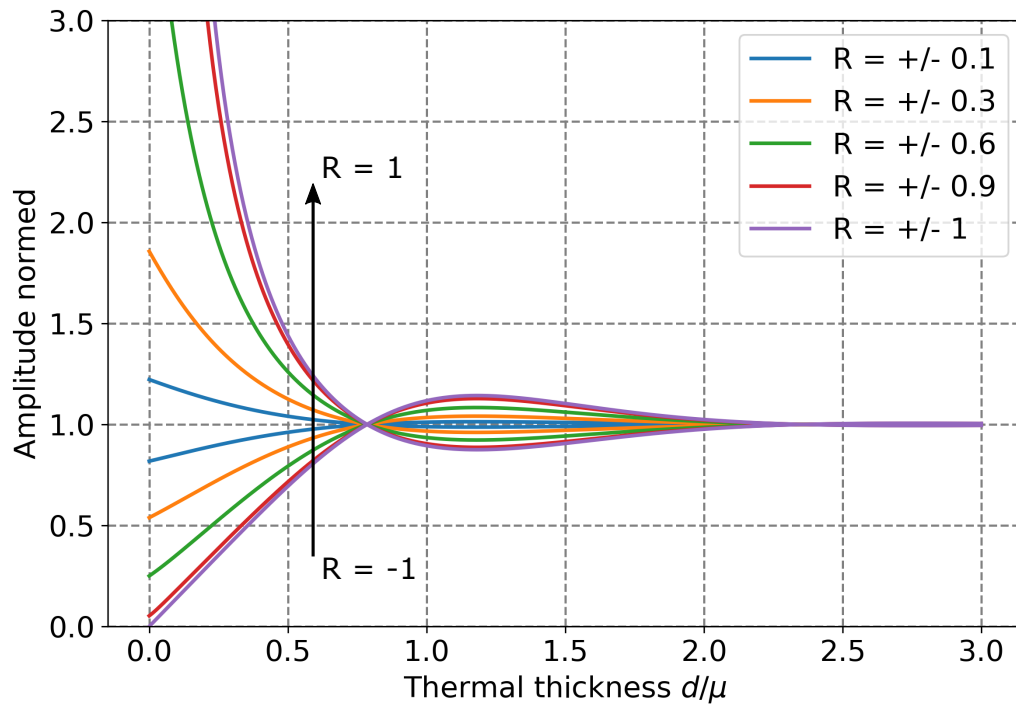
Figure 2.10.: Theoretical amplitude values with respect to the thermal thicknesses d/μ for variable reflection coefficients R according to Equation (2.41)
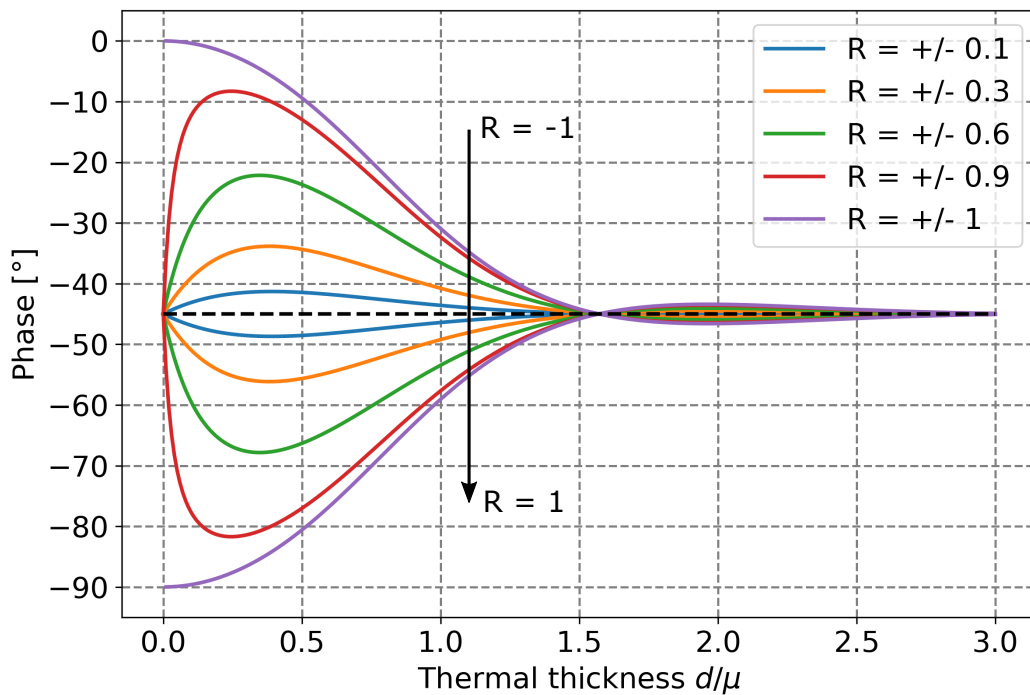
Figure 2.11.: Theoretical phase values with respect to the thermal thicknesses d/μ for variable reflection coefficients R according to Equation (2.41)

Whereas several publications have proven the application of TWI measurements on thermally sprayed coatings [20, 97–99], Equation (2.42) can be used to obtain thermal diffusivity values or thicknesses of coated layers [24]. Measuring the phase value for different excitation frequencies f allows to fit the theoretical expression to the measured phase values, while the fit delivers the two parameters R and η. However, to get either the thermal diffusivity or the thickness of the coating from the expression $\eta = d\sqrt{\frac{\pi}{\alpha}}$, one quantity has to be obtained by a reference method. In general, also the amplitude value could be used to assess the thermal properties of a coating, however phase values are known to obtain greater sensitivity since the phase has double the depth reach compared to the amplitude [80, 95, 99, 100]. The amplitude further contains topography information of the sample surface, which superimposes the information of the underlying coating structure [27, 101]. The expression $\eta\sqrt{f} = \frac{d}{\mu}$ is known as the thermal thickness. For high thermal thicknesses (if the thickness of the layer is much larger than the thermal diffusion length), the expression in Equation (2.42) converges against $-\frac{\pi}{4} = -45°$. Applying thermal waves in thermally thick materials such as bulk materials, reflection and interference effects may not appear leading to a constant phase shift of the surface temperature to the excitation of $-45°$ as already shown in Equation (2.16). The amplitude A and the phase ϕ of the temperature oscillation are shown in Figures 2.10 and 2.11 respectively. Both parameters are plotted for variable reflection coefficients R. The phase values are symmetric to the convergence value of $-45°$, while higher absolute reflection coefficients result in greater amplitudes of the phase values. Both, amplitude and phase values cross the convergence values for the same thermal thicknesses independent of the reflection coefficient.

2.7. Motivation and objectives

The main objective of this work is to characterize the bond strength of thermally sprayed cylinder coatings non-destructively. Whereas destructive off-site testing is applied during the large-scale production of Mercedes-Benz powertrains to ensure the desired quality of the cylinder coatings, a fast and reliable non-destructive testing method showing a quick feedback loop would be highly favorable to increase the efficiency of the production process and reduce additional waste. Since the literature review has shown that microstructure and the resulting defect morphology of such coatings are predominantly controlling the bonding behavior, this work aims to assess the microstructure of thermally sprayed cylinder coatings non-destructively. As the thermal transport properties of thermally sprayed coatings are strongly related to the microstructure, measuring the thermal diffusivity of the cylinder coatings may be used to characterize and assess the defect morphology of wire arc sprayed cylinder coatings [82, 102]. Thermal diffusivity measurements can be performed contactless as well as non-destructively and they allow for a fast feedback loop within an industrial process chain. Conventionally, laser flash analysis (LFA) is seen as the standard method measuring the thermal properties of solid materials. However, while the measurement itself is being non-destructive, LFA requires defined sizes of the measurement samples as well as access to the rear side of the coating. Due to the shape and size of a crankcase, destructive preparation of the cylinder coatings in advance to the LFA measurements would be required thus disqualifying this method for non-destructive testing of cylinder coatings. However, thermal wave interferometry measurements

have developed over the last decades to reliably measure the thermal characteristics of layered structures [20–23, 86, 96]. Since TWI measurements only require one side access to the investigated sample surface without any specific sample preparation, this method is considered to examine thermally sprayed cylinder coatings.

In this context, laser-excited lock-in thermography is used applying TWI measurements to investigate the thermal diffusivity of thermally sprayed cylinder coatings non-destructively. Therefore, a detailed parameter study of laser-excited lock-in thermography need to be examined to obtain a reliable measurement setup of the chosen method. Further, mechanical bond testing evaluates the bond strength of the investigated cylinder coatings. The correlation of thermal and mechanical properties of wire arc sprayed cylinder coatings is the main objective shown in this work. As both coating properties are controlled by the coating microstructure, additional metallographic methods are chosen to assess the coating defect morphology. Therefore, cross section specimens are cut out of the crankcases to evaluate the coating microstructures via optical microscopy. These cross section images are analyzed quantitatively by image analysis algorithms to process the coating defects and correlate them to the measured thermal diffusivity values. Further, analysis of the fracture surface after bond testing allows to understand the bonding mechanisms and the resulting primary coating failure. Additionally, X-ray computed tomography measurements are used to gather further three-dimensional information about coating defects to obtain a holistic consideration of the relation between coating microstructure and thermal as well as mechanical properties.

3. Applied methods

The following chapter describes all applied methods used for this work. While the main focus is set on the non-destructive testing of thermally sprayed cylinder coatings using **laser-excited lock-in thermography**, also several additional method are used to characterize the coating material. Thermal diffusivity measurements using **thermal wave interferometry** are described in Chapter 3.1. Further, the **laser flash method** is introduced since it is used as a reference method for thermal diffusivity measurements of the thermally sprayed cylinder coatings. Destructive **pull-off adhesion testing (PAT™)** is applied to quantify the bond strength of cylinder coatings to the crankcase substrate. PAT™ is used as an off-site testing method during the large-scale production to monitor the quality of the coating bond at Mercedes-Benz. Optical microscopy of cross sections as well as scanning electron microscopy (SEM) are two optical methods commonly used in the **metallography** to obtain information about the composition of coatings. Microscopy images of coating cross sections reveal information about the microstructure of the cylinder coatings and are analyzed quantitatively regarding their defect structure and morphology. The fracture after PAT™ is evaluated using SEM images to analyze the remaining coating material on the substrate thus allowing to quantify the percentage of cohesive and adhesive failure. Additionally, **X-ray computed tomography (CT)** allows to assess the porosity and defect structure of thermally sprayed cylinder coatings from three-dimensional volume data. Finally, **non-destructive thickness measurements** are conducted by a magnetic-inductive method. This method measures the amount of ferromagnetic material (steel coating) beyond a paramagnetic substrate (aluminum alloy).

Further, it is of great importance to introduce the coordinate system of cylinder bores within a crankcase. Figure 3.1 shows the schematic of such a coordinate system. The cylinder coating positions are divided by the individual cylinders, angles of one bore and the height positions along the liner. Numbering the individual cylinders is done consecutively. The cylinder bore closest to the gear box when assembled within the powertrain receives the highest number (commonly four or six, depending on the number of cylinder bores). Further, angle positions of the cylinder bores are noted counter clockwise again starting with the angle facing the surface side orientated to the gear box. Height positions along the liner are measured from the cylinder head sealing surface downwards to the crankshaft.
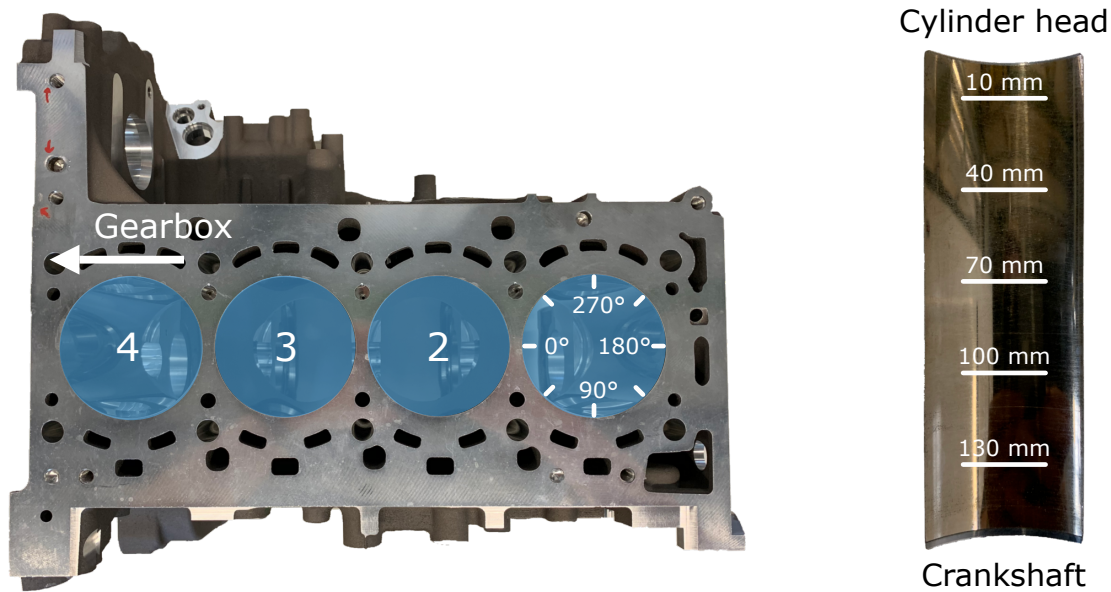
Figure 3.1.: Coordinate system of a crankcase. The cylinders are numbered consecutively, while the cylinder facing the gear box refers to the highest number. Angle positions are measured counter clockwise, starting again with the angle facing the gear box. Height positions along the liner are measured from the cylinder head sealing surface downwards to the crankshaft.

3.1. Laser-excited lock-in thermography

Based on the theory described in Chapter 2.6, thermal wave interferometry measurements are performed using a laser-excited lock-in thermography setup by edevis GmbH (Stuttgart, Germany). The TWI measurements are applied for the cylinder coatings in crankcases of type OM656 (Mercedes Benz AG, Stuttgart, Germany). These crankcases are used for the newest generation of six cylinder diesel type engines manufactured in the large-scale production at Mercedes-Benz. A sketch of the different components involved in the lock-in thermography setup is shown in Figure 3.2 top. The sketch includes the necessary control processes to perform TWI measurements. Additionally, a photography of the thermography setup is also presented in the same figure at the bottom. The marked components are discussed in the following.

The thermography system contains an infrared camera **(1)** of type FLIR X6580 sc (FLIR Systems, Wilsonville, USA) to detect the surface temperature oscillation of the investigated samples. The infrared camera uses an InSb detector with a full field of 640×512 pixels and gets cooled by a Stirling cooler. The detector allows for a maximum frame rate of up to $355 \, \mathrm{Hz}$ at the maximum window size but also for faster frame rates at smaller sub-windows. For all following measurements, the active detector size is chosen to a field of $320 \times 284 \, \mathrm{px}$ and a resulting frame rate of $600 \, \mathrm{Hz}$. Further, the detector's spectral sensitivity is given between $1.5 - 5.5 \, \mathrm{\mu m}$. A detailed data sheet of the FLIR X6580 sc infrared camera can be found in the appendix in Table A.1.

Conventional infrared detectors based on semiconductor materials such as InSb use the photoelectric effect comparable to solar cells [95]. The irradiated photons from the observed sample create electron-hole pairs in the semiconductor material resulting in a charge, which gets stored
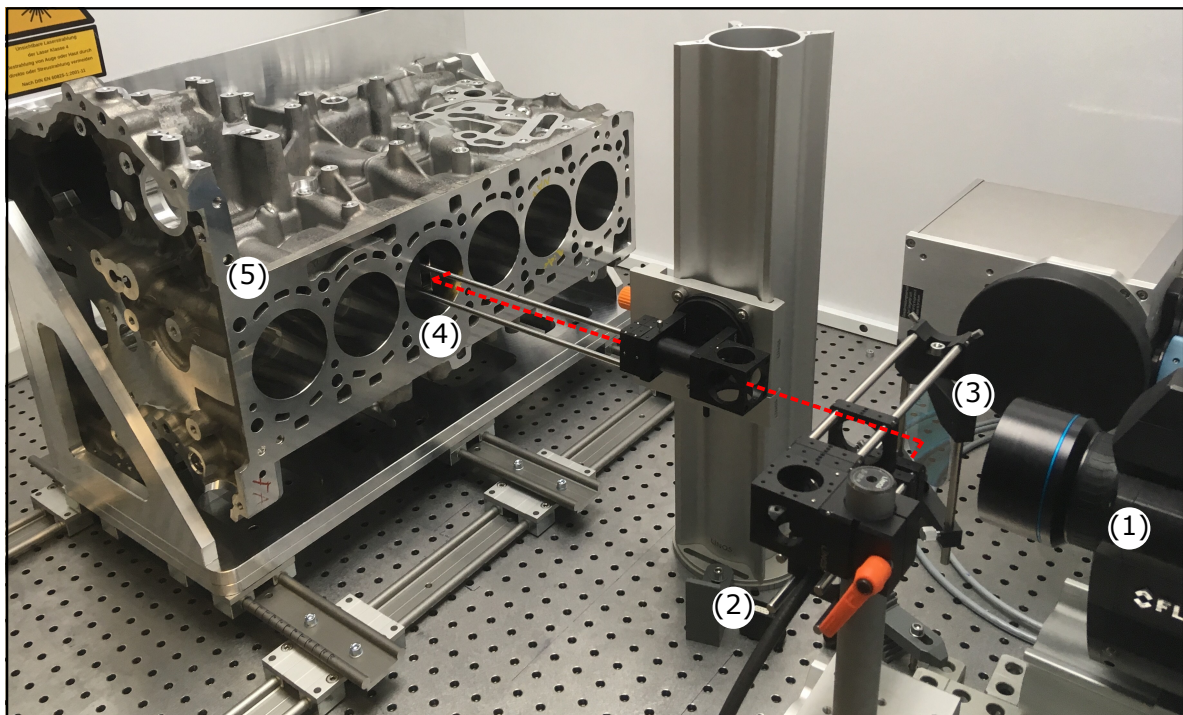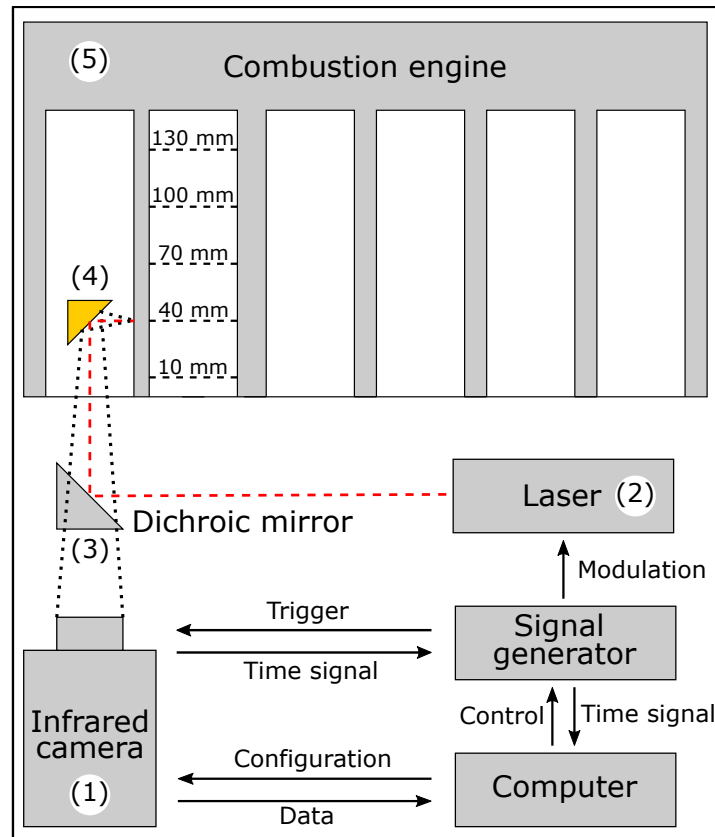
Figure 3.2.: Sketch (top) and photography (bottom) of the used laser-excited lock-in thermography setup. (1) Infrared camera, (2) laser fiber, (3) dichroic mirror, (4) gold-plated aluminum mirror including attachment and (5) combustion engine of type OM656 (Mercedes Benz AG, Stuttgart, Germany). The dotted red line indicates the optical path of the diode laser.

capacitivly in the individual pixels. After a chosen time (also known as the integration time) the electrical information of the pixel is read out, which is proportional to the intensity of the thermal radiation from the subject surface within the spectral sensitivity of the IR camera detector [95]. These pixel information can be calibrated on temperature values using a black body reference sample. The spectrum of the infrared radiation of the black body is known from the Planck's law approximating the emissivity of the black body as nearly 1. Therefore, using this calibration of the infrared camera, one may assume a comparable emissivity of the latter observed sample surface. Due to the relatively low emissivity of metals especially for polished steel surfaces, a precise measurement of the absolute temperature of the surface is anyway quite challenging. However, since TWI measurements are mainly performed gathering the phase information of the temperature oscillation on the sample surface, the absolute temperature value can be neglected and it may not be necessary to calibrate the digital levels of the detector onto absolute temperature values.

Further, the infrared camera is operated using a corresponding objective with a focal length of 50 mm resulting in a working distance of 500 mm between camera objective and focusing plane. The described setup shows an optical resolution of about 0.2 mm per camera pixel. The infrared camera is controlled by a conventional personal computer, allowing to configure and read out the measured temperature images. The computer further analyzes the thermography data of the infrared camera using the software DisplayImg 6 (edevis GmbH, Stuttgart, Germany). The software applies a DFT to the acquired temperature data according to the applied excitation frequency. The DFT allows to obtain the amplitude and the phase values of the surface oscillation with respect to the heat flux from the excitation source. Since each pixel is transferred individually, one obtains an amplitude and a phase image of the sample surface.

The thermography setup does further include a signal generator. This generator controls the heat source of the system. The signal generator receives a timing signal generated by the infrared camera to modulate the amplitude of the heat source. The set frame rate of the camera can be read out by the signal generator allowing to synchronize the infrared camera with the heat source. This results in a minimized time delay between excitation and data acquisition, thus being crucial for precise measurements of the phase information between introduced heat flux from the heat source and the read out temperature oscillation on the sample surface. However, due to the limited camera frame rate of 600 Hz, also the excitation frequency of the heat source is limited. To apply a reliable DFT and thus to obtain detectable amplitude and phase images, a minimum of at least four individual temperature images per excitation period is applied. Therefore, the maximum possible excitation frequency is set to 600 Hz/4 = 150 Hz.

TWI measurements are performed with a high power diode laser of type DSC11 from OsTech e.K. (Berlin, Germany). The laser can be operated with a maximum power of 250 W and shows a wavelength of 938 nm. The amplitude of the laser power is controlled by the signal generator. Further, the laser is transferred onto the sample surface via an optical fiber **(2)**. The optical fiber's end is placed behind a lens system with a focal length of 9 mm to vary shape and size as well as to focus the laser beam on the sample surface. The laser beam is chosen to have a top-hat shape. However, since the laser beam is emitted divergent from the

fiber's end, the laser spot diameter depends on the distance between laser fiber's end and the sample surface. The applied laser spot diameter can be set between $6.5\,\text{mm} - 20\,\text{mm}$. Since the used diode laser operates in the near infrared and is not visible, an additional low power HeNe laser is used to define the position and the focus of the main laser. The HeNe laser is guided through the same optical fiber and follows the optical path of the diode laser. While the excitation of the laser source and IR camera have to focus on the same spot, a coaxial setup with the infrared camera is realized using a dichroic mirror **(3)**. A dielectric coating allows the dichroic mirror to be reflective for wavelengths below $1200\,\text{nm}$, such that the optical fiber's end and the lens system can be placed at an angle of $90°$ to the measured sample. Due to its dichroic coating, the mirror is transmissive for wavelengths above $1200\,\text{nm}$ such that the infrared camera can be placed behind the mirror in line to the measured sample.

The described setup allows to perform TWI measurements of a variety of samples, however the special geometry of cylinder crankcases requires an additional optical and mechanical system. In order to investigate the thermal diffusivity of cylinder coatings in the crankcase non-destructively, laser beam and detected radiation have to be deflected by another $90°$ within the cylinder bore. A gold-plated aluminum mirror **(4)** which is highly reflective for wavelengths ranging from $800\,\text{nm}$ to $12000\,\text{nm}$ is plunged into the crankcase. The mirror's attachment is mounted axially symmetric to the laser beam and can be rotated such that every angle position of the cylinder coating can be accessed. Finally, applying TWI measurements to cylinder coatings, the crankcases **(5)** are mounted horizontally on a mechanical attachment such that the cylinder head sealing surface is facing the infrared camera. The attachment is mounted on a sliding system allowing to move the crankcase in two dimensions manually to access all six cylinders bores and the entire depth of the liners. Combined with the rotating attachment of the gold-plated aluminum mirror, TWI measurements can be performed for every position of the cylinder liners. The entire setup is placed inside a laser protection cabin due to safety regulations regarding the high power infrared laser source. Therefore, TWI measurements can only be initiated with closed cabin doors. While the entire cabin fits the mentioned crankcases and shows enough space to access all six cylinder bores, however working distances and setup configurations of the optical components are limited by the cabin as well as by the crankcase dimensions.

Selected amplitude and phase images of TWI measurements for six different excitation frequencies are shown in Figure 3.3. The applied parameters will be examined and discussed in further detail in the following Chapter 4. Still, the acquired amplitudes of the thermal waves strongly decrease with increasing excitation frequency. Bright spots within the amplitude images can be identified as surface contamination of the cylinder liner or contamination of the optical components. Further, horizontal artifacts within the amplitude images as well as a diffuse artifact at the right edge of the excited area reveal reflections of the optical components and the mirror attachments on the highly reflective coating. These artifacts are further found within the phase images and impact the acquired phase values. The discussed artifacts are highlighted by red circles within the amplitude and phase images of Figure 3.3. In addition,
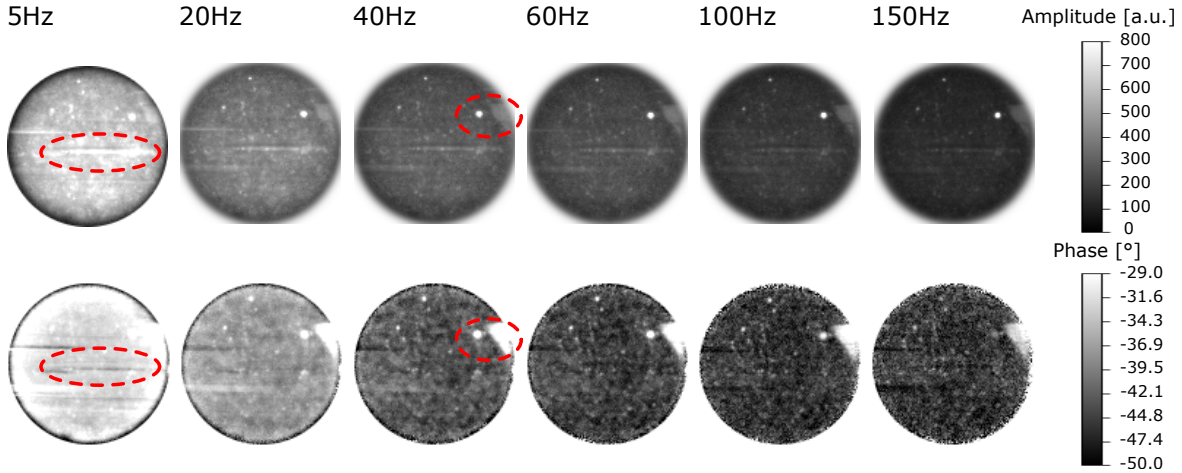
Figure 3.3.: Amplitude (top) and phase (bottom) images of TWI measurements on thermally sprayed cylinder coatings for six different excitation frequencies. Red circles mark artifacts found in both amplitude and phase images. Following parameters are applied for the presented thermography measurements: laser spot size: 20 mm, laser power: 125 W, cond. time: 5 s, meas. time: 5 s.

the phase values decrease towards higher frequencies and the resulting signal-to-noise ratio of the excited area is lowered. According to the camera frame rate of 600 Hz, higher excitation frequencies lead to a lower amount of data points per period, increasing the uncertainty of the applied DFT to the measured data thus lowering the overall signal-to-noise ratio.

TWI measurements are able to obtain the thermal diffusivity of layered structures [20–22]. Phase values acquired for various modulation frequencies are fitted to the model function in Equation (2.42) by nonlinear least square fitting thus calculating the parameters η and R of the cylinder coatings. Since η contains the thickness as well as the thermal diffusivity of the coating, thickness values must be obtained using a reference method. Here, a reference method based on the magnetic properties of the cylinder coating is used to access the necessary thickness values as described in [27] or in Chapter 3.6. Therefore, thermal diffusivity values of the coatings can be calculated from TWI measurements. A repeatability study of the phase measurements is shown in the Appendix A.2. Here, the standard deviations of 30 individual phase measurements are presented over various excitation frequencies. The resulting standard deviations are found to be less than 0.2 ° for all applied frequencies.

3.2. Laser flash analysis

The laser flash analysis (LFA) or simply flash analysis is another method to measure the thermal diffusivity of solids or liquids [78, 79]. The flash method was developed and first described by Parker et al. in 1961 [19]. Several improvements of Parker's description accounting for heat losses of the samples, transient heat flux or effects of the finite heat pulses allow to accurately describe the thermal behavior of material samples [103–105]. A sample with defined size and shape is lighted at the front side by a heat pulse (mostly from a laser source or a halogen lamp). The length of the pulses can be varied depending on the investigated material and its thickness. An infrared detector focused on the rear side of the sample detects and measures the temperature rise on the rear surface. For the one-dimensional adiabatic case the thermal
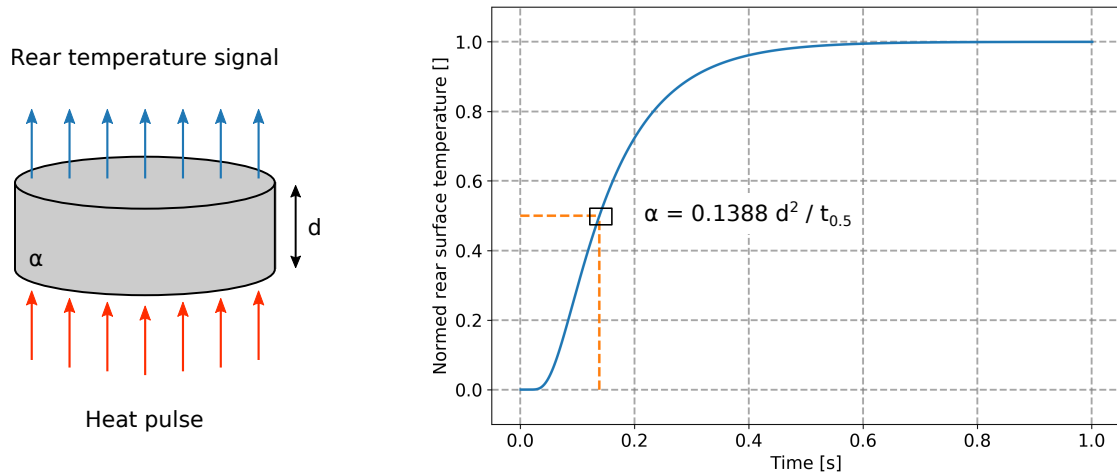
Figure 3.4.: Left: Schematic of the laser flash method detecting the rear surface temperature of the sample. Right: Theoretical curve of the rear temperature for a sample with thickness $d = 2\,\text{mm}$ and thermal diffusivity $\alpha = 4\,\text{mm}^2/\text{s}$ according to Equation (3.1). The thermal diffusivity is calculated by the time $t_{0.5}$ of the half maximum of the rear surface temperature rise.

diffusivity is evaluated from the time-dependent temperature rise of the rear surface according to [19] as

$$\alpha = 0.13883 \cdot \frac{d^2}{t_{0.5}}. \tag{3.1}$$

Here, d represents the thickness of the sample and $t_{0.5}$ is the measured time to the half maximum of the temperature rise. The measurement times of a laser flash measurement range between $1\,\text{ms}$ to $120\,\text{s}$. Knowing the specific heat capacity as well as the density of the sample material, also the thermal conductivity $\lambda = c \cdot \rho \cdot \alpha$ can be obtained from the flash measurement. Modern flash apparatuses are even able to measure the thermal heat capacity of a material, while the density is commonly determined using Archimedes' principle. The basic idea of LFA as well as the theoretical temperature rise is shown in Figure 3.4. Allowing to measure the thermal diffusivity highly accurate and reproducibly [106], however a defined size and shape of the sample as well as access to both sides of the sample is required. Commonly, the required sample sizes are either quadratic $10 \times 10\,\text{mm}$ or circle shaped with a diameter of $12.7\,\text{mm}$. In general, thermal diffusivity measurements can be seen as non-destructive, however the sample size mostly requires additional destructive preparation. Therefore, in-situ measurements of the thermal diffusivity within a crankcase cannot be applied.

While Parker et al. described the flash method for bulk materials, also thermal properties of layered system can be measured by the LFA [107, 108]. In this context, the introduced heat flux is described by Fourier's diffusion equation (2.2) which is applied to a two layered system. Again, the temperature rise on the rear side of the sample surface is recorded by the IR detector. By fitting the acquired temperature signal to the derived theoretical model, the thermal diffusivity of the coating layer can be specified [109]. However, determining the thermal diffusivity of a layered coating system accurately using LFA, several additional material properties are required. In this context, the specific heat capacity and density of the coating layer as well as specific heat capacity, density and thermal diffusivity of the substrate material must be

known. Further, also thickness values of both layer and substrate are required to determine the thermal diffusivity of the coating layer. Therefore, either reference measurements of the substrate material or literature values must be available to determine the thermal conductivity of a coating. In contrast to the thermal diffusivity measurement of bulk material, the required material properties dramatically increase, and also the thermal contact resistance between the two layered structures effects the measurement signal [109].

For reference purposes, TWI measurements described in Chapter 4.8 are compared to the laser flash method using the commercially available system LFA 467 *HyperFlash* (Netzsch-Gerätebau GmbH, Selb, Germany). According to the manufacturer's data sheet, the system shows an accuracy of $\pm 3\,\%$ and a repeatability of $\pm 2\,\%$. However, uncertainties of required material properties such as the sample thickness lower the effective accuracy of the LFA method. In fact, expanding the conventional LFA approach to a layered coating system, a significant reduction of the method's accuracy is expected. Due to the more complex theoretical model function as well as due to the increase of influencing factors and required material properties, certainly a significantly higher uncertainty of thermal diffusivity measurements on layered coating systems is expected.

3.3. Pull-off adhesion testing (PAT™)

The bond strength of cylinder coatings to the substrate is measured destructively by in-situ "Pull-off adhesion testing" (PAT™) of type AT101E (DFD Instruments, Norway) compliant to relevant testing standards [110–112]. Testing stamps with $8\,\mathrm{mm}$ diameter are placed onto the cylinder running surface within the crankcases. In advance, the cylinder coatings are mechanically roughened by sand blasting to guarantee sufficient bond between the test stamps and the cylinder coating. The test elements are glued onto the roughened surface using a one-component adhesive bond based on epoxy resin (Delo Monopox AD 297, DELO Industrie Klebstoffe GmbH & Co. KGaA, Germany). The test elements need to be mounted vertically on the running surface such that the adjacent force can be applied perpendicular to the coating structure as misplaced test elements may cause false bond strength measurements. Afterwards, the crankcases are placed in an oven for $120\,\mathrm{min}$ at $180°\mathrm{C}$ to cure the adhesive. After cooling, the cylinder coatings are milled around the testing stamps to preserve a defined measurement area with $8\,\mathrm{mm}$ diameter and to further remove excessive adhesive material. Finally, the testing elements are pulled of from the crankcase hydraulically causing a break of the cylinder coating and the substrate. Using a convex adapter board, the curvature of the cylinder liner is compensated such that the applied force is always perpendicular to the cylinder liner. By measuring the applied maximum force during the measurement, the bond strength is calculated due to the defined measurement area according to [113]. The operator inspects the fracture surface after PAT™ and allocates the observed failure to adhesive and cohesive failure respectively. However, in general coating is never fully removed from the substrate such that a mixture of adhesive and cohesive failure occurs. Additionally, failure of the adhesive glue may appear. The adhesive is specified to a maximum load of at least $60\,\mathrm{MPa}$, whereas experiments have shown that the adhesive can overcome loads of up to $72\,\mathrm{MPa}$. As mostly the mechanical strength of the glue is sufficient for bond test, failure of the adhesive glue is noted separately in
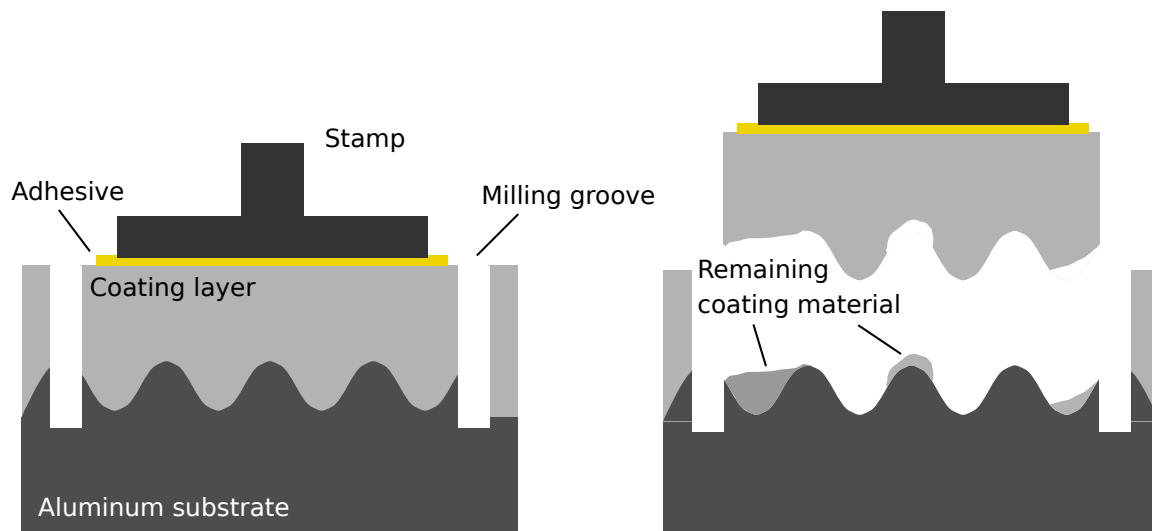
Figure 3.5.: Schematic of the pull-off adhesion testing method (PAT™) before (left) and after (right) bond testing.

Figure 3.6.: PAT™ areas after destructive bond testing along one cylinder liner.

the testing protocol. The accuracy of the testing device according to the associated data sheet is given by $\pm 2\,\%$. The testing procedure is visualized in Figure 3.5 before and after testing. PAT™ is used in the large-scale production of all common crankcase types as an off-site testing method to monitor the quality of the bond between cylinder coating and aluminum alloy substrate. However, due to its destructive character, tested crankcases cannot be feed back into the manufacturing process after testing, but need to be recycled. Respective PAT™ areas along one cylinder liner are presented in Figure 3.6. Further, since PAT™ requires excessive mechanical treatments and preparation of the cylinder surfaces as well as curing the adhesive in an oven, measuring the bond strength of the coatings within an individual crankcase at several liner positions takes up to several hours.

3.4. Metallography

Metallography deals with the study and analysis of metallic samples and their structures using microscopy methods. Metallography observes and investigates the structure and composition of metallic materials revealing its microstructure and phase composition [114, 115]. While different types of microscopy methods can be used to obtain the structure of metallic samples, in the following optical light microscopy (OLM) and scanning electron microscopy (SEM) are discussed. The two different microscopy methods are used to obtain images of cross section specimens to analyze the microstructure of thermally sprayed cylinder coatings as well as to analyze the fracture after destructive bond testing regarding remaining coating material on the aluminum alloy substrate. Further, images taken by either OLM or by SEM are analyzed quantitatively. Applying image analysis (IA) algorithms, subjective optical impressions can be analyzed quantitatively to reveal the necessary information objectively. Two different IA algorithms are introduced to quantify the defects within the microstructure of thermally sprayed cylinder coatings as well as to measure the remaining coating content on the aluminum alloy after bond testing.

3.4.1. Cross section analysis

Analyzing the microstructure of thermally sprayed cylinder coatings, cross section specimens need to be cut out of the crankcases at the respective positions. Depending on the desired field of view, the specimens are cut out along the cylinder liner lengthwise from the cylinder head sealing surface towards the crankshaft. Here, cross section specimen show extensions of about 20 mm. After drying and degreasing, the samples are embedded in resin followed by multiple preparation steps including polishing of the cross section to obtain a flat surface. Cross section images are taken with an Axio Observer microscope (Carl Zeiss AG, Oberkochen, Germany) showing a resolution of up to 0.25 µm/pixel. Due to the high optical resolution even small coating defects within the microstructure are observed. A respective cross section image of a cylinder coating is shown in Figure 3.7 (top left). Since single microscopy images show sizes of about 650×650 µm, the entire cross section specimen is covered by over 30 individual microscopy images. The images are taken consecutively such that assembling of the individual images allows to obtain the microstructure along the entire cross section.

Quantitative image analysis of the cross section images is carried out using an algorithm based on the *OpenCV* library implemented in *Python*. The segmentation algorithm aims to extract the observed information about the coating defects from the microscopy image. The basic idea of the segmentation algorithm is shown in Figure 3.7. The microscopy images are taken with color depth of 8 bit resulting in 256 grey scales. The histogram of the microscopy images reveals three separated peaks representing air and coating defects, the coating material and the aluminum alloy substrate. Using a global-threshold, the cross section images are binarized to separate coating defects from the coating material, while the resulting binarized images only contain the morphology of the coating defects. However, only defects with an area greater than 500 px are processed to reduce the calculation time. Further, connected component labeling enables access to a large variety of features of each individually detected defect [116]. Connected component labeling detects neighboring pixels and recognizes them as a connected

- Binarization with global-threshold based on histogram
- Connected component labeling
- Accessing a variety of features (shape, size, etc.) of each defect
- Filter: Defect area > 500px
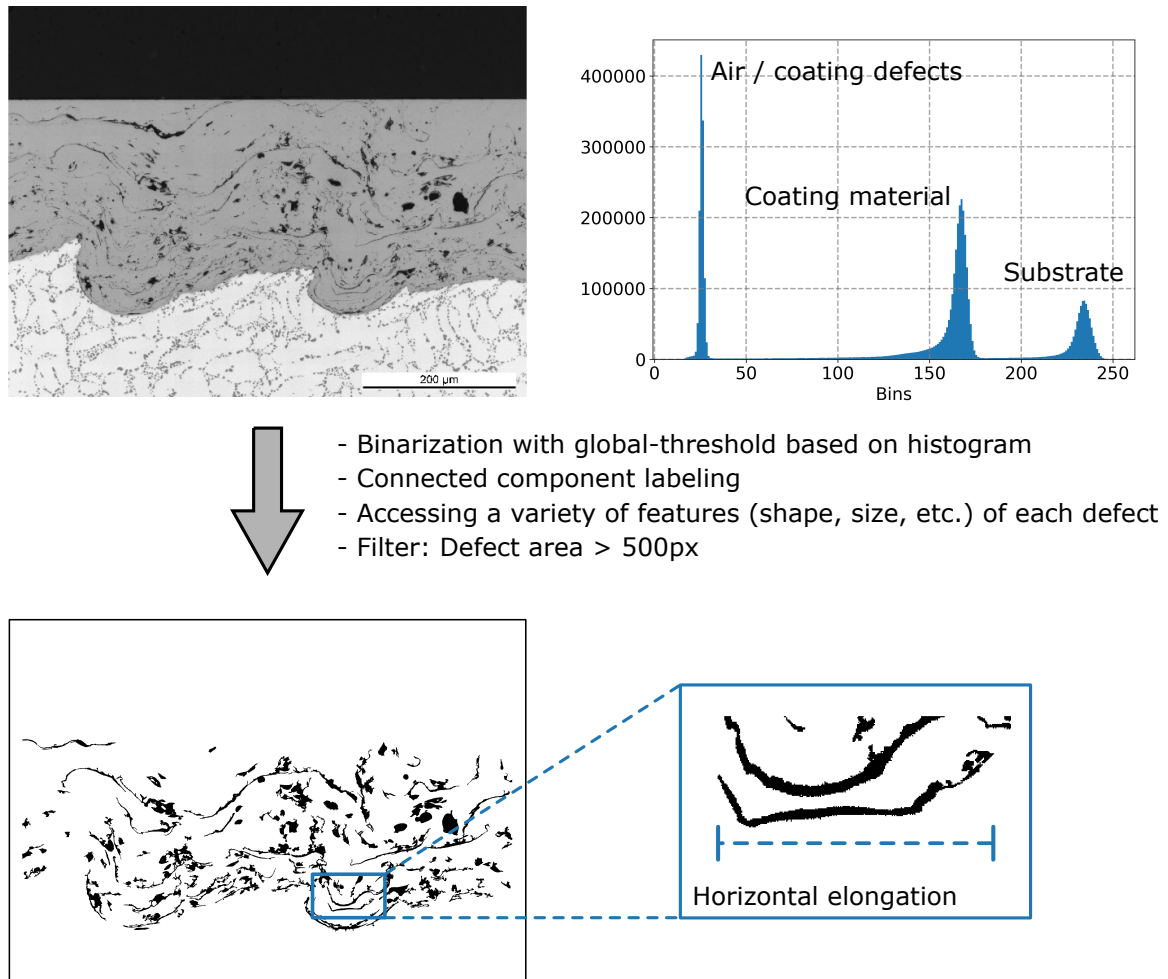
Figure 3.7.: Segmentation algorithm to quantify cross section images of thermally sprayed cylinder coatings. The cross section image (top left) is binarized with respect to the histogram of the image (top right). The binarized image (bottom left) reveals the morphology of the defects within the coating's microstructure. The horizontal elongation of each defect is calculated and summed over all detected defects. The summed elongation is normalized to the cross section area to obtain the "defect factor".
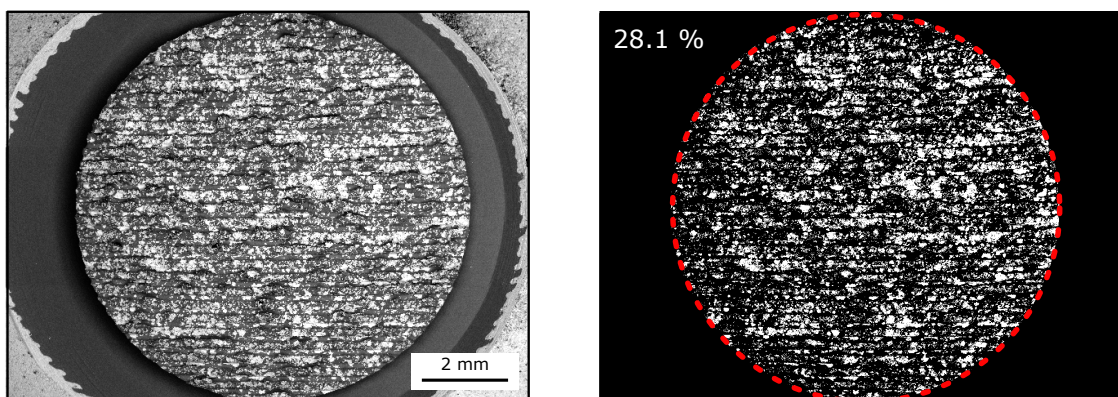
Figure 3.8.: Left: SEM image of the fracture surface after PAT™ testing. Right: Binarized image representing the remaining coating material. The red dotted circle illustrates the former PAT™ testing area of 8 mm diameter. After PAT™ testing, 28.1 % coating material can be found on the aluminum-based substrate.

object. Based on the connected objects, individual features such as size, elongations and circumference can be printed out. The connected component labeling allows to analyze the obtained defect structure quantitatively regarding different approaches.

In the following, the cross section images are evaluated focusing on two different charactersitics. Since the microstructure of thermally sprayed cylinder coatings is investigated regarding its influence on the thermal and mechanical properties, the horizontal elongation of each individual defect is processed. According to Chapter 2.3, coating defects lower the contact between overlapping splats thus decreasing the thermal and mechanical properties of the coating [6–8, 10, 14]. Here, the analysis algorithm calculates and sums the horizontal elongation of every detected defect within one cross section image. This global horizontal defect elongation is normalized on the respective cross section area of the coating to obtain a factor representing the horizontal elongation of all defects. This so-called **"defect factor"** is applied to evaluate the influence of defects and impurities in the coating structure orthogonally to the heat conduction of the thermal waves as well as orthogonally to the applied force of the PAT™ measurements.

Additionally, cross section images can be analyzed quantitatively regarding the **porosity** of the coating material. Therefore, the area of every detected defect is summed and divided by the amount of coating material found for the cross section image.

3.4.2. Fracture analysis

Destructive bond testing of the cylinder coatings using PAT™ allows to quantify the bond strength between cylinder coating and aluminum alloy substrate. While PAT™ delivers an overall bond value, it may not distinguish between adhesive and cohesive break. Hence, qualitative and quantitative analysis of the fracture surface after PAT™ is desired to obtain a second criteria investigating the bonding behavior. First, the fracture is divided by the PAT™ operator into adhesive or cohesive break qualitatively. While certain failure during PAT™ occurs at the interface between coating and substrate (adhesive failure), still parts of the coating material remain bonded to the substrate caused by cohesive failure. A typical image of a fracture area after PAT™ is found in Figure 3.8 left. Quantitative evaluation of the remaining coating material reveals additional information about the interaction of coating and substrate. Quantitative analysis of the fracture is achieved by processing SEM images (acquired in back scattering mode) of the fracture area. These images are analyzed by a segmentation algorithm comparable as described in Chapter 3.4.1. Regarding to the histogram of the SEM images, a global-threshold is applied to separate the remaining coating material from the aluminum alloy substrate binarizing the SEM image. The resulting images only contain the remaining coating material, which is summed and normalized to the related fracture area. The resulting fraction of remaining coating material to substrate material reveals the amount of cohesive and adhesive failure during PAT™ testing. Higher fractions of remaining coating material indicate the presence of metallurgical diffusion bond between coating and substrate [9].
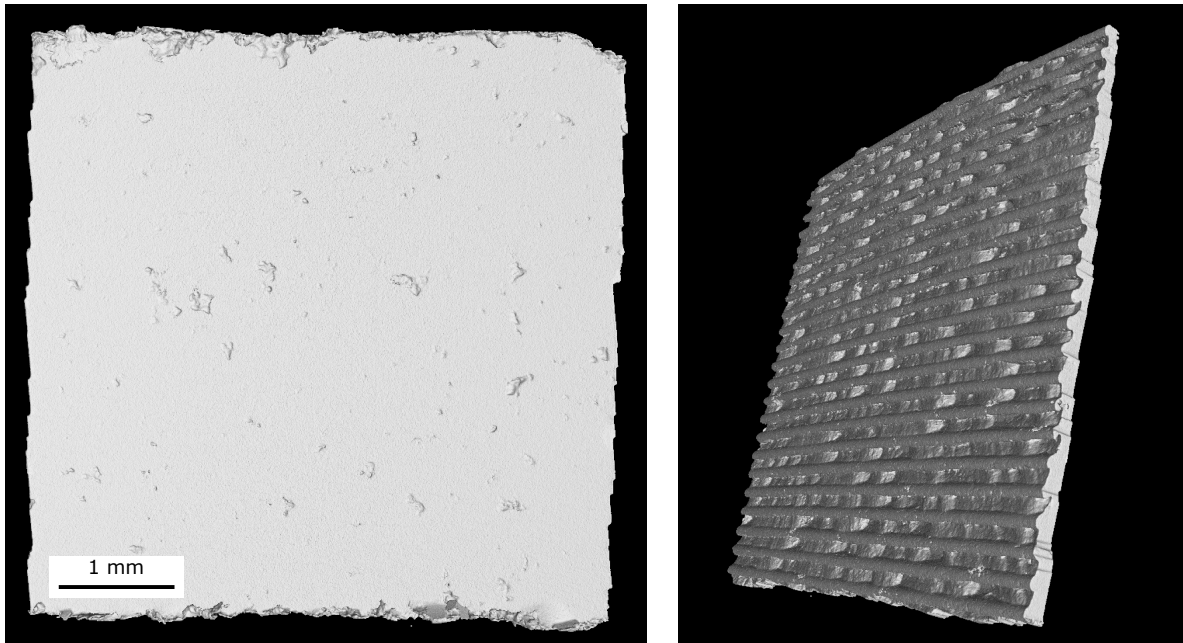
Figure 3.9.: 3D CT rendering of a thermally sprayed cylinder coating sample. **Left:** Liner surface of the thermally sprayed cylinder coating. **Right:** Substrate interface of the cylinder liner including the NMRP structure.

3.5. X-ray computed tomography

X-ray computed tomography (CT) allows to gain additional information about the microstructure of thermally sprayed cylinder coatings. Three-dimensional data sets are evaluated quantitatively regarding the defect distribution using an IA segmentation algorithm [27]. Further, CT can also be used to determine the coating material thicknesses non-destructively.

X-ray computed tomography uses computer-based assembling of many individual X-ray scans to create a three-dimensional volume of the observed object. The X-ray computed tomography is assorted to the non-destructive testing methods, however size of the object and desired resolution of the resulting data set may require destructive sample preparation in advance of the actual measurement. As the industrial CT is a by-product of the prominent medical application of CT-systems [117], still CT obtains a tremendous influence as a non-destructive testing method in industrial environment. CT allows to generate a data set showing the inside of a solid sample non-destructively. As CT is truly three-dimensional, CT data sets obtain volume information about the material constitution of a sample. In contrast to the metallographic methods, CT allows to evaluate the microstructure of a metallic sample (e.g. a thermally sprayed cylinder coating) within an entire volume but not only of a single slice. However, spatial resolution of CT data sets depends on the size of the investigated sample and is in general lower than those of optical microscopy.

The main components of an industrial CT system can be reduced to three parts: X-ray source, sample manipulator and X-ray detector. The investigated sample is placed on the manipulator and is irradiated with X-rays from the source. A two-dimensional X-ray detector records a cross section image representing the X-ray absorption coefficient of the sample. Further, the sample is rotated by the manipulator thus multiple projection images are acquired for different angle

positions. Individual X-ray images are assembled using computer based algorithms to create a single three-dimensional volume. The X-ray source is based on an X-ray tube. By emitting and accelerating free electrons between a cathode and anode, an electron beam is created. The free electrons collide with the target material (anode) thus being drastically decelerated while parts of the resulting energy transfer is emitted as X-ray Bremsstrahlung. The X-ray spectrum depends on the anode material as well as on the applied voltage between cathode and anode. The X-rays are used to irradiate the investigated specimen. The quality of a cross section image depends among others on the energy of the X-rays as well as on the size of the sample [118,119].

The commercially available *phoenix nanotom m* CT system (General Electric, Boston, USA) is used to analyze the microstructure of thermally sprayed cylinder coatings using X-ray computed tomography. Specimens with a size of $5 \times 5 \times 5$ mm are cut out of the cylinder liner. The cathode current is chosen as $100\,\mu$A and the acceleration voltage as 160 kV. The data is acquired using an integration time of 3750 ms per detector pixel and overall 1800 projections for $360°$ rotation of the specimens. A respective 3D CT rendering of a thermally sprayed cylinder coating can be found in Figure 3.9.

The resulting three-dimensional data set is transformed into a two-dimensional image stack parallel to the cylinder running surface. Hence, the 3D data is divided into 2D images thus every single image is being analyzed individually. The quantitative image analysis of CT data uses high-pass filtering, locally adaptive segmentation with a constant quadratic window size and connected component labeling to identify microstructural variations within the coating [27]. The grey-scale of the achieved CT data set is chosen to obtain a high contrast-to-noise ratio such that iron shows highest possible range of contrast within the image, while air as well as aluminum both appear to be black in the data. Hence, the quantitative image analysis may not be able to distinguish between air and aluminum as both materials are detected as porosity. Further on, due to time and sample size limitations, lowest voxel size of $4\,\mu$m could be obtained in this case. CT data have the advantage being truly three-dimensional, while optical microscopy images provide two-dimensional information only. Since the latter can reach structural resolutions of less than $1\,\mu$m, both techniques complement each other in the microstructural characterization of thermally sprayed cylinder bore coatings. While each single image of the CT data is processed by the analysis algorithm individually, mean porosity and the average pore size at each measurement position are calculated based on the two-dimensional image stack. The volume data contain information about local microstructural variations, pore size and position distribution as well as material thickness of the coating.

3.6. Magnetic-inductive coating thickness measurement

The thickness of the coating material is one important parameter of a cylinder coating in terms of functionality for the operation in the powertrain. Due to the roughened aluminum-based substrate, it is of high interest, that the substrate may never exceed through the functional cylinder coating. Due to the enhanced friction of aluminum alloys to the piston rings [25], such failure of the cylinder coating in the crankcase may lead to a collapse of the sprayed system and can cause a fatal break down of the entire powertrain. Hence, the substrate has to
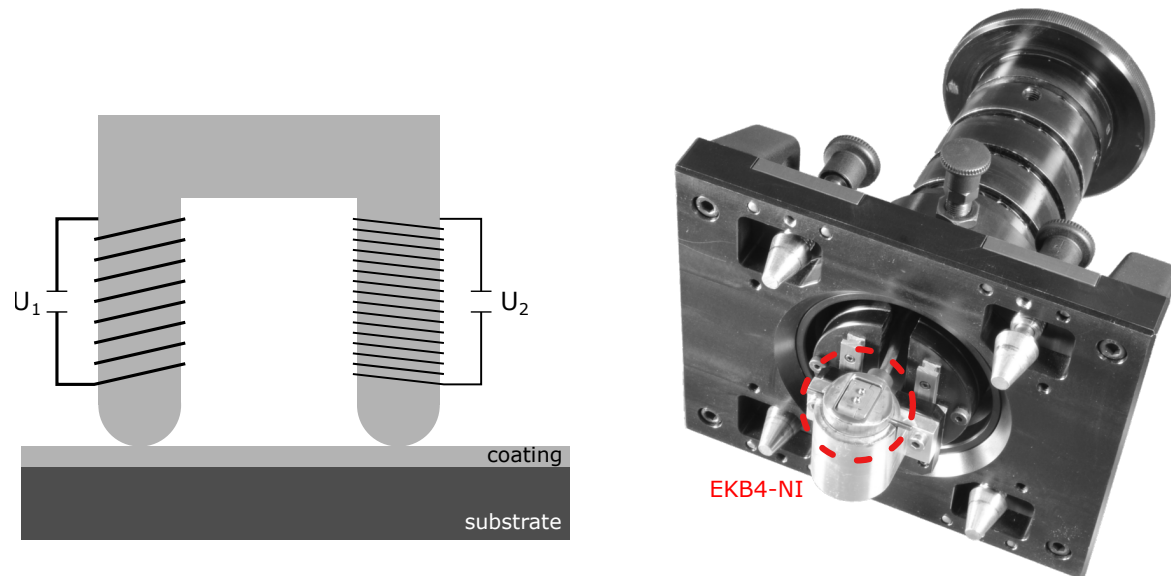
Figure 3.10.: Schematic and picture of the magnetic inductive sensor used for non-destructive thickness measurements.
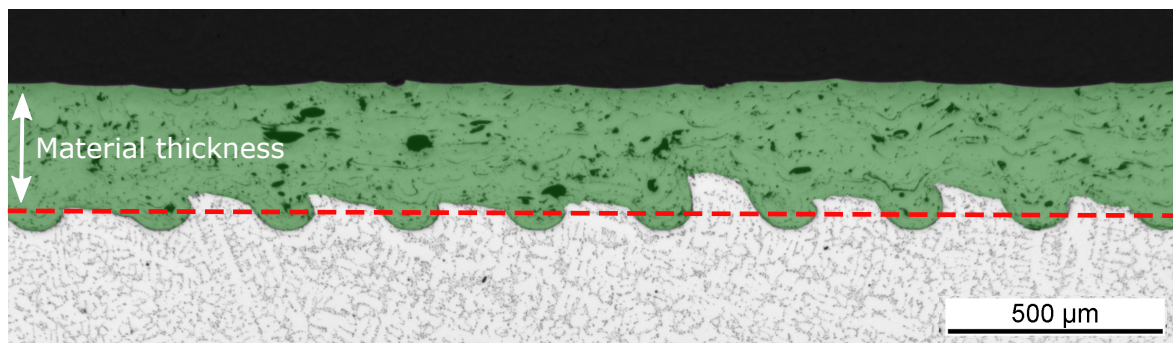
Figure 3.11.: Material thickness of a cylinder coating.

be completely covered with coating material. In terms of quality assurance, Mercedes-Benz developed a magnetic-inductive measurement method, which enables to measure the material thickness of the coating non-destructively [27]. The thickness of the coating material (further also referred as material thickness) is defined as the mean material volume over a defined measurement area. To account for the roughened substrate profile, the measurement area is chosen to be significantly larger than the mean distance between two neighboring substrate peaks.

The measurement method is based on an electromagnetic transformer. The used magnetic sensor contains two individual coils (primary and secondary coil) which are connected by a U-shaped ferromagnetic core. Applying an ac voltage at the primary coil, a magnetic field is induced within the ferromagnetic core further inducing a voltage in the secondary coil. If the ends of the U-shaped core are placed on another ferromagnetic material, the magnetic permeability of the core is changed. Since the induced magnetic field depends on the magnetic permeability of the entire ferromagnetic core, a change in the magnetic permeability due to

the contact with the tested material does result in a change of the voltage at the secondary coil [27]. Assuming a constant magnetic permeability of the tested material, the change of the core permeability only depends on the thickness of the material. As thermally sprayed cylinder coatings are made from ferromagnetic low-alloyed steel over a paramagnetic aluminum-based substrate, magnetic-inductive sensors can be used to determine the material thickness of the coatings.

However, the magnetic sensor only describes an indirect measurement of the coating thickness. As the magnetic sensor may only measure the voltage induced in the secondary coil, the sensor need to be calibrated by a reference method. Therefore, reference samples of size of $20 \times 20 \times 5 \, \text{mm}^3$ showing a big variety of material thicknesses are measured using X-ray computed tomography. CT allows to determine the mean material volume and further the material thickness of the reference sample. The magnetic sensor is later calibrated based on the thicknesses of the reference sample obtained by the CT measurements. Due to the roughened substrate, the material thickness of the coating is defined as the mean material volume over the observed measurement area (Figure 3.11). However, compared to the large measurement area of the magnetic-inductive device of about $10 \times 10 \, \text{mm}^2$ on the cylinder liner surface, lateral local variations of the cylinder coating in the length scale of $200 \, \mu\text{m}$ are averaged. Further, since the magnetic resistance and the homogeneity of the magnetic field lines strongly depend on the contact between the ferromagnetic core and the tested coating, the magnetic sensor must be placed reproducibly on the investigated surface to avoid uncertainties of the measurement by a tilted sensor. Therefore, a measurement device including a sensor attachment is used as shown in Figure 3.10. The used magnetic sensor is of type EKB4-NI (Helmut Fischer GmbH, Stuttgart, Germany.). Using the described measurement device, the non-destructive thickness measurement shows uncertainties of $\sigma_d = 0.73 \, \mu\text{m}$ [27].

4. Parameter study for laser-excited lock-in thermography measurements

Measuring the thermal behavior of thermally sprayed cylinder coatings is the main focus of this work. Therefore, multiple parameters and influences on the measurement method of TWI by laser-excited lock-in thermography have to be examined to obtain a reliable measurement setup. The parameters are not only optimized regarding enhanced repeatability and reliability, but TWI measurements should also show a reduced measurement time for possible later application in an industrial environment. In general, the measurement method should be suitable for operation in the large-scale production as a qualifying method for thermally sprayed cylinder coatings. Previously, research on TWI measurements at cylinder coatings focused on qualifying the method for reliable thickness measurements of the coatings. This research was performed on the same thermography setup and can be found in [27]. Hence, some influences of the applied measurement parameters have already been discussed in this work and are referred at the respective positions in the text.

In the following, results of studies regarding the influence of the following measurement parameters are discussed:

- **Laser spot diameter** on the sample surface: The excited area on the sample surface is known to strongly influence lateral heat flux within the sample [78, 97]. Since the description of the behavior of thermal waves in a one-layer system as shown in Equation (2.42) is derived neglecting lateral heat flux, it is necessary to reduce lateral heat flux as much as possible. Therefore, the laser spot diameter is chosen to minimize influences from lateral heat flow.

- **Analyzed area** on the sample surface: Since lateral heat flux appears mostly in the outer regions of the excited area on the sample surface, it is possible to further reduce the influence of lateral heat flux by limiting the analyzed area. Therefore, an appropriate fraction of the analyzed area to the excited area need to be defined.

- **Applied frequency spectrum** of excitation. The applied excitation frequency defines the thermal diffusion length μ. Hence, controlling the excitation frequencies allows to obtain information of the sample from different depths. Further, also lower excitation frequencies result in stronger lateral heat flux [78, 97]. Therefore, defining the maximum and minimum value of the excitation frequency depends on the desired application.

- **Offset correction**: Whereas the one-dimensional model of Bennett and Patty in Equation (2.42) [24] describes the behavior of thermal waves within thin layers accurately, however deviations of the measured data to the expected convergence behavior are quite common [81,120,121]. The theoretical description of the phase values assumes to converge against $-45°$, while experimental data shows convergence discrepancy of up to $2°$ from the theoretical description. Surface influences of the specimen or systematic errors due to the measurement setup leading to such deviations of the measured phase angles from the theoretical description can be compensated using a reference sample or an offset correction. Both methods are discussed to improve the accuracy of the applied TWI method.

- **Laser power**: To obtain reliable thermal diffusivity values from TWI, an appropriate signal-to-noise ratio has to be gained from the measurements. The quality of TWI measurements depends on the intensity of the thermal wave [27]. Since this intensity can be controlled by the applied laser power, the influence of the laser power on TWI measurements is investigated.

- **Measurement time** and **conditioning time**: The measurement time is defined as the time the infrared camera detects and analyzes the temperature oscillation on the sample surface. Since the signal-to-noise ratio of TWI measurements increases with increasing measurement time, longer measurement times result in more precise measurements [27]. Since the introduced technique should also be suited to evaluate thermally sprayed cylinder coatings in the context of a large-scale production environment, low measurement times are highly desired. Therefore, an optimized measurement time regarding measurement quality and time reduction has to be defined. Further, applying the theoretical description of the surface temperature oscillation as in Equation (2.42), one assumes the sample to be in thermal equilibrium. However, especially during short measurement times, transient non-linear heating of the sample can be observed resulting in systematic phase errors [81,122]. To minimize such phase errors, it is possible to apply the heat excitation already without measuring the temperature oscillation by the infrared camera. This so-called conditioning time is derived to optimize the TWI measurement result but also to keep the entire time scale of the measurement as short as possible.

- **Number of applied phase measurements**: In general, all integer dividers of the camera frame rate (600 Hz) can be used as the excitation frequency. Using TWI for research purposes, all possible excitation frequencies can be applied to obtain the highest possible number of individual measurements. However, besides reducing the measurement and conditioning time of each individual measurement, also reducing the number of applied frequencies results in a significant reduction of the entire measurement procedure. Therefore, to obtain an appropriate measurement setup, applied excitation frequencies should be reduced to a minimum but still allowing to measure thermal diffusivities reliably.

Variations of the explained parameters are used to analyze and quantify the influence of these parameters on amplitude and phase values of TWI measurements. The parameter study

Table 4.1.: Steel properties of the used reference samples. The shown values are taken from the respective data sheets.

Sample	1.4301	1.7225
Therm. conductivity λ [W/m $\cdot$ K]	15	42.6
Spec. heat capacity c [J/kg $\cdot$ K]	500	470
Density ρ [g/cm^3]	7.9	7.72
Thermal diffusivity α [mm^2/s]	3.8	11.7
Therm. diff. length μ (1 Hz) [mm]	1.10	1.93

Figure 4.1.: Cylindrical reference sample (40 mm diameter, 50 mm height).

is performed on **cylinder coating samples**, however also **two bulk material reference samples** are used. The reference samples are chosen to be thermally thick thus no interference effects of the thermal waves are observable. In this context, the chosen reference samples define the simplest case of thermal wave diffusion in a solid material. Hence, phase measurements of the reference samples should show a constant phase to the excitation source of $\phi = -45°$ for all applied frequencies. Here, two different types of steel are taken as the reference samples. The two materials are chosen such that they show an enhanced variation of their thermal properties, but the reference samples should also present thermal properties in the same range of the sprayed cylinder coatings. Since low-alloyed steel is used to coat the cylinder bores, austenitic (1.4301) and non-austenitic steel (1.7225) is selected as the reference materials. The reference samples have cylindrical shape with 40 mm diameter and 50 mm height. The material properties of these samples can be found in Table 4.1, a picture of a reference sample is shown in Figure 4.1.

Based on the introduced parameters, an optimized measurement setup is derived for all upcoming TWI measurements of the following Chapters 5 and 6. The final parameter setup is listed in Table 4.4. Further, the TWI setup is evaluated regarding its repeatability for the measurement of thermal diffusivity values of thermally sprayed cylinder coatings using a bootstrapping approach. Additionally, TWI measurements are compared to the standard method of laser flash analysis (LFA) regarding thermal diffusivity measurements.

4.1. Laser spot diameter (Reference Sample)

The applied laser spot diameter defines the heated area on the investigated samples. The excitation area is one crucial parameter since it influences the lateral heat flux in the sample [78, 97]. The chosen laser excitation source has a defined excitation area between 6.5 mm and 20 mm diameter. Using a top-hat shaped laser amplitude a strong temperature gradient (step-function) between excited and non-excited area occurs on the sample surface. Since the heat flux is proportional to the spatial temperature gradient as seen in the continuum equation

(2.1), strong lateral heat flux is assumed in the outer region of the excitation. However, deriving the thermal wave model of a one-layer system resulting in the expression of the phase angle in Equation (2.42), the applied necessary boundary conditions neglect lateral heat flow and further assume the heat excitation to be applied homogeneously over the entire sample surface. Thus, observed lateral heat flux due to the finite excitation may lead to deviations between the expected theoretical model and the measurement results.

In this context, multiple researches focus on the influence of the laser spot on the accuracy of TWI measurements and the consequences for the applied 1D layer theory [78, 97, 121]. Further, also expansion of the 1D theory model onto a 3D approach has been published to account for such lateral heat flux in a layered system [99, 101]. However, including the lateral heat flow in a one layer theory, the number of required parameters and the complexity of the model function increases drastically, thus lowering the applicability of the 3D model compared to the 1D theory. Therefore, it is highly favorable to lower the observed lateral heat flux and thus to ensure the accuracy of the theoretical description of Bennett and Patty [24] of thermal waves in a one-layer system.

One common approach to lower lateral heat flux is to simply increase the excitation area on the sample surface. Since the thermal diffusion length (Equation (2.9))

$$\mu = \sqrt{\frac{2\alpha}{\omega}} = \sqrt{\frac{\alpha}{\pi f}} \tag{4.1}$$

is independent of the laser spot diameter, the laser spot diameter can be chosen much larger than the thermal diffusivity length to suppress perturbations arising from lateral heat flux [97, 99]. As the thermal diffusivity length μ increases for lower excitation frequencies resulting in stronger lateral heat flow, the laser spot diameter need to be optimized with respect to the lowest applied excitation frequency.

The influence of the laser spot size and the resulting lateral heat flux is presented by the diffusion of thermal waves in bulk material. The reference samples are heated using three different laser spot sizes: $6.5\,\mathrm{mm}$, $11\,\mathrm{mm}$, $18\,\mathrm{mm}$. Due to the simple application of thermal waves in thermally thick samples, phase values of $-45°$ are expected. Deviations of the phase values to the theoretical value may be caused by lateral heat flux. Thus, TWI measurements are performed using excitation frequencies between $1\,\mathrm{Hz}$ and $150\,\mathrm{Hz}$ and a power density of $0.5\,\mathrm{W/mm^2}$. The acquired phase images for a modulation frequency of $1\,\mathrm{Hz}$ can be found in Figure 4.2. Inner regions of the excited areas show expected phase values close to $-45°$ for the larger spot sizes, whereas lowest excitation area of $6.5\,\mathrm{mm}$ reveal deviations of the theory function. Further, slightly enhanced phase values in the center of the excited area are due to the surface topography which result from manufacturing and precision turning of the samples. As the reference samples are centered to the excitation source, the marks of the precision turning are found in the center of the ROI. However, both reference samples show increased phase values in the outer regions of the excited area for all three spot sizes. The yellow circles at the edge of the excited area indicate enhanced phase values of up to $-30°$, whereas a theoretical phase value of $-45°$ is expected over the entire excited area. While the reference sample of 1.7225 shows the higher thermal diffusivity, consequently higher thermal
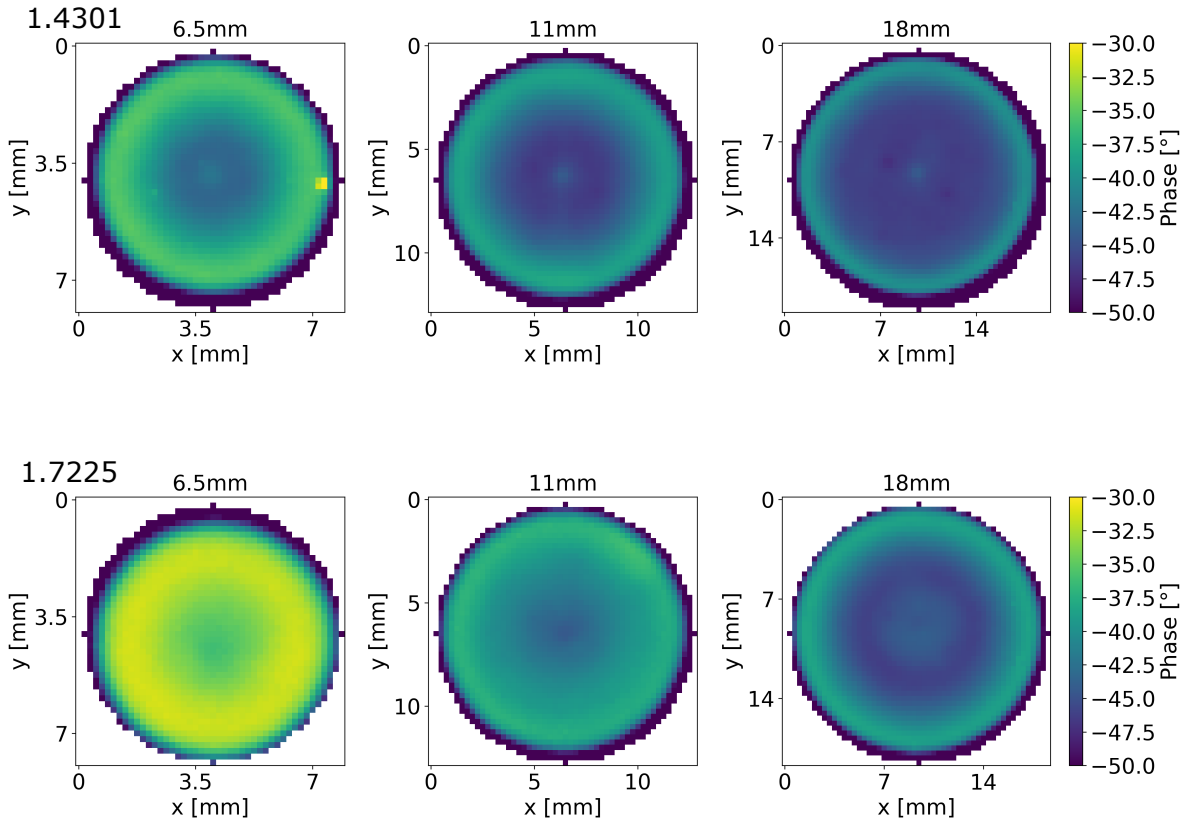
Figure 4.2.: Phase images for varying laser spot diameter at $f = 1\,\mathrm{Hz}$ for the reference samples.

diffusion lengths and stronger lateral heat flux is expected. Therefore, the increase of the phase values in the outer region is enhanced compared to the reference sample 1.4301.

Further, larger spot diameters clearly lower the influence of lateral heat flux, since the fraction of enhanced phase values to the ROI is reduced. As the center areas showing the expected $-45°$ phase values expand for larger spot sizes, a higher fraction of the ROI is accurately described by the theoretical model function for larger spot sizes. In this context, cross sections through the phase images at $f = 1\,\mathrm{Hz}$ from Figure 4.2 are shown in Figure 4.3 and 4.4 on top. The cross section profiles indicate the enhanced phase values in the outer regions of the excited area, whereas a decay of the phase values towards the center is observed. For the 1.4301 reference sample, the phase values converge against $-45°$ in the center of the excited area using either a laser spot diameter of $11\,\mathrm{mm}$ or $18\,\mathrm{mm}$. The phase values acquired for a spot size of $6.5\,\mathrm{mm}$ never reach the saturation value but remain above $-45°$ over the entire excited area. Further, the higher thermal diffusivity of the reference sample 1.7225 leads to stronger lateral heat flow thus the phase values only reach $-45°$ for the largest laser spot diameter of $18\,\mathrm{mm}$. Concluding the cross section profiles, higher laser spot diameters favor the reduction of lateral heat flux and lead to the expected phase values for the reference samples at least in the center of the excited area.

Additionally, averaging the phase values over $80\,\%$ of the excited area and plotting it over multiple excitation frequencies leads to the trend shown in the bottom part of Figure 4.3 and 4.4. These plots allow to estimate the deviation of the measured phase values to the expected
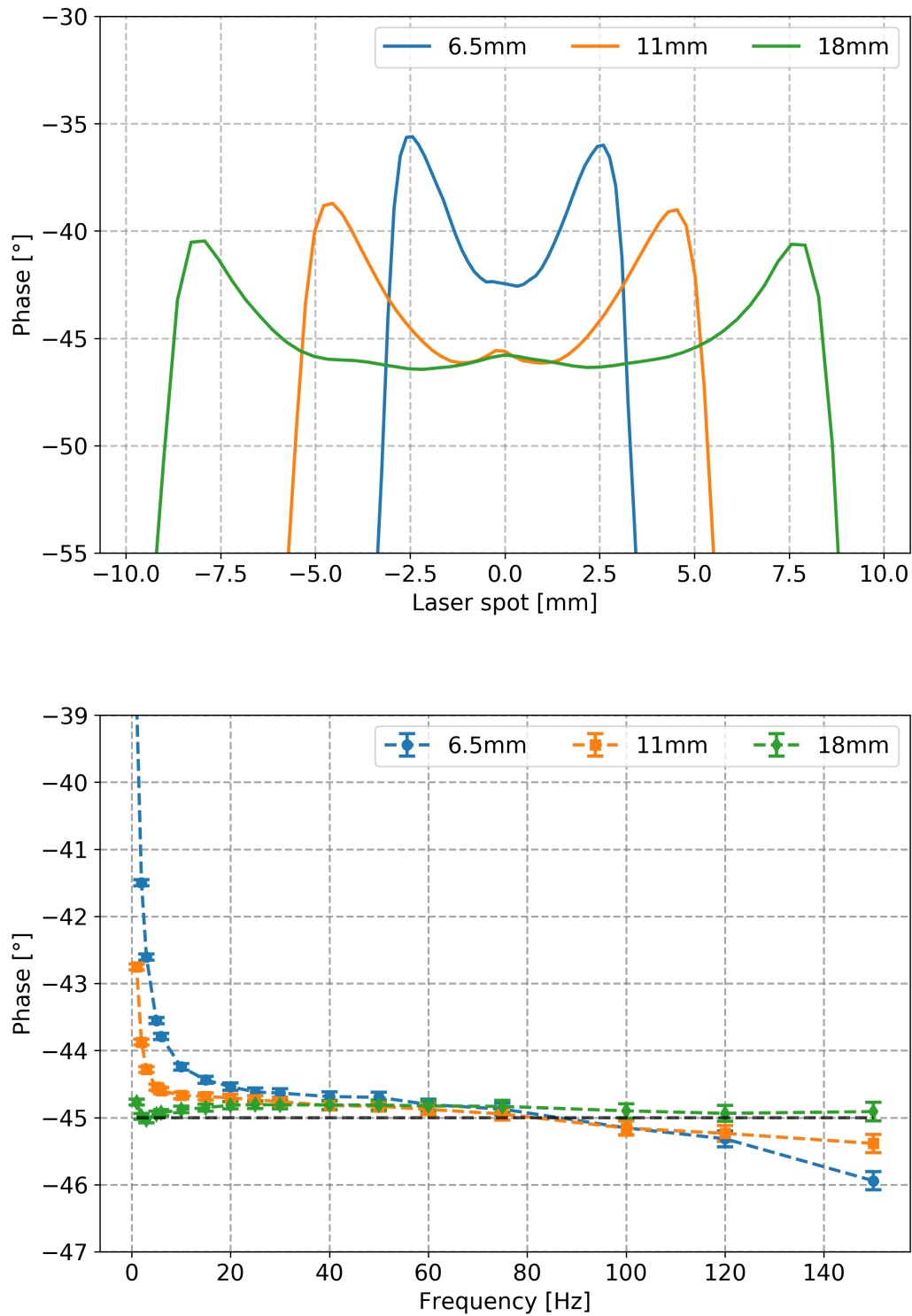
Figure 4.3.: Reference sample 1.4301. Top: Cross section through the phase image at frequency $f = 1\,\mathrm{Hz}$ for varying laser spot diameter. Bottom: Mean phase values over the entire frequency spectrum. Phase values are averaged over $80\,\%$ of the excited area. The error bars result from the repeatability study in the Appendix A.2.
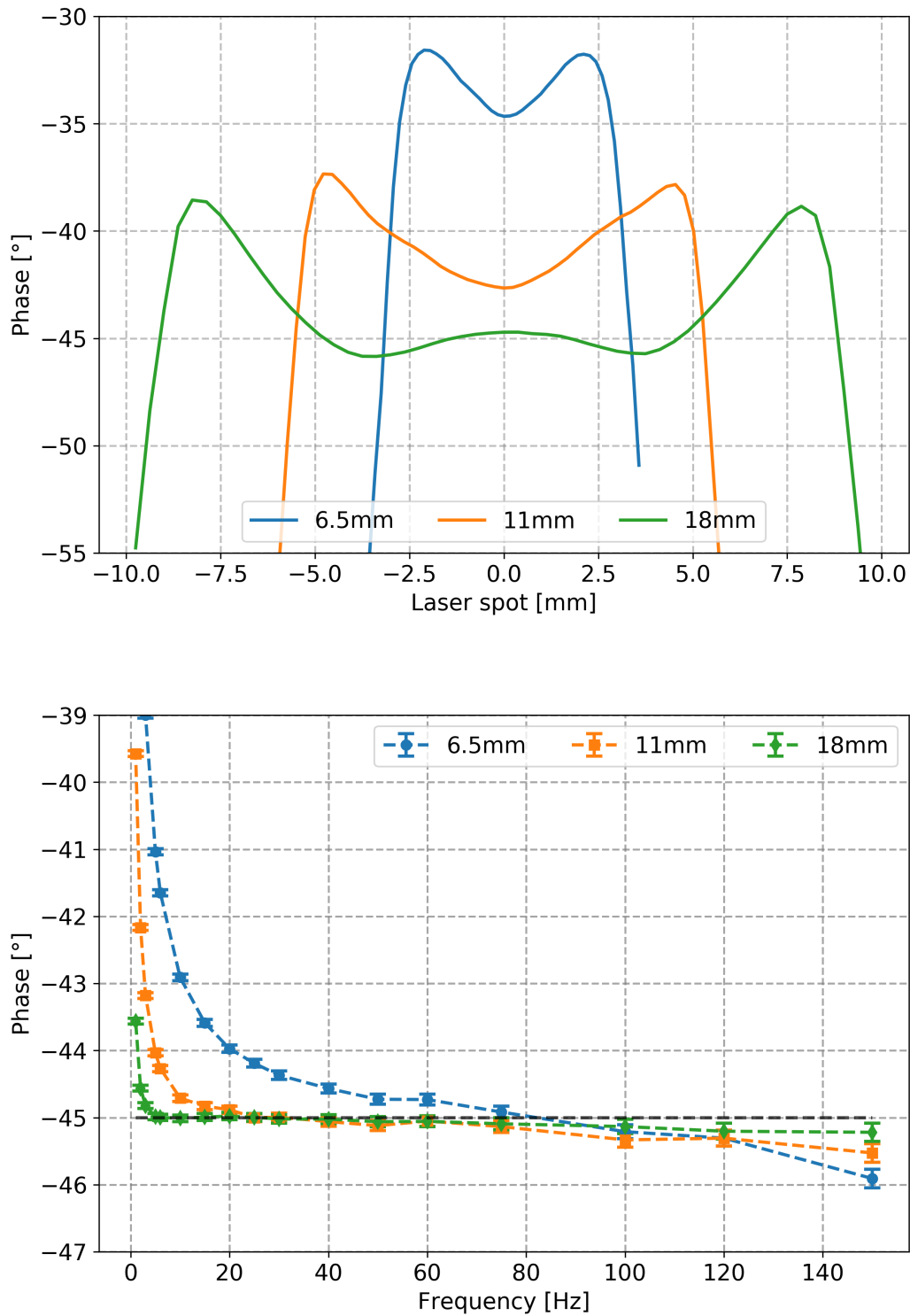
Figure 4.4.: Reference sample 1.7225. Top: Cross section through the phase image at frequency $f = 1\,\mathrm{Hz}$ for varying laser spot diameter. Bottom: Mean phase values over the entire frequency spectrum. Phase values are averaged over $80\,\%$ of the excited area. The error bars result from the repeatability study in the Appendix A.2.

phase values of $-45°$ for all applied modulation frequencies. While phase angles measured for the sample 1.7225 show increased deviations due to the sample's higher thermal diffusivity, still both samples show good accordance to the reference value for excitation frequencies larger than $5\,$Hz and a laser spot diameter of $18\,$mm. Using a spot diameter lower than $18\,$mm, phase values never fully converge against $-45°$ independent of the sample. Larger spot diameters clearly lead to the expected behavior of the phase values over almost the entire frequency spectrum and hence are favorable for all following applications. Consequently, largest possible laser spot diameter is applied for the following measurements. Due to the geometry of the crankcases and the limitations of the safety cabin, the largest possible laser spot diameter can be set to $D = 20\,$mm. Therefore, all following measurements are performed using this laser spot diameter. For further detail, additional cross sections through phase images at multiple excitation frequencies are shown in the appendix in Figures B.2 to B.7.

4.2. Analyzed area and applied frequency spectrum (Layer system)

While the highest possible laser spot diameter reduces the influence of lateral heat flux on the measured phase values, still enhanced phase values deviating from the expected theoretical values are found for the reference samples at the highest observed laser spot diameter (Figure 4.3 and 4.4). Phase values strongly deviate from $-45°$ for the lowest excitation frequencies even if the phase values are averaged over $80\,\%$ of the excitation area. Thus, the analyzed area on the sample surface (region of interest, ROI) and the applied frequency spectrum need to be optimized to further reduce the influence of lateral heat flux even at the lowest frequency. The theoretical model function may only be applied accurately, if lateral heat flux is reduced to a minimum.

In the following, TWI measurements are applied on thermally sprayed cylinder coatings. The TWI measurements are performed on a spot diameter of $20\,$mm and a frequency spectrum ranging from $1\,$Hz $-\,150$Hz. First, cross section profiles through the excitation areas are shown at the top of Figure 4.5. Again, increased phase values are obsereved in the outer regions of the ROI, whereas the phase values decay towards the center of the profile. Lateral heat flow as seen in the previous chapter results in increased phase values especially in the outer region of the excited area and for lower modulation frequencies. Thus, homogeneous phase profiles over the entire excited area can only be observed for high modulation frequencies. Due the superposition of the phase values by the lateral heat flow, TWI measurements show systematic errors especially for low excitation frequencies. Consequently, only the center of the excited area need to be evaluated to reduce the influence of lateral heat flow. However, still an appropriate fraction of the excited area is required, since analyzed areas of only a few pixels may show singularities which are not representative for the observed coating. The NMRP of the roughened aluminum substrate as seen in Figure 2.2 shows horizontal extensions of substrate peaks of about $200 - 300\,\mu$m. As the optical resolution of the measurement setup is specified to about $0.2\,$mm/pixel, the distance between neighboring profile peaks shows about the same scale as the camera resolution. Thus, to neglect influences of the varying vertical material thickness of up to $100\,\mu$m, the phase values need to be averaged over several peaks of the roughened profile to assume a constant phase value. Additionally, by averaging the
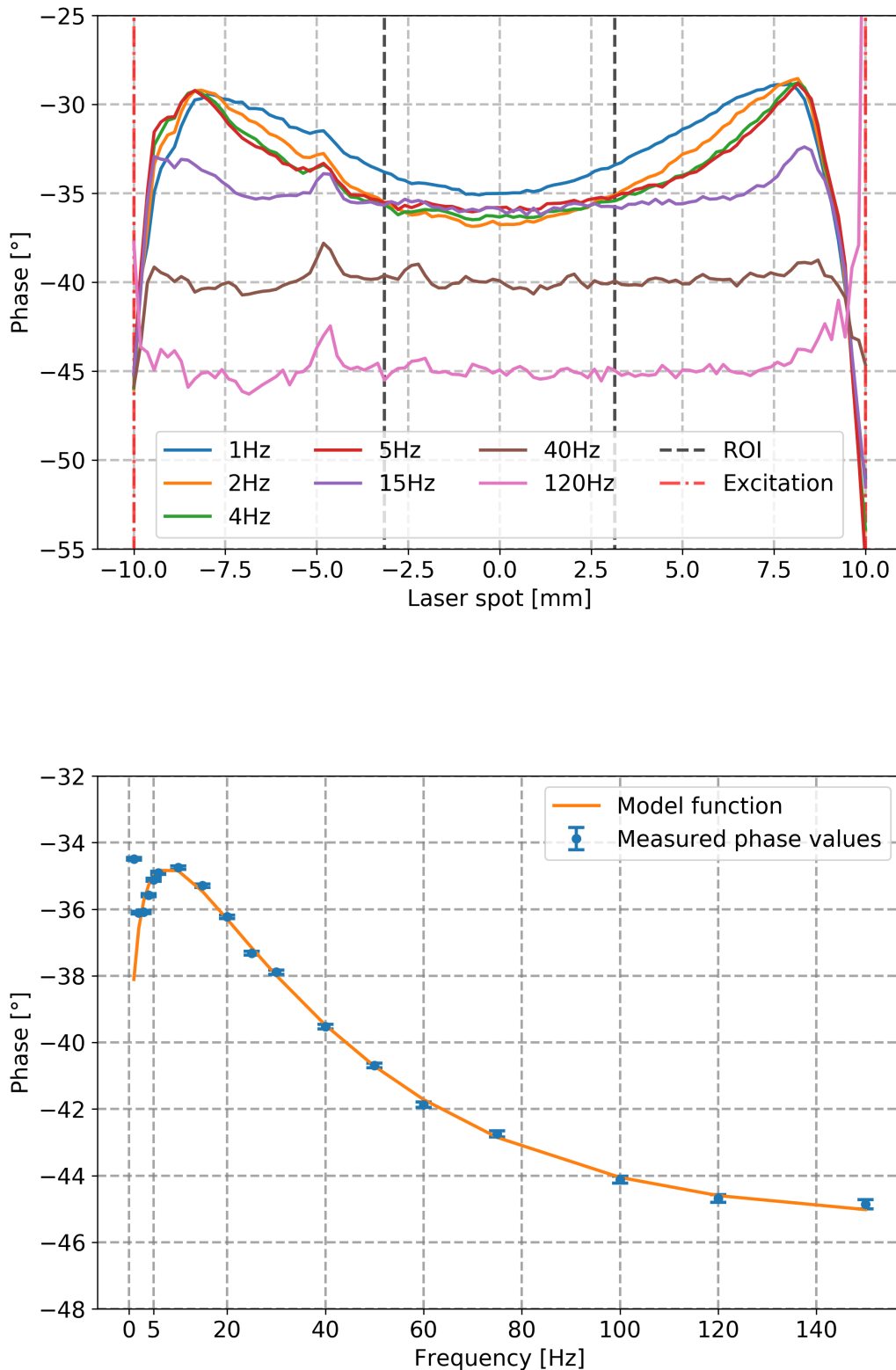
Figure 4.5.: Top: Cross sections through acquired phase images of a cylinder coating for various modulation frequencies. The excited area is illustrated by the vertical red lines and the analyzed area (ROI) of 33 % of the excited area is highlighted by the vertical black lines. Bottom: Averaged phase values from the ROI over the entire frequency spectrum. The model function in (2.42) from [24] is fitted to the measured data for the frequency range of $5 - 150\,\mathrm{Hz}$. The error bars result from the repeatability study in the Appendix A.2.

phase values over an extended area, artifacts resulting from the measurements setup or other influences as seen in Figure 3.3 can be reduced. Therefore, all following measurements are analyzed in the center of an area representing $33\,\%$ of the laser spot diameter.

Even for the limited ROI, still phase deviations of over $1°$ are found within the applied ROI at the lowest modulation frequency of $1\,Hz$. Thus, to further improve the accuracy of TWI measurements, the applied frequency spectrum need to be shortened. At the bottom of Figure 4.5 averaged phase values over the entire frequency spectrum are shown. The illustrated phase values are taken from the described ROI of $33\,\%$ of the laser spot diameter. Further, the model function of Equation (2.42) is fitted to the phase values within a frequency spectrum ranging from $5\,Hz - 150\,Hz$. While the theory shows good accordance to the measured values, still phase values obtained at the lowest frequencies diverge from the model function. As the model function should peak for a frequency higher than $5\,Hz$, phase values obtained at $1\,Hz$ are found to be higher than the designated peak. As already observed and discussed for bulk material in Chapter 4.1, lateral heat transfer at frequencies lower than about $5\,Hz$ cause deviations from the one-dimensional theoretical model of thermal waves. Therefore, to ensure a reliable fit between theory and measured values, the minimum applied frequency is set to $5\,Hz$. Since the fitted function shows good accordance over the entire spectrum above $5\,Hz$, the highest applied frequency is set to $150\,Hz$. The measurement setup does not allow for higher frequencies, since the maximum possible frequency is defined by the maximum camera's frame rate of $600\,Hz$. To obtain the highest possible reliability fitting the model function to the measured data, all available modulation frequencies are applied. Since only integer dividers of the camera frame rate are allowed, following frequencies are further considered: $5, 6, 10, 12, 15, 20, 25, 30, 40, 50, 60, 75, 100, 120, 150\,Hz$.

4.3. Offset correction (Layer system)

The one-dimensional theoretical model of thermal waves within a layered structure as found in Equation (2.42) assumes a constant phase shift between the incoming heat flux and the detected surface temperature oscillation of $-\frac{\pi}{4} = -45°$ for a thermally thick sample. As the thermal diffusion length μ decreases with increasing excitation frequency f, the model function yields convergence of the measured phase values for a layered sample against $-45°$ with increasing excitation frequency. However, deviations of experimental data to the expected convergence value are quite common [81, 120, 121]. Figure 4.6 illustrates experimental phase data acquired for thermally sprayed cylinder coatings deviating from the model function (green dashed line) for frequencies larger than $60\,Hz$. Systematical phase errors due to signal delays between camera and excitation source as well as surface influences of the specimen may cause the experimental data to converge against phase values deviating from $-45°$ [120, 121, 123, 124]. Literature often recommends to use a thermally thick reference sample to calibrate the acquired phase values as it is assumed that such a thermally thick reference sample should return a constant phase value of $-45°$ [120, 121, 123, 124]. However, as shown in Figures 4.3 and 4.4 using bulk material as a reference sample for determining the appropriate laser spot diameter, the measured phase values are already found to converge closely to $-45°$ for the largest spot diameter even without additional calibration. Hence, systematical phase errors due to the
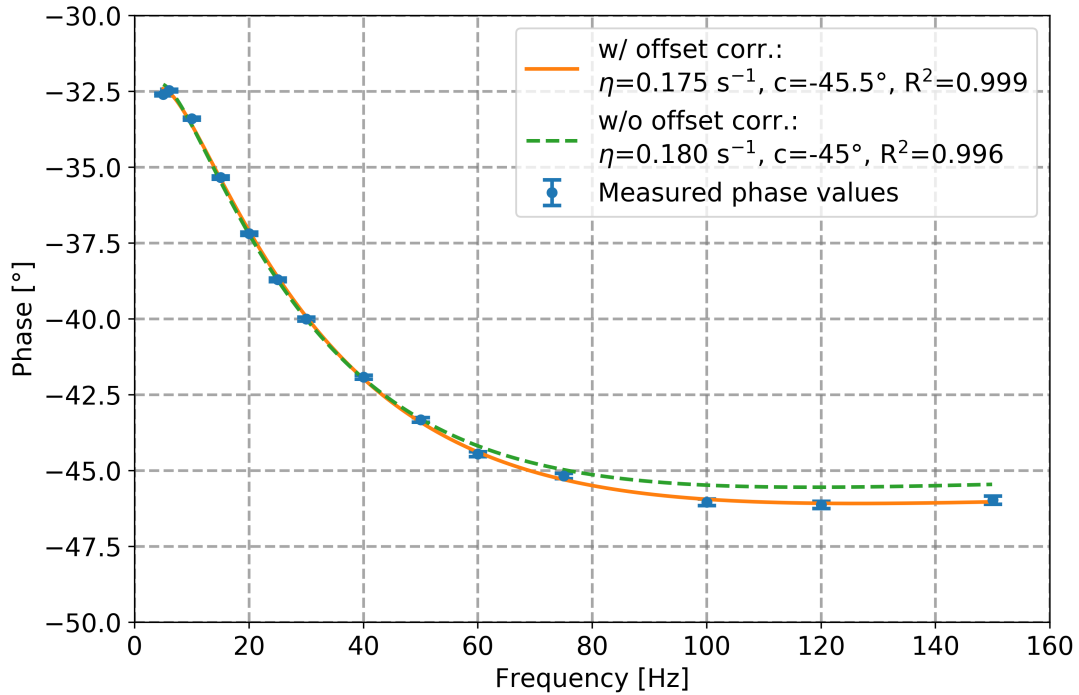
Figure 4.6.: Acquired phase values fitted by the model function in (2.42) with (solid orange line) and without (dashed green line) offset correction.

measurement setup may not be the reason for the observed deviations found for thermally sprayed cylinder coatings.

Therefore, surface influences such as open porosity or grooves from the mechanical treatments are assumed to cause the described deviations. Since a reference sample is not applicable to represent multiple types of surface structures, an alternative approach is presented to account for such influences. The model function in Equation (2.42) is expanded by an empirical correction term C allowing the model function to converge against values different to $-45°$ as:

$$\phi(f) = \tan^{-1} \left(\frac{-2 \cdot R_i \cdot \exp(-2\eta\sqrt{f}) \cdot \sin(2\eta\sqrt{f})}{1 - (R_i \cdot \exp(-2\eta\sqrt{f}))^2} \right) - C. \tag{4.2}$$

Fitting the measured data using the expanded function with offset correction as shown in Figure 4.6, the coefficient of determination R^2 increases from 0.996 to 0.999 in this example. Applying the offset correction, the model function describes the measured data truly accurate and improves the fitting quality compared with the uncorrected model function.

Further, acquired offset values are compared to the surface structure of thermally sprayed cylinder coatings. Therefore, fitting of the model function is not applied to the averaged phase values within 33 % of the spot size as shown in Chapter 4.2, but the acquired phase values of each camera pixel within the excited area are fitted with respect to the expanded model function in (4.2) resulting in a parameter map. Each pixel of the parameter map represents the calculated fit parameter based on the phase information found only for this single camera pixel. The maps of the offset correction parameter C are compared to images showing the surface
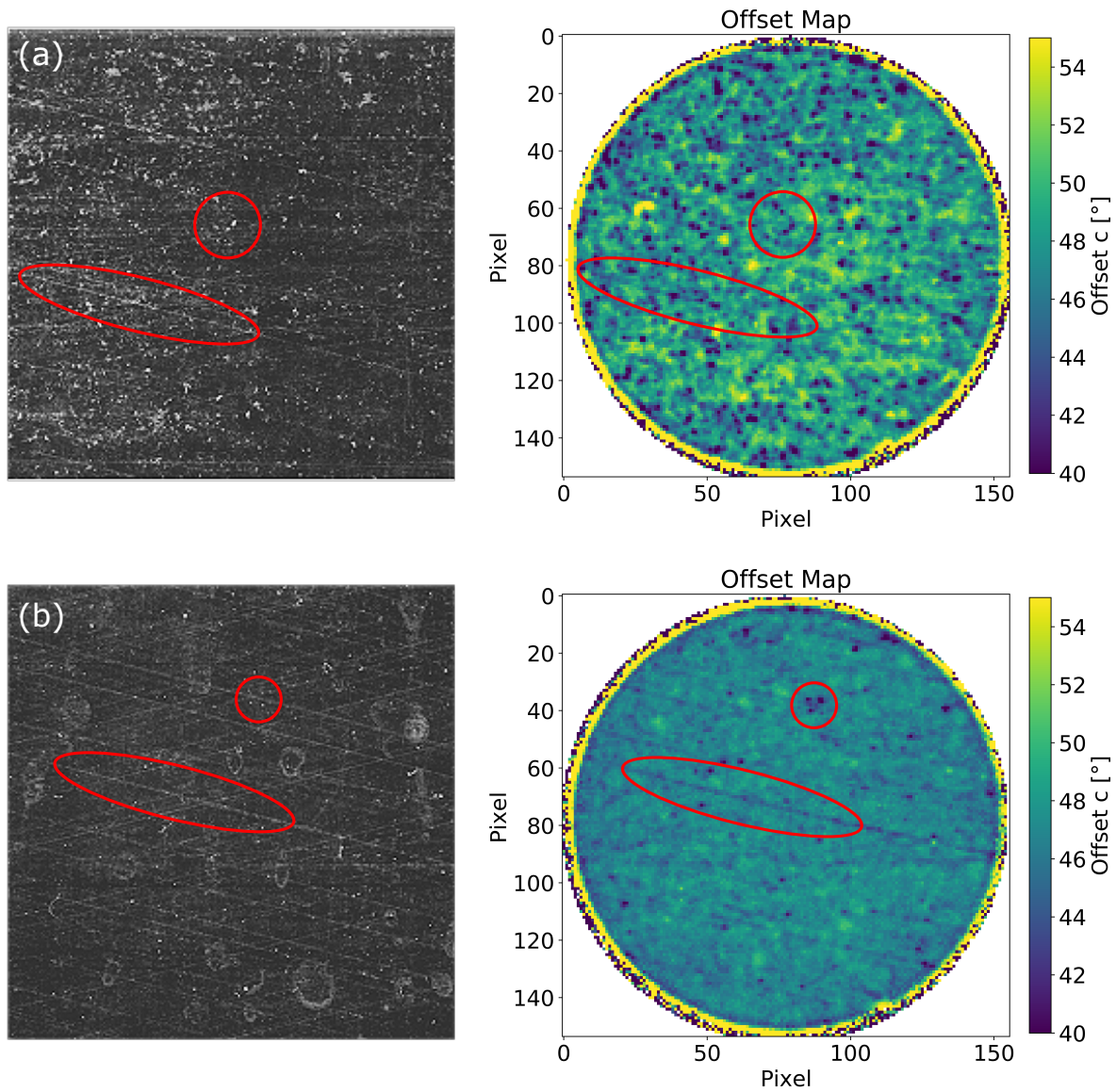
Figure 4.7.: Comparison between surface structure and offset maps shown for two different liner positions (a) 10 mm and (b) 100 mm. The red marks indicate surface structures which can be traced back to the offset maps on the right.

structure of the cylinder coatings at the respective measurement positions. This comparison is illustrated in Figure 4.7. The figure shows two different liner positions, whereas the surface image taken at liner position 10 mm indicates enhanced amount of open porosity and surface defects correlated to high fluctuations within the offset map. For instance, a cluster of surface pores as well as a diagonal groove on the liner surface are highlighted in red and can be found in the surface image as well as in the offset map. Further, the surface structure found at position 100 mm shows less open pores, but still certain defects can be seen. Again, surface structures such as grooves and pores can be traced back to the offset map highlighted in red. However, the resulting offset map presents less fluctuations thus being more homogeneous compared to position 10 mm. Here, observed surface defects lead to anisotropic heat absorption on the sample surface causing local spots of high heat concentration. Thus, these defects can be seen as point-like heat sources on the surface causing radial heat conduction. The resulting
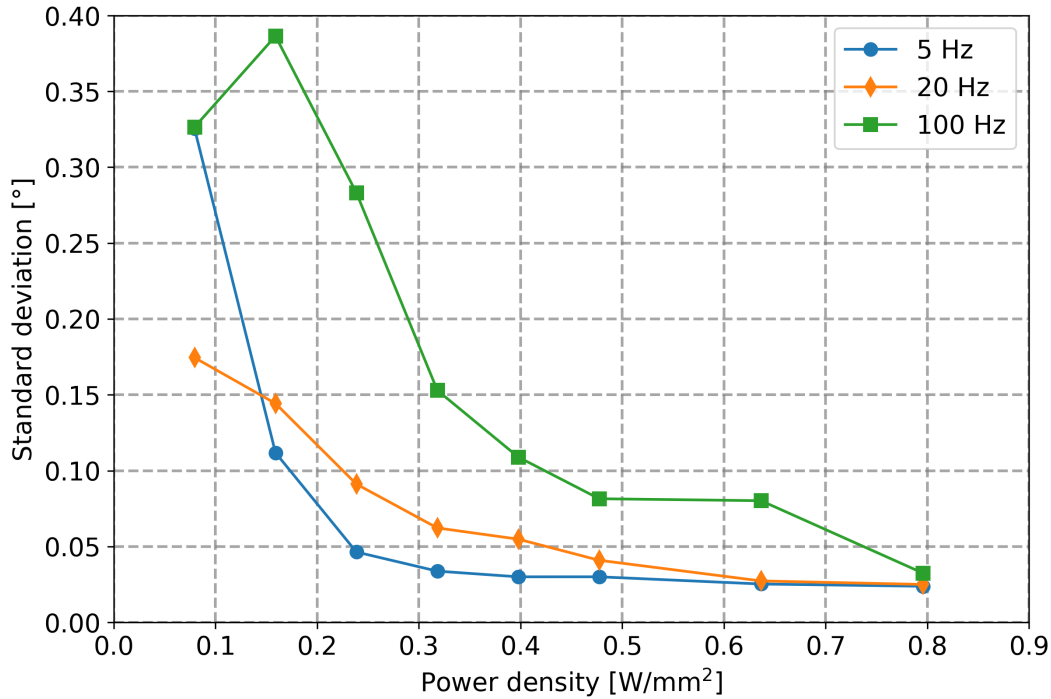
Figure 4.8.: Standard deviation of phase measurements for 10 repetitions regarding the respective excitation frequencies.

heat flux on the surface cannot be seen as homogeneous anymore leading to enhanced local lateral heat flow. As the theoretical description of thermal waves in a layered structure only assumes through-layer heat flux neglecting all inhomogeneous heating of the sample surface, the open porosity on the sample surface lead to deviations of the measured phase values to the theoretical description. In this context, the adaption of the theoretical model function by the introduced offset parameter C allows to account for the local surface structure of the thermally sprayed cylinder coatings.

4.4. Laser power (Layer system)

The quality of a measurement depends among others on the signal-to-noise ratio. While the intensity of the thermal signal on the sample surface is related to the amplitude of the thermal waves, higher amplitudes of thermal waves lead to an increased signal-to-noise ratio of the measurement [27]. As seen in Equation (2.16), the amplitude of a thermal wave is proportional to the introduced heat flux from the excitation source. Hence, increasing the heat flux from the laser may lead to an increased signal-to-noise ratio and thus a more accurate TWI measurement. As shown in reference [27], the standard deviation of a TWI measurement decreases strongly by increasing the power density on the sample surface up to $1\,\mathrm{W/mm^2}$. However, higher laser power does not further lower the standard deviation of the measurement, but stay constant up to $4\,\mathrm{W/mm^2}$. Hence increasing the heating power beyond a certain limit does not benefit the quality of the measurement, but increases the risk of damage of the sample or other optical components as well as the risk of burn for the operator by changing or adjusting the sample

between the measurements. Further, high laser power can cause non-linear heating effects of the samples, which should be avoided as they result in systematical phase errors lowering the accuracy of TWI measurements [81]. Non-linear heating effects are further discussed in Chapter 4.5.

The influence of the applied power density is evaluated measuring the mean phase and the resulting standard deviation of 10 repetitions at frequencies 5, 20 and 100 Hz for varying power densities. The highest possible laser power for the described measurement setup is limited by the used laser generator and set to 250 W resulting in the highest possible power density of $0.8\,\mathrm{W/mm^2}$. As shown in Figure 4.8, the observed standard deviation increases with decreasing power density, while the lowest standard deviation can be found for $0.8\,\mathrm{W/mm^2}$. Further, the measurements reveal a frequency dependent standard deviation as higher excitation frequencies lead to higher standard deviations over the entire power density spectrum. Since the amplitude of a thermal wave is inversely proportional to the square root of the applied excitation frequency, lower amplitudes at higher excitation frequencies result from a reduced signal-to-noise ratio thus causing a higher standard deviation regarding the repeated measurements. Therefore, achieving the lowest possible standard deviation, the applied power density should be set to $0.8\,\mathrm{W/mm^2}$. However, to lower the risk of damage of the sample, optical components and the operator as well as to reduce non-linear heating of the samples, also lower power densities are favorable. Comparing the obtained standard deviation with the maximum phase contrast of about $10°$ as seen in Figure 4.5, a standard deviation of $1\,\%$ or less compared the maximum phase contrast is chosen. Therefore, all following measurements are performed using a power density of $0.4\,\mathrm{W/mm^2}$ which equals a laser power of 125 W. Additionally, a study about the repeatability of individual phase measurements and the resulting standard deviations are shown in the Appendix A.2.

4.5. Measurement time and conditioning time (Layer system)

The total time of TWI measurements is one crucial characteristic of the investigated method for later application in the context of a large-scale production for cylinder coatings. While the accuracy of TWI measurements in general benefits from a longer measurement time [27], this directly contradicts with the cycle time during the series production. Therefore, the total measurement time of TWI should be as short as possible, but still deliver reliable and accurate results. The total time can be divided into two individual time intervals. The **measurement time** represents the time the infrared camera detects and analyzes the temperature oscillation on the sample surface. Increasing the measurement time does lead to an increased signal-to-noise ratio and therefore increases the accuracy of the measurement. Further, theoretical

Table 4.2.: Combinations of conditioning and measurement time to investigate the influence of transient heating

Cond. Time [s]	1	1	5	5	10	20	60	90
Meas. Time [s]	1	2	1	5	5	5	5	5
Total Time [s]	2	3	6	10	15	25	65	95
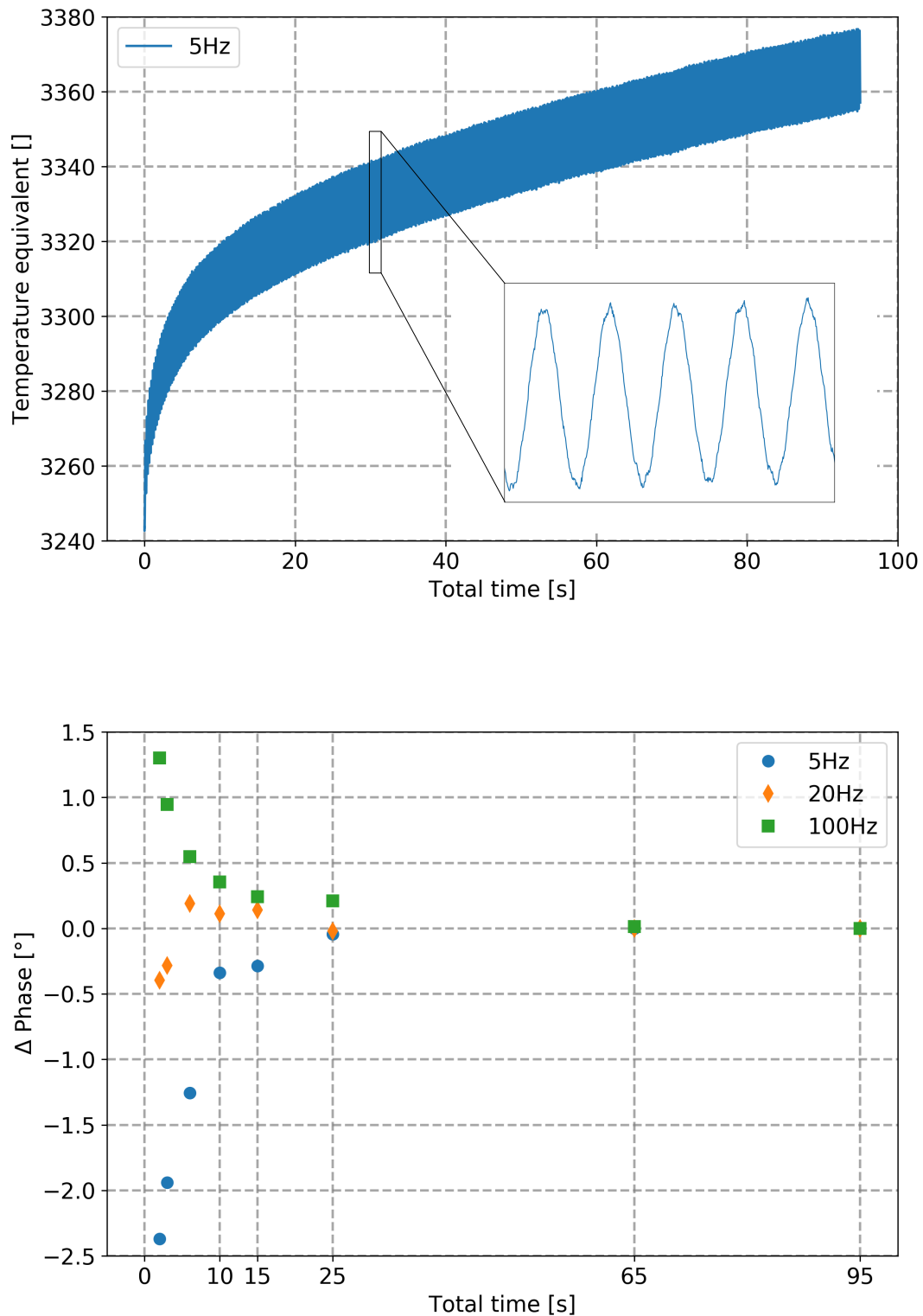
Figure 4.9.: Top: Surface temperature of a cylinder coating sample during a TWI measurement with frequency $f = 5\,\mathrm{Hz}$. Bottom: Using varying conditioning and measurement times, the influence of the transient heating on the phase values are analyzed. The difference between the phase value for the depicted total time compared to the phase value obtained from the measurement at total time of $95\,\mathrm{s}$ is shown.

descriptions of the thermal waves applied in coatings assume the investigated samples to be in thermal equilibrium. However, especially during short measurement times, transient non-linear heating of the sample can be observed [122]. Due to the high heat load from the excitation source, the incoming energy cannot be emitted fast enough by radiation, convection or conduction such that the sample heats up continuously. Evaluating the temperature oscillation during the early stages of the transient response, systematical phase errors can be observed [122]. To minimize such errors, it is possible to apply the heat excitation already without measuring the temperature oscillation. This time interval is called **conditioning time**. The total time of the TWI measurement is represented by the sum of conditioning time and measurement time and should show a good compromise between low total time but high accuracy and reliability. The temperature oscillation on the surface of a cylinder coating sample during a TWI measurement is shown at the top of Figure 4.9. The measurement is performed using an excitation frequency of 5 Hz for a total time of 95 s. Transient non-linear heating of the sample can be observed during the first 20 s of the measurement followed by an almost linear increase for the rest of the measurement. However, even for a measurement time of larger than 90 s the sample is not in a steady state but still heating up. As shown in [27], thermal equilibrium can be only expected after a time period of about 1000 s. Since this order of total time is not applicable for operation during the large-scale production, TWI cannot be performed during thermal equilibrium to monitor cylinder coatings. However, it is known that TWI measurements may also be performed outside the thermal equilibrium and still deliver accurate results [122, 125]. Therefore, multiple measurements using different combinations of conditioning times and measurement times are evaluated regarding their measured phase values (Table 4.2). In the following, TWI measurements are shown using three different modulation frequencies: 5, 20 and 100 Hz. Using the phase values obtained from the longest total time of 95 s as a reference point, the difference between the measured phase value and the reference is shown in Figure 4.9 bottom. Especially for low total time periods, significant phase deviations are observed compared to the reference phase. While the modulation frequency influences the value and the sign of the deviations, still the higher the total time the lower the deviation to the reference. However, conditioning times of 20 s or higher do not show a drastic improvement of the deviations from the reference phase, while especially there is no observed improvement from 60 s to 90 s in conditioning time, independent of the applied modulation frequency. The most applicable range in terms of suitability for low measurement times and low phase errors lies between 10 s and 25 s. To achieve the lowest possible total time of TWI measurements, the conditioning time and the measurement time are set to 5 s resulting in a total time of 10 s per measurement for each applied excitation frequency.

4.6. Number of applied phase measurements (Layer system)

The overall time of the entire TWI measurement using multiple excitation frequencies is compound by the total time of 10 s of an individual measurement and the number of applied modulation frequencies. Using TWI for research purposes, all possible modulation frequencies can be applied to obtain the highest number of individual measurements since measurement time may not play a too crucial role in designing the experiment. However, focusing on a

Table 4.3.: Comparison between the fitting values calculated from a full frequency and a reduced frequency setup. The measurements are performed for two different positions within a crankcase for 30 times (15 measurements per day, at 2 days). Phase values for fitting of the function in Equation (4.2) are selected randomly from the available measurements, while fitting is repeated 1000 times. The shown mean and standard deviations are calculated from the resulting individual R, η and C values.

Measurement	$\overline{R}$	σ_R	$\overline{\eta}$ [1/s]	σ_η [1/s]	$\overline{C}$ [°]	σ_C [°]
Full Freq, Pos. 1	-0.3510	0.00117	0.1749	0.00058	45.46	0.045
Red. Freq, Pos. 1	-0.3450	0.00222	0.1743	0.00114	45.42	0.086
Rel. Diff [%]	-1.7	89.7	-0.3	96.6	-0.16	91.1
Full Freq, Pos. 2	-0.2731	0.00273	0.1373	0.00094	44.88	0.106
Red. Freq, Pos. 2	-0.2731	0.00368	0.1367	0.00123	44.92	0.140
Rel. Diff [%]	0.0	34.8	-0.4	30.9	0.1	32.1

reduced measurement time setup for an industrial application, additional approaches lowering the overall time are addressed. Besides reducing the total time of an individual measurement as presented in Chapter 4.5, also reducing the number of applied frequencies results in a significant reduction of the overall time. So far, applying all 15 possible frequencies, a TWI measurement at a single position takes about 150 s. However, to monitor the quality of cylinder coatings, one may not only measure the thermal properties of the coating at a single spot but also for various cylinders, angles and positions along the liner resulting in a strong increase of the time consumption. Consequently, the time scale of TWI measurements need to be further reduced.

Aiming to reduce the total time of a TWI measurement using multiple excitation frequencies, comparison between a reduced frequency setup and a full frequency setup is discussed in the following. Two different positions along a cylinder liner are measured 15 times with reduced as well as with full frequency setup. Between each individual measurement the sample is cooled down for 300 s. The reduced frequency setup contains six modulation frequencies 5, 20, 40, 60, 100 and 150 Hz, whereas the full setup contains the 15 individual frequencies which are listed in Chapter 4.2. The reduced frequency spectrum is chosen to cover the entire range of available excitation frequencies within appropriate intervals. The same measurement procedure is repeated again at the following day.

To compare both frequency setups, the repeatability of the measurements is calculated using a **bootstrapping** approach [126]. Therefore, the phase values are drawn randomly from the available 30 measurements (15 repetitions per measurement position per day, at 2 days) for both measurement positions individually. Further fitting of the theory function using Equation (4.2) is applied to the randomly selected phase values and the parameters R, η and C are calculated. This procedure is performed 1000 times for each measurement position. The mean values $\overline{x}$ and the standard deviations σ from these 1000 calculations can be found in Table 4.3. This bootstrapping approach allows to estimate the influence of the measurement variance on the fitting values but not only on the individual phase values.

Comparing the mean values $\overline{R}$, $\overline{\eta}$ and $\overline{C}$ of the fitting parameters for the full and the reduced frequency spectrum, the values obtained with the reduced frequency setup show great accordance to the full setup. Highest deviation of about $1.7\,\%$ from reduced to full frequency spectrum can be found for the reflection coefficient R at position 1, while all other fitting values of the reduced setup show deviations lower than $1\,\%$ to the mean values obtained with the full frequency spectrum. However, the standard deviations calculated from the fitting values of the reduced frequency setup increase for all parameters R, η and C at both positions. In general, an increase of the standard deviations of up to $90\,\%$ can be observed by comparing the two frequency setups. Consequently, lowering the number of available frequencies leads to a lowered repeatability of TWI measurements. However, the highest standard deviation with respect to the measured mean value using a reduced frequency setup is found to be less than $1.4\,\%$. Thus, increasing the standard deviation by reducing the number of applied frequencies still leads to a comparably low standard deviation for the reduced setup. Further, the difference of the fitting parameters between the two measurements positions is compared to the obsereved standard deviations. In this context, the standard deviations of the reduced frequency setup account for less than $5\,\%$ of the the calculated contrast between the fitting parameters. Thus, the two different levels of thermal properties can clearly be identified and separated with respect to the calculated uncertainty of the TWI measurements. Consequently, TWI measurements still show appropriate fitting results even using the reduced frequency spectrum. While in general enhanced amount of data points improve the quality and accuracy of a measurement, lowering the overall measurement time per position from $150\,\mathrm{s}$ to $60\,\mathrm{s}$ by $60\,\%$, this benefit of time reduction clearly outstrips the shown reduction of accuracy. In context of a large-scale production, the average cycle time per crankcase lies between $50-60\,\mathrm{s}$ for a six-cylinder crankcase. Thus, the suggested measurement setup could match the cycle time, if one single TWI measurement would be applied per crankcase. Consequently, multiple in-line measurements at various positions within one crankcase are not achievable with the proposed approach. Thus, one have to prioritize between full-scale in-line testing of every crankcase at a single measurement position or extensive off-line random sample testing of single crankcases at multiple measurement positions.

4.7. Repeatability of thermal diffusivity measurements using TWI

Finally, an optimized measurement setup according to the previous sections is presented in Table 4.4. The table sums all conclusions from the previous sections in a final parameter setup. This setup is optimized delivering TWI measurements showing a compromise of reliability and short overall measurement time. All following TWI measurements in Chapters 5 and 6 are acquired using the described setup. In this context, the study discussed in Chapter 4.6 is further used to estimate the repeatability of thermal diffusivity measurements on cylinder coatings by TWI using the described final setup. The resulting mean values and standard deviations of the fitting value η are taken from Table 4.3 to calculate the repeatability of thermal diffusivity measurements. The previously described bootstrapping approach allows to estimate the repeatability of the fitting parameter η from the measurement variance of the individual phase values. Therefore, the calculated mean and standard deviation values may be

Table 4.4.: Final parameter setup for all following TWI measurements.

Parameter	Value
Laser spot diameter [mm]	20
Percentage of laser spot diameter [%]	33
Laser power [W]	125
Power density on surface [W/mm^2]	0.4
Conditioning time [s]	5
Measurement time [s]	5
Applied frequencies [Hz]	5, 20, 40, 60, 100, 150
Overall time per meas. position [s]	60

used to further calculate the repeatability of thermal diffusivity values.

According to Equation (2.42), the thermal diffusivity of thermally sprayed cylinder coatings is calculated using the fitting parameter η, since

$$\eta = d \cdot \sqrt{\frac{\pi}{\alpha}} \tag{4.3}$$

$$\rightarrow \alpha = \pi \cdot \frac{d^2}{\eta^2}. \tag{4.4}$$

Thus, to calculate the thermal diffusivity from η, the material thickness d of the coating layer must be known. Therefore, the material thickness is measured using the magnetic-inductive method as described in [27] and Chapter 3.6. The corresponding standard deviation σ_d of the thickness measurement is specified to $0.73\,\mu\text{m}$.

Using the Gaussian propagation of uncertainty with respect to the expression of α in Equation (4.4), the standard deviation σ_α is calculated as

$$\sigma_\alpha = \sqrt{\left(\frac{\partial \alpha}{\partial d} \cdot \sigma_d\right)^2 + \left(\frac{\partial \alpha}{\partial \eta} \cdot \sigma_\eta\right)^2} \tag{4.5}$$

The calculated standard deviations σ_α are evaluated for both measurement positions independently, while the results are shown in Table 4.5. Here, repeatability calculations of the TWI measurements show standard deviations of less than 2 % at both measurement positions, thus concluding a comparable repeatability as found for the laser flash analysis in Chapter 3.2. In the following, the standard deviation σ_α of thermal diffusivity measurements by TWI is specified to 2 % as a representative of the repeatability.

4.8. Comparison between thermal wave interferometry to laser flash analysis

Since the laser flash analysis (LFA) is commonly seen as the standard method for measuring thermal properties of solid and liquid materials [78, 79], TWI and LFA measurements of the same cylinder coating samples are compared. Therefore, two samples of thermally sprayed cylinder coatings with varying thermal diffusivity are first measured by TWI using laser-excited lock-in thermography and afterwards by a laser-flash system. TWI measurements are performed

Table 4.5.: Uncertainty of thermal diffusivity measurements using TWI. The mean value of η and its standard deviation are taken from Table 4.3. Thickness values are measured by the magnetic-inductive method described in Chapter 3.6 and the corresponding standard deviation is shown in [27].

Position	η [1/s]	σ_η [1/s]	d [μm]	σ_d [μm]	α [mm^2/s]	σ_α [mm^2/s]	σ_α [%]
1	0.1743	0.00114	204.5	0.73	4.325	0.064	1.47
2	0.1369	0.00123	223.2	0.73	8.375	0.160	1.91

using the described measurement and parameter setup. Due to the required size and shape of the samples for later LFA measurements, the samples are cut out of the cylinder liner at the respective positions. The samples show quadratic shape with a size of $10 \times 10 \times 2\,\text{mm}$. Thus, the laser flash samples show both, coating material as well as substrate. To obtain the thermal properties of the coating material applying the LFA method to a two layer sample, further thermophysical properties of the layer and the substrate are required [79, 107, 109]. The substrate material need to be fully characterized such that thermal diffusivity, specific heat capacity and density must be known. Further, also the specific heat capacity of the coating material as well as its density are required. While specific heat capacities c_{Al} of the substrate and c_{c} of the coating are taken from literature [127, 128], the thermal diffusivity of the aluminum-based substrate α_{Al} is measured separately. Therefore, two reference samples are cut out of the cylinder liner right next to the original samples at the same heights for both measurement positions. The reference samples are prepared such that the cylinder liner material is removed entirely by dragging down the coating to the substrate. Hence, only substrate remains and the reference samples can be used to quantify the thermal transport properties of the aluminum alloy separately. The densities of the aluminum alloy samples ρ_{Al} are measured according to the Archimedes' principle. Further, the coating densities ρ_{c} are calculated by using cross section images to obtain the coating porosity. Cross section specimens are cut out of the liner next to the original samples and are evaluated quantitatively as described in Chapter 3.4. As the original density of the coating material is taken from literature [128], its final density after thermal spraying is reduced by the obtained coating porosity. Additionally, material thicknesses of coating and substrate are required. Coating thickness is obtained non-destructively as described in Chapter 3.6, while the total sample thickness is measured using a micrometer screw allowing to access the thickness of the substrate.

Comparing the thermal diffusivities of the cylinder coatings obtained by LFA and TWI in Table 4.6, both methods show comparable results for both measurement positions. As found for position 2, the TWI measurement shows a difference of about $2.8\,\%$ to the LFA measurement, which is lower than the specified accuracy of the LFA apparatus. Greater deviation is found for position 1 as the TWI measurement is about $20\,\%$ lower than the LFA value. As this deviation is certainly outside the specified accuracy of the LFA, however the accuracy of TWI and LFA may be reduced due to the two layer system. While a two layer analysis of the LFA requires seven coating and substrate properties (**Substrate:** layer thickness, density, specific heat capacity, thermal diffusivity; **Coating:** layer thickness, density, specific heat capacity),

Table 4.6.: Comparison between LFA and TWI thermal diffusivity measurements on cylinder coatings. Measurements are performed for samples taken from two different positions along the cylinder liner showing varying thermal diffusivities. Thermal diffusivities of the coatings obtained from a two-layer analysis of the flash measurements are noted by α_{FA}. Further, the index TWI represents the thermal diffusivity measurements obtained from thermal wave interferometry.

Pos	$c_{\text{Al}} \left[\frac{\text{kJ}}{\text{kg·K}}\right]$	$\rho_{\text{Al}} \left[\frac{\text{g}}{\text{cm}^3}\right]$	$\alpha_{\text{Al}} \left[\frac{\text{mm}^2}{\text{s}}\right]$	$c_{\text{c}} \left[\frac{\text{kJ}}{\text{kg·K}}\right]$	$\rho_{\text{c}} \left[\frac{\text{g}}{\text{cm}^3}\right]$	$\alpha_{\text{LFA}} \left[\frac{\text{mm}^2}{\text{s}}\right]$	$\alpha_{\text{TWI}} \left[\frac{\text{mm}^2}{\text{s}}\right]$
1	0.9	2.74	66.2	0.46	6.88	5.29	4.32
2	0.9	2.73	68.9	0.46	6.81	8.23	8.46

uncertainties of these parameters can cause a significant reduction of the LFA's accuracy in sharp contrast to the TWI method only requiring one additional parameter (coating layer thickness). Therefore, an estimation of a measurement deviation of the aluminum alloy bulk material is required to evaluate the resulting uncertainty on the calculated two-layer model. In accordance to the specified uncertainty of the LFA apparatus, the two-layer analysis is again performed with $\pm 5\,\%$ of the measured α_{Al} value. Here, the newly calculated α_{LFA} values all deviate by about $\pm 15\,\%$ to the originally measured thermal diffusivity. In this context, satisfying accordance of the thermal diffusivity values obtained by LFA and TWI are found. Since following investigations shown in Chapters 5 and 6 mainly focus on relative differences of thermal diffusivity values between the investigated positions within the crankcases, the main objective of this method is to measure detectable relative differences of the thermal properties between different coating samples. Still, TWI delivers reliable results for thermal diffusivity measurements on thermally sprayed coatings.

While LFA is generally known to accurately characterize the thermal properties of metals, it has several major disadvantages for the application in the environment of a large-scale production. While LFA is in general non-destructive, two side access as well as defined sample sizes do not allow to measure the thermal diffusivity of cylinder coatings non-destructively. Further, several thermophysical properties of the substrate and the coating must be known to obtain the thermal diffusivity of the coating. In contrast, the one-dimensional TWI theoretical model described in Chapter 2.6.2 does only require the material thickness of the coating, which is anyway already monitored during the large-scale production of the crankcases by magnetic-inductive measurements. Additionally, specific size and shape of the samples require additional preparation steps resulting in expensive and time consuming pretreatments. Therefore, even for the investigation in a laboratory environment, the availability of LFA measurements is strongly limited. While TWI can be performed truly non-destructively, thermal diffusivity measurement of a single sample takes about 60 s per position. Combining these advantages, TWI is highly favorable for the evaluation of thermal properties of cylinder coatings in a large-scale production environment compared to LFA.

5. Characterization of thermally sprayed cylinder coatings

The following chapter discusses non-destructive TWI thermal diffusivity measurements of wire arc sprayed cylinder coatings and compares these results to destructive bond strength testing. Statistical analysis as introduced in Chapter 5.1 helps to understand the deciding influencing factors on the observed data sets. The shown measurements are performed for four crankcases of type OM656 (Mercedes-Benz AG, Stuttgart, Germany) which were randomly selected from the large-scale production. Further, metallographic analysis and X-ray computed tomography measurements are used to investigate the microstructure of the cylinder coatings. The microstructure analysis is taken to explain distinct relations between the observed thermal and mechanical properties.

The shown results and discussions have already entirely or partially been published in the following journal articles: *"Thermal wave interferometry measurements and microstructural analysis of twin wire arc spray cylinder coatings for passenger car engines"* [82] and *"Thermal wave interferometry measurements correlated to microstructural properties and bonding behavior of thermally sprayed coatings"* [102]. A complete list of all publications related to the presented work is shown in Chapter *Publications.*

5.1. Applied statistical analysis

In experimental studies, it is a common approach to test if certain categories have a statistically significant influence on the observed data set. In this context, statistic tests mostly use a null hypothesis, that the investigated category has no influence on the measured data. Such tests calculate a probability value based on the underlying data, if this null hypothesis can be accepted. If the calculated probability P_x is below a significance level, the null hypothesis needs to be rejected thus the investigated category has a statistically significant influence on the data. Conventionally, significance levels of 0.01 or 0.05 are applied to test such hypothesis. Thus, in all following statistical tests, a significance level of 0.05 is chosen.

One of the most common statistical tests is the analysis of variance (ANOVA). The ANOVA compares the variance of the data within one category to the variance of individual data groups within this category [129–131]. In the context of this work, one possible category is the *liner position*, whereas the individual groups within this category are the measurement positions along the liner $10\,\mathrm{mm}, 40\,\mathrm{mm}, 70\,\mathrm{mm}, 100\,\mathrm{mm}$ and $130\,\mathrm{mm}$ (Figure 3.1). In this case, the ANOVA would calculate the probability P, if the liner position has no statistically

significant influence on the measured data. The calculated probability P is based on a Fischer distribution, which represents the probability if the null hypothesis can be accepted [130]. In general, high F-values as well as P-values lower than the significance level indicate a statistically significant influence of the investigated category on the measurement data and the null hypothesis needs to be rejected. Further, the ANOVA is used to calculate the sum of squares (SoS) of the underlying data for the different categories as well as for a residual part. The residual part defines a category for the remaining data variation which cannot be described by the introduced main categories. This residual part does also include any type of statistical and systematical uncertainties of the measurement method. Based on the calculated sum of squares, a contribution ratio can be expressed representing the percentage of the individual sum of squares to the accumulated sum of squares. The contribution ratio defines the percentage of the data variation attributed to the respective category.

Using an ANOVA to test the statistical significance of a category, certain assumptions about the tested data set are required to obtain a reliable probability value P. Thus, the variations of the data within the investigated category need to be independent, identical as well as normally distributed [130]. Especially in terms of violating the assumed normal distribution of the variations, other statistical approaches are available to test the proposed null hypothesis. In this context, a Kruskal-Wallis test by ranks can be applied which does not assume a normal distribution of the variances within the categories [132]. However, the calculated sum of squares and the related distribution ratios presented by the ANOVA are independent of the required assumptions.

In the following, thermophysical properties as well as mechanical bond strengths are evaluated in Chapters 5.2 and 5.3. The measured data is analyzed using an ANOVA and presented in Tables 5.1 and 5.4. Further, probability values P_{anova} calculated by the ANOVA are compared with probability values $P_{kruskal}$ from a Kruskal-Wallis test presented in Tables 5.3 and 5.6. All shown statistical analysis of the data sets are performed using the *scipy* library and the *statsmodels* library implemented in *Python*.

5.2. TWI study

TWI thermal diffusivity measurements of the cylinder coatings are performed for four individual crankcases within all six cylinder bores. The used crankcase coordinate system is described in Figure 3.1. The TWI measurements are divided into four angle positions $0°, 90°, 180°$ and $270°$ and applied at five liner positions $10\,\mathrm{mm}, 40\,\mathrm{mm}, 70\,\mathrm{mm}, 100\,\mathrm{mm}$ and $130\,\mathrm{mm}$ below the cylinder head sealing surface resulting in overall 480 individual data points. The individual data points of the TWI study are listed in the appendix in Chapter C.2. TWI measurements are applied according to the attained parameter setup as described in Table 4.4. The obtained phase values are fitted to the model function in Equation (4.2) by non-linear least square fitting resulting in the fitting parameters R, η and C. However, Equation (4.4) shows that only η is used to calculate the thermal diffusivity α. Consequently, additional information about the coating thicknesses d is required. Therefore, using the non-destructive thickness measurement method as shown in Chapter 3.6, material thickness values of the thermally sprayed cylinder coatings are gathered at the same measurement positions as TWI is applied.
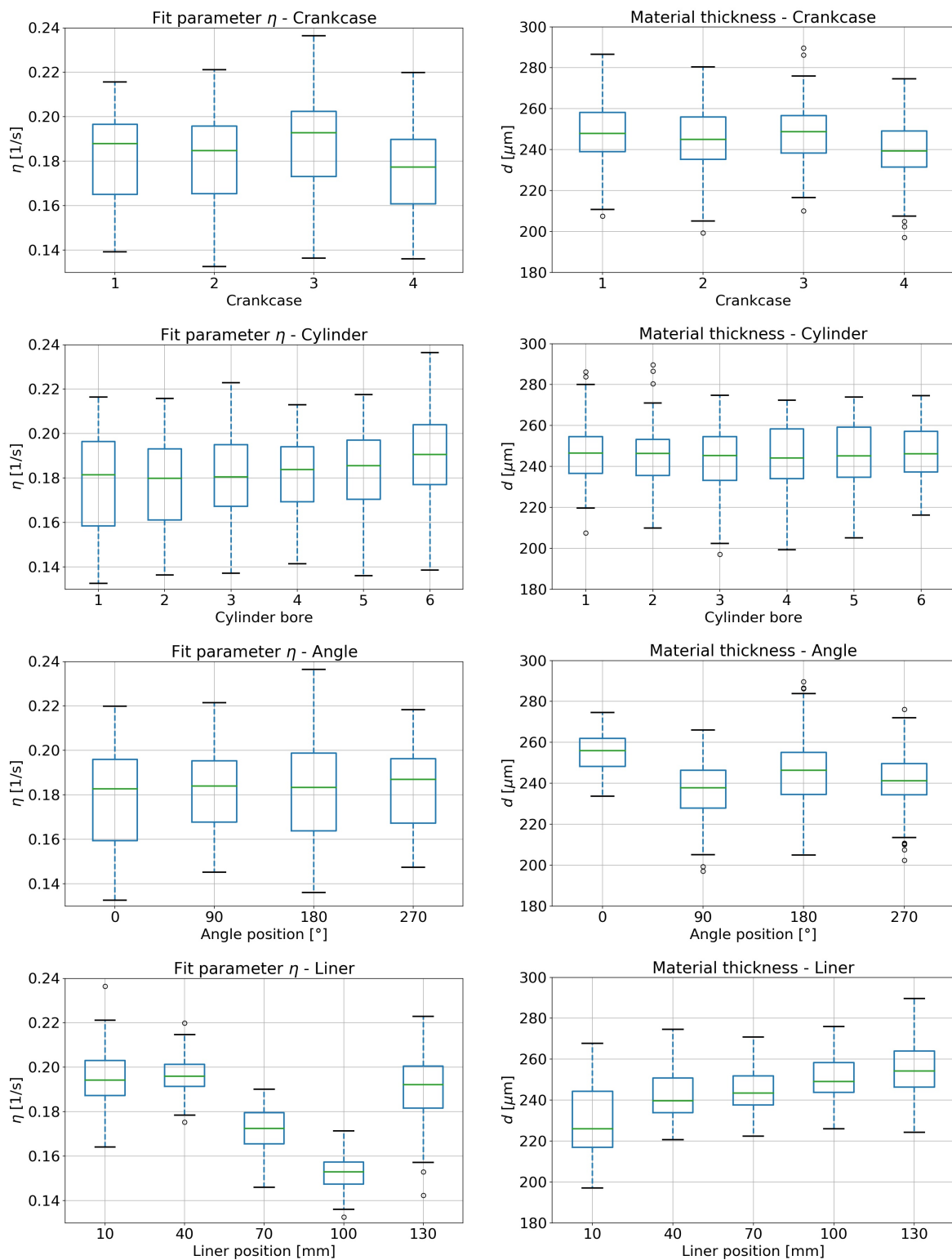
Figure 5.1.: Fitting parameter η and material thickness d of thermally sprayed cylinder coatings with respect to the individual crankcases, cylinders bores, angle positions and liner positions. All shown plots include 480 individual data points. Boxplots: The green lines represent the median of the underlying data; boxes indicate the upper/lower quartiles; the whiskers are set to a maximum of 1.5 times the interquartile range. Circles mark data outside the whiskers.
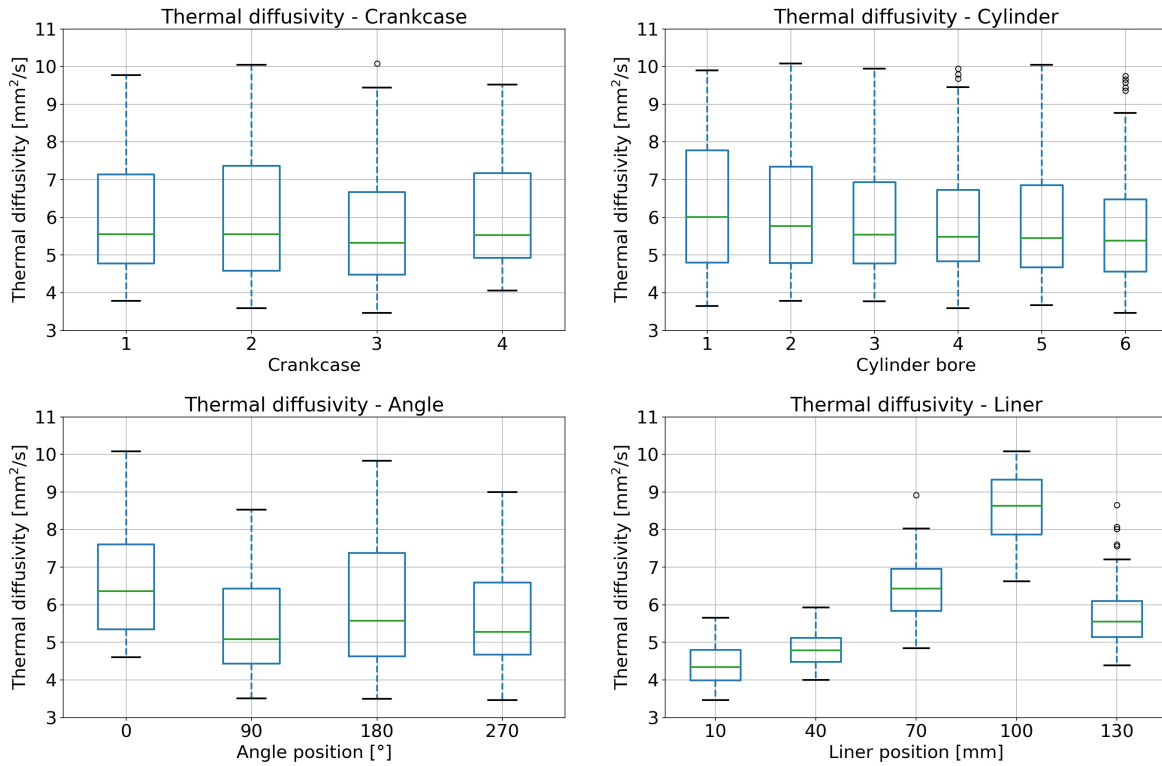
Figure 5.2.: Thermal diffusivity measurements of thermally sprayed cylinder coatings with respect to the individual crankcases, cylinders bores, angle positions and liner positions. All shown plots include 480 individual data points. Boxplots: The green lines represent the median of the underlying data; boxes indicate the upper/lower quartiles; the whiskers are set to a maximum of 1.5 times the interquartile range. Circles mark data outside the whiskers.

In the following, measured and calculated data is divided into four different categories *crankcase*, *cylinder bore*, *angle position* and *liner position*. The data is visualized using *boxplots*. The green lines in the boxes represent the medians of the underlying data, while the blue boxes show the upper and lower quartiles. Each quartile contains 25 % of the data points below and above the median values. Further, whiskers are set to a maximum of 1.5 times the respective quartile range. If data points are found outside the whiskers, these outliers are marked by circles. The fitting parameter η, the material thicknesses d and the calculated thermal diffusivity values α are shown in Figures 5.1 and 5.2. The additional two fitting parameters R and C are listed in the appendix in Chapter C.1. The ANOVA results of the fitting parameter η, the material thicknesses d and the calculated thermal diffusivity values α are shown in Table 5.1. Further, median values as well as the upper and lower limits of the boxes for η, d and α with respect to the liner positions are listed in Table 5.2. The ANOVA of the two additional fitting parameters R and C are also listed in the appendix in Chapter C.1.

The calculated fitting parameter η and the measured material thickness values d are illustrated in Figure 5.1. Both, η and d are found to show evenly distributed levels without major separation between the individual **crankcases**. The median values of the fitting parameter η is constant between $0.17 - 0.20\,1/\text{s}$ for all four crankcases, however crankcase 3 shows slightly enhanced variations of its η-values represented by the larger upper whisker. According to the

Table 5.1.: ANOVA results of TWI and coating thickness measurements. The significance level is set to 0.05. The SoS values represent the sum of squares for the different categories, DF are the degrees of freedom, F are the F-values of the Fischer distribution and P presents the probability that the null hypothesis is correct. Further, cont. ratio stands for the contribution ratio as being calculated from the resulting sum of squares.

Parameter	Category	SoS	DF	F	P	Cont. ratio [%]
η	Crankcase	0.0088	3	31.0	$3.0\,e-18$	4.5
	Cylinder	0.0056	5	12.2	$5.0\,e-11$	2.9
	Angle	0.0014	3	4.9	$2.5\,e-3$	0.7
	Liner	0.1360	4	358.6	$2.7\,e-140$	69.5
	Residuals	0.0440	463			22.4
Coating thick.	Crankcase	5078	3	14.9	$2.8\,e-9$	4.3
	Cylinder	1271	5	2.2	$5.0\,e-2$	1.1
	Angle	22982	3	67.4	$3.6\,e-36$	19.5
	Liner	35725	4	78.6	$7.7\,e-51$	30.4
	Residuals	52629	463			44.7
Therm. diff.	Crankcase	12.7	3	17.1	$1.5\,e-10$	1.0
	Cylinder	18.5	5	15.0	$1.2\,e-13$	1.4
	Angle	104.6	3	141.4	$5.0\,e-65$	8.1
	Liner	1036.9	4	1051.2	$1.0\,e-230$	80.6
	Residuals	114.2	463			8.9

Table 5.2.: TWI and thickness measurements of thermally sprayed cylinder coatings along the cylinder liner position. The interval between the lower and upper quartile describes 50 % of all acquired data points.

	10 mm	40 mm	70 mm	100 mm	130 mm
Median η [1/s]	0.194	0.196	0.172	0.153	0.192
Lower quart. η [1/s]	0.188	0.191	0.166	0.148	0.182
Upper quart. η [1/s]	0.203	0.201	0.180	0.157	0.200
Median d [µm]	226.6	239.8	243.5	249.2	254.3
Lower quart. d [µm]	217.4	233.8	237.7	243.8	246.3
Upper quart. d [µm]	244.5	250.9	251.8	258.3	264.0
Median α [mm^2/s]	4.33	4.79	6.43	8.68	5.57
Lower quart. α [mm^2/s]	3.98	4.48	5.84	7.87	5.09
Upper quart. α [mm^2/s]	4.80	5.05	6.96	9.32	6.08

shown results of the ANOVA in Table 5.1, the crankcases themselves present a significant influence on the shown η-values as the probability P is lower than the significance level and close to zero. Thus, the null hypothesis that this category has no influence needs to be rejected. Consequently, the crankcases have a statistically significant influence on η, however the contribution ratio is relatively low. The overall variance of the data according to the individual crankcases is low compared to the other introduced categories. Therefore, considering the median values as well as the quartile and whisker ranges, no major differences between the four crankcases can be found for the fitting parameter η.

Comparable behavior is seen for the material thicknesses as the median values of crankcases 1-3 are on an equal level and crankcase 4 is found to show a slightly lower median value below 240 μm compared to the others. However, the quartile ranges as well as the whiskers do not reveal major differences of the material thickness variations between the individual crankcases as they all cover thicknesses between $200 - 280$ μm. Again, the ANOVA also presents a statistical significance based on the crankcases as the P value is close to zero. However, comparable to the η-value, the contribution ratio for the material thickness is below 5 % thus the overall variation of the data along the category is low compared to other influencing factors. Further, the calculated thermal diffusivities α using the parameters η and d based on Equation (4.4) are shown in Figure 5.2. The median values of the thermal diffusivities with respect to the individual crankcases are all on an equal level of $5.5 \, \mathrm{mm}^2/\mathrm{s}$, whereas the whiskers indicate great variation of the thermal diffusivity ranging from $3.5 - 10 \, \mathrm{mm}^2/\mathrm{s}$ found for all four crankcases. Still, the investigated cylinder coatings show quite the same ranges and medians of their thermal diffusivity values for all four crankcases. The ANOVA shows a statistical significance of the introduced category, however the contribution ratio of the crankcases is again quite low. For the thermal diffusivity, even lowest overall contribution ratio of 0.98 % is found with respect to the crankcases. Therefore, even though the crankcases show statistical significance in all parameters, the observed variations are low compared to other categories.

Classifying the calculated fitting parameter η into the category **cylinder bores**, median values increase from bore 1 to 6. Whereas lower whiskers indicate an almost constant level over all six cylinders, upper whiskers show significant variations as especially bore 6 tends to higher η-values. In this context, the analysis of the variances reveal a statistical significant influence of the respective cylinder bore on the η-values. However, again the contribution ratio is low thus the influence of the category is quite irrelevant compared to the remaining influencing factors.

Further, material thicknesses are found to stay almost constant along the cylinder crankcases. However lower whiskers of cylinder bores 3 and 4 indicate lower minimum thickness values. In general, material thicknesses are distributed anisotropically over the crankcases. The crankcases exhibit a strong heat load due to the thermal spraying as well as due to preheating of the uncoated crankcases. After thermal spraying, the unique shape of a crankcase causes anisotropic cooling thus leading to nonuniform mechanical deformation of the crankcases. Especially the middle parts of the crankcases exhibit stronger mechanical deformation orthogonally to the elongation of the crankcases (between 90° and 270°). The parts tend to tighten primarily in the

middle of the crankcases causing an elliptical shape of the bores. In turn, circular mechanical treatments finish the cylinder coatings after cooling thus removing increased amount of coating material for cylinder bores 3 and 4 primarily at the angle positions 90° and 270°. Therefore, the material thicknesses at the described positions are often reduced compared to the other positions in the crankcases. These variations are indicated by increased lower whiskers at the respective positions, whereas the median values are equally distributed along the crankcases. Even though the minimum values of the coating thicknesses are anisotropically distributed along the cylinder bores, lowest significance is found for the influence of the cylinder bore based on the shown ANOVA results. Here, the probability P is 0.05 thus equal to the significance level. As this category can still be seen to have a statistical significant influence on the coating thickness, however the cylinder bores show the highest probability value of all categories as well as being unequal to zero. Also the contribution ratio is found to be the lowest of all categories with respect to the material thickness. Consequently, no major differences of the coating thickness with respect to the cylinder bore are assumed.

Besides, as the overall material thickness is found to be quite constant over the six cylinder bores, the increasing η from bore 1 to 6 represents a decreasing thermal diffusivity as found in Figure 5.2 top right. Both, medians and the range of the upper and lower quartiles decrease towards the higher cylinder bores. Statistical evaluation of the thermal diffusivity values according to cylinder bores does show statistical significance as the P value is close to zero and clearly below the significance level. However, the maximum and minimum values indicate a comparable range of the measured thermal diffusivity values over all six bores. Consequently, the contribution ratio of the thermal diffusivity variation with respect to the cylinder bore is found to be quite low at about 1.44 %. In this context, thermal diffusivity variations along the cylinder bores may be neglected.

Further, median η-values are distributed equally over the different **angle positions** as these values are constantly above 0.18 1/s. Whereas the quartiles at position 180° are slightly enhanced compared to the other angle positions, no clearly separated levels of the η-values can be identified according to their angle positions. Thus, lowest significance of the η-values along the angle positions is predicted by the ANOVA. Here, highest probability value of about 0.25 % is found. Still, the calculated probability is less than the chosen significance level of 0.05. Further, also lowest contribution ratio of less than 1 % is calculated as the angle positions may not show major influences on the measured η-values.

However, material thickness measurements reveal differences between the longitudinal (0° and 180°) and the transverse direction (90° and 270°). As already described above, mechanical deformation due to anisotropic cooling behavior causes elliptical bores. The circular mechanical machining removes enhanced amount of coating material at the angle positions 90° and 270° which can be clearly seen by dividing the thickness measurements by their angle positions. Median as well as maximum thickness values are higher along the longitudinal axis than those of the transverse axis. However, a maximum difference of the median values of about 20 μm comparing positions 0° and 90° reveal that the mechanical deformation of the crankcase is comparably low to the bore diameter of 82 mm. Further, even lowest material thickness of

197 µm still shows significant amount of remaining coating material over the substrate. The ANOVA predicts second lowest probability value close to zero for the respective angle position. Thus, a statistical significant influence of the angle position on the material thickness can be expected. Further, also comparably high contribution value of about 20 % shows that a significant amount of the observed material thickness variations can be traced back to the angle positions.

Additionally, also thermal diffusivity values are found to be higher along the axis of the crankcase elongation compared to the orthogonal direction. Median values found at positions $0°$ and $90°$ are separated by about $1.5 \, \mathrm{mm^2/s}$. Further, the upper whiskers along the longitudinal direction indicate that the respective thermal diffusivity values of the cylinder coatings reach higher levels compared to the transverse directions. These observed variations are also represented by the ANOVA since second lowest probability value of $P = 5.00 \, \mathrm{e} - 65$ is calculated. Here, for sure statistical significant influence of the angle position on the thermal diffusivity can be assumed, however the contribution ratio of 8.13 % still indicates that the observed variations are low compared to other categories. Thus, the angle position may show a high statistical influence on the thermal diffusivity values, however other categories still present stronger variations.

The most relevant changes of the fitting parameter η are found along the cylinder **liner position**. Whereas the categorization of the data by crankcase, cylinder bore and angle position only showed minor variations with contribution ratios of less than 5 %, the liner position appears to have the strongest influence on the thermophysical properties. Comparing liner positions 10 mm and 40 mm to the position 100 mm, two clearly separated levels are found. The η-values in the upper parts of the liner indicate a comparable level, whereas the calculated values at position 100 mm do not overlap with those at position 40 mm. Median values, quartile ranges and whiskers are separated comparing the upper and lower parts of the cylinder liner. Further, η-values calculated for positions 70 mm show transient behavior as they range in between the described two η-levels. The whiskers overlap with the median values of positions 10 mm, 40 mm and 100 mm, whereas the box at position 70 mm is separated from those at 10 mm and 40 mm as well as at 100 mm. As the median values decrease from top to bottom, η is found to be on the same level at 130 mm as in the upper liner positions 10 mm and 40 mm. In this context, the calculated results of the ANOVA present a probability that the liner position has no statistical significant influence of about $2.72 \, \mathrm{e} - 140$ thus being zero. Consequently, the liner position is found to be statistically significant for the η-values and further the contribution ratio is found to be highest along all four categories. Therefore, about 70 % of the η-variations observed in the TWI study may be described by the liner position. However, still a high amount of the data variations may not be described by one of the introduced categories as the residuals still present a contribution ratio of over 22 %. Thus, still other influences than the four introduced categories are present influencing the thermal transport properties of the cylinder coatings. Further, also measurement uncertainties are included in the residual part.

Further, material thicknesses are constantly increasing from liner position 10 mm to 130 mm.

Again, such variations result from mechanical deformation of the crankcases during the cooling process. Mechanical deformation is known to be significantly higher in the upper parts of the crankcase as these parts are cooling much faster due to lower amount of surrounding material. Crankcases show a trapeze-like shape since the crankshaft requires enhanced space and stability. Thus, the crankcase builds-up broader at the crankshaft compared to the cylinder head sealing surface. Therefore, the upper parts of the crankcases contract stronger than at lower liner positions during the cooling phase resulting in a cone-shaped cylinder bore with a lowered diameter at the top of the bore compared to the bottom. While mechanical machining is set to create constant bore diameters along the entire cylinder liner, greater amount of coating material is removed in the upper parts of the bores. Therefore, the ANOVA shows a significant influence of the liner position for the material thickness values. Again, the probability P is close to zero. Further, the contribution ratio is about 30% thus in a comparable range as the angle position. However, the ANOVA also predicts that about 45% of the data variations are represented by the residuals. Therefore, highest amount of the data variation may not be traced back to the four introduced categories.

As already shown for the fitting parameter η, strongest variation of the thermal diffusivity of the cylinder coatings is found with respect to the liner positions. The obtained thermal diffusivity values can be divided into two separated levels for the upper parts of the liners at $10\,\mathrm{mm}$ and $40\,\mathrm{mm}$ and the lower parts at $100\,\mathrm{mm}$. The respective whiskers for position $10\,\mathrm{mm}$ and $40\,\mathrm{mm}$ do not overlap with those for position $100\,\mathrm{mm}$. The median thermal diffusivity values show a strong increase from the cylinder head sealing surface towards $100\,\mathrm{mm}$, whereas the median value more than doubles from $4.33\,\mathrm{mm^2/s}$ at liner position $10\,\mathrm{mm}$ to $8.68\,\mathrm{mm^2/s}$ at liner position $100\,\mathrm{mm}$. Further, narrow whiskers and boxes found for the data at the upper positions indicate only small variations of the measured thermal diffusivity values of about $2\,\mathrm{mm^2/s}$. Thermal diffusivity values found for position $70\,\mathrm{mm}$ follow the increase of the thermal diffusivity from cylinder head sealing surface towards lower positions as the measured mean value of $6.43\,\mathrm{mm^2/s}$ lies in between the two described levels. However, the described increase of the thermal diffusivity is followed by a strong decrease towards position $130\,\mathrm{mm}$ with a median value of $5.57\,\mathrm{mm^2/s}$ lying in between the separated levels. The ANOVA predicts lowest overall probability of $1.00\,\mathrm{e}-230$. Therefore, the liner position itself can truly be seen as statistically significant. Further, about 80% of the data variation is found for the thermal diffusivity along the cylinder liner thus being the major influence factor along all four categories. The residual part of 8.87% is comparably low such that one may conclude from the ANOVA that the introduced categories represent over 90% of the data variations and that the thermal diffusivity values are primarily dominated by the liner position.

Since the ANOVA assumes the variances within one category to be normally distributed, a Kruskal-Wallis test by ranks is additionally applied to counter test the calculated probability values of the ANOVA. Table 5.3 presents a comparison between P_{anova} and $P_{kruskal}$ for the thermal diffusivity values. Here, all calculated probability values raise using the Kruskal-Wallis test in contrast to the ANOVA. Further, the probabilities that categories *crankcase* and *cylinder bore* do not have a statistical significant influence on the thermal diffusivity, exceed the

Table 5.3.: Comparison of statistical significance testing for categorized thermal diffusivity values. The significance level is set to 0.05. Bold digits show probability values above the chosen significance level.

Parameter	Category	P_{anova}	$P_{kruskal}$
Therm. diff.	Crankcase	$1.5\,e-10$	$\mathbf{1.5\,e-1}$
	Cylinder	$1.2\,e-13$	$\mathbf{2.1\,e-1}$
	Angle	$5.0\,e-65$	$2.4\,e-9$
	Liner	$1.0\,e-230$	$4.7\,e-80$

significance level of 0.05. Consequently, assuming the variances to be non-normally distributed, certain categories cannot be seen as statistically significant by the Kruskal-Wallis test. However, both other categories *angle position* and *liner position* remain below the significance level. Still lowest probability value can be found for the liner position. Combining the ANOVA analysis with the Kruskal-Wallis test, highest contribution value as well as statistical significance at both applied tests still conclude the major influence on the thermophysical properties arising from the liner position.

The boxplots and the ANOVA of the two additional fitting parameters R and C are listed in the appendix in C.1. Here, also the reflection coefficient R shows variations along all four categories, whereas the liner position is found to have the strongest statistical influence on the R-values. The contribution ratio is calculated to $63\,\%$ with respect to the liner position, whereas all other categories are found to be below $20\,\%$. The R-value does increase from the cylinder head sealing surface towards liner position $100\,\mathrm{mm}$, however it does not reveal the same shape of the trend as found for the thermal diffusivity. The R-values are already found on a comparable high level at liner position $70\,\mathrm{mm}$ as shown at $100\,\mathrm{mm}$, whereas the values do not drop at the lowest liner position of $130\,\mathrm{mm}$. Additionally, the introduced offset correction value C is also found to depend on the four different categories as they all can be seen as statistically significant according to the applied ANOVA. However, all four categories reveal only low contribution ratios, indeed the residuals account for over $50\,\%$ of the data variation. Still, the liner position appears to have an effect on the offset C as the median values tend to converge against $45°$ at liner position $70\,\mathrm{mm}$ and $100\,\mathrm{mm}$, whereas the remaining liner positions are found to be above $45°$.

Another approach to visualize the variations of the thermophysical properties of the cylinder coatings along the liner position is shown in Figure 5.3. Here, 13 individual parameter maps of the fitting parameter η are taken along one liner and assembled to one continuous map. The individual parameter maps are acquired similar to the introduced offset maps shown in Chapter 4.3 and Figure 4.7. Here, the acquired phase values per camera pixel are not averaged over the ROI as described in Chapter 4.2, but each camera pixel is analyzed individually. The acquired phase information per camera pixel is fitted to the model function resulting in an individual η-value for each pixel such that an η-map can be calculated. These 13 individually measured parameter maps are overlapped to continuously visualize the η-values along the
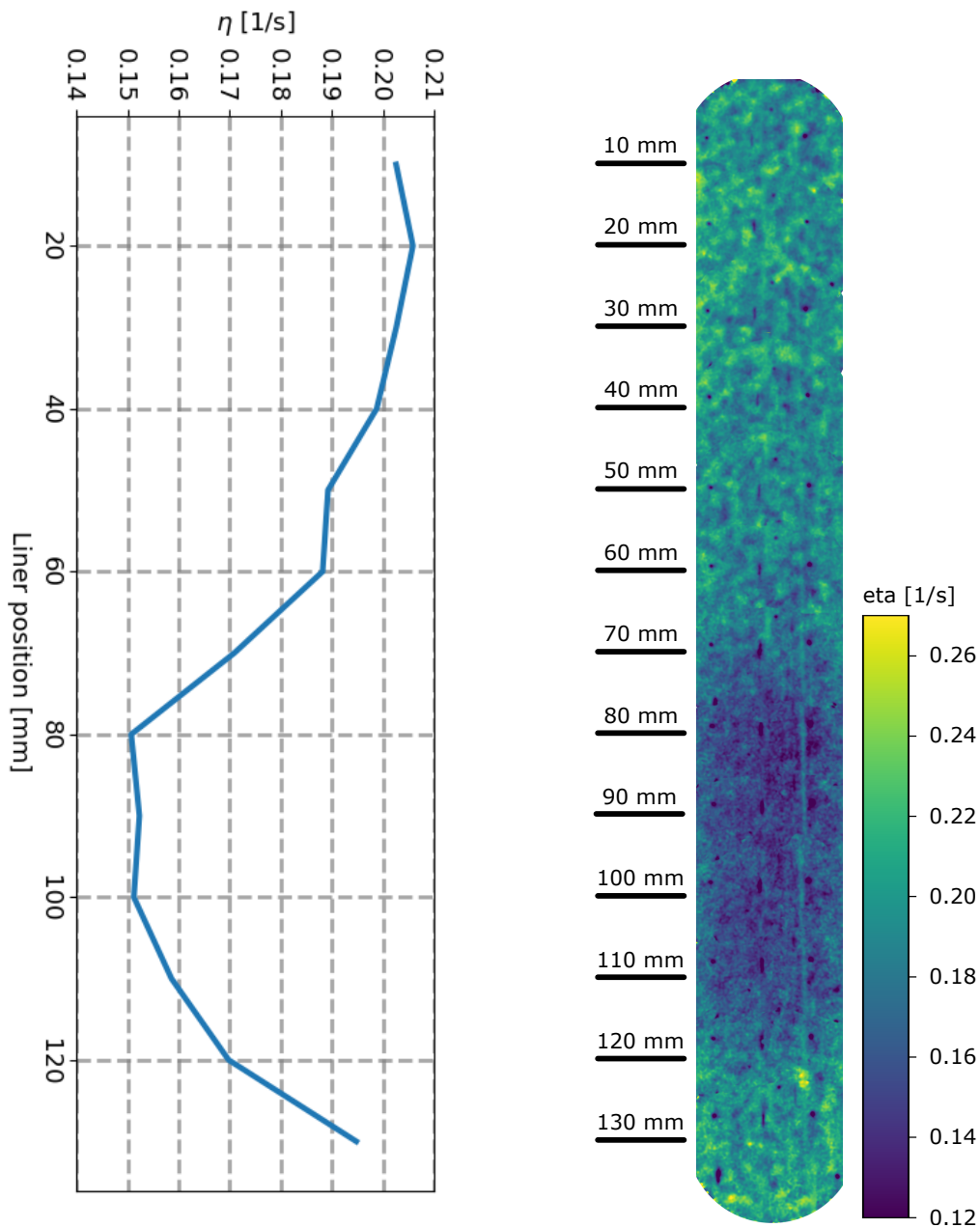
Figure 5.3.: Continuous fitting map of the parameter η along the cylinder liner. The shown map is assembled by 13 individual fitting maps. The plotted η-values represent the mean values over an area with $6.7\,\text{mm}$ diameter per measurement position.

cylinder liner.

First, the map shows repeating observable artifacts, such as dark spots on the left and the right edges of the map. It is assumed that these artifacts result from contamination of the optical components and the sample surface during the measurements. Additionally, a vertical bright line on the right lower side of the map results from surface reflections of the optical components and the infrared camera. However, the map supports the conclusion of two separated levels of the thermal properties comparing the upper and the lower part of the cylinder liner. Since the parameter η contains both, thermal diffusivity and material thickness, the parameter map does not simply show the thermal characteristic of the cylinder coatings

along the liner. As a matter of fact, the coating thickness cannot be determined for every camera pixel individually without destructive preparation thus it is not possible to calculate a thermal diffusivity map from the η-map. However, even such η-maps can be used to gather information about the thermal behavior of the cylinder coatings. Whereas the coating thickness appears to slightly increase along the liner, however it does not show two separated levels. Therefore, major changes of the η-values result from varying thermal diffusivity values of the investigated coating layers. In the upper parts, the map shows enhanced η-values, whereas a spotted structure is present. It is assumed that these variations of the map result from open porosity on the surface of the liner. As previously described in Chapter 4.3, surface porosity leads to enhanced lateral heat flux thus causing unexpected temperature variations on the sample surface. As such fluctuations cannot be found in the range between $80\,\text{mm} - 110\,\text{mm}$, however they become present again in the lowest part of the liner at position $130\,\text{mm}$. The lower part of the liner ranging from $80\,\text{mm} - 100\,\text{mm}$ shows constant η-values thus thermal diffusivity is assumed to stay almost constant over this interval. Further, the map reveals that liner position $60\,\text{mm} - 80\,\text{mm}$ constitutes as a transition region where the thermal properties change significantly. Therefore, thermal properties of the cylinder coating may not increase constantly along the liner but change rapidly in the region of about $70\,\text{mm}$. The constant level of thermal diffusivity over the range of $80 - 100\,\text{mm}$ is again followed by a rapid change of the coating's characteristics towards position $130\,\text{mm}$ to a comparable level as found in the upper parts of the liner.

Summarizing this TWI study, thermal diffusivity values of wire arc sprayed cylinder coatings are calculated by determining the fitting parameter η and the material thickness of the coatings d for four different crankcases. The resulting thermal diffusivity values α are divided into four different categories to discuss the distribution of the thermophysical properties. Whereas the TWI measurements reveal a wide range of the thermal diffusivity values from $3.5 - 10\,\text{mm}^2/\text{s}$ in the individual crankcases, the calculated values may not be randomly distributed within this interval. In fact, the applied ANOVA predicts that introduced categories *crankcase*, *cylinder bore*, *angle position* and *liner position* all show a statistically significant influence on the measured thermal diffusivity values for a conventional significance level of 0.05. However, using a Kruskal-Wallis test by ranks to counter test the statistical significance of the introduced categories assuming the variances to be non-normally distributed, certain categories do not show a statistically significant influence. Here, the calculated probability values for the influence of the crankcase and cylinder bore do exceed the chosen significance level. Still, lowest probability value P below the significance level as well as highest contribution ratio of about $80\,\%$ of the calculated sum of squares is found for the cylinder liner positions at both statistical tests. In this context, the majority of the data variance is represented by the influence of the liner position. The cylinder coatings obtain their lowest thermal diffusivity values in the upper parts of the liners close to the cylinder head sealing surface, whereas the values increase by over $100\,\%$ towards the liner position $100\,\text{mm}$ below the sealing surface. Both levels can be clearly separated as the maximum thermal diffusivity found in the upper parts of the liner is still lower than the minimum values at position $100\,\text{mm}$. Additionally, the η-maps conclude
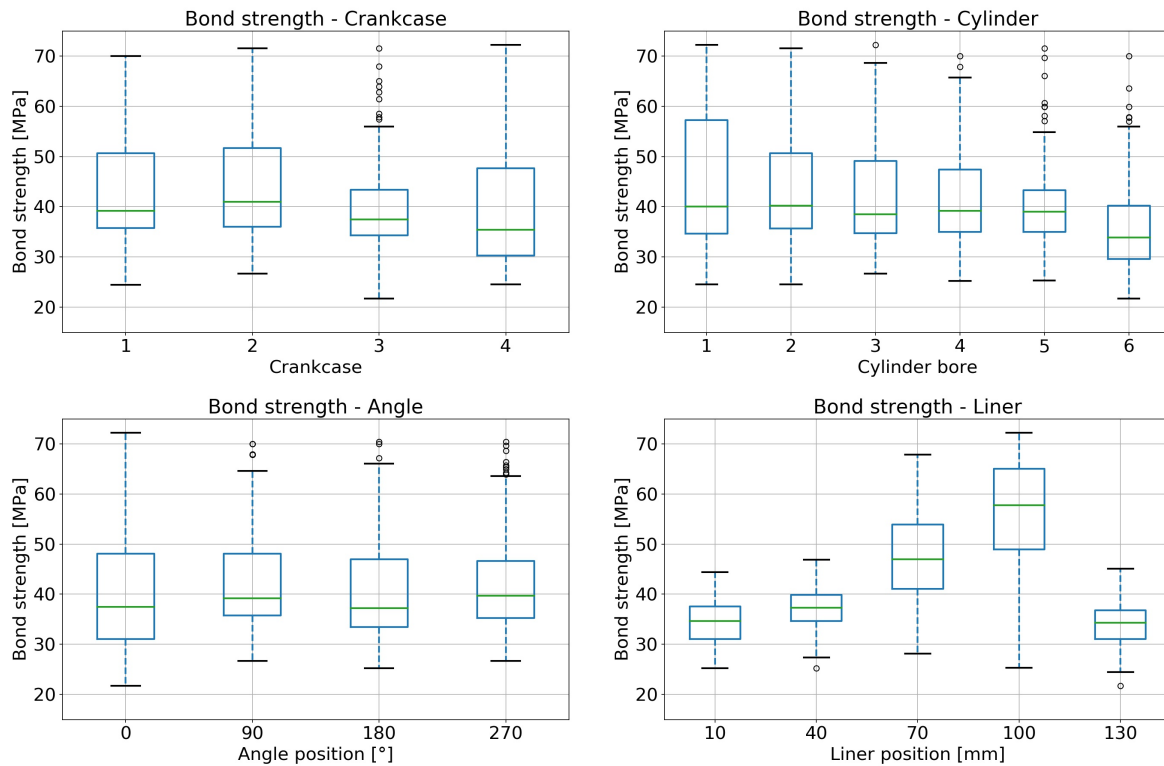
Figure 5.4.: Bond strength measurements using PAT™ for thermally sprayed cylinder coatings with respect to the individual crankcases, cylinder bores, angle positions and liner positions. All shown plots include 480 individual data points. Boxplots: The green lines represent the median of the underlying data; boxes indicate the upper/lower quartiles; the whiskers are set to a maximum of 1.5 times the interquartile range. Circles mark data outside the whiskers.

that the thermal transport properties are found to be almost constant within the region of $80 - 110\,\mathrm{mm}$, whereas the values change rapidly around the liner position of $70\,\mathrm{mm}$. Further, a drop of the thermal diffusivity of about $36\,\%$ towards the lowest position at $130\,\mathrm{mm}$ close to the crankcase shaft reveal thermal diffusivities of the cylinder coating comparable as found in the upper positions.

5.3. PAT™ study

Beyond characterizing the thermophysical properties of wire arc sprayed cylinder coatings, a study about the bonding behavior of such coatings is presented in the following. The study includes destructive bond strength testing according to the introduced pull-off adhesion testing (PAT™) in Chapter 3.3. PAT™ is used in the large-scale production to monitor the bonding behavior of the manufactured cylinder coatings by destructive off-site testing. Therefore, the same four crankcases as already evaluated in the previous section are tested on the exact same measurement positions and the measurement results are also divided into the four categories *crankcase*, *cylinder bore*, *angle position* and *liner position*. The obtained PAT™ values can be found in Figure 5.4, while the individual data points are listed in the appendix in Chapter C.2. Again, boxplots are chosen to present the distribution of the 480 individual data points over the different categories. Further, an analysis of variance (ANOVA) is performed to evaluate the sta-

Table 5.4.: ANOVA results of bond strength measurements. The significance level is set to 0.05. The SoS values represent the sum of squares for the different categories, DF are the degrees of freedom, F are the F-values of the Fischer distribution and P presents the probability that the null hypothesis is correct. Further, cont. ratio stands for the contribution ratio as being calculated from the resulting sum of squares.

Parameter	Category	SoS	DF	F	P	Cont. ratio [%]
PAT™	Crankcase	2196.7	3	18.3	$3.2\,e-11$	3.6
	Cylinder	3054.4	5	15.3	$7.0\,e-14$	5.0
	Angle	529.8	3	4.4	$4.5\,e-3$	0.9
	Liner	36890.1	4	230.2	$1.3\,e-108$	60.2
	Residuals	18550.9	463			30.3

Table 5.5.: Bond strength measurements using PAT™ of thermally sprayed cylinder coatings along the cylinder liner position. The interval between the lower and upper quartile describes 50 % of all acquired data points.

	10 mm	40 mm	70 mm	100 mm	130 mm
Median PAT™ [MPa]	34.7	37.3	46.9	57.8	34.3
Lower quart. PAT™ [MPa]	31.0	34.7	41.1	48.9	31.0
Upper quart. PAT™ [MPa]	37.7	39.9	53.9	65.0	36.8

tistical significance of the four introduced categories on the bond strength values. The applied significance level is again set to 0.05. The results of the ANOVA can be found in Table 5.4. Additionally, a comparison between ANOVA and Kruskal-Wallis testing is presented in Table 5.6.

The median of the PAT™ values for the individual crankcases range from $30-40$ MPa, while the individual values are spread over a range of $22-72$ MPa. Whereas crankcases 1 and 2 show almost the exact same results, a relevant drop of the median bond strength can be found for crankcases 3 and 4. Further, crankcase 3 shows lowered lower and upper whisker values as well as narrow quartile ranges compared to the remaining crankcases. However, the circles representing data beyond the whiskers indicate that the maximum bond strength found for crankcase 3 also lies above 70 MPa as found for the remaining three crankcases. The boxplots indicate that the PAT™ values are not randomly distributed over the crankcases. In fact, as the lower quartiles and whiskers are in general shorter than the upper ones, the variance of the data towards the minimum is less than 20 MPa, whereas the maximum values exceed the median values by over 30 MPa. The maximum bond strength is about $75-100$ % higher than its median for all four crankcases. Overall, the four crankcases show comparable results as minimum, maximum and median values do not deviate drastically between the individual crankcases compared to their observed variations. Still, minor differences between these crankcases can be found thus coating bond quality does vary within the large-scale production. Therefore, the ANOVA shows a statistically significant influence of the category *crankcase* on the bond strength values as the probability P is close to zero. Still, the contribution ratio is below 4 % thus the observed variations may not present the majority of the data variation

with respect to the introduced categories.

Further, the bond strength is found to be dependent on the respective **cylinder bore**. While the median values of the bond strength are constantly at about $40\,\text{MPa}$ for cylinder bores 1 to 5, cylinder bore 6 clearly shows a decreasing median value of less than $35\,\text{MPa}$. Further, lowest overall bond of $22\,\text{MPa}$ is found in cylinder bore 6. The upper quartiles and whiskers minimize continuously from cylinder bore 1 to 6, whereas the lower whiskers and boxes remain constant especially for bores 1 to 5. Still, all six cylinder bores obtain maximum bond strength of the cylinder coatings above $70\,\text{MPa}$. These variations are assumed to result from the thermal spraying process of the cylinder coatings. Besides preheating the crankcases in advance of the coating process to favor diffusion bonds between coating and substrate, the crankcases are further heated during the spraying process. Since the coating process starts at the bottom of cylinder 6, "coldest" interface conditions are observed for this cylinder bore. The coating process introduces additional heat to the substrate surface thus the interfaces of the following cylinder bores are additionally preheated. As increased interface temperatures support the development of diffusion bonds, increasing bond values are expected from cylinder bores 6 to 1 as shown in Figure 5.4. This assumption is supported by the ANOVA as it predicts statistical significance of the cylinder bore on the bond values. Here, a probability value of $7.00\,\text{e}-14$ is calculated. However, again the contribution value is found to be below 0.05 does reveal only minor data variation with respect to the cylinder bore. Other categories appear to show higher variances than the cylinder bore.

The bond strength of the cylinder coatings to the crankcase substrate does not reveal any enhanced variations with respect to the **angle position**. Median values all range at about $40\,\text{MPa}$, whereas maximum and minimum values are on comparable levels independent of the angle position. Angle position $0°$ presents the largest spread of bond strength measurements, however still no distinct differences to the other angle positions are deduced. Even highest probability value P of about $4.5\,\text{e}-3$ is found for the angle position. This value may reveal even a probability lower than chosen significance level that the angle position has no influence on the data. Since the contribution is less than $1\,\%$, however the angle position may not have a major influence on the bonding behavior of the cylinder coatings.

Finally, acquired bond strength measurements are categorized by their **liner positions**. Here, major variations of the bond strength values can be found with respect to their liner positions as already found for the thermophysical properties. Lowest median bond strength of $34.7\,\text{MPa}$ is shown in the upper parts of the cylinder liner at position $10\,\text{mm}$, which is followed by a strong increase of about $66\,\%$ towards position $100\,\text{mm}$ with highest median bond strength of $57.8\,\text{MPa}$. Further, bond strength decreases towards position $130\,\text{mm}$ where the values show a comparable range as close to the cylinder head sealing surface at liner position $10\,\text{mm}$. Lowest bond values are found at position $130\,\text{mm}$, however all five investigated liner positions reveal minimum bond strength on a comparable level less than $30\,\text{MPa}$. Still, highest bond values of up to $72\,\text{MPa}$ can only be found at position $100\,\text{mm}$. Further, bond values shown

Table 5.6.: Comparison of statistical significance testing for categorized PAT™ values. The significance level is set to 0.05.

Parameter	Category	P_{anova}	$P_{kruskal}$
PAT™	Crankcase	$3.2\,\mathrm{e} - 11$	$2.2\,\mathrm{e} - 5$
	Cylinder	$7.0\,\mathrm{e} - 14$	$1.7\,\mathrm{e} - 5$
	Angle	$4.5\,\mathrm{e} - 3$	$1.9\,\mathrm{e} - 2$
	Liner	$1.3\,\mathrm{e} - 108$	$1.3\,\mathrm{e} - 55$

for positions $10\,\mathrm{mm}$ and $40\,\mathrm{mm}$ spread over an interval of about $20\,\mathrm{MPa}$, whereas the median bond value only slightly increases by $3\,\mathrm{MPa}$ from position $10\,\mathrm{mm}$ to $40\,\mathrm{mm}$. Further, bond strength values obtained at the liner position $70\,\mathrm{mm}$ widely spread over an interval of about $40\,\mathrm{MPa}$, whereas the values are almost equally distributed above and below the median value of $46.9\,\mathrm{MPa}$. Highest median and maximum bond strength values are found for liner position $100\,\mathrm{mm}$, however the lower whisker indicates minimum bond strength on a comparable level as for the remaining liner positions. Still, the lower quartile does not overlap the maximum values found in the upper parts of the liner thus revealing a separated level of bond strength in the lower part of the cylinder bore compared to the upper liner parts. Further, the strong increase of the bond strength from liner position $10\,\mathrm{mm}$ towards $100\,\mathrm{mm}$ is followed by a decrease to position $130\,\mathrm{mm}$. Here, the median bond strength is reduced by about $40\,\%$, whereas the variation of the bond values shows about $20\,\mathrm{MPa}$. The lowest liner position near the crankcase shaft shows comparable bond values as found in the upper parts right below the cylinder head sealing surface. Additionally, PAT™ measurements reach their detection limit between $60 - 72\,\mathrm{MPa}$ due to failure of the adhesive bond which limits the maximum possible applicable load of the PAT™ measurements to the coating structure (see Chapter 3.3). The resulting median values as well as the lower and upper quartiles of the PAT™ measurements with respect to the liner positions are listed in Table 5.5. Additionally, the ANOVA highlights the statistical significance of this category. Here, lowest P value of $1.3\,\mathrm{e} - 108$ indicates that the liner position has truly statistical significant influence on the bond strength. Further, the contribution ratio shows that about $60\,\%$ of the data variation can be explained by the variance of the data along the liner position thus being the major influencing factor of the bond strength. However, further $30\,\%$ of the variances cannot be described by any of the introduced categories. Therefore, other influences besides the four categories are present determining the bonding behavior of the cylinder coatings.

Again, the ANOVA is counter tested using a Kruskal-Wallis test by ranks for non-normally distributed variances. Here, a comparison of the probability values, if the four introduced categories have no statistically significant influence on the PAT™ measurements is presented in Table 5.6. As already seen for the thermal diffusivity, all probability values raise using the Kruskal-Wallis test. However, non of the probability values $P_{kruskal}$ exceed the chosen significance level. Whereas the probability of the angle position shows the highest value, it still remains below 0.05. Thus, independent of the chosen statistical tests, all four cate-

gories show a statistically significant influence on the mechanical bond strength. Still, lowest probability value can be found for the liner position with respect to the two applied statistic test.

Summarizing the presented PAT™ measurements which evaluate the bond strength of thermally sprayed cylinder coatings, major variations of the bond strength along the liner positions are revealed. Besides minor differences between the individual crankcases as well as between the different cylinder bores, the bond strength increases by about 66 % from the cylinder head sealing surface towards lower positions in the crankcase. Highest bond strength is found at the liner position 100 mm, whereas lowest coating bond is observed in the upper parts of the liner as well as in the lowest part of the liner near the crankshaft. Also the applied statistical tests predict a highly statistical significant influence of the liner position on the bond strength. Here, the liner position is obviously the main factor influencing the coating bond.
Compared to the thermal diffusivity, the mechanical bond strength shows a similar behavior along the liner, especially since both bond strength and thermal diffusivity increase from the cylinder head sealing surface towards position 100 mm and further decrease towards 130 mm. However, to confirm correlations between these two characteristics further excessive studies of the coatings are necessary. Following investigations focus on the dependence of the coating microstructure on the respective liner positions. Therefore, quantitative analysis of the coating microstructure as well as fracture analysis after PAT™ is introduced in the following section. Metallographic measurements are used to gather additional information about the coating composition, whereas further X-ray computed tomography measurements are applied as an additional method to characterize the coating microstructure.

5.4. Metallography

In order to assess the composition of wire arc sprayed cylinder coatings, detailed metallographic analysis is introduced. The applied methods focus on the coating microstructure and the influence of present defects in the microstructure on the coating's thermal and mechanical characteristics. The defect morphology is processed and analyzed quantitatively by a segmentation algorithm which is introduced in Chapter 3.4.1. Also, fracture areas after PAT™ measurements are analyzed regarding their remaining coating material on the fracture area using scanning electron microscopy (SEM), which allows to determine the fraction of cohesive and adhesive failure during PAT™ testing (Chapter 3.4.2). As this work aims to correlate thermal and mechanical properties of the wire arc sprayed coatings, microstructure analysis is performed along the categories showing the main influences on these characteristics. As the analysis of the thermal diffusivity and the bond strength in the previous chapters revealed their main dependence along the liner position, any further investigations only focus on this category.

5.4.1. Cross section analysis

The coating microstructure is assessed using multiple cross section specimens and microscopy images along the cylinder liners. The cross section specimens are cut out of the liner and prepared for optical microscopy images as described in Chapter 3.4.1. Two respective cross
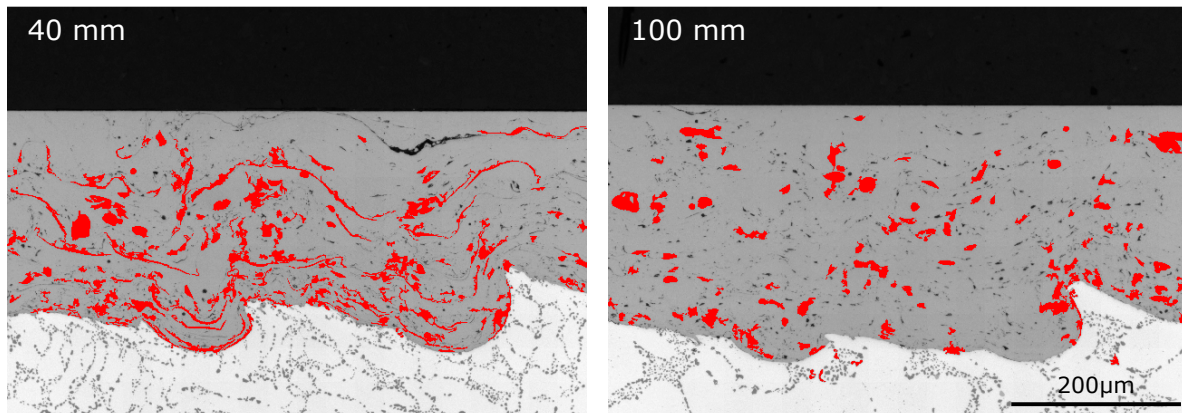
Figure 5.5.: Optical microscopy images of the coating cross section specimens including segmented coating defects highlighted in red (left: 40 mm, right: 100 mm). The coating material is shown in dark grey, whereas the aluminum-based substrate material is light grey.

section images obtained at the liner positions 40 mm and 100 mm are illustrated in Figure 5.5. Here, coating material is shown in dark grey and aluminum-based substrate material is shown in light grey, whereas the cross section images include coating defects highlighted in red. The defects are segmented using the IA algorithm described in Chapter 3.4.1. Comparing both liner positions, the respective microstructure already reveals major differences regarding the observed defect morphology qualitatively. As shown for the liner position 40 mm, the coating microstructure shows enhanced amount of laterally orientated defects. The coating defect morphology shows a typical layered structure of partially separated particles. Thin long voids parallel to the substrate interface contribute the majority of the observed defects, whereas vertical defects missing entirely within this cross section. Further, enhanced amount of bonding defects occur along the coating-substrate interface. The interface appears to be almost entirely covered by several bonding defects. Besides, laterally orientated splat interfaces are missing entirely for the cross section image taken at liner position 100 mm. In absence of horizontal defects, the coating microstructure exhibits rather spherical-like, globular pores without distinct elongation. Further, the substrate is not completely covered by bonding defects, however certain amount of defects can still be found on top of the interface.

The segmentation algorithm detects the defects reliably, whereas the majority of the defects are processed. Smaller defects below an area of 500 px are not processed to reduce the overall calculation time of the algorithm. However, coating defects close to the coating surface are not entirely highlighted as found for some defects within the cross section image taken at position 40 mm. In these cases, the embedding material and the segmented defects show the same grey scale level thus both being binarized after the threshold step. If coating defects close to the surface are connected to the embedding material after the binarization, these defects will be assigned to the embedding material and are not detected as individual coating defects. Since the image analysis algorithm deletes the embedding material before the evaluation of the defect factor, these coating defects do not get processed by the algorithm. Further, the grain structure of the aluminum-based substrate gets partially segmented and processed by the algorithm. As the grey scale of these grains match the threshold of the coating defects,

the algorithm cannot separate between coating defects and grains. However, both types of inaccuracy can be neglected compared to the amount of detected and processed coating defects.

While the two presented cross section images already reveal differences between the coating microstructure depending on the liner position, however quantitative analysis of a certain amount of cross section images is needed to validate significant variations of the defect morphology. Therefore, five cross section specimens are cut out of the known liner positions, whereas one sample shows vertical elongation of about 20 mm. The entire cross section specimen is covered by about $30 - 40$ individual microscopy images with a size of $650 \times 650\,\text{mm}^2$. Combining the cross specimens at the five measurement positions, overall about $70\,\%$ of the cylinder liner is covered by the $150 - 200$ individual microscopy images. These cross section images are analyzed quantitatively using the described segmentation algorithm thus calculating the introduced "defect factor" for every individual cross section image. The calculated defect factor of each image is arranged with respect to its original position along the liner, whereas liner sectors showing no cross section preparation are interpolated by a linear regression. The resulting trend of the defect factor along one cylinder liner is shown in Figure 5.6 top. Additionally, the porosity distribution of the coating material is calculated for each cross section image. The resulting porosity values are arranged as already described for the defect factor and can be found in Figure 5.6 bottom.

The calculated defect factor reveals a strong dependence of the shape and orientation of the coating defects with respect to liner position. Starting below the cylinder head sealing surface, the defect factor shows a moderate decline towards position 40 mm. In the following, a strong gradient of the defect factor can be observed between 40 mm and 70 mm, while the defect factor decreases by over $30\,\%$. This strong gradient overlaps with the region between the cross sections at position 40 mm and 70 mm, thus missing data is linearly interpolated. Further, the defect morphology remains on a comparably low level in the range between 80 mm and 110 mm, since the defect factor does not change significantly in this interval. However, a slight increase between these two liner segments can be observed towards the bottom of the cylinder liner. Again, a stronger increase is found in the lowest liner position between $120 - 140$ mm, since the defect factor again increases up to a comparable level as in position 60 mm. As the defect factor only sums the horizontal elongation of all detected defects, a decreasing defect factor may be the result of a decrease of the coating porosity or of a change of the defect morphology. Therefore, the coating porosity is also calculated along the cylinder liner. Whereas mean the coating porosity does slightly decrease from the cylinder head sealing surface towards the crankshaft, it does not show strong gradients at positions 70 mm and 130 mm. The mean coating porosity does not vary significantly along the entire liner, whereas the upper and the lower parts of the liner do not show clearly separated porosity levels. Therefore, the behavior of the defect factor along the cylinder liner including the rapid change of the defect factor as well as the lowered defect factor in the interval between $70 - 110$ mm may not result from a lowered amount of detect defects but from a change of the defect morphology. Consequently, comparing position 40 mm to position 100 mm, two separated levels of the defect morphology are revealed by the defect factor along the cylinder liner. Laterally orientated splat interfaces are present in
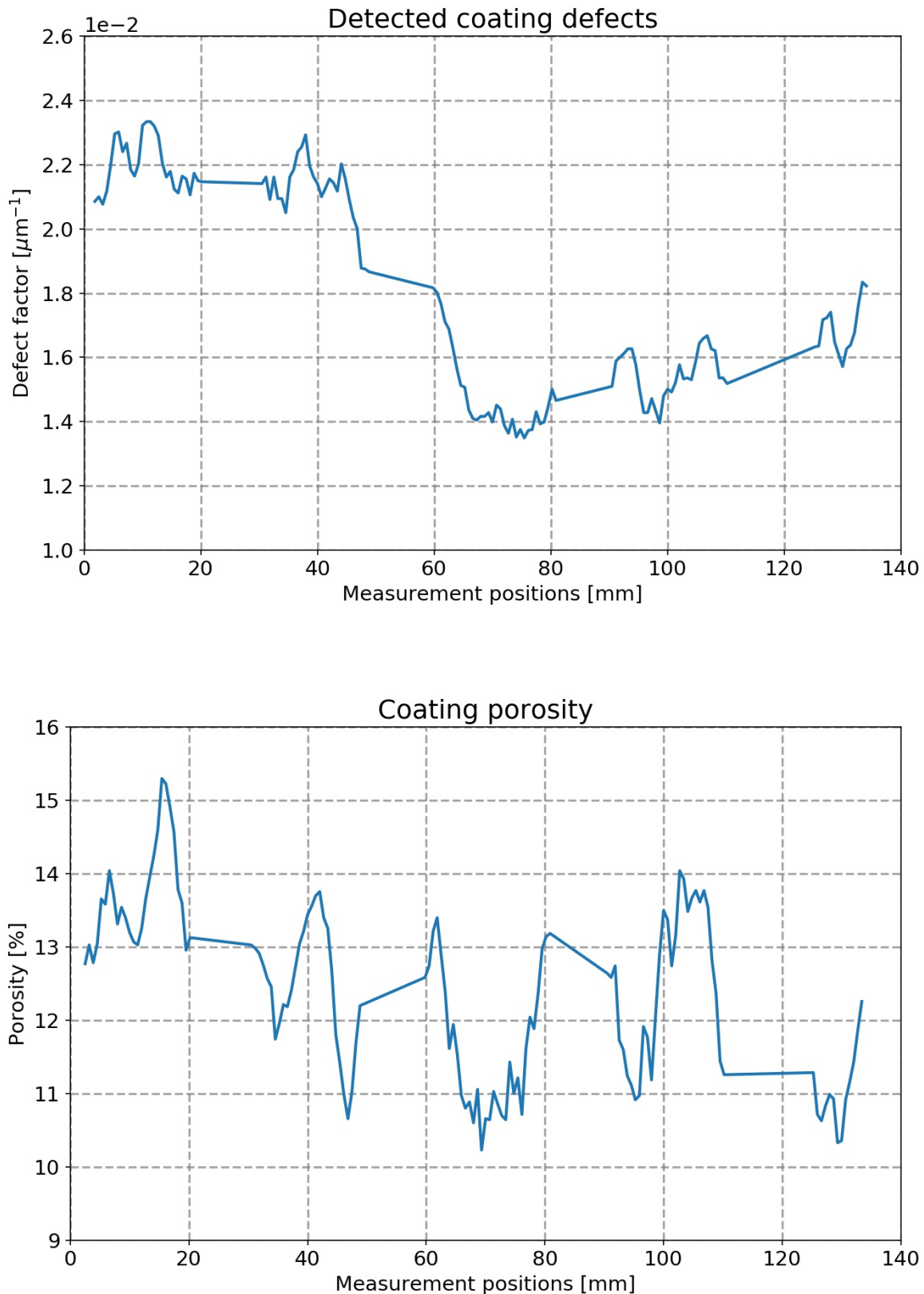
Figure 5.6.: Quantitative analysis of the coating microstructure using an automated segmentation algorithm. **Top:** The shown defect factor represents the horizontal elongation of all defects in the microstructure over the substrate. The defect factor is normalized to the cross section area. **Bottom:** Calculated coating porosity based on the segmented coating defects. Both quantities are calculated for each cross section image individually and assembled to observe the influence of the coating defects along an entire cylinder liner.

the regions showing a high defect factor, whereas the absence of such defects results in a low defect factor. This conclusion covers the previous results found for the cross section images in Figure 5.5, whereas enhanced amount of laterally orientated splat interfaces can be found in the upper parts of the cylinder liner as well as the lowest part near the crankshaft. Almost no laterally voids can be found in the section between 70 mm and 110 mm thus the quantitative analysis of the cross section images results in a significant decrease of the calculated defect factor at this liner region.

The defect morphology based on the introduced defect factor was analyzed following the methodology in [14, 15] as the horizontal elongation of the defects plays a significant role increasing the thermal resistance of a two-phase material thus influencing the thermal conductivity as well as lowering the cohesive bond strength of the material. The approach is chosen to extract significant differences of the coating microstructure at the respective liner segments. Further, also other approaches might be applicable such as approximating the observed defect with spheroidal shape [10, 12, 13, 67]. Therefore, the thermal resistance of the defects can be traced back to the circumference of the spheroids and their orientation with respect to the incoming heat flux. Investigations showed that analyzing the coating microstructure with respect to the circumference of the spheroids also leads to comparable results as the defect factor analysis but did not deliver any further information about the defect morphology. Even by approximating the defects by a spheroidal shape, the observed defect morphology shows way more complex shapes and windings. Thus, such a description might not be appropriate for the presented microstructure as it does not represent the actual shape of the defects. Therefore, the introduced defect factor presents a robust approach describing the coating defects and can easily and reliably be applied to the cross section images. This approach is obviously sufficient to describe the major differences of the coating microstructure along the cylinder liner.

5.4.2. Fracture analysis

Besides the evaluation of the coating microstructure, analyzing the fracture after PAT™ measurements allows to further investigate the mechanical behavior of the cylinder coatings. In this context, 40 fracture segments are cut out of the crankcases after PAT™. The fracture areas of each liner segment are analyzed quantitatively using SEM images thus allowing to determine the fraction of remaining coating material on the substrate. Two SEM images of the fracture area at positions 40 mm and 100 mm can be found in Figure 5.7. The two fracture images show the defined PAT™ area with 8 mm diameter, whereas remaining coating material is shown in light grey and aluminum-based substrate is shown in dark grey. Horizontal structures in the fracture area result from the mechanical roughening profile of the substrate. The illustrated fracture areas already reveal major qualitative differences regarding the remaining coating material on the substrate. Enhanced coating material remains bonded to the aluminum substrate after PAT™ at the upper liner position 40 mm. Since the area is largely covered by coating material, a significant amount of cohesive failure is assumed for the respective liner position. In contrast, the lower liner position does only reveal a small amount of coating material on the fracture area after PAT™. The NMRP structure can be clearly identified for this image as the majority of the coating material was removed from the

| SEM HV: 15.0 kV | WD: 20.04 mm | | | SEM HV: 15.0 kV | WD: 19.98 mm | | |
| View field: 12.2 mm | Det: BSE | 2 mm | MIRA3 TESCAN | View field: 12.2 mm | Det: BSE | 2 mm | MIRA3 TESCAN |
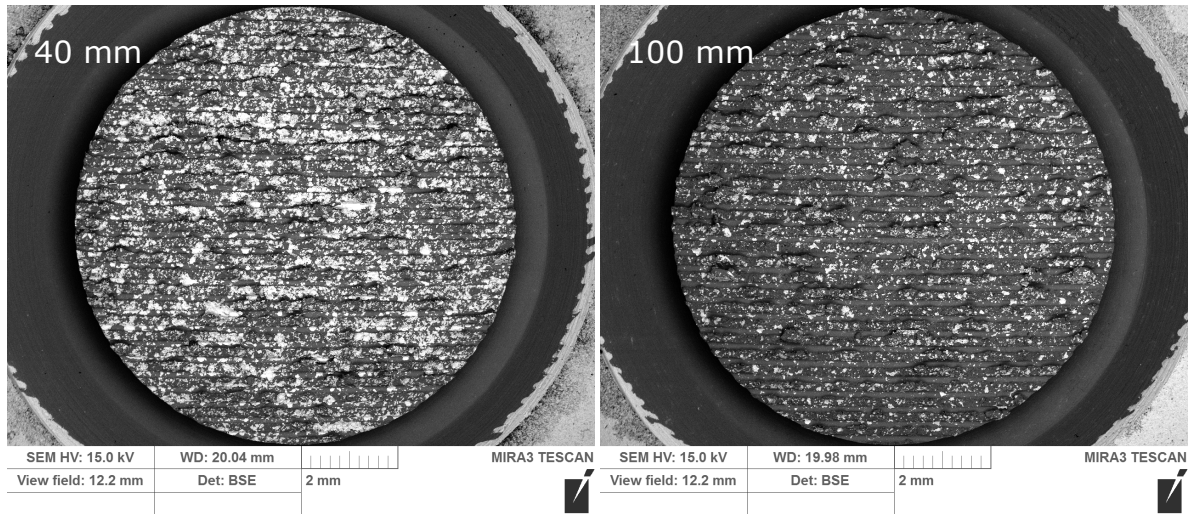
Figure 5.7.: SEM images (back scattering mode) of the fracture area after PAT™ at two different liner positions 40 mm and 100 mm. The remaining coating material is shown in light grey, whereas aluminum-based substrate is depicted in dark grey
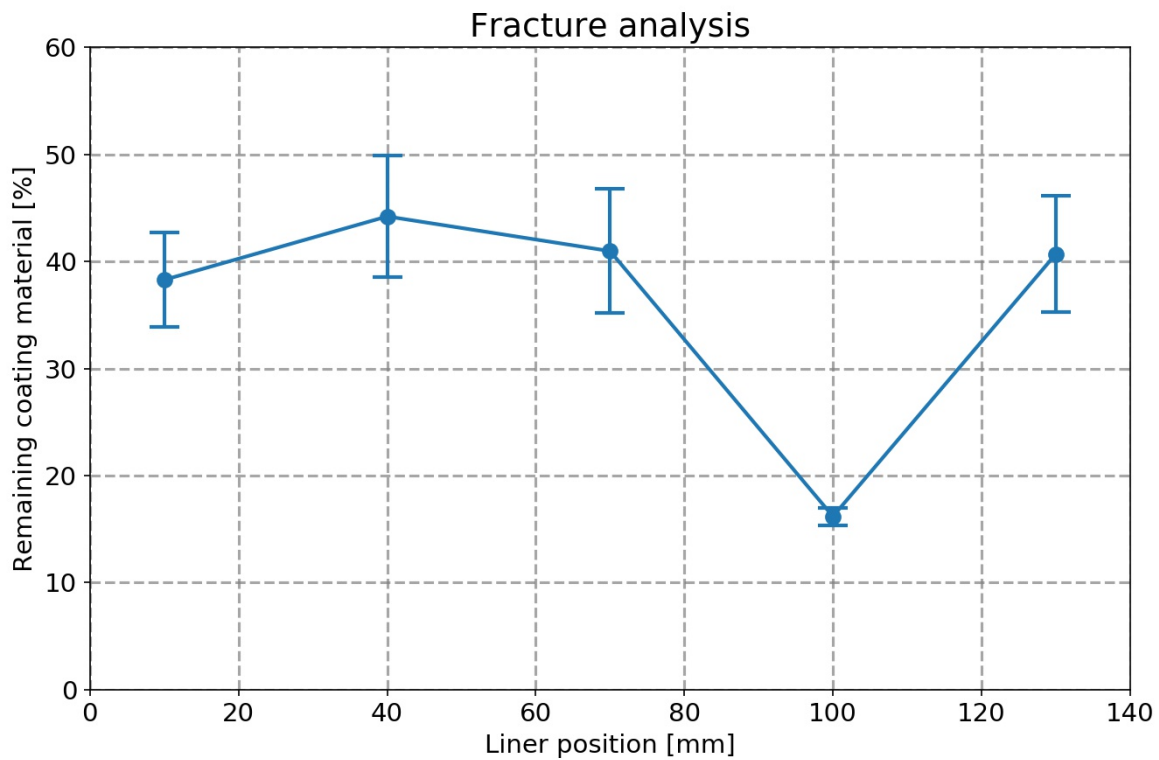
Figure 5.8.: Quantitative fracture analysis of the remaining coating material on the aluminum-based substrate after PAT™. Circles represent mean values, whereas the error bars indicate the standard deviation of the underlying data.

substrate during the PAT™ measurement. Consequently, enhanced cohesion is assumed for this measurement position since failure is predominately of adhesive type.

As the qualitative examination of the fracture areas after PAT™ revealed a liner-dependence of the remaining coating material, the selected liner segments are analyzed quantitatively by an image processing algorithm according to the introduced method in Chapter 3.4.2. Therefore, SEM images are processed while the remaining coating material on the fracture area is separated from the substrate material using a global threshold. Further, the fraction of coating to substrate material is determined for all 40 segments and assigned to the respective liner position. The resulting liner-dependence of the remaining coating material can be found in Figure 5.8. In this context, reduced amount of coating material is found on the fracture areas at position 100 mm. Compared to the rest of the liner positions showing over 35 % of remaining coating material, the fraction shrinks down to about 15 % at position 100 mm. All other liner positions indicate a comparable level between $35 - 40\,\%$ of remaining coating material after PAT™, whereas no clear variation along the liner can be concluded for these positions. The shown standard deviations of the data points overlap with their mean values thus no additional separated levels are identified. However, the narrow standard deviation found for position 100 mm reveals quite reproducible fracture analysis. Summarizing the fracture analysis, again strong variations of the investigated characteristic are found along the cylinder liner. The remaining coating material reduces drastically at position 100 mm thus enhanced adhesive failure of the cylinder coatings can be concluded. Consequently, PAT™ measurements show enhanced amount of cohesive failure for the remaining liner positions.

5.5. X-ray computed tomography

X-ray computed tomography (CT) measurements are taken to gain additional information about the microstructural composition of wire arc sprayed cylinder coatings. Therefore, five CT samples of size $5 \times 5 \times 5\,\text{mm}^3$ are cut out of the cylinder liners at the known measurement positions $10, 40, 70, 100$ and $130\,\text{mm}$ and measured by the commercially available *phoenix nanotom m* CT system (General Electric, Boston, USA). Further, the resulting 3D CT data sets of the cylinder coatings are analyzed quantitatively by a segmentation algorithm as described in Chapter 3.5 and in [27]. Two CT data sets of thermally sprayed cylinder coatings taken at positions 10 and 100 mm are compared in Figure 5.9. The 3D data sets are divided into a longitudinal cross section (a) and three CT images parallel to the cylinder liner surface ((b)-(d)) at three coating depths ($20\,\mu\text{m}$, $70\,\mu\text{m}$ and $120\,\mu\text{m}$). Both data sets show high contrast-to-noise ratio such that coating porosity can be clearly identified against the coating material. However, slight CT artifacts can be observed as horizontal lines across the CT images. Since the grey scale of these artifacts is still close to the coating material, these artifacts do not interfere with the segmentation algorithm. Additionally, the wave-shaped NMRP is found in the cross section images (a). Further, images (d) reveal beginning roughening structure as the peaks of the NMRP can be found at a depth of about $120\,\mu\text{m}$. Comparing the images (b) and (c), less porosity is pronounced close to the liner surface, whereas increased amount of globular pores is found at $70\,\mu\text{m}$ coating depth. Due to the high contrast-to-noise ratio of the iron-based coating, however CT images do not differentiate between aluminum-based substrate and air
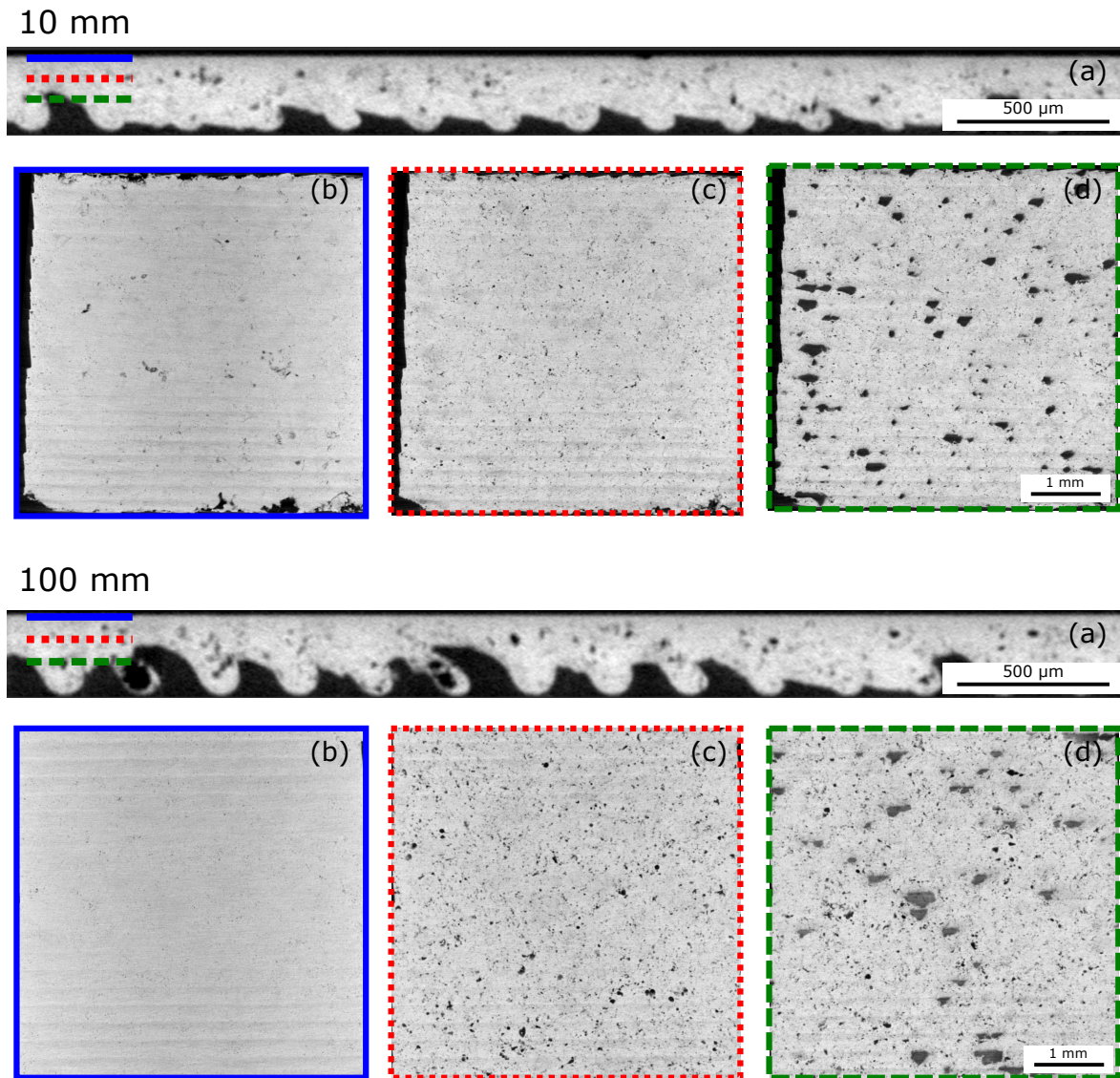
10 mm

100 mm

Figure 5.9.: Two CT data sets of cylinder coatings at liner positions 10 mm (upper) and 100 mm (lower). (a) Cross section images of the cylinder coatings including the roughened substrate. (b)-(d) CT images parallel to the liner surface at coating depths of 20 μm, 70 μm and 120 μm respectively. In (d), beginning roughening structure of the aluminum-based substrate can be observed.

filling the coating defects, thus both materials appear black. Therefore, proper segmentation of the coating defects may not be possible as soon as the CT images reach the peaks of the roughening profile since the segmentation algorithm detects the arising NMRP as coating defects.

Comparing the CT images taken at positions 10 mm and 100 mm, porosity differences can be observed between the two data sets especially at a coating depth of 70 μm. Coating porosity is found to be enhanced at the liner position 100 mm, whereas the coating microstructure reveals less globular pores in the upper parts of the cylinder liners. Both CT images show significantly reduced porosity in the upper coating depth at about 20 μm (images (b)). Subsequently, cross section images of both data sets do not show significant differences of the coating microstructure along the roughening profile.
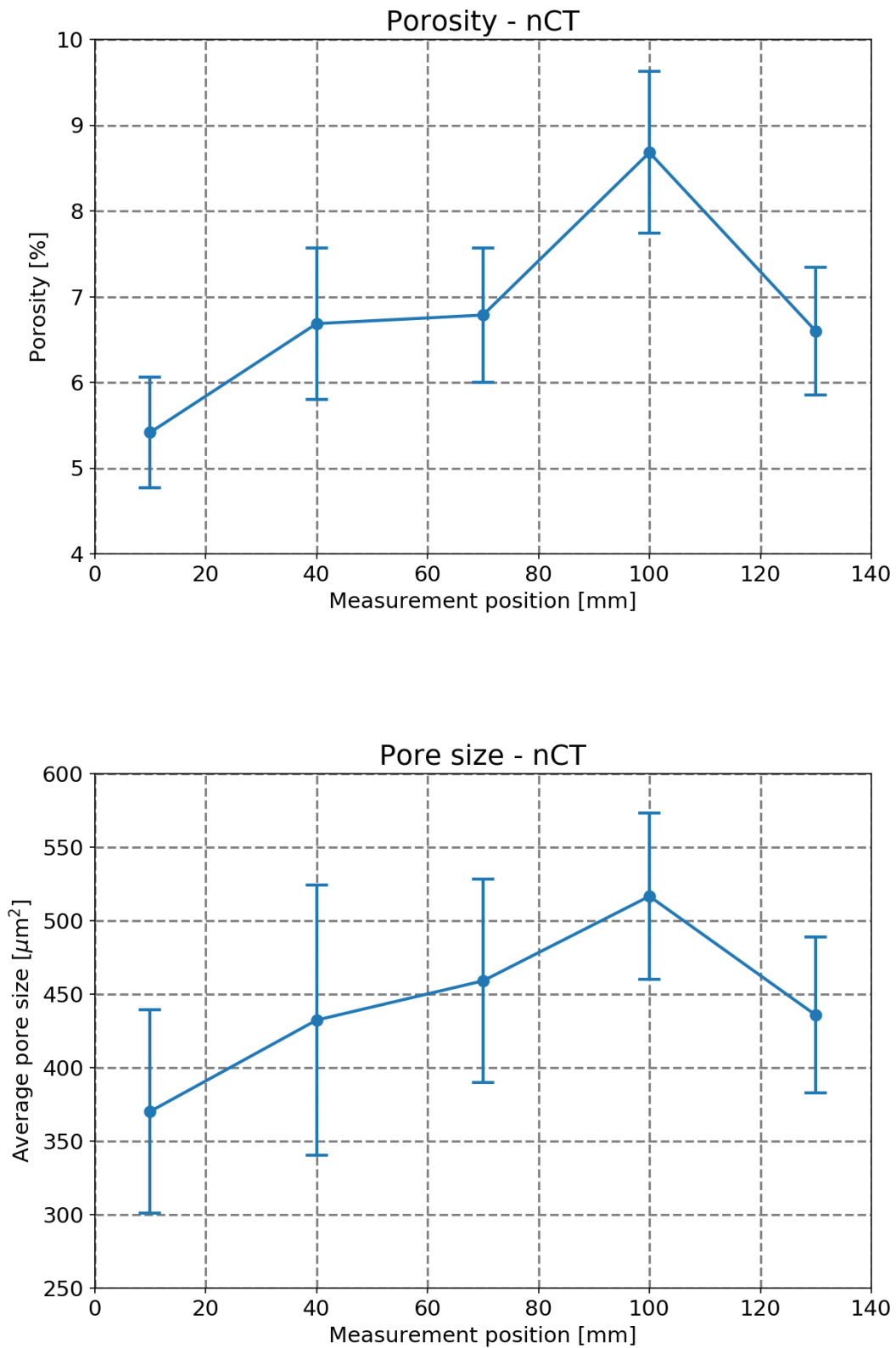
Figure 5.10.: Quantitative analysis of the computed tomography results. The respective CT samples are taken at the shown measurement positions along the cylinder liner. The shown data represents mean values of the available 2D CT images and the error bars indicate the mean absolute deviations to the shown mean values.

Quantitative analysis of the CT data sets with respect to the pore distribution of the thermally sprayed cylinder coatings can be found in Figure 5.10. Since the 3D data set is divided into a stack of 2D images parallel to the surface of the coating towards the aluminum-based substrate, each image is analyzed individually by the segmentation algorithm regarding the pore distribution within the coating material. Both porosity and average pore size are averaged over all available CT images within one CT data set and plotted over the measurement position along the cylinder liner. The variations of the investigated quantities are represented by the mean absolute deviation. Again, the liner positions reveal major influence on the microstructural composition of the cylinder coatings. Comparing the porosity levels along the cylinder liner, highest porosity of about 9 % within the cylinder coating is found at liner position 100 mm, whereas positions 40, 70 and 130 mm reveal comparable value levels. The lowest porosity of the coating material measured by CT appears for the liner position 10 mm with about 5.5 %. Further, the error bars indicate that the porosity levels in liner position 10 mm and 100 mm can be separated as their error bars do not overlap. The remaining three data sets are set in between these two values and do partially overlap with the error bars of the minimum and maximum porosity. The mean pore sizes correlate with the observed percentages of porosity such that positions with increased porosity also show increased average pore size and vice versa. CT measurements show mean pore sizes ranging from over $500\,\mu m^2$ at position 100 mm, while lowest pore sizes of around $350\,\mu m^2$ can be found at 10 mm. However, the presented error bars reveal a strong variation of the mean pore size within all three data sets, thus the mean absolute deviations overlap with mean values of neighboring data points. Consequently, a clear separation of the mean pore size along the cylinder liner position can not be identified.

Comparing the 3D CT data in Figure 5.10 with the obtained cross section analysis in Figure 5.6, CT data is not able to resolve laterally orientated splat interfaces. Thin, lateral voids with a typical gap opening of a few micrometer are not detectable with the CT measurements as they miss entirely in the CT images thus the local resolution of $4\,\mu m$ is too low to access all coating defects. The associated structural resolution does not allow for a reliable identification of all laterally expanded splat interfaces, which typical gap opens only a few micrometers. In this case, major coating defect structures found in the metallographic cross sections are missing entirely within the CT data, while especially these defect types seem to be predominate defining the thermal properties of the coatings. Comparing the porosity analysis of the cross section images to the CT data, CT data is found to show a varying porosity along the liner whereas the detected porosity from the cross section analysis remains almost constant. As the CT measurements are missing out the thin lateral voids, these defects do not constitute to the overall porosity evaluated with CT. Thus, the coating porosity level analyzed by the cross section images ranges above 10 % over the entire cylinder liner, whereas CT data consequently reveals porosity levels below 10 % even down to about 5 %. Since lateral defect are mainly found in the upper and the lowest part of the cylinder liner, the varying coating porosity can be traced back to the varying defect morphology along the liner. The analysis of the defect factor showed that the coating defects show great horizontal elongation in the upper liner parts

whereas the detected defects are found to be rather of spherical-like shape in the lower parts. As CT is able to detect spherical-like pores reliably, the varying coating porosity found with CT can be traced back to enhanced amount of rather globular-shaped defects in the lower liner sections around 100 mm. Consequently, higher CT resolutions would be required to observe the thin lateral voids. As higher CT resolution can only be achieved by reducing sample sizes, cubic samples of about $1 \times 1 \times 1 \, mm^3$ are necessary. However, covering the entire cylinder liner with such small CT samples is beyond reasonable effort.

5.6. Correlation of thermal and mechanical properties

This chapter presents an excessive study including statistical analysis of thermal as well as mechanical properties of wire arc sprayed cylinder coatings for modern combustion engines. The investigated coating characteristics are found to vary strongly within the different crankcase positions and strongest and statistical significant influence is revealed along the *liner positions*. Laser-excited lock-in thermography measurements as well as mechanical bond strength testing by PAT™ present major variations of the coatings' thermal and mechanical properties along the cylinder liner positions. Whereas other categories such as *crankcase*, *cylinder bore* or *angle position* also show statistical significant variance, however the *liner position* is found to present the main influence factor for both mechanical and thermal properties. Highest variances and contribution ratios are found along the liner position by the ANOVA test. In this context, further investigations and discussion focus only on the influence of the liner position on the investigated coating properties.

As widely discussed in the literature review shown in Chapter 2, thermal and mechanical properties of thermally sprayed coatings found on the resulting microstructure of the coatings. Consequently, the defect morphology of the investigated coatings may explain the varying thermal and mechanical properties. Latest research of the spraying process and the influence of the coating atmosphere on the formation of thermally sprayed cylinder coatings is published in [9]. This research focuses on the influence of oxygen content during the coating of thermally sprayed cylinder bore coatings and how process parameters influence the oxidation of the sprayed particles. As Schilder et al. [9] presented in their work, the occurrence of defects and impurities in the microstructure of thermally sprayed cylinder coatings depends on the amount of oxygen during wire arc spraying. Computational fluid dynamic (CFD) simulations of the complex gas flow during the coating process as well as coating experiments have shown that the mass fraction of oxygen in the atmosphere surrounding the spray jet strongly varies along the cylinder liner depending on the torch position during the coating process. CFD simulations further revealed that a high oxygen mass fraction occurs in the upper parts of the cylinder bore during the coating process. Figure 5.11 illustrates the simulated oxygen mass fraction during the coating process for two different crankcase positions. Due to the flow conditions in the upper position, ambient atmosphere flows into the cylinder bore and interacts directly with the process gas [9]. The resulting mixed gas stream of nitrogen and ambient air encloses the sprayed particles, where the high oxygen content leads to enhanced oxidation of the droplets. In-flight oxidation of the spraying droplets forms an oxide shell around the particles which is entrapped

between already solidified material and the impinging particles thus causing laterally expanded voids [5–7, 9]. The resulting microstructure at these positions show significant high amount of lateral splat interfaces. Further, lower burner positions lead to a reduction of the oxygen mass fraction within the gas atmosphere due to the crankcase geometry and the resulting gas flow [9]. The lowered oxygen mass fraction within the spray jet leads to a significantly lower amount of laterally orientated splat interfaces compared to the defect morphology in the upper liner positions [9]. During the coating formation of the cylinder liner at the lower positions, almost no oxygen can be found in the atmosphere causing a dense microstructure without significant amount of laterally orientated splat interfaces. However, lowest liner positions close to the crankshaft again present increasing amount of laterally orientated splat interfaces and a resulting lowered bond strength [9]. As the cylinder bore is also opened towards the crankshaft, again ambient air may flow into the bore during the coating process of the lowest liner positions causing the coating microstructure to include several lateral voids. Analyzing the material's constitution of the coating defects, energy dispersive X-ray spectroscopy (EDX) allows to quantify the amount of oxygen within the observed splat interfaces. EDX analysis presented in [9] proves the presence of oxygen at the edges of the lamellar defect structures as well as along splat boundaries. Homogeneous regions showing no defect structures do not present any oxygen content within the EDX spectra. Thus, oxygen is only present within the observed coating defects thus oxidation of the spraying droplets cause the observed lamellar coating formation of the wire arc sprayed cylinder coating [9].

To emphasize the influence of the oxidation process during wire arc spraying of cylinder liners in crankcases, substantial bond strength testing has further been published in [9]. The experimental study supports the shown strong variations of the bond strength along the cylinder liners of the combustion engines. The obtained microstructures of the cylinder coatings are strongly related to the bonding behavior. The unique gas flow of the atmosphere during wire arc spraying of cylinder liners leads to the described varying oxygen content depending on the torch position along the liner. Thus, the degree of oxidation of the spraying droplet also varies along the liner, leading to a varying coating microstructure and hence to a varying bonding behavior [9]. If oxygen is excluded almost entirely during the coating process, rather dense thermally sprayed coatings with very few splat interfaces may appear thus drastically increasing the bond strength.

Consequently, the shown variations of thermal and mechanical bonding behavior presented in Chapters 5.2 and 5.3 can be explained by the investigated coating microstructure. In fact, since various publications have proven the influence of lamellar coating defects on the thermal as well as mechanical properties [8–10, 14, 82, 102], the observed variations of thermal diffusivity as well as coating bond strength can be traced back to the observed varying defect morphology in Figure 5.6. Therefore, quantitative analysis of the cross section images focus on the horizontal elongation of the observed defects by calculating the introduced defect factor allowing to connect the influence of coating defects with its thermal and mechanical properties. In this context, the introduced defect factor is calculated along the cylinder liner to reveal strongly varying coating defect morphologies. Laterally orientated splat interfaces dominate the defect morphology in the upper parts of the cylinder liner resulting in an en-
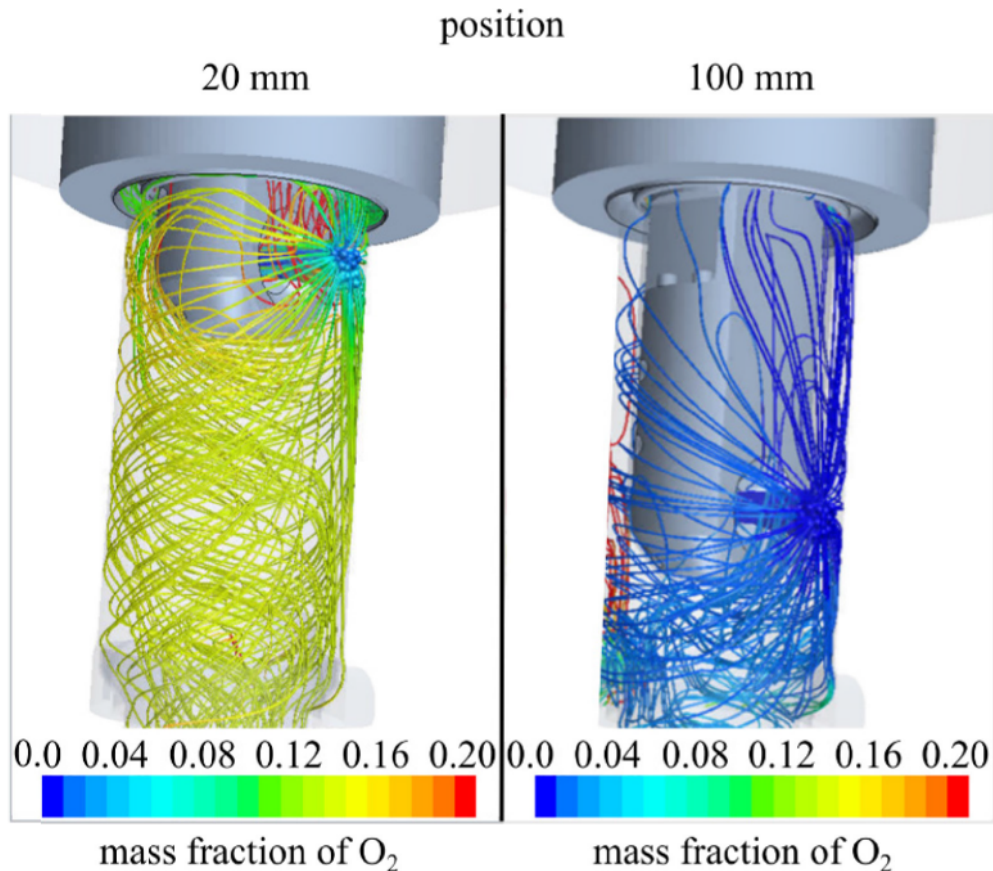
Figure 5.11.: CFD simulations of the oxygen mass fraction during wire arc spraying of cylinder coatings. The oxygen mass fraction is shown for two different burner positions 20 mm and 100 mm below the cylinder head sealing surface. This figure was first published in [9].

hanced defect factor. As the defect factor shows a strong gradient between the liner positions 40 mm and 70 mm, the shape of the coating defects is changing significantly from laterally orientated voids to rather spherical-like globular pores. The obtained coating microstructure can be seen as almost unchanged over the interval of $70 - 110$ mm. A stronger increase of the defect factor towards the crankcase shaft below 130 mm shows that the microstructure again changes rapidly over a short interval towards a comparable level as found in the upper parts of the liner, where defects are mostly found to be of thin, laterally orientated shape.

Laterally orientated splat interfaces appear to be dominant influencing the vertical heat conduction, as such defects build up multiple thermal barriers lowering the thermal diffusivity from surface to substrate [10, 12–15]. TWI measurements can be seen as integral measurements of the total influence of the microstructure defects on the thermal behavior of the coatings. Hence, the observed presence of laterally orientated splat interfaces in the upper parts of the cylinder liners lowers the vertical heat flux measured by laser-excited lock-in thermography as presented in Chapter 5.2 [10, 11]. In the absence of these horizontal voids between the liner position position $70 - 110$ mm (Figure 5.6 top), an increase of the thermal diffusivity of over $100\,\%$ is observed. The evaluated defect factors reveal two clearly separated levels of coating microstructure comparing the upper and lower parts of the liner, causing two separated levels

of the thermal diffusivity at the respective positions 10 mm and 40 mm compared to 100 mm. Consequently, TWI measurements of the thermal diffusivity seem to be obviously sensitive to the underlying coating microstructure and its defect morphology [40, 61, 63]. The observed rapid change of the defect factor close to liner position 70 mm and 130 mm result in a greater change of the thermal diffusivity over a short liner interval of about 20 mm. As the measured thermal diffusivity values are averaged over an area of 6.7 mm diameter, it is assumed that the obtained thermal diffusivity values also average the underlying rapidly changing microstructure. Therefore, enhanced variations of TWI measurements at positions 70 mm and 130 mm are the consequence of the changing microstructure within the short liner section.

As the thermal diffusivities of the coatings are strongly affected by the underlying microstructure, thermal diffusivity values are correlated with additional analysis of cross section specimens which is shown in Figure 5.12 top. In this figure, thermal diffusivity values are plotted over defect factors from several individual cross section specimens. The thermal diffusivity values are acquired in advance of the sample preparation at the conventional liner positions. The plotted data points indicate an inversely proportional behavior of the thermal diffusivities to the calculated defect factors. In this case, a lowered amount of horizontal defects clearly results in higher thermal diffusivity values of the coatings and vice versa. A distinct relation between the quantitative analysis of the coating microstructure to the measured thermal diffusivity is observed. The presence of lateral splat interfaces reduces the through-plane heat flux thus resulting in an overall lowered thermal diffusivity value. Consequently, no data pairs are found aside from the observed trend showing high thermal diffusivty combined with high defect factors. Therefore, high thermal diffusivity values can only be observed, if the coating microstructure is almost free of horizontal defects. To emphasize the correlation of thermal diffusivity and microstructure, a Pearson correlation factor is calculated for the presented data points [129, 130]. The shown data points relate with a correlation factor of -0.824. Thus, TWI measurements seem to be obviously sensitive regarding this microstructural characteristic. As the curve appears to slightly flatten for higher defect factors and respective lowered thermal diffusivity values, however the shown correlation may reveal a rather quadratic trend than a linear correlation. Such flattening is anyway assumed due to a "shadowing effect" of the lateral defects. With increasing defect factor multiple lateral defects overlap each other such that the influence of the thermal barriers on the thermal diffusivity is reduced. Defect structures in the lower parts of the coating are found in the "shadow" of upper defects such that the heat flux may not propagate around each individual defect as they are found closely to the thermal resistance of the upper defects.

Besides influencing the thermal diffusivity of the cylinder coatings, the observed microstructure further defines the mechanical bonding behavior of the thermally sprayed coatings. Whereas bonding failure occurs at the weakest part of the system, any type of microstructure defects may lower the integrity of the coatings [5–7, 16]. Therefore, the overall bonding behavior of the investigated coatings need to be separated into the two different mechanisms of adhesive and cohesive bond. Horizontal coating defects reduce the cohesive coating bond by reducing the bonded coating zones, thus lowering its vertical bond [15, 28]. The occurrence of laterally orientated splat interfaces is traced back to the presence of oxygen during the coating formation
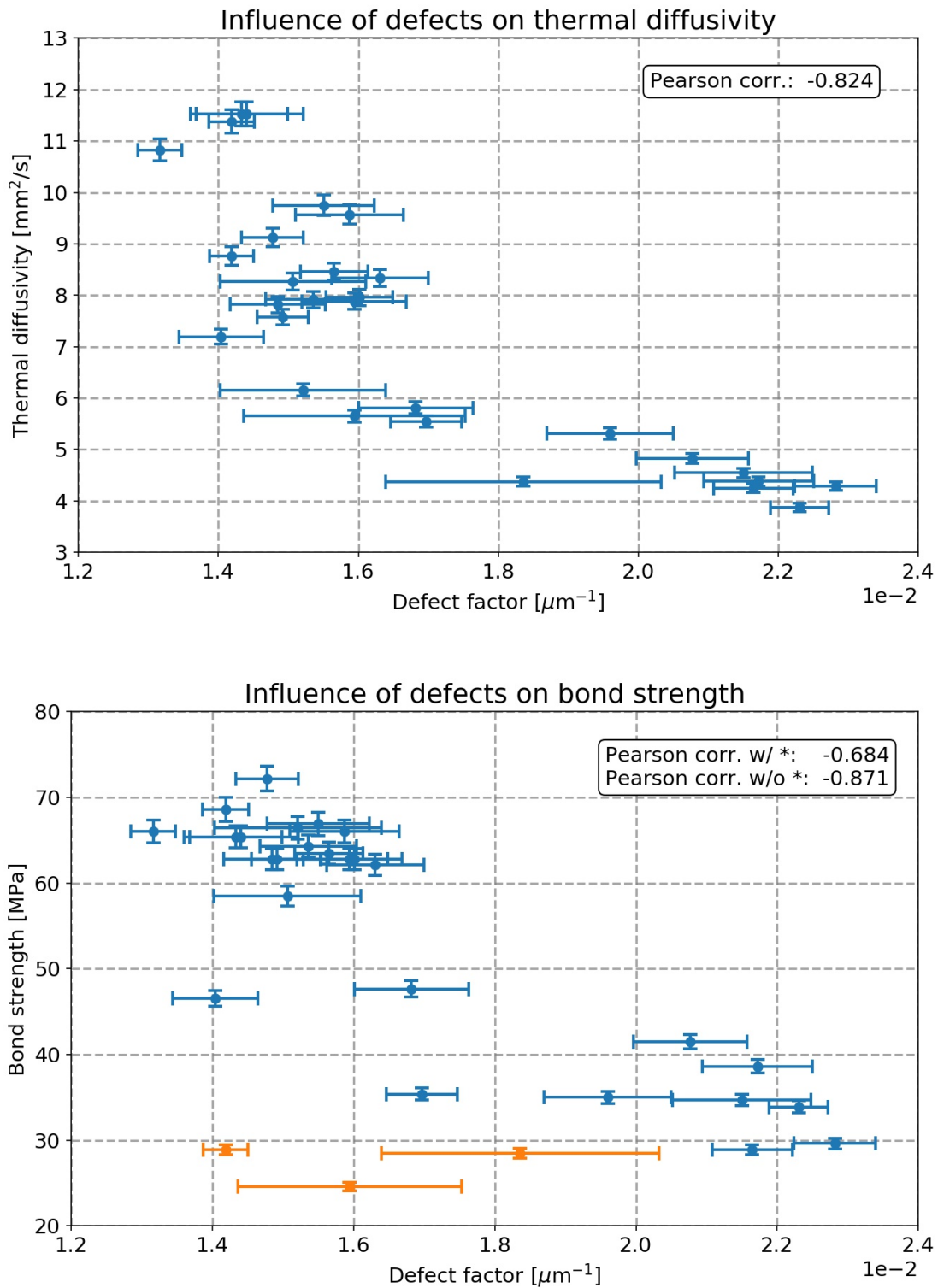
Figure 5.12.: Analysis of multiple cross section specimens regarding their defect morphology. The data points represent the median of the defect factors summarizing the calculated values of all individual microscopy images per cross section. Error bars of the defect factors represent the mean absolute deviations of the cross section images to the median values, whereas error bars of thermal diffusivity and bond strength are calculated to the stated deviation of 2%. Both, thermal diffusivity and bond strength measurements are performed at the conventional liner positions in advance of the cross section preparation. Due to the destructive character of the bond strength measurements, cross section specimens are cut out of the liner closest possible to the fracture area.

and the resulting in-flight oxidation of the droplets. In general, oxides are known to influence the bond between individual splats, while increased oxide content in a sprayed layer reduces the interlamellar bond of the coating thus reducing the cohesive bond strength [1, 30]. Since PAT™ is applied orthogonally to the substrate orientation, the horizontal defect elongation can be seen as a quantity which is responsible for the representative interlamellar cohesive bond. Consequently, a distinct relation between the coating microstructure and the tested bond strength is found with the applied methods.

In this context, bond strength values are correlated to the calculated defect factor of multiple cross section specimens as shown in Figure 5.12 bottom. Due to the destructive character of PAT™, the cross section specimens are cut out of the liner as close as possible to the fracture area. Horizontal defects cause an overall lowered bond strength of the coating system, while the shown reduction of the defect factor in Figure 5.6 bottom leads to an increase of the bond strength by over 72% at liner position $100\,\text{mm}$. In general, the bonding behavior is assumed to be inversely proportional to the defect factor comparing PAT™ measurements with the cross section analysis as illustrated in Figure 5.12. High bond values are the consequence of low defect factors. Condensed data points showing high bond strength and low defect factors support the idea that the absence of laterally expanded splat interfaces increases the cohesive bond strength thus causing high overall bonding properties of the coating system. The observed correlation of the defect factor and the bond strength in Figure 5.12 does not reveal any data points combining high bond strength and enhanced defect factors. Hence, the presence of defects and impurities directly causes a distinct reduction of the bond strength of thermally sprayed cylinder coatings. Highest bond strength values can only be observed if a dense coating is formed showing no lateral defects lowering the cohesive compound. However, as the defect factor does only represent the microstructural characteristics of the coatings, data points are found showing low defect factor and low bond strength (highlighted in orange). Aside from the reciprocal trend, weakened adhesion can cause bond failure even for a coating showing almost no defects in its microstructure. Contamination of the substrate interface or defective roughening structures are known to influence the adhesive bond of a coating to a substrate [5]. Oily contamination prevent diffusion bonds between coating and substrate, which leaves the adhesion mechanism to be only mechanical. While the production process of the crankcases is set to protect the interface from contamination in advance of the spraying process, still the substrate cannot be kept clean and protected entirely. Defective roughening structures caused by broken roughening tools can also lower the mechanical clamping of the solidified coating to the substrate interface. While roughening tools are monitored after machining of each individual crankcase, abrasive wear or break of the used tools may cause variations in the roughening profile thus leading to a lowered adhesive bond. Both influences cannot be observed and explained by correlating the introduced defect factor of the cross section images to the PAT™ measurements. The statistical analysis of all shown data points in Figure 5.12 reveals a correlation factor of -0.684. Even higher statistical significance is observed in the absence of the apparent adhesive failure, while a Pearson correlation of -0.871 between the defect factor and the bond strength can be calculated. Thus, also the bonding behavior depends significantly on the coating microstructure and cohesive behavior is mainly related to

the observed defect morphology. Further analysis of the influence of adhesive failure on the bonding behavior is shown in Chapter 6.1.

Additionally, quantitative SEM image analysis of the fracture surface after PAT™ presented in Figure 5.8 underline the influence of laterally expanded defects on the bond strength of the coatings. The quantitative fracture analysis can be seen as an indicator of the proportion of cohesive to adhesive failure during PAT™. Since enhanced amount of laterally expanded defects in the microstructure leads to increased cohesive break, SEM images exhibit an enhanced amount of remaining coating material on the aluminum substrate of up to 40% at positions $10\,\mathrm{mm}$, $40\,\mathrm{mm}$, $70\,\mathrm{mm}$ and $130\,\mathrm{mm}$. Consequently, microstructure analysis at measurement position $100\,\mathrm{mm}$ shows almost no laterally expanded splat interface in the cross section analysis as well as lowered amount of remaining coating material on the substrate. If cylinder coatings are manufactured showing no lateral defects as in position $100\,\mathrm{mm}$, PAT™ removes almost the entire coating from the substrate and coating failure mainly appears at the substrate interface due to adhesive break. In contrast, reduced bond values result in enhanced remaining coating material after testing. Here, lateral defects weaken the inner coating bond thus increasing the fraction of cohesive break within the coating. Therefore, the calculated defect factor appears to represent the main influence of coating failure during bond testing and can be used to characterize the bond properties of thermally sprayed cylinder bore coatings.

The presented thermal, mechanical and microstructural analysis emphasize a strong correlation between the thermal diffusivity and the bonding behavior of thermally sprayed cylinder coatings based on their underlying microstructure and coating formation. In this context, all acquired thermal and bond data are correlated and presented in Figure 5.13. The underlying grey area indicates the envelope of all shown data pairs. Additionally, TWI-PAT™ data pairs are divided by their respective liner positions in Figure 5.14 to obtain a reduced overview over particular correlations. Here, data pairs acquired at positions $10\,\mathrm{mm}$ and $40\,\mathrm{mm}$ are combined as they show comparable values and condensed data pairs. Both liner positions only indicate low thermal and mechanical properties as a consequence of the enhanced amount of laterally orientated splat interfaces in the respective microstructure. As already discussed previously, liner position $70\,\mathrm{mm}$ is found to represent a transition range of thermal and mechanical properties. The shown data spread over a great interval containing data pairs comparable to the upper liner positions found at $10\,\mathrm{mm}$ and $40\,\mathrm{mm}$ but also exhibit high thermal diffusivity and high mechanical bond strength as found for liner position $100\,\mathrm{mm}$. The majority of the data points at these liner segments is established between about $5 - 8\,\mathrm{mm^2/s}$ and $30 - 60\,\mathrm{MPa}$. Further, highest thermal diffusivity and bond strength is shown for liner position $100\,\mathrm{mm}$ as the majority of the data condenses between $8 - 10\,\mathrm{mm^2/s}$ and $50 - 70\,\mathrm{MPa}$. However, several data points can be seen showing low bond strength while obtaining high thermal diffusivity. Finally, liner position $130\,\mathrm{mm}$ presents again low thermal and mechanical characteristics of the cylinder coatings comparable to positions $10\,\mathrm{mm}$ and $40\,\mathrm{mm}$. However, the data points are slightly shifted towards higher thermal diffusivities whereas bond strength is comparably low. Several data points showing comparable high thermal diffusivity combined with lowest
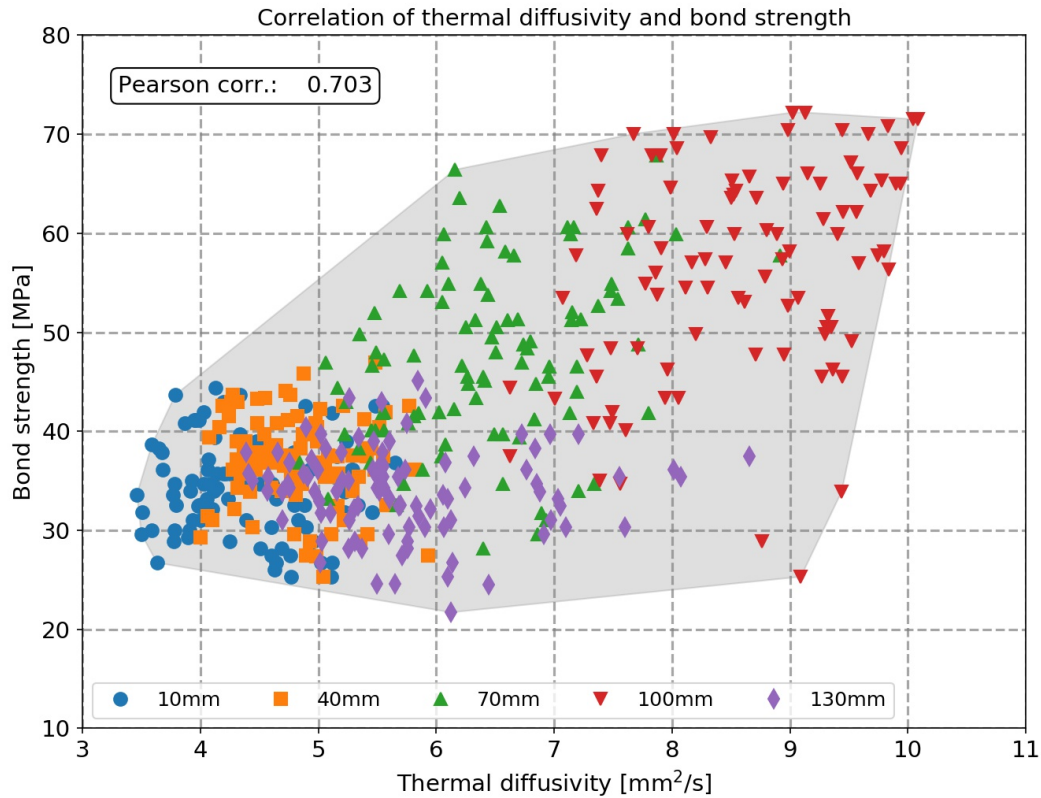
Figure 5.13.: Correlation between thermal diffusivity and bond strength measurements of cylinder coatings based on the data shown in Figures 5.2 and 5.4. The illustrated data is divided by color and shape according to the respective measurement position along the cylinder liners. The grey shading represents the envelope of all acquired data points.
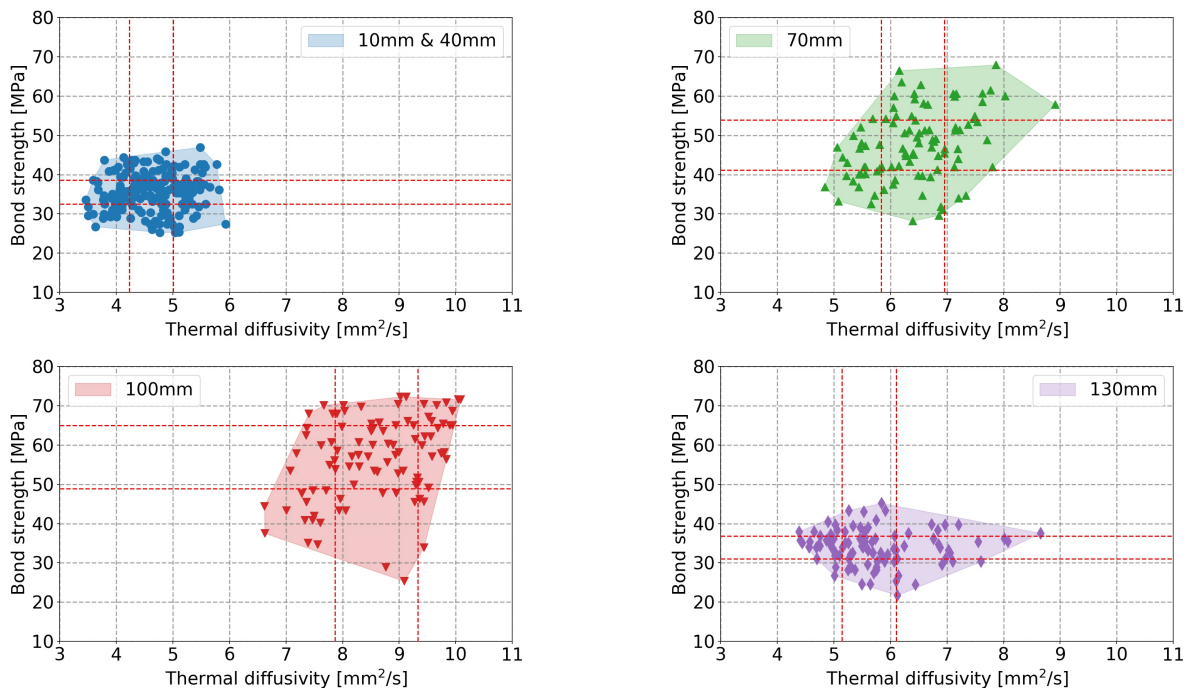
Figure 5.14.: Correlation of thermal diffusivity and bond measurements separated by the respective liner position. Measurements taken at liner positions 10 mm and 40 mm are combined in one diagram (top left). The red dashed lines represent the upper and lower quartiles of the underlying data.

bond strength as found for position 100 mm can be observed. Overall, a statistical correlation factor of 0.703 is calculated for the individual data pairs in Figure 5.13.

Due to the lamellar coating formation and the presence of laterally orientated splat interfaces as a result of in-flight oxidation of the spraying droplets, high bond strengths presume high thermal diffusivity values. High thermal diffusivity values indicate a coating structure with absence of horizontal voids thus the cohesive bond of the coating is also enhanced. As a matter of fact, no measurement data can be found in Figure 5.13 showing low thermal diffusivity and high bond strength. Since the failure of the coating system occurs at its weakest part, enhanced coating defects lower the cohesion bond and lead to failure of the entire coating system. Consequently, low bond strength correlates with low thermal diffusivity values of the coatings and the correlation between low thermal diffusivity and weakened cohesive bond strength can be linked to the defect factor. In general, a proportional trend of thermal diffusivity and bond strength is assumed. Both, thermal diffusivity and bond strength show a reciprocal behavior to the defect factor as shown in Figure 5.12. In both cases, high thermal and mechanical values are the consequence of low defect factors. The relation between thermal diffusivity and bond strength measurements reveal the expected trend, however no distinct correlation can be concluded. Whereas connecting the thermal and mechanical properties reveals enhanced variations of the values along the linear trend, still the relation shows a distinct characteristic that high bond strengths base on high thermal diffusivity values. However, particular data points can be detected aside from the general trend showing lowered bond strength and high thermal diffusivity. Especially in the lower liner positions of 100 mm and 130 mm, several data pairs present unexpected behavior. Here, the adhesion bonding behavior is assumed to be reduced while the inner coating strength is not affected by coating defects.

Since the presented TWI measurements are used to determine the integral thermal diffusivity of the coating, singular effects at the coating-substrate-interface can hardly be recognized. As interface contamination in advance of the coating spraying process may cause lowered adhesion strength, this could cause failure of the coating system even showing high cohesive bond. However, several publications have shown promising results characterizing the adhesion strength of layered system by the evaluation of the reflection coefficient R of the TWI [133–135]. The reflection coefficient describes the mismatch of the thermal properties from the layered structure to the substrate. Thus, possible thermal resistances arising from defects at the coating-substrate interface may lead to a drop of the reflection coefficient. Therefore, measured reflection coefficients are correlated with the bond strength values in Figure 5.15. However, the shown correlation does not present a precise trend of the behavior between reflection coefficient R and the bond strength. Whereas liner positions 10 mm and 40 mm show low reflection coefficients, the remaining liner segments are found showing higher R-values. A strong correlation between reflection coefficient and bond strength cannot be observed as the Pearson correlation coefficient is calculated to 0.46. According to the presented trend, liner positions 70 mm to 130 mm all represent comparable R-values, whereas their bond strengths deviate significantly. Combining the fracture analysis shown in Figure 5.8 with the data pairs in Figure 5.15, measurements at liner positions 100 mm and 130 mm show different bond
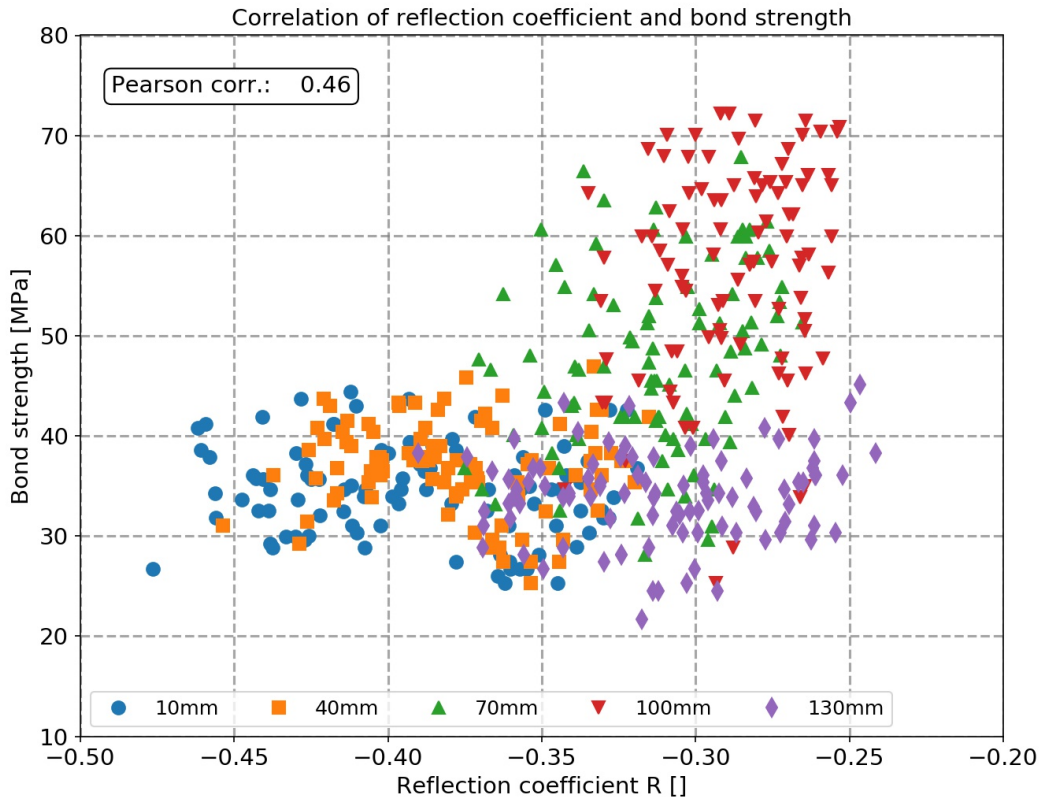
Figure 5.15.: Correlation between reflection coefficient and bond strength measurements of cylinder coatings. The illustrated data is divided by color and shape according to the respective measurement position along the cylinder liners.

strengths combined with different mechanical failure types during bond testing. However, both liner positions present comparable reflection coefficients R. Thus a separation of the failure mechanism by the reflection coefficient cannot be concluded from this correlation.

Therefore, adhesive influences cannot simply be extracted from the TWI study, but additional investigations regarding the failure mechanism of wire arc sprayed coatings and the resulting effect on TWI and bond strength measurements are required. In this context, the following chapter presents a study about process parameters influencing the cleanliness of the substrate surface. This study focuses on interface contaminated coating systems and the resulting thermal and mechanical properties of these layers. Again, TWI and PAT™ measurements are performed to evaluate the influence of a contaminated substrate interface on the correlation between thermal and mechanical properties. Further, the influence of process optimization lowering the oxygen content within the spraying atmosphere on the thermal and mechanical properties of wire arc sprayed coatings are investigated. Two different approaches are applied to prevent the ambient air to flow into the cylinder bore during thermal spraying.

6. Process influences on thermally sprayed cylinder coatings

The previous chapter reveals major relationships between the thermophysical and mechanical properties based on the microstructure and the respective defect morphology of the investigated cylinder coatings. The tested coatings are taken from randomly drawn crankcases of the large-scale production. To evaluate the applicability of TWI measurements quantifying the bond strength of the coatings to the crankcase substrate, one may further analyze influences of large-scale process variations on the measurement results and their interpretation on the resulting thermal and mechanical properties of the cylinder coatings. In the following, substrate surface contamination in advance of the thermal spraying process as well as variations of the oxygen content during the spraying process are inspected separately to quantify their influences on the TWI and PAT™ results.

In fact, as the thermal diffusivity measurements can be seen as integral measurements of the summarized elongation of the present coating defects, TWI allows to conclude certain information about the cohesive bonding behavior of the thermally sprayed coatings. However, singular effects at the interface influencing the adhesive bond such as oily contamination, are not addressed by the TWI measurements yet. Hence, further analysis about the relation between TWI and PAT™ of coating interfaces with weakened adhesive bond is investigated in Chapter 6.1.

Additionally, the coating atmosphere has proven to greatly influence the coating formation process and the resulting coating microstructure [5–7, 9, 28]. To produce coating systems showing almost no laterally oriented splat interfaces along the entire liner, the spraying process needs to be performed with lowest possible oxygen content in the coating atmosphere. In this context, two experimental approaches are presented in Chapter 6.2, which potentially reduce the oxygen content along the entire cylinder liner during thermal spraying. The resulting experimental cylinder coatings are analyzed regarding their thermophysical and mechanical properties. Further, microstructural analysis is performed to assess the resulting coating microstructure and to correlate the observed quantities.

6.1. Interface contamination of substrate material

The cleanliness of the aluminum alloy substrate surface in advance of the spraying process is one of the most important requirements to achieve sufficient adhesion between coating and substrate [5]. Contamination of the substrate interface or defective roughening structures

are known to influence the adhesive bond of a coating to a substrate [5]. Oily contamination prevent diffusion bond between coating and substrate, which leaves the adhesion mechanism to be only mechanical. As described in Chapter 2.2, the entire mechanical machining including the wire arc spraying process of the crankcases is divided into several individual steps. Whereas pre- and post-treatments in advance and after thermal spraying are performed under oily conditions, roughening the cylinder bores and thermal spraying of the coatings is done without any use of oil. It is most important, that any oily residuals are removed from the entire crankcase before the roughening process. In this context, the crankcases are washed and dried after the mechanical pretreatments (Chapter 2.2). However, due to the complex structure as well as multiple holes and screwing threads at the crankcases, small amounts of remaining oily composites mixed with washing water remain on the crankcases surfaces. Therefore, preheating of the crankcases after the roughening process and in advance of the thermal spraying has another benefit for the coating quality. Here, oily residuals mixed with washing water evaporate from the crankcase surface into the oven atmosphere. However, due to the high capacity of the production line, multiple crankcases pass the preheating step thus the oven atmosphere contains increased amount of oily particles over time. Experiments have proven that long preheating times do not simply benefit the coating bonding behavior but may also result in significantly reduced coating bond strengths. Here, the oven atmosphere partially condenses on the substrate interface thus contaminates the roughened NMRP with oily droplets. Therefore, the maximum oven preheating time is limited to 10 h. However, to investigate the influence of reduced adhesion based on contaminated interfaces for the relation between TWI and PAT™ measurements, four crankcases were selected from the large-scale production which exceeded the maximum oven time by at least 6 h and remained in the oven atmosphere for over 16 h. These crankcases have further been coated and finished within the conventional series production cycle.

6.1.1. TWI and PAT™ study

Extended preheating duration within a contaminated oven atmosphere is one known large-scale production characteristic, which can influence the bonding behavior. In this context, the described relation between thermal diffusivity and bond strength measurements is studied for the four contaminated crankcases. TWI and PAT™ measurements are applied along the cylinder liners at the known liner positions 10, 40, 70, 100 and 130 mm for all six cylinder bores at the angle position 0°. Again, boxplots are used to visualize the data. The shown lines, boxes, whiskers and circles represent the same values and ranges as introduced in Chapter 5.2. Further, non-destructive thickness measurements are applied at the same measurement positions to calculate the thermal diffusivity from the η-values gained with the TWI.

Both, thermal and mechanical properties of the evaluated contaminated cylinder coatings are presented in Figure 6.1. Thermal diffusivity values of the coatings with contaminated interfaces reveal the known behavior from Figure 5.2, whereas again strong variations can be observed along the cylinder liner. Median thermal diffusivity values are found to be on a comparable level of about 5 mm^2/s at the upper liner positions 10 mm and 40 mm, whereas the
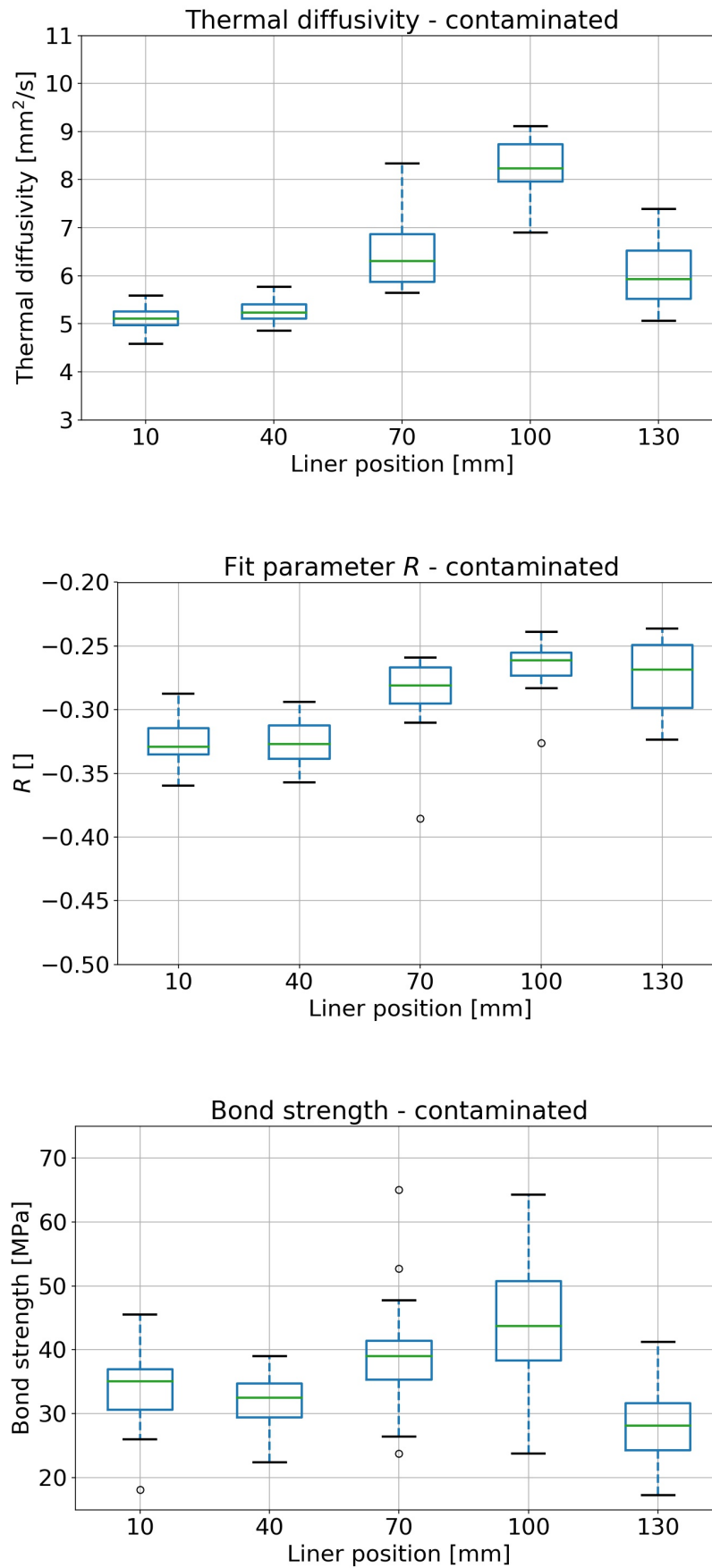
Figure 6.1.: Thermal diffusivity, reflection coefficient and PAT™ measurements of interface contaminated coating systems.

upper and lower quartiles indicate narrow variations. Again, a strong increase of the thermal properties from liner position 40 mm towards liner position 100 mm can be observed, thus the median thermal diffusivity value increases by about 60 %. The distribution of thermal diffusivity values of the contaminated coatings at liner position 70 mm lead to an enhanced upper whisker indicating stronger variation at this position. However, contaminated coating systems again reveal a relevant drop of the thermal properties to a comparable level of about $6 - 6.5\,\mathrm{mm^2/s}$ towards the lowest liner position from 100 mm to 130 mm.

The measured reflection coefficients of contaminated coating systems can be found in Figure 6.1 in the middle. As the reflection coefficients R follow the conventional trend already discussed in Chapter 5.2, no significant differences are observed between contaminated and non-contaminated coating systems shown in the appendix C.1 in Figure C.8. Reflection coefficients are found to be higher in the lower part of the cylinder liner at a comparable level for all three liner positions 70 mm, 100 mm and 130 mm. Reflection coefficients close to the cylinder head sealing surface reveal lowest overall values. However, as contaminated and non-contaminated coating systems show almost the same behavior along the cylinder liner, interface contamination does not significantly affect the thermal mismatch of the coating layer and the substrate material.

Additionally, the bonding behavior of contaminated coating systems is shown in Figure 6.1 at the bottom. Median bond strength values at the upper liner positions 10 mm and 40 mm are found to be a comparable level at about $32 - 35\,\mathrm{MPa}$, whereas also the upper and lower quartiles as well as the whiskers indicate comparable results for the upper liner positions. In the following bond strength values again increase towards the lower liner position at 100 mm, however the median value at position 100 mm is only found to be at 43.7 MPa for the contaminated coating. Compared to the non-contaminated systems in Chapter 5.3 Figure 5.4, the highest median value found at position 100 mm was at 60.6 MPa, thus over 38 % higher than for the contaminated system. Also the median bond strength at liner position 70 mm is found to be below 40 MPa, while the upper whisker of the contaminated coatings is on the same level as the median bond strength of the non-contaminated system. PAT™ reveals overall reduced bonding properties at both liner positions 70 mm and 100 mm comparing the contaminated and non-contaminated coating structures. Again the increasing bond strength along the cylinder liner is followed by a drop of the mechanical properties whereas both coating types have lowest bond strength in the lowest liner position 130 mm near the crankshaft. Concluding the mechanical bond testing showed in Figure 6.1, bond strength is generally reduced along the cylinder liner comparing the contaminated and non-contaminated systems. Especially at liner sectors conventionally showing highest bond strengths, the median bond strength is significantly reduced in contaminated systems.

6.1.2. Metallography

In addition to the previous TWI-PAT™ study of contaminated coating-substrate-interface systems, optical microscopy images are obtained to investigate the respective coating microstructure and defect morphology from cross sections specimens. In this case, two optical
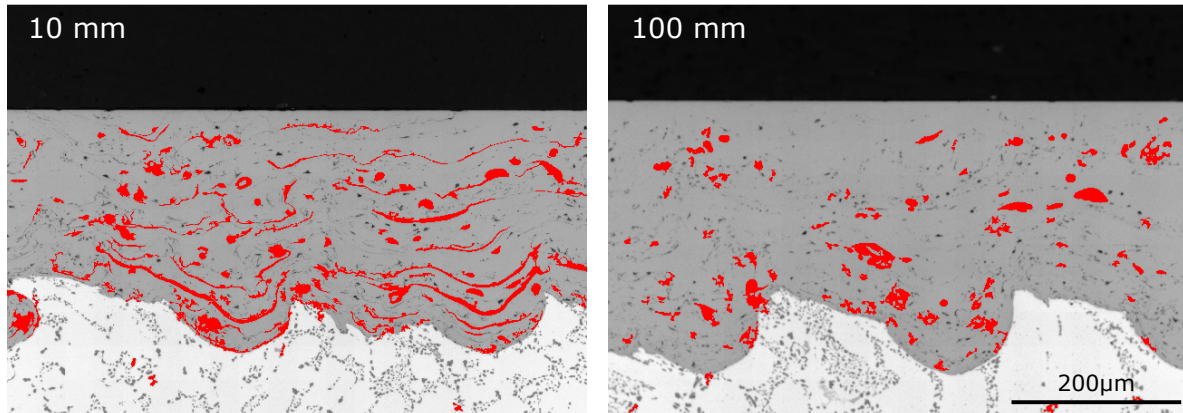
Figure 6.2.: Optical microscopy images of cross section specimens of contaminated coating systems at the two liner positions 10 mm and 100 mm including the highlighted coating defect morphology in red.

Table 6.1.: Quantitative cross section analysis of contaminated coating systems. The individual optical microscopy images are analyzed regarding their global defect factors and averaged for the entire cross section specimen.

Cylinder	Liner pos. [mm]	Mean def. fac. $[\mu m^{-1}]$	Mean abs. dev. $[\mu m^{-1}]$
5	10	$1.95\,e-2$	$1.48\,e-3$
6	10	$2.02\,e-2$	$1.68\,e-3$
5	100	$1.12\,e-2$	$1.04\,e-3$
6	100	$1.43\,e-2$	$1.50\,e-3$
Non-contaminated	10	$2.19\,e-2$	$1.35\,e-3$
coating systems	100	$1.54\,e-2$	$1.39\,e-3$

microscopy images of cross section specimens are shown in Figure 6.2, whereas the defect morphology is highlighted in red. The cross section specimens are cut out of the cylinder liners at the measurement positions 10 mm and 100 mm for a contaminated crankcase. Again, enhanced amount of laterally expanded splat interfaces can be observed in the upper parts of the cylinder liner. The observed defect morphology is dominated by lateral voids, whereas also globular pores without distinct elongation can be found. Additionally, the surface of the roughening structure is partially covered by coating defects. However, no significant differences of the coating microstructure found at liner position 10 mm are observed in contrast to the non-contaminated coating systems shown in the previous chapter in Figure 5.5. Additionally, also the coating microstructure of liner position 100 mm does not reveal any unexpected defect structures. Again, globular pores are majorly observed, while lateral voids are missing entirely in this cross section image. Also, the coating-substrate interface does not show any significant defects covering the interface.

Quantitative analysis of optical microscopy images is shown Table 6.1. Here, four cross section specimens are cut out of the cylinder liner and analyzed regarding their coating microstructure as described in Chapter 3.4.1. Therefore, the global defect factors of the individual optical images are calculated and further averaged for the entire cross section specimens. The variation

of the defect factor within this cross section is represented by the mean absolute deviation. The reference values of the non-contaminated coatings are calculated from the cross section series shown in Figure 5.6. The quantitative analysis reveals a liner dependent coating microstructure of the contaminated coating systems as the defect factors show two different levels comparing liner position 10 mm to 100 mm. Therefore, again the upper liner positions clearly indicate higher defect factors of the coating microstructure thus representing enhanced amount of laterally orientated splat interfaces. Further, the defect factors decreases significantly for the cross section specimens taken at liner position 100 mm by up to 45 % per liner segment. With respect to the obtained variations, the microstructural analysis reveals two separated levels of coating defect morphology. As the analysis reveals, the defect factors of contaminated and non-contaminated coating systems present similar values, whereas both coating systems show enhanced defect factors at liner position 10 mm. Thus, contaminated and non-contaminated coating systems present comparable behavior with respect to the analyzed defect morphology along the cylinder liner as the interface contamination does not appear to influence the overall coating microstructure. Concluding the microstructure analysis, the defect morphology is not found to be significantly modified for the contaminated coating systems compared to the non-contaminated coatings shown in Chapter 5.

Additionally, quantitative fracture analysis of 30 PAT™ segments is applied to investigate the adhesive and cohesive behavior of the contaminated coating systems after mechanical bond testing. The evaluated remaining coating material on the fracture area is shown in Figure 6.3 on the top. Comparing the contaminated and non-contaminated coating systems, the remaining coating material is reduced at all liner positions for the contaminated coatings. The absolute difference of the remaining coating material between non-contaminated and contaminated coatings is presented in Figure 6.3 bottom. While positions 10 mm and 40 mm still show a high level of remaining coating material, significant differences between contaminated and non-contaminated coating systems can be found for positions 70 mm and 130 mm. At the liner position 70 mm, the remaining coating material decreases from over 40 % to about 25 %. Also, the remaining coating material on the aluminum-based substrate drops from 40 % to about 20 % at the lowest liner position. However, comparing the liner segment at position 100 mm, no relevant changes are observed between contaminated and non-contaminated coatings as a difference of less than 5 % is calculated. The shown analysis reveals a relevant influence of the interface contamination on the fracture mechanics. In this context, enhanced amount of adhesion failure is observed due to the lowered remaining coating material especially in the lower liner segments of 70 mm and 130 mm. As the remaining coating material indicates the ratio of adhesion to cohesion failure, the contaminated systems exhibit more adhesion failures as expected compared to the non-contaminated coatings.

6.1.3. Correlation of thermal and mechanical properties of contaminated coating systems

As the cleanliness of the aluminum substrate surface is one important requirement to achieve sufficient adhesion between coating and substrate [5], contamination of the substrate interface is
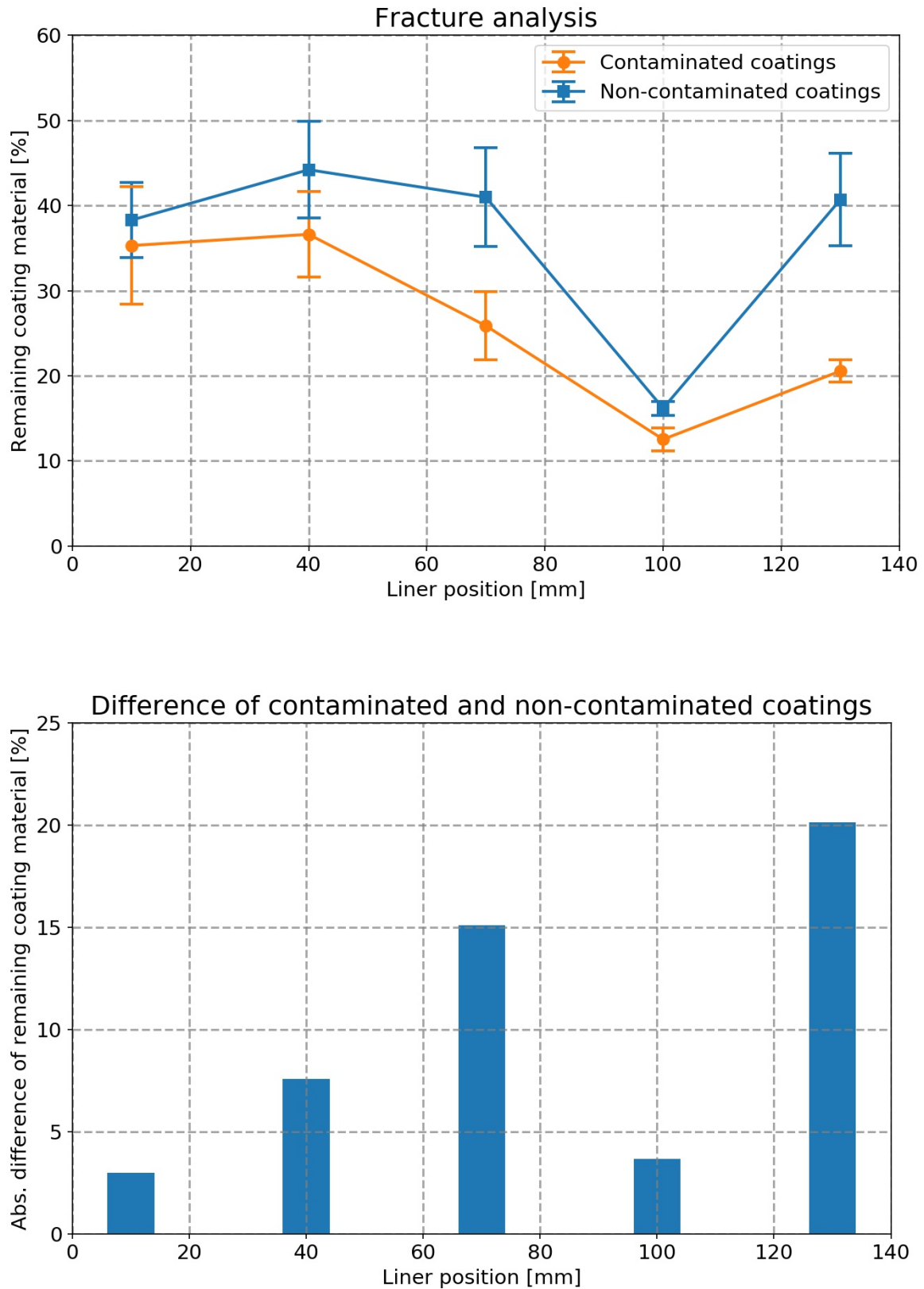
Figure 6.3.: Top: Quantitative fracture analysis of the remaining coating material on the aluminum-based substrate after PAT™ for contaminated and non-contaminated coating systems. Symbols (circles, squares) represent mean values, whereas the error bars indicate the standard deviation of the data. Bottom: Difference of the remaining coating material comparing both coating systems.

known from literature and this work to influence the adhesive bond of a coating to a substrate. In this context, the influence of oily substrate contamination on the bonding behavior as well as on thermal diffusivity values and the coating microstructure is investigated. Excessive preheating duration of the roughened crankcases in advance of thermal spraying combined with a contaminated oven atmosphere is known to contaminate the roughened substrate structures. Therefore, four crankcases are intentionally contaminated in the oven atmosphere as described in Chapter 6.1.

The investigation of thermal diffusivity and mechanical bond shows that median thermal diffusivity values are not mainly affected by the interface contamination. The contaminated systems show the known increase of the thermal diffusivity from the cylinder head sealing surface towards liner positions 100 mm followed by the strong decrease towards the lowest liner position at 130 mm. In contrast, bond values reveal strong influence by the contaminated interfaces as the bond strength is found to be significantly reduced at the liner segments 70 mm and 100 mm. Here, a relevant drop of the mechanical bond is observed compared to the non-contaminated coatings, which is not indicated by the thermal diffusivity of the coating. For non-contaminated coatings, median bond strength and median thermal diffusivity correlate, as the coating microstructure and the horizontal defect elongation define both charactersitics. However, as the substrate interface is contaminated by oily residuals, deviations from this correlation are observed. The microstructural analysis of the contaminated coating systems shows that the defect factor is still low at the liner segments of 100 mm. Therefore, laterally orientated splat interfaces are missing at this liner segment causing the thermal properties to be on a comparable level as for the non-contaminated systems. Also, the cross section images in Figure 6.2 show the known behavior of the defect structure as discussed in the previous Chapter 5.4. Therefore, thermal transport properties still found on the underlying microstructure, whereas the coating bonding behavior is influenced by the substrate contamination. In this context, significant differences of the adhesion behavior are found between contaminated and non-contaminated coatings with the fracture analysis of the PAT™ segments. The oily contamination promotes adhesive break especially at the liner regions 70 mm and 130 mm. The remaining coating material is drastically reduced at these liner segments thus indicating enhanced adhesive failure. However, upper liner segments are found to be not as influenced by the interface contamination, whereas the cohesive failure is still on a comparable level as for non-contaminated coatings. While the cylinder coatings are sprayed from bottom to top, additional heating of the substrate during the spraying process is assumed. Especially the upper liner regions are additionally preheated by the up-moving spraying jet due to the introduced heat load. This causes the oily contamination to partially evaporate from the substrate surface thus lowering the overall oily residuals on the interface. Consequently, the upper liner segments are not as affected by the interface contamination compared to the lower liner segments.

Additionally, as discussed in Chapter 5.6, the reflection coefficient R cannot be used to separate cohesive from adhesive failure. Since the reflection coefficient reveals the thermal properties mismatch of layer to substrate, contaminated interfaces may be expected to show a varied reflection coefficient. However, as found in Figure 6.1, contaminated coating systems do not
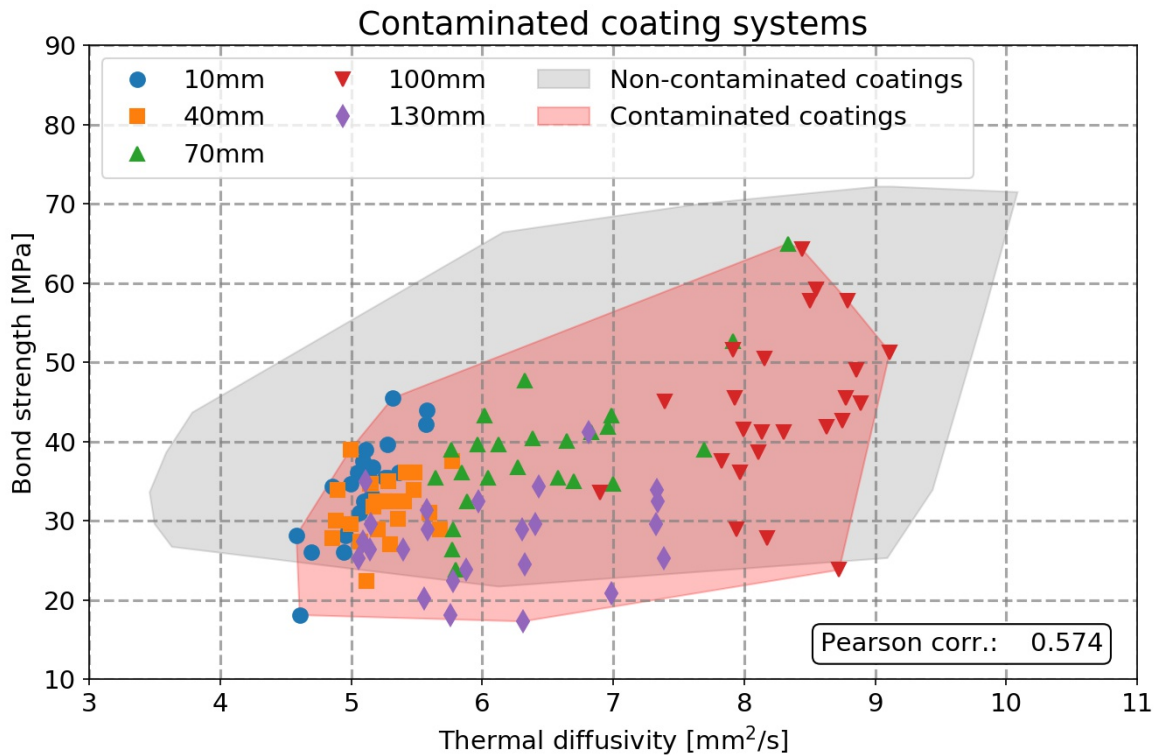
Figure 6.4.: Correlation between thermal diffusivity and bond strength measurements of contaminated coating systems based on the data shown in Figure 6.1. The illustrated data is divided by color and shape according to the respective measurement position along the cylinder liners. The grey shading represents the envelope of the data pairs presented in Figure 5.13.

show any differences of their reflection coefficients compared to non-contaminated coatings. Thus, the contamination has no measurable effect on the thermal resistance at the interface. In fact, the integral measurement of TWI does not allow to measure singular effects at the coating-substrate interface. The effect on the thermal properties due to the defects in the coating microstructure overlaps the effect of a potentially changed thermal resistance at the interface. Thus, TWI is not capable to measure such effects at the coating-substrate interface.

Correlation between thermal and mechanical properties of the contaminated coating systems is shown in Figure 6.4. The relation of the bond strength to the thermal diffusivity of the contaminated coatings shows that the data points taken at liner positions 10 mm, 40 mm, 70 mm and 130 mm condense at the bottom left region showing low thermal diffusivity and low bond strength. Data points taken at liner position 100 mm reveal high thermal diffusivity values but lowered bond strength compared to the non-contaminated coating systems. Again, several data points are found showing high thermal diffusivity combined with low bond strength. The correlation is less pronounced towards the upper right corner, as adhesion strength lowers the overall bond even for dense coating microstructures. The underlying grey shading marks the envelope of the data pairs of non-contaminated coatings presented in Chapter 5.6 in Figure 5.13. Here, the data taken from the contaminated coatings are shifted to the bottom right corner of the shading, whereas data close to the top left edge is again missing entirely

for this study. Thus, contamination of the coating substrate interface does have a relevant influence on the correlation between thermal and mechanical properties of wire arc sprayed cylinder coatings. Statistical analysis of the contaminated coatings show a difference in the calculated Pearson correlation factor compared to non-contaminated coatings in Figure 5.13. Contaminated coating systems only correlate with a value of about 0.574, whereas higher correlation factor of 0.703 is found for the non-contaminated systems. Thus, the correlation is less statistically pronounced compared to the non-contaminated coating systems.

Summarizing the influence of the interface contamination on the thermal and mechanical properties, thermal diffusivity values are not as affected by the interface contamination as the bond values. Consequently, the observed coating microstructure is not found to be affected by the interface contamination, while cross section images as well as quantitative microstructure analysis show comparable behavior as non-contaminated systems. The resulting thermophysical properties of the contaminated coatings present the conventional behavior along the cylinder liner, as these thermal properties are caused by the underlying defect morphology. However, strong influences of the oily contamination on the bonding behavior are observed. Whereas the coating microstructures reveal no changes to the non-contaminated system, the cohesive behavior of contaminated coatings are found to be unchanged. Therefore, changes of the overall bond strength base on a changed adhesive behavior of the coatings. The fracture analysis indicates that enhanced adhesive failure occurs due to the interface contamination thus lowering the overall bond strength at the respective positions. Statistical correlation of the contaminated coating systems is less pronounced compared to the non-contaminated coatings. Consequently, the changed adhesive mechanics reveal that the correlation of thermal and mechanical properties based on the coating microstructure and the respective defect morphology can only be applied, if the adhesive mechanics are not affected by any additional influences such as interface contamination.

6.2. Reduction of oxygen content during wire arc spraying

The oxygen content within the atmosphere during the wire arc spraying process has proven to show a significant influence on the coating formation and the resulting coating microstructure [9, 40]. Based on the publication of Schilder et. al [9] and the discussion in Chapter 5.6, the oxygen content varies along the cylinder liner during the wire arc spraying process. Enhanced amount of oxygen is found in the upper parts of the bore during the coating formation, whereas almost no oxygen is at the lower liner positions at $100\,\mathrm{mm}$. Due to the flow conditions in the upper positions, ambient atmosphere flows into the cylinder bore and interacts directly with the process gas [9]. Also the crankshaft opening at the bottom of the cylinder liner allows ambient atmosphere to be sucked into the cylinder bores, thus oxidizing the spraying particles during the coating formation at the bottom of the liners [6, 7, 9, 136]. The resulting in-flight oxidation of the spraying particles leads to the known lamellar coating structure thus lowering the overall thermal and mechanical properties of the coatings. In this context, the thermal spraying technology can be improved by reducing the oxygen content along the entire liner during thermal spraying of the cylinder coatings [9]. Thus, two approaches to lower the oxygen
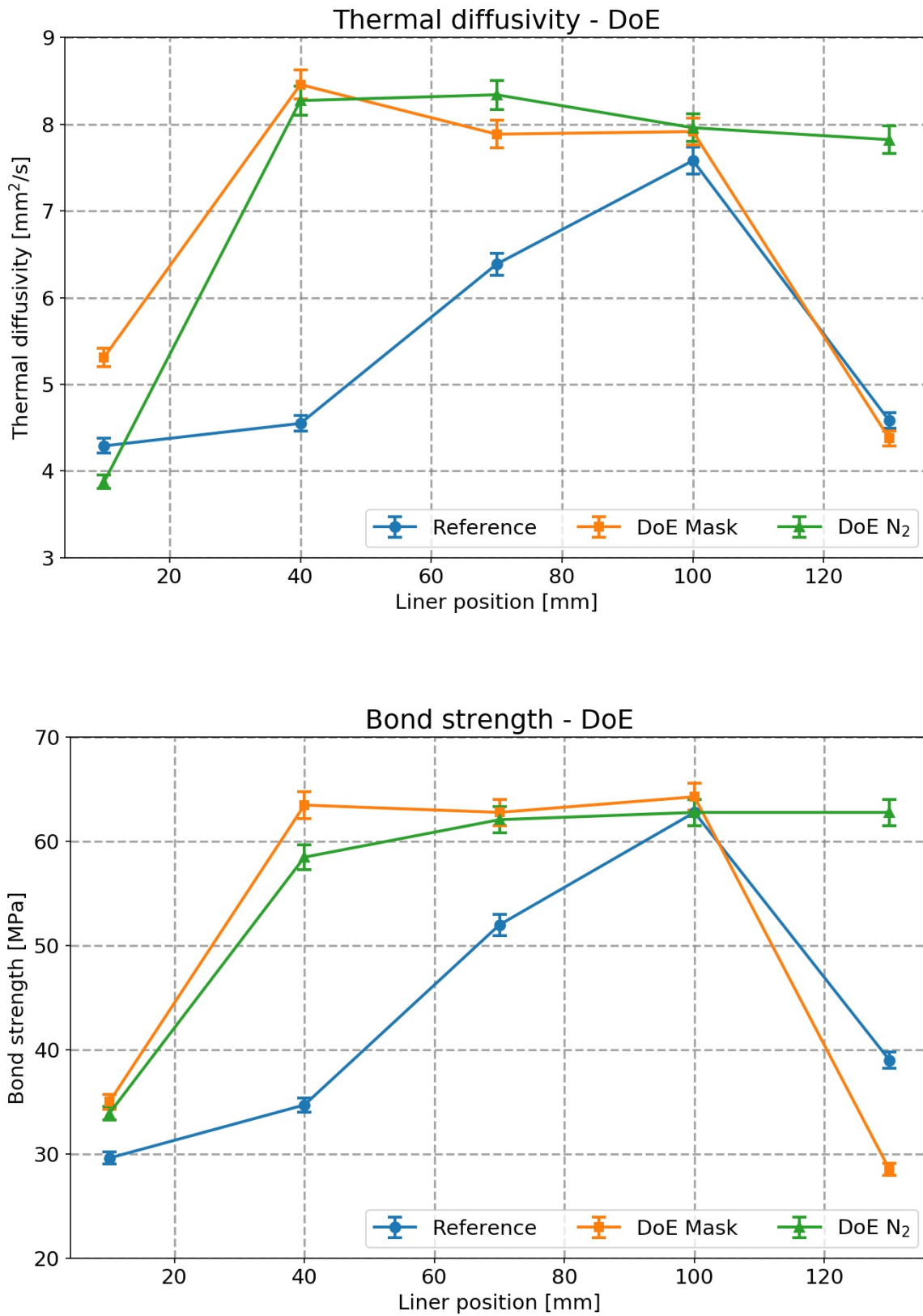
Figure 6.5.: Thermal and mechanical measurements of the DoE coatings.

content in the spraying atmosphere are discussed in the context of a "Design of Experiments" (DoE)[5]. An optimized circular mask is placed on the cylinder head sealing surface to reduce the spacing between the rotating burner and the mask as published in [9]. The resulting narrow gap between burner and mask should protect the bore atmosphere from ambient air outside the crankcase. Secondly, the cylinder bore is flooded by additional nitrogen during the coating process to drive out the gratuitous oxygen without the use of the additional mask [137]. Both approaches are meant to lower the oxygen content during the spraying process thus producing dense coatings without lateral splat interfaces. Therefore, two crankcases have been coated under laboratory conditions applying the two described methods separately by a coating system of type CBC200 (Gebr. Heller Maschinenfabrik GmbH, Germany). These two types are labeled as "DoE crankcases". One additional crankcase is coated under conventional spraying conditions to obtain a reference crankcase. Influences resulting from the large-scale production such as interface contamination due to the oil-contaminated atmosphere of the preheating oven are not expected under the applied laboratory conditions.

6.2.1. TWI and PAT™ study

In order to investigate the thermal and mechanical properties of the DoE coatings, TWI and PAT™ measurements are applied for all three crankcases along one cylinder liner. Non-destructive thickness measurements further allow to calculate the thermal diffusivity from the TWI measurements. The obtained thermal diffusivity and bond strength measurements are illustrated in Figure 6.5. TWI measurements of the reference crankcase reveal the known characteristics of the thermal diffusivity with respect to the liner position as found in the previous Chapter 5.2 in Figure 5.2. The thermal diffusivity is found to be lowered in the upper parts of the crankcase followed by a strong increase of the thermal properties towards liner position 100 mm by about 77 %. The increase of the thermal diffusivity is followed by the known decrease towards the lowest liner position 130 mm to a comparable level as found in the upper parts of the liner. In contrast to the reference crankcase, both DoE coatings reveal major differences of the thermal properties along the cylinder liners. Whereas the thermal diffusivity is found to be on a comparable level for all three crankcases at the top liner position 10 mm, the DoE coatings reveal a strong increase of the thermal diffusivity at position 40 mm. Both DoE coatings show thermal properties on the same level at position 40 mm as the reference crankcase reveals at 100 mm. Further, the thermal properties of the DoE coatings remain constantly enhanced over the liner range between 40 mm to 100 mm. While both DoE coatings behave almost similarly from the cylinder head sealing surface to position 100 mm, their thermal properties deviate towards the crankshaft. The cylinder coatings sprayed using the improved mask geometry exhibit the same decrease of its thermal properties as the reference crankcases at position 130 mm, while the DoE N_2 coatings remain almost constant down to the lowest position of the cylinder liner.

Additionally, bond strength measurements of the DoE coatings using PAT™ are shown in

---

[5]The design, application and process execution of the presented DoE was performed by Schilder et al. [9] and the team PT/TFT at the Mercedes-Benz AG (Stuttgart, Germany). The shown PAT™ results and cross section images have been taken under the supervision of B. Schilder and have been generously provided for this work.
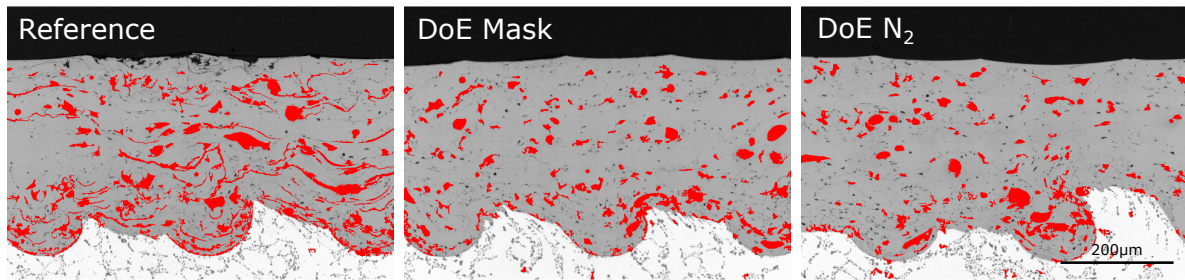
Figure 6.6.: Optical microscopy images of cross section specimens of the DoE crankcases cut out of the cylinder liner at positions 40 mm. The coating defect morphology is highlighted in red.

Figure 6.5 bottom. Here, bond strength values follow the thermal characteristics of the cylinder coatings. Again, the reference coatings reveal the known behavior with increasing bond strength towards liner position 100 mm followed by a drop of the mechanical properties towards the crankshaft as already seen in Figure 5.4. The bond strength of the DoE coatings start at the same level as the reference coatings right below the cylinder head sealing surface. However, the bond strength deviates strongly from the reference coatings as highest bond strengths can already be found at liner position 40 mm. Both DoE coatings exhibit continuous high bond strengths between 40 mm to 100 mm, while the DoE Mask coatings show a drop of the bond towards the crankshaft. In contrast, DoE N_2 coatings keep the high bond strength towards the lowest liner position 130 mm.

6.2.2. Metallography

Since the thermal and mechanical properties of the DoE coatings deviate significantly to the reference coating along the cylinder liner, microstructure analysis is applied to investigate the defect structures of the DoE coatings. Therefore, three optical microscopy images of cross section specimens are shown in Figure 6.6. The three shown cross section specimens are all cut out of the liners at 40 mm. Comparing the three microscopy images of the coatings, major differences of the defect morphology can be observed. The microstructure of the reference coating shows the expected dominant formation of lateral splat interfaces. The microstructure is mostly covered by thin horizontal voids causing lowered thermal and mechanical properties at the respective liner position 40 mm. Again, also the coating-substrate interface is majorly covered by thin lateral voids. In contrast, both DoE cross section images do not show significant amount of lateral voids. The coating defect morphology is dominated by globular pores without major elongation, whereas splat interfaces are missing entirely in these images. Further, substrate interface structures are mainly defect free, however certain amount of pores can be found between the peaks and the valleys of the NMRP structure near the substrate interface. Still, the observed coating microstructure allows the conclusion that the resulting variation of thermal and mechanical properties result from the varying coating microstructure and the respective defect morphology.

In this context, a quantitative analysis of several cross section specimens is shown in Figure 6.7. Here, a total of 15 cross section specimens are cut out of the cylinder liners of the reference
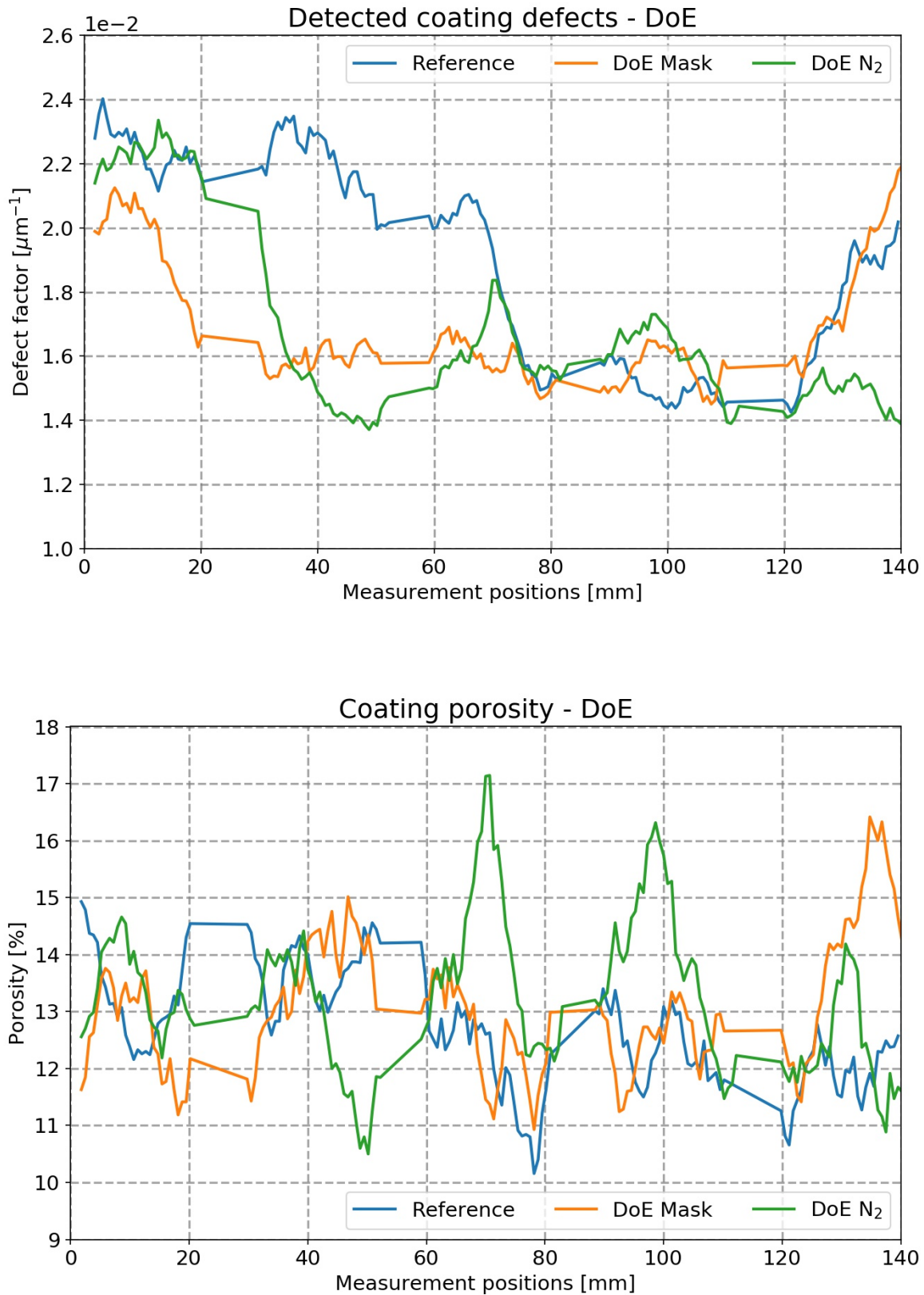
Figure 6.7.: Quantitative microstructure analysis of the DoE coatings **Top:** The shown defect factor represents the horizontal elongation of all defects in the microstructure over the substrate. **Bottom:** Calculated coating porosity based on the segmented coating defects. Both quantities are calculated for each cross section image individually and assembled to observe the influence of the coating defects along an entire cylinder liner.

crankcase and the two DoE crankcases at the five liner positions $10, 40, 70, 100$ and $130\,$mm. Again, the cross section specimens are covered by 30-40 individual microscopy images, which are analyzed with respect to the defect factor and their porosity separately. The calculated defect factors and porosity values are aligned according to their original position in the crankcase to achieve a coating microstructure profile of almost the entire cylinder liner. The liner regions not covered by the cross section specimens are linearly interpolated. The reference coatings show a comparable behavior of the defect factor as already found in the previous Chapter 5.4 in Figure 5.6. The defect factors slightly decreases towards $70\,$mm followed by a strong gradient within a short range of about $10\,$mm to a drastically lowered level of the defect factor. The calculated defect factors remain almost constant in the liner range of $80 - 120\,$mm, whereas a strong increase of the horizontal elongation of the coating defects is observed at liner position $130\,$mm. In contrast, the mean porosity distribution slightly decreases from the cylinder head sealing surface towards the crankshaft, but does not reveal any systematic variations along the liner.

Comparing the DoE coatings with the reference part, the microstructure changes of the coating defects are shifted towards the cylinder head sealing surface. The DoE Mask samples present the strong decrease of the defect factor at the liner position around $20\,$mm, whereas the value remains almost constant over a wide range up to $120\,$mm. Further, the strong increase of the defect factor in the lowest part of the liner can also be found for the DoE mask coatings. The defect factor increases parallel to the reference coatings at the same depth region. Thus, defects of the reference and the DoE mask coatings show comparable horizontal elongation at this liner interval. Consequently, the applied mask does not influence the defect morphology in the lowest liner segments.

The DoE N_2 coatings also reveal a varied defect morphology in contrast to the reference coatings. The drop of the defect factor is present at a liner position of about $30\,$mm and decreases to the same level as found for the reference and the DoE Mask coatings. However, the DoE N_2 coatings exhibit stronger variation of the lowered defect factor compared to the remaining two coating types. Further, the defect factor remains on a constantly low level through the whole liner regions even at the lowest position $130\,$mm near the crankshaft. Again, mean coating porosity is found to slightly decrease towards the bottom of the liner, however major porosity peaks are found at about $70\,$mm and $100\,$mm. These observed peaks explain the defect factor variations, since also the defect factor locally peaks at $70\,$mm and $100\,$mm. As the defect factor sums the horizontal elongation of all detected defects, an increase of the defect factor may result from an increase of the individual horizontal elongation of the defects or an enhanced amount of defects within the analyzed cross section image. In this case, enhanced porosity found at the respective liner positions causes the defect factor to increase, while the defect morphology is assumed to stay constant within that liner region. However, the coating porosity is found to exhibit strong but no systematic variations along the cylinder liners for all three coating types. Thus, the observed systematic changes of the defect factors do not result from a systematically changing porosity, but can be traced back to he changing horizontal elongation of the observed coating defects.

6.2.3. Correlation of thermal and mechanical properties of DoE coating systems

Concluding the thermal and mechanical measurements as well as the microstructure analysis of the DoE coatings, again major variations of the coating properties can be observed with respect to the liner positions. However, the DoE showed, that the applied process variations of an optimized mask geometry as well as flooding of the cylinder bore with additional nitrogen changed the defect morphology in the coating microstructure significantly compared to the reference coatings. The process adaptions lead to less laterally orientated splat interfaces even in the upper liner segments, whereas the optimized mask geometry reduce the defect factor drastically even up to the liner regions at 20 mm. In this context, thermal and mechanical properties increase significantly over the center part of the liner, keeping the thermal diffusivity and the bond strength on a high level between the liner positions 40 mm and 100 mm. The mentioned property values increase to a comparable level which can be originally found at liner position 100 mm of the reference coatings. The optimized mask geometry is an effective way to prevent the ambient air to be sucked into the cylinder bore at the cylinder head sealing surface during the thermal spraying and thus to reduce the oxidation of the spraying droplets in the upper liner parts [9]. However, the coating microstructure in the lower liner segments is found to be independent of the upper mask geometry. Here similar behavior of the DoE Mask coatings and the reference coatings are observed, as the defect factor, the thermal diffusivity and the bond strength behave similarly at the lowest liner position at 130 mm.

Additionally, flooding the cylinder bore with additional nitrogen also showed promising results influencing the coating microstructures and reducing the amount of lateral splat interfaces in the coatings. Whereas the defect factor decreases to the lowered defect factor level at position 30 mm, the defect morphology remains constant over the rest of the liner down to the crankshaft. Therefore, the additional nitrogen seems to be efficient improving the defect microstructure in the lowest liner segments keeping the defect factor constant, while reference and DoE Mask coatings show increasing horizontal elongation of the coating defects in this region. Also thermal diffusivity and mechanical bond increase in the lowest liner positions compared to the reference parts as the values remain on a constantly high level at the lowest liner position.

In general, bond strength values follow the thermal properties of the DoE coatings, thus a strong relation is still present between both properties. The measured thermal diffusivity values still allow to deduce concrete conclusions about the mechanical bonding behavior. Therefore, thermal diffusivity values and bond strength measurements are correlated in Figure 6.8. Here, a strong linear correlation showing a Pearson factor of 0.934 is observed, as the correlation of the data of the DoE is presented using a linear regression model. Data points are positioned near the top left edge of the grey shaded area representing the envelope of the reference coating study of Chapter 5. In fact, a strong correlation of thermal and mechanical properties is observed for cylinder coatings sprayed under controlled and defined conditions. Thus, it can be assumed that adhesive influences on the bonding behavior are drastically reduced for these DoE coatings. Therefore, coating the cylinder bores under laboratory conditions and further reducing the influences of a large-scale production on the coating quality, adhesive influences
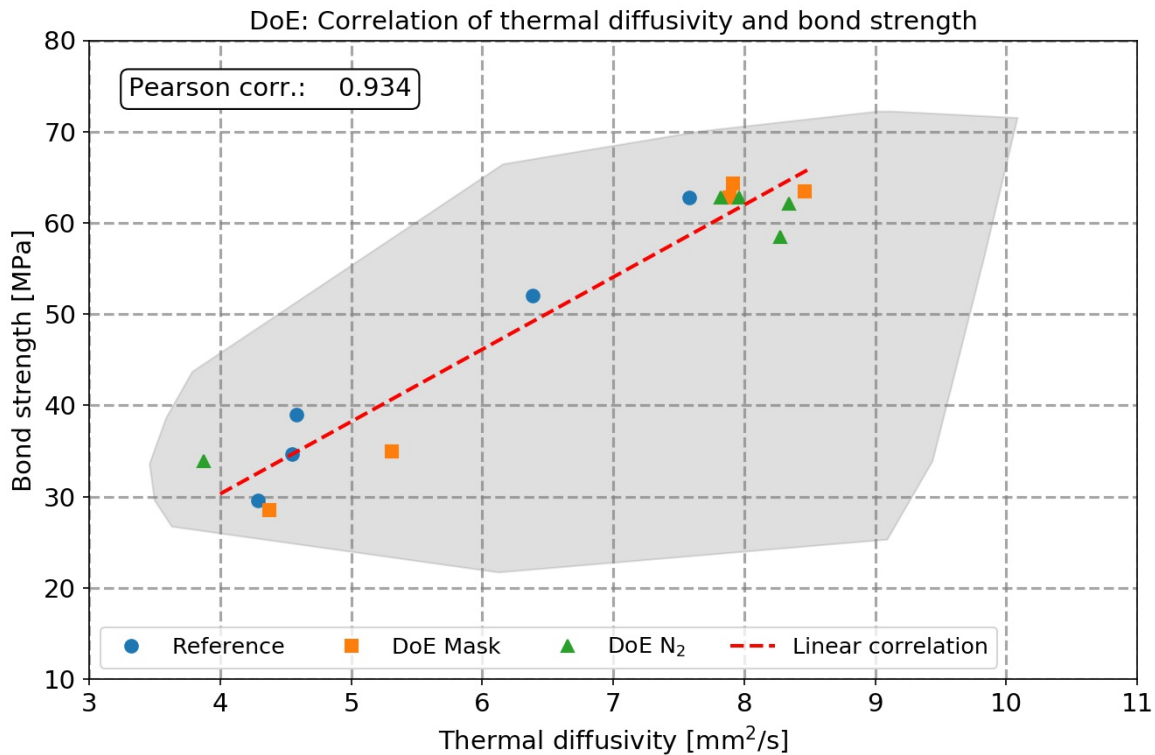
Figure 6.8.: Correlation between thermal diffusivity and bond strength measurements for DoE coatings. The illustrated data is divided by color and shape according to the respective measurement position along the cylinder liners. The grey shading represents the envelope of the data pairs presented in Figure 5.13.

on the overall bonding behavior may be reduced.

The DoE has shown, that the observed relation between thermal diffusivity and bond strength discussed in the previous Chapter 5.6 can be reproduced even with varied process parameters. High mechanical bond strength comes along with high thermal diffusivity values, whereas liner segments showing low thermal diffusivity also deduce lowered bond strength. The presence of laterally orientated splat interfaces again determines the mechanical and thermal properties of the coatings even with varied process parameters. The defect morphology is found to be the crucial microstructural characteristic influencing the thermal and mechanical properties of thermally sprayed cylinder coatings. The introduced process variations have proven to significantly improve the coating microstructure, which result in an enhancement of the thermal diffusivity and bond strength of the tested coatings. By changing the mask geometry as well as the nitrogen content within the spraying atmosphere, the oxygen content is significantly reduced along the cylinder liner thus lowering in-flight oxidation of the spraying particles [9]. Consequently, thermal and mechanical properties are found to be enhanced in the upper and the lowest liner positions, while reference coatings reveal lower thermal and mechanical properties at the respective liner positions. Hence, the shown DoE proved the observed relation between thermal, mechanical and microstructural properties even for varied process parameters but also showed an improvement of the cylinder liner quality.

7. Summary and conclusions

The main emphasis of this work is to characterize laser-excited lock-in thermography as a non-destructive testing method to validate the bond strength of wire arc sprayed cylinder coatings. Bond strength testing of cylinder coatings is one crucial step in the quality control process of manufactured crankcases to guarantee its lifelong integrity and functionality for Mercedes-Benz combustion engines. Debonding of the cylinder coating during operation of the engine may cause a fatal breakdown of the entire powertrain due to the enhanced friction between the piston rings and the bared crankcase substrate material. So far, destructive off-site testing by Pull-off adhesion testing (PAT™) is applied in the large-scale production to assess the bond strength of the manufactured cylinder coatings. However, as an approach for increasing the efficiency of the large-scale production, a fast and reliable non-destructive testing method to quantify the coating bond strength is highly desired. Since the coating microstructures are known to strongly influence the mechanical properties of the cylinder coatings, assessing these coating microstructures non-destructively may open the ability to monitor the bond strength even without destructive testing. In this context, thermal wave interferometry (TWI) is chosen to assess the coatings' microstructures by measuring their thermal transport properties non-destructively using laser-excited lock-in thermography. Lock-in thermography is a non-destructive and contactless method showing a fast feedback loop to measure the thermal diffusivity of layered structures.

In order to characterize the cylinder coatings' thermophysical properties using laser-excited lock-in thermography, a reliable measurement setup is required. Lock-in thermography stands out showing high signal-to-noise ratios, fast measurement times and variable geometrical setups as one-side access to the measured specimen. Indeed, multiple measurement parameters need to be optimized to obtain a parameter setup delivering reliable and highly accurate thermal diffusivity results combined with fast measurement times. Thus, optimizing the laser spot size and power, the theoretical layer model function as well as the applied frequency spectrum and the resulting measurement times, thermal diffusivity measurements of cylinder bore coatings show a repeatability of more than $98\,\%$ by an overall measurement time of $60\,\mathrm{s}$. Further, comparison of TWI to conventional laser flash analysis (LFA) delivers convincing agreement between both methods. Whereas LFA is the standard method measuring thermal diffusivities, however it requires defined sample sizes as well as two side access to the sample thus disqualifying its application as a non-destructive testing method for cylinder coatings. In this context, laser-excited lock-in thermography proves to reliably measure the thermal

diffusivity of wire arc sprayed cylinder coatings non-destructively and contactless.

For the purpose of evaluating laser-excited lock-in thermography as a non-destructive testing method for the bond strength of cylinder bore coatings, an extended measurement study about their thermophysical and mechanical properties is performed. Thermal diffusivity measurements as well as destructive bond testings are acquired for four combustion engine crankcases resulting in overall 480 data pairs. The data is statistically analyzed regarding certain categories, whereas an analysis of variances (ANOVA) concludes that the position along the cylinder liners reveal statistically significant and dominant influences on both characteristics. Thermal diffusivity as well as bond strength vary strongly along the liner positions, while both properties increase from the cylinder head sealing surface downwards to peak at liner position 100 mm followed by a strong decline towards the crankshaft at 130 mm. A statistical correlation of 0.703 is observed by relating the individual thermal diffusivity values with the acquired bond strength measurements.

The observed correlation is induced by the coating microstructure and the related defect morphology, whereas laterally orientated splat interfaces appear to be dominant forming the coatings' defect structures. Quantitative microstructural analysis showed that laterally orientated splat interfaces strongly influence both thermal diffusivity and bond strength of the coating systems. Coating defects and impurities build up multiple thermal barriers orthogonally to the vertical heat conduction, revealing a direct correlation of the measured thermal diffusivity values and the observed coating defect morphology. Further, since coating defects are found to reduce the interlamellar cohesive bond strength of sprayed layers, the observed microstructure has also a dominant influence on the overall coating bond. Quantitative analysis of the fracture surface after bond testing allows to separate between adhesive and cohesive failure. This analysis indicates enhanced cohesive failure in the presence of laterally orientated splat interfaces in the coating, whereas rather adhesive failure is observed in absence of such defects. Conclusively, the strong correlation between thermal and mechanical properties of cylinder bore coatings founds on the underlying microstructure and the related defect morphology.

As the TWI method only assesses the integral coating composition, it allows to quantify the cohesive bond strength of the investigated samples. Still, singular defects at the coating substrate interface lowering the adhesive bond strength are not simply detectable by TWI. In this context, an additional measurement study about cylinder coatings with oily contaminated substrate interfaces is conducted. Here, oily substrate contamination cause overall lowered bond strength, whereas thermal diffusivity values are found on the same level as for non-contaminated coating systems. As the coating microstructures appear to be unaffected by the oily contamination, fracture analysis after PAT™ presents overall enhanced adhesive failure along the entire cylinder liners. The resulting correlation of thermal diffusivity to bond strength of contaminated coatings decreases to a correlation factor of 0.574. Thus, TWI is not able to reliably detect interface failure as it only reveals the integral coating formation and the related microstructure.

Further, since the integrity of the cylinder coatings founds on the underlying microstruc-

tures, an additional experimental study (Design of Experiment, DoE) about the applied process parameters during thermal spraying attempts to create dense coating structure without the presence of laterally orientated splat interfaces. As these defects are a consequence of oxidation of the spraying particles, lowering the oxygen content during the spraying process limits the development of lateral voids. Microstructural analysis proved, that the applied process variations cause improved coating microstructures, while laterally orientated splat interfaces can be drastically reduced. Thus, thermal diffusivity and bond strength measurements reveal that lowering the oxygen content within the spraying atmosphere leads to an effective increase of the thermophysical as well as mechanical properties. Here, thermal diffusivity and bond strength show strong correlation of up to 0.934.

Concluding the major findings of this work, correlations of the thermal diffusivity and the cohesive bond strength of wire arc sprayed cylinder coatings are observed. Laser-excited lock-in thermography allows to apply TWI to measure the thermal diffusivity of such cylinder coatings non-destructively and contactless. The correlation between coating bond and thermal diffusivity results from the observed coating microstructure, whereas laterally orientated splat interfaces primarily dominate both characteristics. However, as interface defects and resulting adhesive weaknesses cannot be determined by TWI measurements, entirely replacing the PAT™ by TWI might not be appropriate. Process variations resulting from the large-scale production lead to additional influencing factors weakening the adhesion mechanisms. Therefore, if process influences such as oily contamination of the substrate interface can be reduced to a minimum, TWI can provide a reliable measurement method determining the cohesive strength and subsequently the overall coating bonding behavior. TWI measurements show that the presence of laterally orientated splat interfaces causes reduced thermal diffusivity of the coating and cohesive bond. Thus, if low thermal diffusivities are measured by TWI, an overall low coating bond is always expected.

Additionally, one may also consider alternative methods to the applied PAT™ testing which might be sufficient to ensure the lifelong durability and functionality of the cylinder coatings. Since the coating microstructure has major influence on the mechanical properties of the coating, simply evaluating the defect morphology might yield an even more precise feature to characterize the coating quality. For sure, extended studies and cross references about the correlation between the integrity of the cylinder coatings and their coating microstructures would be necessary to define an alternative coating characteristic feature. However, as laser-excited lock-in thermography has proven to reliably assess the coating microstructures, this technique would open the ability to evaluate the functionality and durability of wire arc sprayed cylinder coatings non-destructively and contactless.

Bibliography

[1] J. König, M. Lahres, and O. Methner, "Quality designed twin wire arc spraying of aluminum bores," *Journal of Thermal Spray Technology*, vol. 24, no. 1-2, pp. 63–74, 2015.

[2] M. Schmidt, H. Spieth, J. Bauer, and C. Haubach, "Prozesskette NANOSLIDE®," *100 Betriebe für Ressourceneffizienz–Band 1*, pp. 234–237, 2017.

[3] J. Schommers, H. Scheib, M. Hartweg, and A. Bosler, "Reibungsminimierung bei Verbrennungsmotoren," *MTZ-Motortechnische Zeitschrift*, vol. 74, no. 7-8, pp. 566–573, 2013.

[4] M. Hahn and A. Fischer, "Characterization of thermal spray coatings for cylinder running surfaces of diesel engines," *Journal of Thermal Spray Technology*, vol. 19, no. 5, pp. 866–872, 2010.

[5] P. L. Fauchais, J. V. Heberlein, and M. I. Boulos, *Thermal Spray Fundamentals: From Powder to Part.* Springer Science & Business Media, New York, USA, 1 ed., 2014.

[6] I. Gedzevicius and A. Valiulis, "Analysis of wire arc spraying process variables on coatings properties," *Journal of Materials Processing Technology*, vol. 175, no. 1-3, pp. 206–211, 2006.

[7] S. Deshpande, S. Sampath, and H. Zhang, "Mechanisms of oxidation and its role in microstructural evolution of metallic thermal spray coatings - case study for Ni–Al," *Surface and Coatings Technology*, vol. 200, no. 18-19, pp. 5395–5406, 2006.

[8] L. Pawlowski and P. Fauchais, "Thermal transport properties of thermally sprayed coatings," *International Materials Reviews*, vol. 37, no. 1, pp. 271–289, 1992.

[9] B. Schilder, A. Garling, F. Reimer, M. Hamann, R. Joos, J. Hüger, M. Pöhlmann, and T. Lampke, "CFD enhanced thermal spray process for coating of cylinder bores of car engines," *Journal of Thermal Spray Technology*, vol. 29, pp. 546–559, 2020.

[10] Z. Wang, A. Kulkarni, S. Deshpande, T. Nakamura, and H. Herman, "Effects of pores and interfaces on effective properties of plasma sprayed zirconia coatings," *Acta Materialia*, vol. 51, no. 18, pp. 5319–5334, 2003.

[11] Y. Tan, J. P. Longtin, and S. Sampath, "Modeling thermal conductivity of thermal spray coatings: Comparing predictions to experiments," *Journal of Thermal Spray Technology*, vol. 15, no. 4, pp. 545–552, 2006.

[12] B. Schulz, "Thermal conductivity of porous and highly porous materials," *High Temperatures - High Pressures*, vol. 13, no. 6, pp. 649–660, 1981.

[13] F. Cernuschi, S. Ahmaniemi, P. Vuoristo, and T. Mäntylä, "Modelling of thermal conductivity of porous materials: Application to thick thermal barrier coatings," *Journal of the European Ceramic Society*, vol. 24, no. 9, pp. 2657–2667, 2004.

[14] R. McPherson, "A model for the thermal conductivity of plasma-sprayed ceramic coatings," *Thin Solid Films*, vol. 112, no. 1, pp. 89–95, 1984.

[15] S. Boire-Lavigne, C. Moreau, and R. Saint-Jacques, "The relationship between the microstructure and thermal diffusivity of plasma-sprayed tungsten coatings," *Journal of Thermal Spray Technology*, vol. 4, no. 3, pp. 261–267, 1995.

[16] S. Torquato, *Random Heterogeneous Materials: Microstructure and Macroscopic Properties*, vol. 16. Springer Science & Business Media, New York, USA, 1 ed., 2002.

[17] F. Cernuschi, P. Bison, and A. Moscatelli, "Microstructural characterization of porous thermal barrier coatings by laser flash technique," *Acta Materialia*, vol. 57, no. 12, pp. 3460–3471, 2009.

[18] R. Yang and Y. He, "Optically and non-optically excited thermography for composites: A review," *Infrared Physics & Technology*, vol. 75, pp. 26–50, 2016.

[19] W. Parker, R. Jenkins, C. Butler, and G. Abbott, "Flash method of determining thermal diffusivity, heat capacity, and thermal conductivity," *Journal of Applied Physics*, vol. 32, no. 9, pp. 1679–1684, 1961.

[20] A. Bento and D. Almond, "The accuracy of thermal wave interferometry for the evaluation of thermophysical properties of plasma-sprayed coatings," *Measurement Science and Technology*, vol. 6, no. 7, pp. 1022–1027, 1995.

[21] G. Busse, D. Wu, and W. Karpen, "Thermal wave imaging with phase sensitive modulated thermography," *Journal of Applied Physics*, vol. 71, no. 8, pp. 3962–3965, 1992.

[22] X. Maldague, *Theory and Practice of infrared Technology for nondestructive Testing*. Wiley Series in Microwave and Optical Engineering, John Wiley & Sons, Inc., New York, USA, 2001.

[23] D. Wu and G. Busse, "Lock-in thermography for nondestructive evaluation of materials," *Revue générale de thermique*, vol. 37, no. 8, pp. 693–703, 1998.

[24] C. Bennett and R. Patty, "Thermal wave interferometry: A potential application of the photoacoustic effect," *Applied Optics*, vol. 21, no. 1, pp. 49–54, 1982.

[25] K. Bobzin, F. Ernst, J. Zwick, T. Schlaefer, D. Cook, K. Nassenstein, A. Schwenk, F. Schreiber, T. Wenz, G. Flores, and M. Hahn, "Coating bores of light metal engine blocks with a nanocomposite material using the plasma transferred wire arc thermal spray process," *Journal of Thermal Spray Technology*, vol. 17, no. 3, pp. 344–351, 2008.

[26] V. S. Zolotorevsky, N. A. Belov, and M. V. Glazoff, *Casting aluminum alloys*, vol. 12. Elsevier Ltd., Amsterdam, The Netherlands, 1 ed., 2007.

[27] S. Lindemann, *Zerstörungsfreie Charakterisierung thermisch gespritzter Zylinderlauf-flächen.* Dissertation, Otto von Guericke Universiät Magdeburg, Germany, 2019.

[28] X. Wang, J. Heberlein, E. Pfender, and W. Gerberich, "Effect of nozzle configuration, gas pressure, and gas type on coating properties in wire arc spray," *Journal of Thermal Spray Technology*, vol. 8, no. 4, pp. 565–575, 1999.

[29] J. König, *Auslegung eines optimierten Lichtbogendrahtspritzprozesses für Zylinderlauf-bahnen von Verbrennungsmotoren.* Dissertation, TU Chemnitz, Germany, 2016.

[30] G. Jandin, H. Liao, Z. Feng, and C. Coddet, "Correlations between operating conditions, microstructure and mechanical properties of twin wire arc sprayed steel coatings," *Materials Science and Engineering: A*, vol. 349, no. 1-2, pp. 298–305, 2003.

[31] H.-D. Steffens and K. Nassenstein, "Influence of the spray velocity on arc-sprayed coating structures," *Journal of Thermal Spray Technology*, vol. 8, no. 3, pp. 454–460, 1999.

[32] C.-J. Li, G.-J. Yang, and C.-X. Li, "Development of particle interface bonding in thermal spray coatings: A review," *Journal of Thermal Spray Technology*, vol. 22, no. 2-3, pp. 192–206, 2013.

[33] C. Berndt and R. McPherson, "Fracture Mechanics Approach to the Adhesion of Flame and Plasma Sprayed Coatings.," *Transactions of the Institution of Engineers, Australia*, vol. ME6, no. 1, pp. 53–58, 1981.

[34] C.-J. Li, W.-Z. Wang, and Y. He, "Dependency of fracture toughness of plasma sprayed Al2O3 coatings on lamellar structure," *Journal of Thermal Spray Technology*, vol. 13, no. 3, pp. 425–431, 2004.

[35] R. McPherson, "A review of microstructure and properties of plasma sprayed ceramic coatings," *Surface and Coatings Technology*, vol. 39, pp. 173–181, 1989.

[36] A. Newbery and P. Grant, "Droplet splashing during arc spraying of steel and the effect on deposit microstructure," *Journal of Thermal Spray Technology*, vol. 9, no. 2, pp. 250–258, 2000.

[37] K. Tani, H. Nakahira, K. Miyajima, and Y. Harada, "Thermal and elastic anisotropy of thermally sprayed coatings," *Materials Transactions, JIM*, vol. 33, no. 6, pp. 618–626, 1992.

[38] D. Hu, X. Zheng, Y. Niu, H. Ji, F. Chong, and J. Chen, "Effect of oxidation behavior on the mechanical and thermal properties of plasma sprayed tungsten coatings," *Journal of Thermal Spray Technology*, vol. 17, no. 3, pp. 377–384, 2008.

[39] H. Yao, Z. Zhou, Y. Wang, D. He, K. Bobzin, L. Zhao, M. Öte, and T. Königstein, "Microstructure and properties of FeCrB alloy coatings prepared by wire-arc spraying," *Journal of Thermal Spray Technology*, vol. 26, no. 3, pp. 483–491, 2017.

[40] H. Yao, Z. Zhou, G. Wang, D. He, K. Bobzin, L. Zhao, M. Öte, and T. Königstein, "Influence of Feedstock Materials and Spray Parameters on Thermal Conductivity of Wire-Arc-Sprayed Coatings," *Journal of Materials Engineering and Performance*, vol. 26, no. 3, pp. 1108–1113, 2017.

[41] P. Fauchais, A. Vardelle, and B. Dussoubs, "Quo vadis thermal spraying?," *Journal of Thermal Spray Technology*, vol. 10, no. 1, pp. 44–66, 2001.

[42] M. Staia, E. Ramos, A. Carrasquero, A. Roman, J. Lesage, D. Chicot, and G. Mesmacque, "Effect of substrate roughness induced by grit blasting upon adhesion of WC-17% Co thermal sprayed coatings," *Thin Solid Films*, vol. 377, pp. 657–664, 2000.

[43] Y.-Y. Wang, C.-J. Li, and A. Ohmori, "Examination of factors influencing the bond strength of high velocity oxy-fuel sprayed coatings," *Surface and Coatings Technology*, vol. 200, no. 9, pp. 2923–2928, 2006.

[44] D. Greving, J. Shadley, and E. Rybicki, "Effects of coating thickness and residual stresses on the bond strength of ASTM C633-79 thermal spray coating test specimens," *Journal of Thermal Spray Technology*, vol. 3, no. 4, pp. 371–378, 1994.

[45] C. Lima and J. Guilemany, "Adhesion improvements of thermal barrier coatings with HVOF thermally sprayed bond coats," *Surface and Coatings Technology*, vol. 201, no. 8, pp. 4694–4701, 2007.

[46] R. Varavallo, M. Manfrinato, L. Rossino, O. Maluf, and F. Camargo, "Adhesion of Thermally Sprayed Metallic Coating," *Journal of ASTM International*, vol. 9, no. 2, pp. 559–573, 2012.

[47] A. Vencl, S. Arostegui, G. Favaro, F. Zivic, M. Mrdak, S. Mitrović, and V. Popovic, "Evaluation of adhesion/cohesion bond strength of the thick plasma spray coatings by scratch testing on coatings cross-sections," *Tribology International*, vol. 44, no. 11, pp. 1281–1288, 2011.

[48] L. Erickson, R. Westergård, U. Wiklund, N. Axen, H. Hawthorne, and S. Hogmark, "Cohesion in plasma-sprayed coatings — a comparison between evaluation methods," *Wear*, vol. 214, no. 1, pp. 30–37, 1998.

[49] G.-J. Yang, C.-J. Li, C.-X. Li, K. Kondoh, and A. Ohmori, "Improvement of adhesion and cohesion in plasma-sprayed ceramic coatings by heterogeneous modification of nonbonded lamellar interface using high strength adhesive infiltration," *Journal of Thermal Spray Technology*, vol. 22, no. 1, pp. 36–47, 2013.

[50] H. Liao, B. Normand, and C. Coddet, "Influence of coating microstructure on the abrasive wear resistance of WC/Co cermet coatings," *Surface and Coatings Technology*, vol. 124, no. 2-3, pp. 235–242, 2000.

[51] C. Berndt and R. McPherson, "The Adhesion of Plasma Sprayed Ceramic Coatings to Metals," in *Surfaces and Interfaces in Ceramic and Ceramic — Metal Systems* (J. Pask and A. Evans, eds.), pp. 619–628, Springer US, Boston, USA, 1981.

[52] D. Branagan, M. Breitsameter, B. Meacham, and V. Belashchenko, "High-performance nanoscale composite coatings for boiler applications," *Journal of Thermal Spray Technology*, vol. 14, no. 2, pp. 196–204, 2005.

[53] N. Zeoli, S. Gu, and S. Kamnis, "Numerical simulation of in-flight particle oxidation during thermal spraying," *Computers & Chemical Engineering*, vol. 32, no. 7, pp. 1661–1668, 2008.

[54] F. Cernuschi, P. Bison, S. Marinetti, A. Figari, L. Lorenzoni, and E. Grinzato, "Comparison of thermal diffusivity measurement techniques," *Quantitative InfraRed Thermography Journal*, vol. 28, pp. 211–221, 2002.

[55] J. B. J. Fourier, "Théorie du mouvement de la chaleur dans les corps solides," *Ire Paris Mémoires de l'Académie des Sci.*, vol. 4, pp. 185–555, 1824.

[56] C. Kittel, *Introduction to solid state physics.* John Wiley & Sons, Inc., New York, USA, 8 ed., 2005.

[57] S. Hunklinger, *Festkörperphysik.* Oldenbourg Verlag, München, Germany, 3 ed., 2011.

[58] T. M. Tritt, *Thermal conductivity: Theory, Properties, and Applications.* Kluwer Academic/Plenum Publishers, New York, USA, 1 ed., 2004.

[59] G. Mayr, B. Plank, J. Sekelja, and G. Hendorfer, "Active thermography as a quantitative method for non-destructive evaluation of porous carbon fiber reinforced polymers," *NDT & E International*, vol. 44, no. 7, pp. 537–543, 2011.

[60] H. I. Ringermacher and B. N. Cassenti, "Dethermalization theory: thermal/dielectric analogy for heat flow through porosity in composites," *Journal of Nondestructive Evaluation*, vol. 32, no. 4, pp. 418–422, 2013.

[61] W. Chi, *Thermal transport properties of thermally sprayed coatings: an integrated study of materials, processing and microstructural effects.* Dissertation, The Graduate School, Stony Brook University: Stony Brook, NY, USA, 2007.

[62] C.-J. Li and G.-J. Yang, "Relationships between feedstock structure, particle parameter, coating deposition, microstructure and properties for thermally sprayed conventional and nanostructured WC–Co," *International Journal of Refractory Metals and Hard Materials*, vol. 39, pp. 2–17, 2013.

[63] D.-I. Shin, F. Gitzhofer, and C. Moreau, "Thermal property evolution of metal based thermal barrier coatings with heat treatments," *Journal of Materials Science*, vol. 42, no. 15, pp. 5915–5923, 2007.

[64] R. E. Meredith and C. W. Tobias, "Conductivities in emulsions," *Journal of the Electrochemical Society*, vol. 108, no. 3, pp. 286–290, 1961.

[65] D. McLachlan, "An equation for the conductivity of binary mixtures with anisotropic grain structures," *Journal of Physics C: Solid State Physics*, vol. 20, no. 7, pp. 865–877, 1987.

[66] J. N. Zalameda and W. P. Winfree, "Thermal diffusivity measurements on composite porosity samples," in *Review of progress in quantitative nondestructive evaluation* (D. O. Thompson and D. E. Chimenti, eds.), pp. 1541–1548, Springer US, Boston, USA, 1990.

[67] G. Mayr, *Charakterisierung von porösen carbonfaserverstärkten Kunststoffbauteilen mit optisch angeregter Puls-Thermografie.* Dissertation, Johannes Kepler Universität, Linz, Austria, 2016.

[68] J. C. Maxwell, *A treatise on electricity and magnetism*, vol. 1. Clarendon Press, Oxford, UK, 1873.

[69] L. Rayleigh, "LVI. On the influence of obstacles arranged in rectangular order upon the properties of a medium," *The London, Edinburgh, and Dublin Philosophical Magazine and Journal of Science*, vol. 34, no. 211, pp. 481–502, 1892.

[70] D. A. G. Bruggeman, "Berechnung verschiedener physikalischer konstanten von heterogenen Substanzen. I. Dielektrizitätskonstanten und Leitfähigkeiten der Mischkörper aus isotropen Substanzen," *Annalen der Physik*, vol. 416, no. 7, pp. 636–664, 1935.

[71] W. Niesel, "Die Dielektrizitätskonstanten heterogener Mischkörper aus isotropen und anisotropen Substanzen," *Annalen der Physik*, vol. 445, no. 6-7, pp. 336–348, 1952.

[72] U. Stille, "Der Entmagnetisierungsfaktor und Entelektrisierungsfaktor für Rotationsellipsoide," *Archiv für Elektrotechnik*, vol. 38, no. 3-4, pp. 91–101, 1944.

[73] H. Fricke, "A mathematical treatment of the electric conductivity and capacity of disperse systems," *Physical Review*, vol. 24, no. 5, pp. 678–681, 1924.

[74] H. Ringermacher, D. Howard, and R. Gilmore, "Discriminating porosity in composites using thermal depth imaging," *AIP conference proceedings*, vol. 615, no. 1, pp. 528–535, 2002.

[75] F. P. Bowden and D. Tabor, *The friction and lubrication of solids.* Oxford University Press, Oxford, UK, 1 ed., 1950.

[76] I. Golosnoy, S. Tsipas, and T. Clyne, "An analytical model for simulation of heat flow in plasma-sprayed thermal barrier coatings," *Journal of Thermal Spray Technology*, vol. 14, no. 2, pp. 205–214, 2005.

[77] W. Chi, S. Sampath, and H. Wang, "Microstructure-Thermal Conductivity Relationships for Plasma-Sprayed Yttria-Stabilized Zirconia Coatings," *Journal of the American Ceramic Society*, vol. 91, no. 8, pp. 2636–2645, 2008.

[78] F. Cernuschi, A. Figari, and L. Fabbri, "Thermal wave interferometry for measuring the thermal diffusivity of thin slabs," *Journal of Materials Science*, vol. 35, no. 23, pp. 5891–5897, 2000.

[79] L. Vozár and W. Hohenauer, "Flash method of measuring the thermal diffusivity. A review," *High Temperatures - High Pressures*, vol. 36, no. 3, pp. 253–264, 2004.

[80] G. Busse, "Optoacoustic phase angle measurement for probing a metal," *Applied Physics Letters*, vol. 35, no. 10, pp. 759–760, 1979.

[81] O. Breitenstein, W. Warta, and M. C. Schubert, *Lock-in Thermography: Basics and Use for Evaluating Electronic Devices and Materials*, vol. 10. Springer, Berlin, Germany, 2 ed., 2019.

[82] J. Arbogast, R. Schaller, S. Lindemann, B. Schilder, M. Rohde, and H. J. Seifert, "Thermal wave interferometry measurements and microstructural analysis of twin wire arc spray cylinder coatings for passenger car engines," *Infrared Physics & Technology*, vol. 105, p. 103216, 2020.

[83] A. Bendada, M. Lamontagne, and H. Roberge, "Influence of thermal properties on the sensitivity of thermal wave interferometry for the characterization of plasma-sprayed coatings," *International Journal of Thermophysics*, vol. 24, no. 1, pp. 207–222, 2003.

[84] D. Wu, *Lockin-Thermographie für die zerstörungsfreie Werkstoffprüfung und Werkstoffcharakterisierung.* Dissertation, Universität Stuttgart, Germany, 1996.

[85] A. Rosencwaig and A. Gersho, "Theory of the photoacoustic effect with solids," *Journal of Applied Physics*, vol. 47, no. 1, pp. 64–69, 1976.

[86] P. Patel and D. Almond, "Thermal wave testing of plasma-sprayed coatings and a comparison of the effects of coating microstructure on the propagation of thermal and ultrasonic waves," *Journal of Materials Science*, vol. 20, no. 3, pp. 955–966, 1985.

[87] D. Almond, P. Patel, I. Pickup, and H. Reiter, "An evaluation of the suitability of thermal wave interferometry for the testing of plasma sprayed coatings," *NDT International*, vol. 18, no. 1, pp. 17–24, 1985.

[88] J. H. Scofield, "Frequency-domain description of a lock-in amplifier," *American Journal of Physics*, vol. 62, no. 2, pp. 129–133, 1994.

[89] F. Cernuschi, I. Golosnoy, P. Bison, A. Moscatelli, R. Vassen, H.-P. Bossmann, and S. Capelli, "Microstructural characterization of porous thermal barrier coatings by IR gas porosimetry and sintering forecasts," *Acta Materialia*, vol. 61, no. 1, pp. 248–262, 2013.

[90] P. Scardi, M. Leoni, F. Cernuschi, and A. Figari, "Microstructure and heat transfer phenomena in ceramic thermal barrier coatings," *Journal of the American Ceramic Society*, vol. 84, no. 4, pp. 827–835, 2001.

[91] A. G. Bell, "ART. XXXIV.- On the Production and Reproduction of Sound by Light," *American Journal of Science (1880-1910)*, vol. 20, no. 118, p. 305, 1880.

[92] W. C. Röntgen, "On tones produced by the intermittent irradiation of a gas," *The London, Edinburgh, and Dublin Philosophical Magazine and Journal of Science*, vol. 11, no. 68, pp. 308–311, 1881.

[93] J. Tyndall, "Action of an intermittent beam of radiant heat upon gaseous matter," *Proceedings of the Royal Society of London*, vol. 31, no. 206-211, pp. 307–317, 1881.

[94] G. Busse, "From photothermal radiometry to lock-in thermography methods," *Journal of Physics: Conference Series*, vol. 214, no. 1, p. 012003, 2010.

[95] C. Spießberger, *Merkmalsanalyse mit thermischen Wellen in der zerstörungsfreien Werkstoff- und Bauteilprüfung.* Dissertation, Universiät Stuttgart, Germany, 2012.

[96] W. Karpen, *Berührungslose und zerstörungsfreie Prüfung von Kunststofflackierungen mit thermischen Wellen.* Dissertation, Universität Stuttgart, Germany, 1993.

[97] J. Garcia, A. Mandelis, B. Farahbakhsh, C. Lebowitz, and I. Harris, "Thermophysical properties of thermal sprayed coatings on carbon steel substrates by photothermal radiometry," *International Journal of Thermophysics*, vol. 20, no. 5, pp. 1587–1602, 1999.

[98] A. Bendada, N. Baddour, A. Mandelis, and C. Moreau, "Experimental investigation on the reliability of thermal wave interferometry in the thermophysical characterization of plasma sprayed coatings," *International Journal of Thermophysics*, vol. 26, no. 3, pp. 881–892, 2005.

[99] L. Fabbri and F. Cernuschi, "Finite laser beam size effects in thermal wave interferometry," *Journal of Applied Physics*, vol. 82, no. 11, pp. 5305–5311, 1997.

[100] M. Luukkala, A. Lehto, J. Jaarinen, and M. Jokinen, "Photothermal imaging and thermal surface waves as a NDT tool for coatings," *1982 Ultrasonics Symposium, IEEE Transactions on Sonics and Ultrasonics, San Diego, USA*, vol. 30, no. 3, pp. 591–594, 1982.

[101] L. Fabbri and P. Fenici, "Three-dimensional photothermal radiometry for the determination of the thermal diffusivity of solids," *Review of Scientific Instruments*, vol. 66, no. 6, pp. 3593–3600, 1995.

[102] J. Arbogast, R. Schaller, M. Rohde, and H. J. Seifert, "Thermal wave interferometry measurements correlated to microstructural properties and bonding behavior of thermally sprayed coatings," *Surface and Coatings Technology*, vol. 402, p. 126298, 2020.

[103] R. D. Cowan, "Proposed method of measuring thermal diffusivity at high temperatures," *Journal of Applied Physics*, vol. 32, no. 7, pp. 1363–1370, 1961.

[104] J. Cape and G. Lehman, "Temperature and finite pulse-time effects in the flash method for measuring thermal diffusivity," *Journal of Applied Physics*, vol. 34, no. 7, pp. 1909–1913, 1963.

[105] J. Blumm and J. Opfermann, "Improvement of the mathematical modeling of flash measurements," *High Temperatures - High Pressures*, vol. 34, no. 5, pp. 515–521, 2002.

[106] T. Baba and A. Ono, "Improvement of the laser flash method to reduce uncertainty in thermal diffusivity measurements," *Measurement Science and Technology*, vol. 12, no. 12, pp. 2046–2057, 2001.

[107] H. J. Lee, *Thermal Diffusivity in layered and dispersed composites.* Dissertation, Purdue University, West Lafayette, USA, 1975.

[108] T. Lee, A. Donaldson, and R. Taylor, "Thermal diffusivity of layered composites," in *Thermal Conductivity 15*, pp. 135–148, Editior: V. Mirkovich, Springer, Boston, USA, 1978.

[109] J. Hartmann, O. Nilsson, and J. Fricke, "Thermal diffusivity measurements on two-layered and three-layered systems with the laser-flash method," *High Temperatures - High Pressures*, vol. 25, no. 4, pp. 403–410, 1993.

[110] "*DIN EN ISO 4624:2016-08*: Paints and varnishes - Pull-off test for adhesion." Norm, 2016. Beuth Verlag, Berlin, Germany.

[111] "*ASTM D 4541:2017*: Standard Test Method for Pull-Off Strength of Coatings Using Portable Adhesion Testers." Norm, 2017. Beuth Verlag, Berlin, Germany.

[112] "*DIN EN 24624:1992-09*: Products and systems for the protection and repair of concrete structures - test methods - measurement of bond strength by pull-off." Norm, 1992. Beuth Verlag, Berlin, Germany.

[113] "*DIN EN ISO 14916:2017-08*: Thermal spraying - determination of tensile adhesive strength." Norm, 2017. Beuth Verlag, Berlin, Germany.

[114] G. F. Vander Voort, S. R. Lampman, B. R. Sanders, G. J. Anton, C. Polakowski, J. Kinson, K. Muldoon, S. D. Henry, and W. W. Scott Jr, *ASM Handbook Volume 9: Metallography and Microstructures*. ASM International, Materials Park, USA, 1 ed., 2004.

[115] K. Geels, D. B. Fowler, W.-U. Kopp, and M. Rückert, *Metallographic and Materialographic Specimen Preparation, Light Microscopy, Image Analysis, and Hardness Testing*, vol. 46. ASTM International, West Conshohocken, USA, 2007.

[116] C. Ronse and P. Denjiver, *Connected Components in Binary Images: The Detection Problem*. John Wiley & Sons, Inc., New York, USA, 1 ed., 1984.

[117] R. Kramme, K.-P. Hoffmann, and R. S. Pozos, *Springer Handbook of Medical Technology*. Springer-Verlag, Berlin, Heidelberg, Germany, 1 ed., 2011.

[118] J. Banhart, *Advanced tomographic methods in materials research and engineering*. Oxford University Press, Oxford, UK, 1 ed., 2008.

[119] G. T. Herman, *Fundamentals of computerized tomography: Image Reconstruction from Projections*. Springer, London, UK, 2 ed., 2009.

[120] S. Pickering and D. Almond, "Matched excitation energy comparison of the pulse and lock-in thermography NDE techniques," *NDT & E International*, vol. 41, no. 7, pp. 501–509, 2008.

[121] C. Wallbrink, S. Wade, and R. Jones, "The effect of size on the quantitative estimation of defect depth in steel structures using lock-in thermography," *Journal of Applied Physics*, vol. 101, no. 10, p. 104907, 2007.

[122] R. Krankenhagen, M. Ziegler, and C. Maierhofer, "Systematic errors in the evaluation of uncorrected data from thermographic lock-in measurements," *Conference Proceedings QIRT 2018*, pp. 539–547, 2018.

[123] A. Gleiter, C. Spießberger, and G. Busse, "Phase angle thermography for depth resolved defect characterization," *AIP Conference Proceedings*, vol. 1096, no. 1, pp. 526–532, 2009.

[124] W. Bai and B. Wong, "Photothermal models for lock-in thermographic evaluation of plates with finite thickness under convection conditions," *Journal of Applied Physics*, vol. 89, no. 6, pp. 3275–3282, 2001.

[125] S. Quek, D. Almond, L. Nelson, and T. Barden, "A novel and robust thermal wave signal reconstruction technique for defect detection in lock-in thermography," *Measurement Science and Technology*, vol. 16, no. 5, pp. 1223–1233, 2005.

[126] J. Fox, *Applied regression analysis and generalized linear models.* Sage Publications, Thousand Oaks, USA, 3 ed., 2015.

[127] L. Yao, S. Qing-Lin, and X. Shan-Hong, "Calculation of specific heat for aluminium thin films," *Chinese Physics Letters*, vol. 22, no. 9, pp. 2346–2348, 2005.

[128] F. Richter, "Die physikalischen Eigenschaften der Stähle, „Das 100 - Stähle - Programm" Teil I: Tafeln und Bilder," *Abschlussbericht Arbeitskreis Thermophysik in der GEFTA: Berlin, Germany*, 2010.

[129] L. Fahrmeir, A. Hamerle, and G. Tutz, *Multivariate statistische Verfahren.* Walter de Gruyter GmbH & Co KG, Berlin, Germany, 2 ed., 1996.

[130] L. Fahrmeir, C. Heumann, R. Künstler, I. Pigeot, and G. Tutz, *Statistik: Der Weg zur Datenanalyse.* Springer, Berlin, Heidelberg, Germany, 6 ed., 2016.

[131] B. G. Tabachnick and L. S. Fidell, *Experimental designs using ANOVA.* Thomson/Brooks/Cole, Belmont, USA, 1 ed., 2007.

[132] W. H. Kruskal and W. A. Wallis, "Use of ranks in one-criterion variance analysis," *Journal of the American statistical Association*, vol. 47, no. 260, pp. 583–621, 1952.

[133] E. Neubauer, G. Korb, C. Eisenmenger-Sittner, H. Bangert, S. Chotikaprakhan, D. Dietzel, A. Mansanares, and B. Bein, "The influence of mechanical adhesion of copper coatings on carbon surfaces on the interfacial thermal contact resistance," *Thin Solid Films*, vol. 433, no. 1-2, pp. 160–165, 2003.

[134] E. Neubauer, S. Chotikaprakhan, D. Dietzel, B. Bein, J. Pelzl, C. Eisenmenger-Sittner, C. Schrank, and G. Korb, "Loss of adhesion strength of PVD Cu films on carbon substrates after heat treatment and correlated effects on the thermal interface properties," *Applied Surface Science*, vol. 252, no. 15, pp. 5432–5436, 2006.

[135] J. Pelzl, S. Chotikaprakhan, D. Dietzel, B. Bein, E. Neubauer, and M. Chirtoc, "The thermal contact problem in nano-and micro-scale photothermal measurements," *The European Physical Journal Special Topics*, vol. 153, no. 1, pp. 335–342, 2008.

[136] J. Wang, C.-J. Li, G.-J. Yang, and C.-X. Li, "Effect of oxidation on the bonding formation of plasma-sprayed stainless steel splats onto stainless steel substrate," *Journal of Thermal Spray Technology*, vol. 26, no. 1-2, pp. 47–59, 2017.

[137] "*DE 10 2018 007 559 A1*." Patent/Offenlegungsschrift, 2018.

Appendix

A. Characteristics of laser-excited lock-in thermography setup

A.1. Data sheet of the used infrared camera FLIR X6580 sc

Table A.1.: Detailed data sheet of the infrared camera FLIR x6580 sc

Detector type	Digital focal plane array
Sensor material	InSb
IR resolution	640×520
Detector pitch	$15\,\mu m$
Maximum image frequency	$355\,Hz$
Maximum frame rate at subwindow	$670\,Hz\ @\ 320 \times 256$
Integration time range	$500\,ns - 20000\,\mu s$
Cooler type	Closed-cycle Stirling cooler
Cooling temperature	$77\,K$
Weight	$4.8\,kg$
Spectral range	$1.5 - 5.5\,\mu m$
Thermal sensitivity	$< 25\,mK$
Temperature measurement accuracy	$\pm 1°C$ or $\pm 1\,\%$
Maximum temperature without filter	$300°C$

A.2. Repeatability of TWI phase measurements

A repeatability study of TWI measurements on thermally sprayed cylinder coatings allows to estimate the standard deviation of the phase measurements for different frequencies. Thus, two different positions along a cylinder liner are measured 30 times (two days, 15 measurements per day) at frequencies $5, 6, 10, 12, 15, 20, 25, 30, 40, 50, 60, 75, 100, 120, 150\,Hz$. Between each individual measurement the sample is cooled down for $300\,s$. The calculated standard deviations of the phase measurements are shown over the respective frequencies in Figure A.1. Due to the linear behavior of the obtained standard deviations, a linear regression is used to calculate the resulting standard deviations of phase measurements based on the repeatability study.
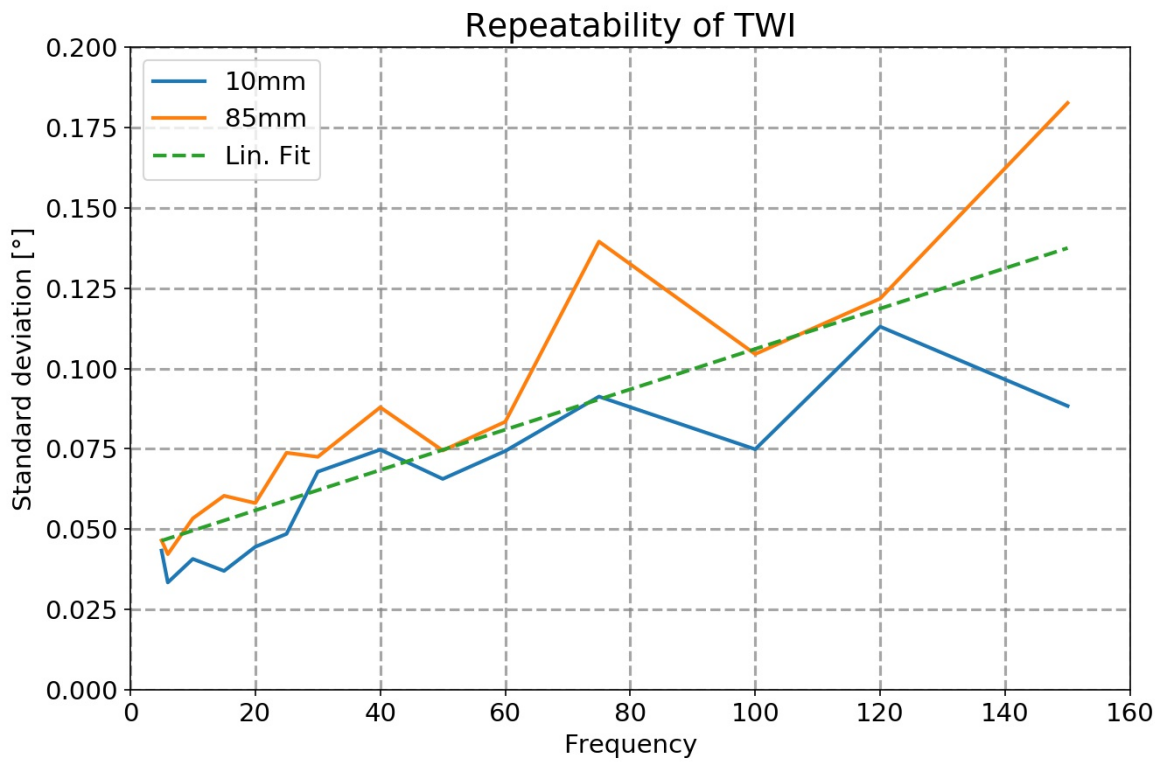
Figure A.1.: Repeatability study of TWI phase measurements for various excitation frequencies.

B. Additional parameter study of TWI measurements

Laser spot diameter
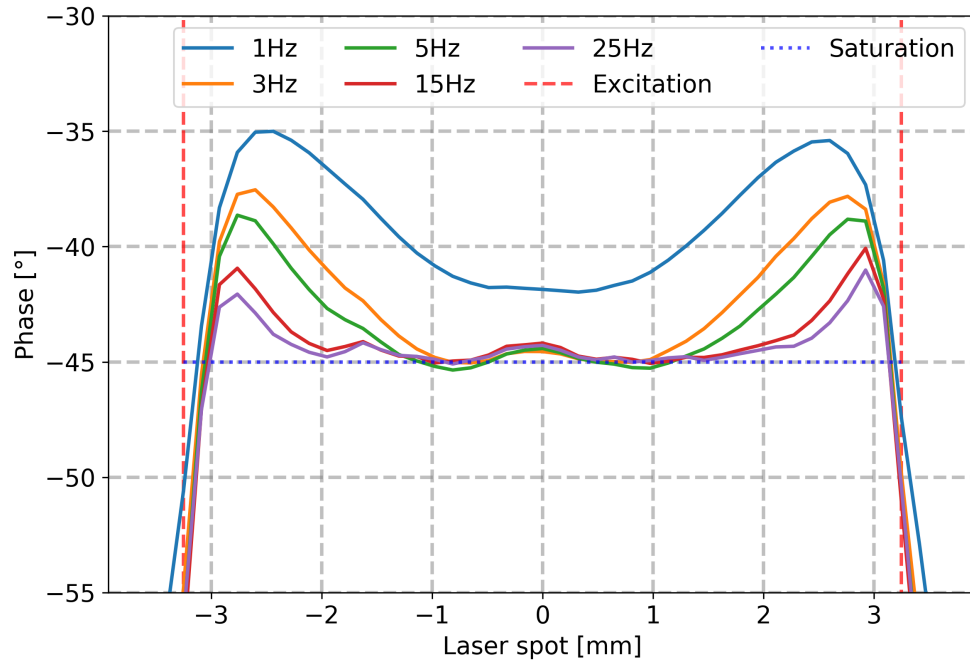
Figure B.2.: Sample 1.4301: Cross section through phase images for varying modulation frequency. The excited laser spot diameter of 6.5 mm is represented by the vertical red lines.
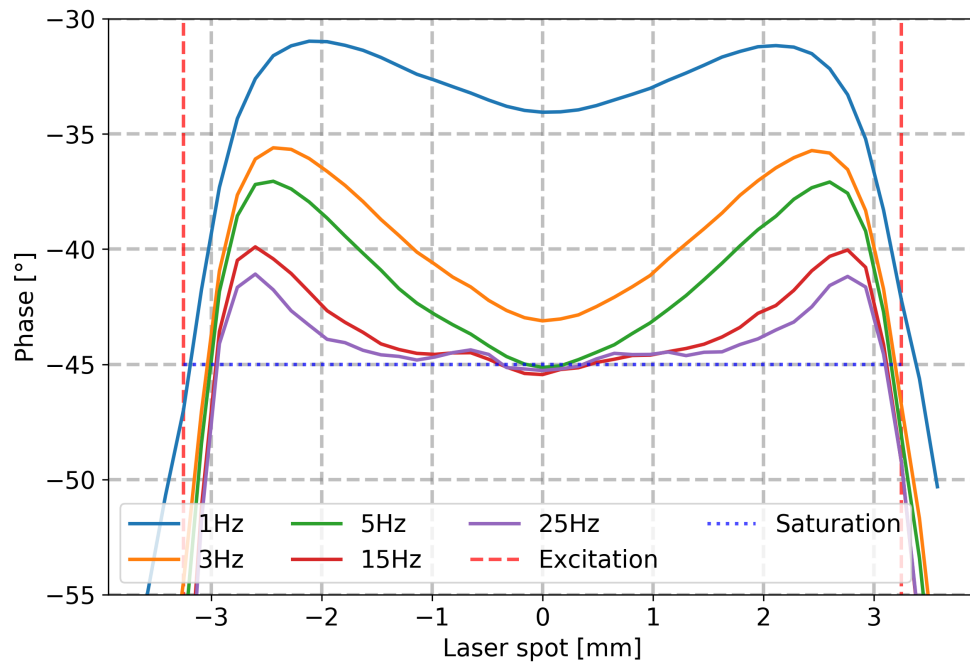
Figure B.3.: Sample 1.7225: Cross section through phase images for varying modulation frequency. The excited laser spot diameter of 6.5 mm is represented by the vertical red lines.
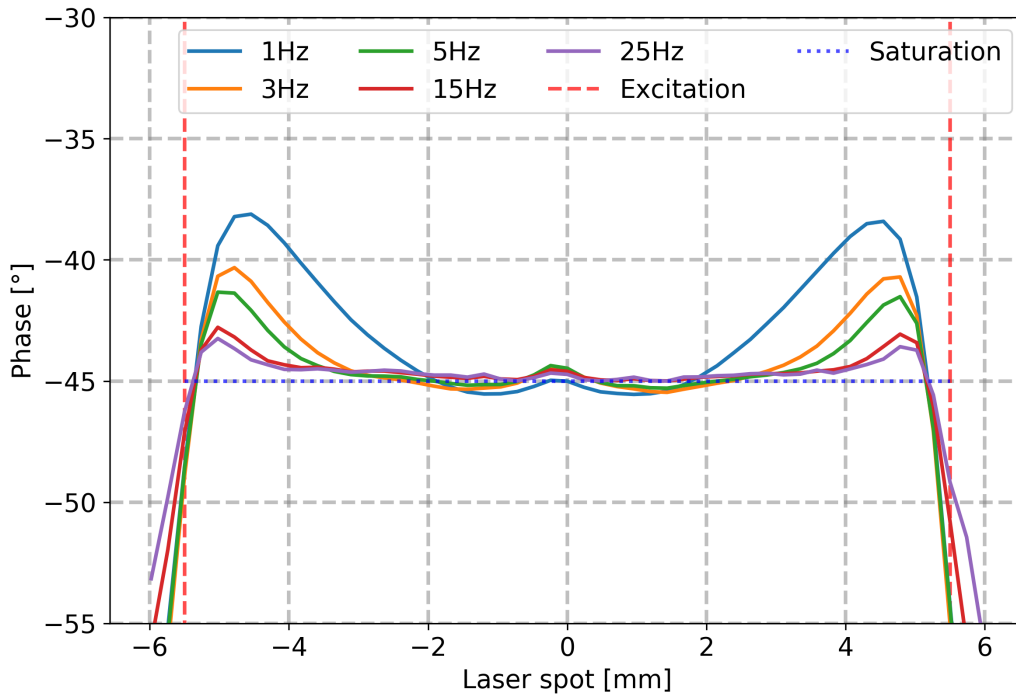
Figure B.4.: Sample 1.4301: Cross section through phase images for varying modulation frequency. The excited laser spot diameter of 11 mm is represented by the vertical red lines.
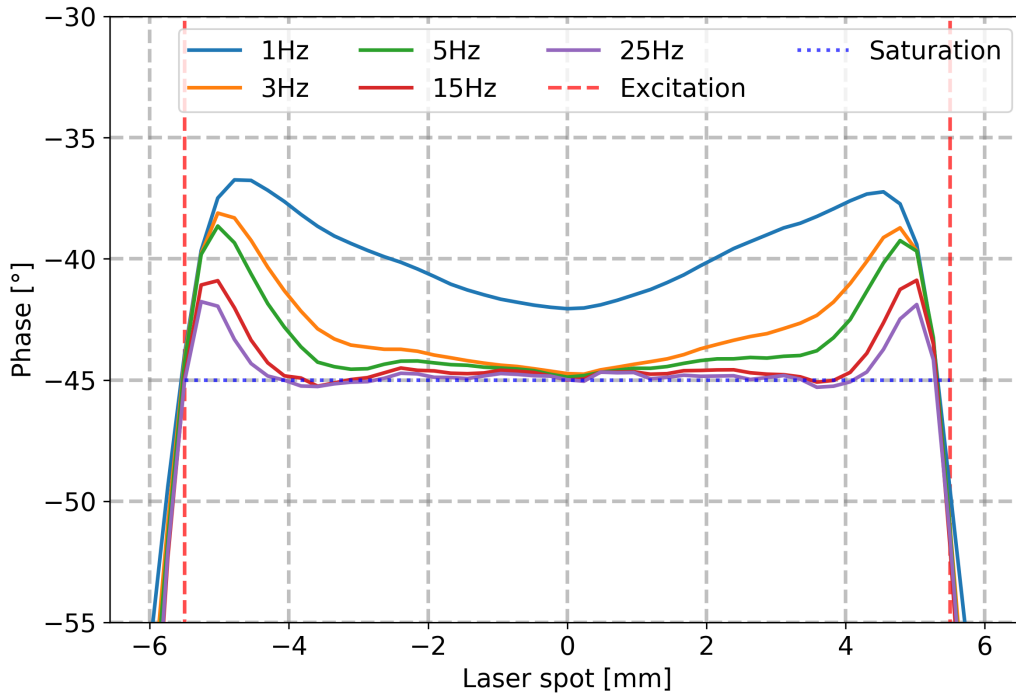
Figure B.5.: Sample 1.7225: Cross section through phase images for varying modulation frequency. The excited laser spot diameter of 11 mm is represented by the vertical red lines.
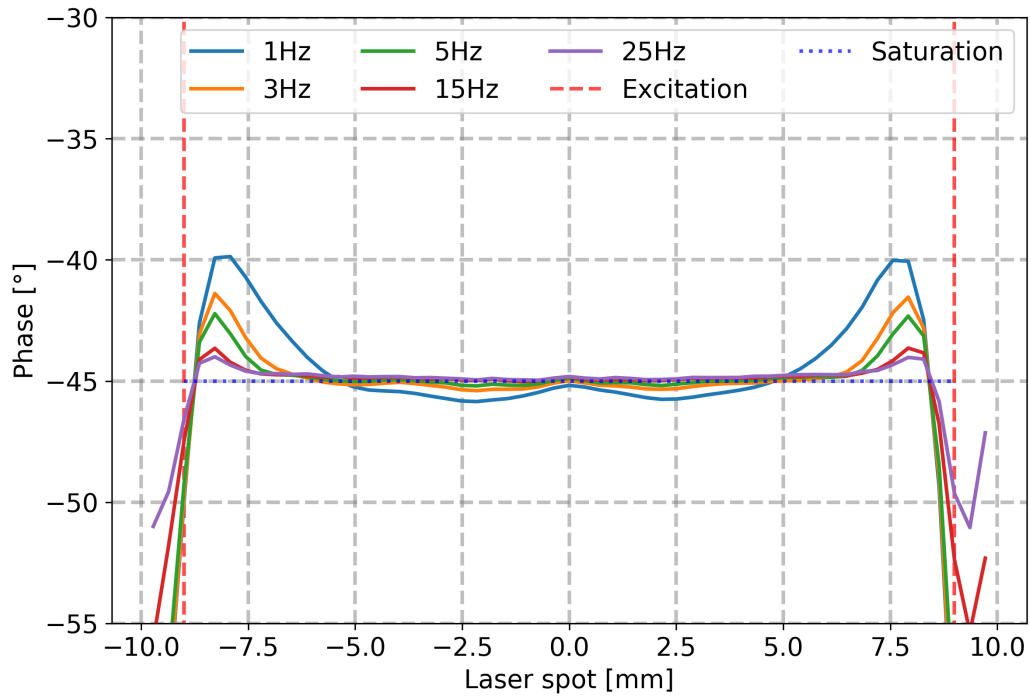
Figure B.6.: Sample 1.4301: Cross section through phase images for varying modulation frequency. The excited laser spot diameter of 18 mm is represented by the vertical red lines.
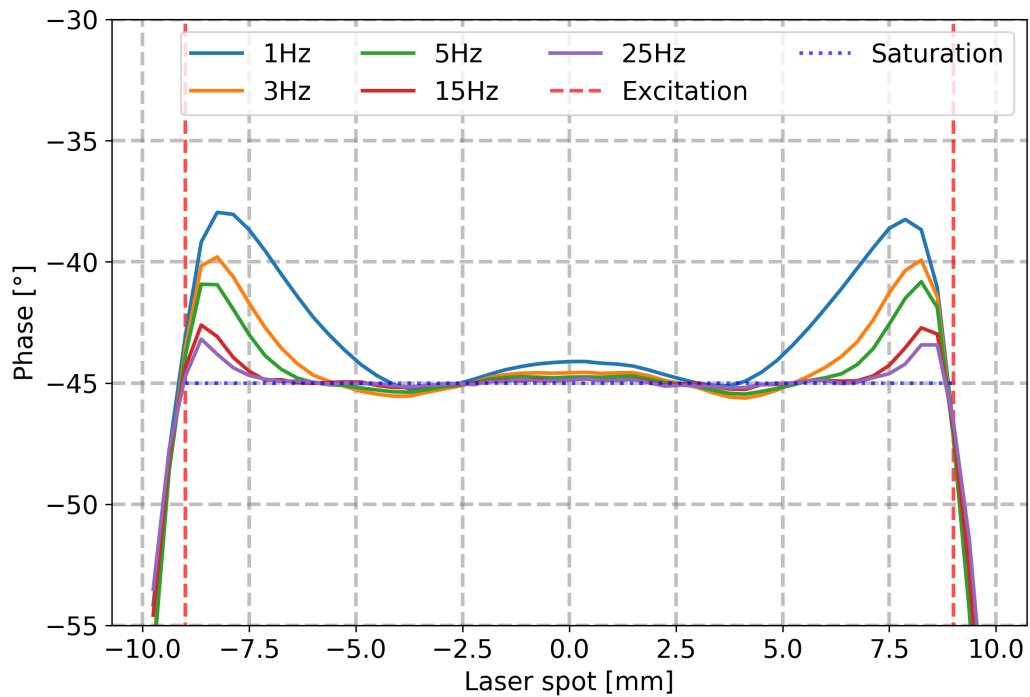
Figure B.7.: Sample 1.7225: Cross section through phase images for varying modulation frequency. The excited laser spot diameter of 18 mm is represented by the vertical red lines.

C. Measurement data of serial coating study

C.1. Additional fitting parameters of the TWI study

Table C.2.: ANOVA results of TWI measurements. SoS represents the sum of squares for the different categories, DF are the degrees of freedom, F is the F-value of the Fischer distribution, P presents the probability that the null hypothesis is correct. The significance level is set to 0.05. Further cont. ratio stands for the contribution ratio thus being calculated from the resulting sum of squares.

Parameter	Category	SoS	DF	F	P	Cont. ratio [%]
R	Crankcase	0.021	3	15.1	$2.2\,\mathrm{e}-9$	1.7
	Cylinder	0.030	5	12.7	$1.3\,\mathrm{e}-11$	2.4
	Angle	0.200	3	141.4	$4.8\,\mathrm{e}-65$	15.6
	Liner	0.805	4	427.0	$8.0\,\mathrm{e}-154$	63.2
	Residuals	0.218	463			17.1
C	Crankcase	48.78	3	47.8	$6.4\,\mathrm{e}-27$	16.2
	Cylinder	14.19	5	8.3	$8.3\,\mathrm{e}-7$	4.7
	Angle	14.31	3	14.0	$9.2\,\mathrm{e}-9$	4.7
	Liner	66.93	4	49.2	$1.8\,\mathrm{e}-34$	22.2
	Residuals	157.57	463			52.2

Table C.3.: TWI measurements of thermally sprayed cylinder coatings along the cylinder liner position.

	10 mm	40 mm	70 mm	100 mm	130 mm
Median R	-0.395	-0.380	-0.313	-0.289	-0.314
Lower quart. R	-0.427	-0.403	-0.333	-0.304	-0.339
Upper quart. R	-0.357	-0.357	-0.293	-0.270	-0.286
Median C [°]	46.01	45.98	45.13	45.09	45.35
Lower quart. C [°]	45.51	45.48	44.82	44.83	44.86
Upper quart. C [°]	46.69	46.31	45.69	45.55	46.02
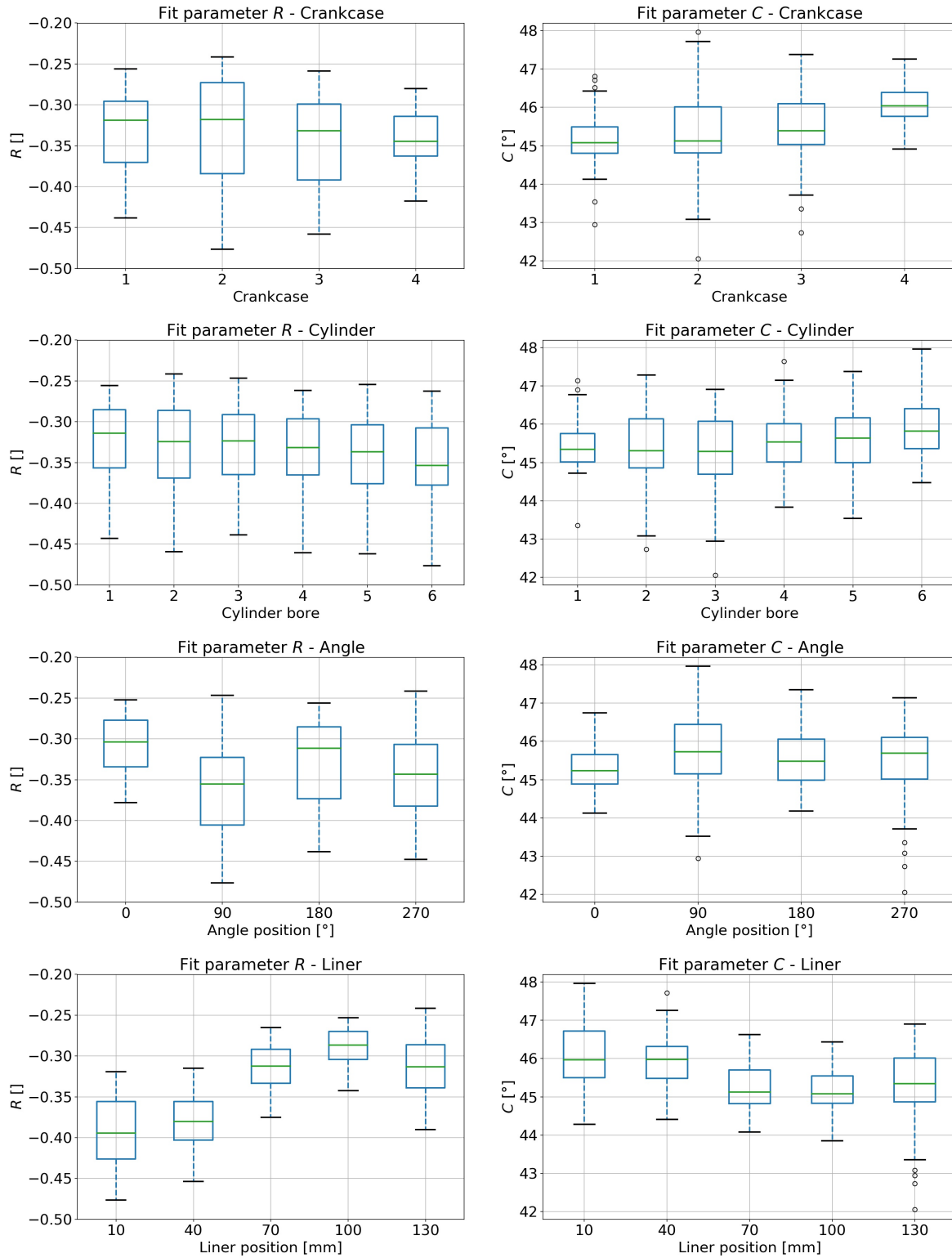
Figure C.8.: Fitting parameter R and C of the TWI measurements with respect to the individual crankcases, cylinder bores, angle positions and liner positions. All shown plots include 480 individual data points. Boxplots: The green lines represent the medians of the underlying data; boxes indicate the upper/lower quartile; the whiskers are set to a maximum of $1.5\times$ the interquartile range. Circles mark data outside the whiskers.

C.2. Raw data of the TWI and PAT™ studies

Table C.4.: Measurement data of the TWI and PAT™ studies used for the ANOVA in Chapters 5.2 and 5.3.

Crankcase	Cylinder bore	Angle pos. [°]	Liner pos. [mm]	R	η [1/s]	C [°]	d [μm]	PAT [MPa]	α [mm²/s]
1	1	0	10	-0.328	0.187	44.8	249.1	42.6	5.55
1	1	0	40	-0.334	0.192	45.0	254.3	40.4	5.52
1	1	0	70	-0.276	0.153	44.7	238.1	58.5	7.63
1	1	0	100	-0.277	0.139	45.3	239.3	61.4	9.28
1	1	0	130	-0.272	0.160	45.2	240.0	30.3	7.10
1	1	90	10	-0.408	0.195	45.4	222.9	33.9	4.11
1	1	90	40	-0.390	0.198	45.5	238.4	39.7	4.54
1	1	90	70	-0.314	0.164	45.2	244.6	45.5	6.96
1	1	90	100	-0.309	0.154	45.2	245.6	70.0	8.01
1	1	90	130	-0.334	0.206	45.1	248.3	33.9	4.57
1	1	180	10	-0.388	0.200	45.5	235.1	34.7	4.35
1	1	180	40	-0.348	0.202	45.0	255.8	36.8	5.05
1	1	180	70	-0.280	0.159	44.8	267.2	57.8	8.92
1	1	180	100	-0.276	0.156	45.2	275.4	65.3	9.78
1	1	180	130	-0.296	0.204	45.5	283.8	33.6	6.06
1	1	270	10	-0.397	0.195	45.9	226.6	33.2	4.24
1	1	270	40	-0.382	0.194	45.4	239.7	35.4	4.77
1	1	270	70	-0.303	0.167	45.0	248.9	46.6	6.96
1	1	270	100	-0.292	0.153	44.9	255.3	63.5	8.72
1	1	270	130	-0.305	0.201	45.0	276.1	32.1	5.95
1	2	0	10	-0.322	0.190	44.5	251.5	42.6	5.48
1	2	0	40	-0.315	0.187	44.4	249.3	41.9	5.57
1	2	0	70	-0.273	0.163	44.6	245.9	52.0	7.15
1	2	0	100	-0.264	0.144	44.9	248.0	50.5	9.31
1	2	0	130	-0.273	0.168	45.3	249.8	39.7	6.97
1	2	90	10	-0.395	0.191	45.1	219.1	35.7	4.14
1	2	90	40	-0.383	0.188	45.1	237.0	39.0	4.99
1	2	90	70	-0.316	0.165	44.8	239.0	51.3	6.61
1	2	90	100	-0.309	0.151	45.2	244.0	57.0	8.17
1	2	90	130	-0.333	0.197	44.6	247.7	37.2	4.95
1	2	180	10	-0.386	0.205	45.6	245.1	36.8	4.50
1	2	180	40	-0.368	0.205	45.4	258.9	42.2	5.02
1	2	180	70	-0.284	0.168	44.8	262.6	48.7	7.71
1	2	180	100	-0.272	0.155	44.9	270.0	67.1	9.52
1	2	180	130	-0.287	0.211	45.0	286.6	30.3	5.77
1	2	270	10	-0.379	0.184	45.2	216.3	39.7	4.34
1	2	270	40	-0.372	0.196	44.9	242.0	36.8	4.77
1	2	270	70	-0.314	0.174	44.8	246.1	44.8	6.27
1	2	270	100	-0.302	0.156	45.2	257.9	64.3	8.54
1	2	270	130	-0.319	0.201	45.4	271.0	36.1	5.74
1	3	0	10	-0.319	0.195	44.6	262.0	36.8	5.65
1	3	0	40	-0.320	0.200	44.5	260.5	35.4	5.35
1	3	0	70	-0.286	0.170	44.7	256.1	59.9	7.14
1	3	0	100	-0.270	0.145	45.0	253.7	62.1	9.56
1	3	0	130	-0.300	0.183	45.5	255.7	26.7	6.14
1	3	90	10	-0.386	0.180	44.6	215.3	39.0	4.47
1	3	90	40	-0.385	0.193	45.3	231.7	37.9	4.53
1	3	90	70	-0.321	0.167	44.8	239.1	49.5	6.47
1	3	90	100	-0.298	0.155	44.8	247.7	64.6	7.99
1	3	90	130	-0.314	0.208	42.9	253.1	37.9	4.66
1	3	180	10	-0.378	0.188	45.1	222.3	38.6	4.38
1	3	180	40	-0.370	0.197	45.5	243.7	41.5	4.82
1	3	180	70	-0.293	0.169	44.6	255.1	46.6	7.19
1	3	180	100	-0.263	0.153	44.5	266.9	66.1	9.57
1	3	180	130	-0.297	0.207	45.1	274.7	35.4	5.55
1	3	270	10	-0.356	0.171	44.3	210.7	37.9	4.79
1	3	270	40	-0.358	0.178	44.4	231.5	33.9	5.29
1	3	270	70	-0.303	0.170	44.5	235.7	59.9	6.07
1	3	270	100	-0.271	0.149	44.3	244.6	65.3	8.51
1	3	270	130	-0.313	0.195	45.2	259.3	34.3	5.56

Crankcase	Cylinder bore	Angle pos. [°]	Liner pos. [mm]	R	η [1/s]	C [°]	d [µm]	PAT [MPa]	α [mm^2/s]
1	4	0	10	-0.330	0.190	44.9	250.7	31.8	5.46
1	4	0	40	-0.323	0.194	44.5	258.2	37.5	5.55
1	4	0	70	-0.287	0.173	44.8	261.5	44.0	7.20
1	4	0	100	-0.268	0.150	45.0	260.1	62.1	9.45
1	4	0	130	-0.299	0.192	45.2	258.3	32.5	5.69
1	4	90	10	-0.410	0.191	45.9	220.2	43.0	4.20
1	4	90	40	-0.393	0.191	45.8	237.3	38.3	4.85
1	4	90	70	-0.339	0.170	45.5	241.0	43.3	6.34
1	4	90	100	-0.302	0.154	45.0	242.6	67.9	7.83
1	4	90	130	-0.338	0.196	44.5	245.1	40.4	4.90
1	4	180	10	-0.390	0.188	46.3	222.0	37.2	4.38
1	4	180	40	-0.363	0.188	45.6	230.7	44.0	4.72
1	4	180	70	-0.295	0.165	45.0	239.0	58.1	6.59
1	4	180	100	-0.273	0.144	45.0	252.7	64.3	9.69
1	4	180	130	-0.302	0.192	45.3	249.8	32.5	5.34
1	4	270	10	-0.388	0.177	45.9	207.5	36.5	4.29
1	4	270	40	-0.388	0.184	46.0	231.8	40.8	4.98
1	4	270	70	-0.313	0.171	44.9	241.2	45.5	6.26
1	4	270	100	-0.287	0.150	45.1	252.9	65.0	8.94
1	4	270	130	-0.324	0.199	45.8	264.0	37.9	5.55
1	5	0	10	-0.328	0.196	44.5	252.6	31.8	5.22
1	5	0	40	-0.332	0.196	44.8	261.8	32.5	5.58
1	5	0	70	-0.282	0.181	44.1	266.8	44.8	6.84
1	5	0	100	-0.270	0.157	44.9	272.3	59.9	9.40
1	5	0	130	-0.303	0.197	45.4	273.9	25.3	6.10
1	5	90	10	-0.427	0.198	45.7	225.4	37.2	4.07
1	5	90	40	-0.404	0.197	45.8	234.0	37.2	4.42
1	5	90	70	-0.339	0.184	45.0	243.0	40.1	5.48
1	5	90	100	-0.304	0.161	44.8	253.2	60.6	7.80
1	5	90	130	-0.316	0.213	43.5	257.5	35.4	4.58
1	5	180	10	-0.393	0.197	45.6	225.5	39.3	4.12
1	5	180	40	-0.373	0.201	45.5	235.8	37.2	4.31
1	5	180	70	-0.297	0.169	44.9	242.5	39.7	6.49
1	5	180	100	-0.256	0.146	44.3	246.4	59.9	8.89
1	5	180	130	-0.304	0.192	45.1	249.0	35.0	5.26
1	5	270	10	-0.402	0.198	45.8	233.7	38.6	4.37
1	5	270	40	-0.402	0.196	46.2	239.8	37.5	4.69
1	5	270	70	-0.323	0.181	45.0	240.5	41.9	5.54
1	5	270	100	-0.286	0.154	44.8	250.4	69.7	8.33
1	5	270	130	-0.335	0.210	45.5	262.0	35.7	4.87
1	6	0	10	-0.357	0.194	45.3	245.0	26.7	5.02
1	6	0	40	-0.339	0.196	45.4	258.5	36.1	5.48
1	6	0	70	-0.301	0.177	45.0	261.7	41.2	6.83
1	6	0	100	-0.265	0.149	44.9	261.7	57.8	9.75
1	6	0	130	-0.293	0.184	45.5	264.0	24.5	6.45
1	6	90	10	-0.438	0.211	46.5	235.3	29.2	3.89
1	6	90	40	-0.417	0.212	46.0	248.5	34.3	4.32
1	6	90	70	-0.350	0.190	45.6	256.7	40.8	5.76
1	6	90	100	-0.318	0.160	45.5	263.9	59.9	8.53
1	6	90	130	-0.366	0.200	46.4	266.0	36.5	5.55
1	6	180	10	-0.402	0.216	46.3	241.3	31.0	3.93
1	6	180	40	-0.372	0.208	45.7	247.9	30.3	4.44
1	6	180	70	-0.306	0.177	45.1	246.4	38.6	6.08
1	6	180	100	-0.265	0.144	44.8	252.9	70.0	9.66
1	6	180	130	-0.302	0.188	45.7	251.1	39.0	5.61
1	6	270	10	-0.433	0.197	46.8	216.3	30.0	3.78
1	6	270	40	-0.423	0.198	46.7	233.3	35.7	4.34
1	6	270	70	-0.347	0.182	45.9	237.3	38.3	5.34
1	6	270	100	-0.294	0.151	45.1	247.7	63.5	8.50
1	6	270	130	-0.323	0.197	45.5	259.4	39.0	5.47
2	1	0	10	-0.343	0.191	45.8	246.7	39.0	5.23
2	1	0	40	-0.327	0.188	45.8	247.4	38.3	5.42
2	1	0	70	-0.273	0.153	45.0	236.7	53.4	7.54
2	1	0	100	-0.256	0.133	45.0	235.4	65.0	9.90
2	1	0	130	-0.262	0.142	45.0	236.4	37.5	8.66
2	1	90	10	-0.443	0.187	46.9	219.7	35.7	4.34
2	1	90	40	-0.423	0.198	46.8	236.6	40.8	4.48
2	1	90	70	-0.332	0.174	45.7	248.9	59.2	6.43
2	1	90	100	-0.308	0.162	45.1	247.7	62.5	7.36
2	1	90	130	-0.328	0.188	45.3	244.8	39.3	5.34

Crankcase	Cylinder bore	Angle pos. [°]	Liner pos. [mm]	R	η [1/s]	C [°]	d [µm]	PAT [MPa]	α [mm^2/s]
2	1	180	10	-0.407	0.200	46.4	227.6	34.7	4.09
2	1	180	40	-0.355	0.206	45.1	253.0	37.2	4.75
2	1	180	70	-0.285	0.167	45.1	260.5	60.6	7.63
2	1	180	100	-0.265	0.158	44.8	271.5	51.6	9.32
2	1	180	130	-0.266	0.181	44.9	280.0	35.4	7.56
2	1	270	10	-0.428	0.191	46.8	224.5	43.7	4.33
2	1	270	40	-0.406	0.197	46.6	242.6	41.2	4.75
2	1	270	70	-0.314	0.166	45.1	242.6	48.7	6.74
2	1	270	100	-0.292	0.153	44.9	249.1	60.6	8.29
2	1	270	130	-0.292	0.187	44.7	263.0	34.3	6.25
2	2	0	10	-0.335	0.202	45.5	258.6	37.5	5.16
2	2	0	40	-0.334	0.207	45.1	257.9	34.7	4.86
2	2	0	70	-0.265	0.168	44.5	255.1	51.3	7.22
2	2	0	100	-0.253	0.143	44.7	252.6	70.8	9.83
2	2	0	130	-0.252	0.157	44.7	251.0	36.1	8.02
2	2	90	10	-0.459	0.188	46.8	211.0	41.2	3.95
2	2	90	40	-0.396	0.193	45.5	225.1	43.0	4.26
2	2	90	70	-0.327	0.165	45.2	228.7	53.1	6.05
2	2	90	100	-0.296	0.152	44.9	233.0	67.9	7.40
2	2	90	130	-0.283	0.180	43.5	237.4	35.7	5.48
2	2	180	10	-0.415	0.202	46.5	227.3	32.5	3.98
2	2	180	40	-0.381	0.202	45.8	241.3	36.8	4.50
2	2	180	70	-0.273	0.172	44.2	247.8	48.0	6.51
2	2	180	100	-0.259	0.153	44.5	264.6	70.4	9.44
2	2	180	130	-0.261	0.188	44.5	280.4	31.0	6.97
2	2	270	10	-0.393	0.192	45.4	210.4	43.7	3.79
2	2	270	40	-0.366	0.193	45.0	234.4	40.8	4.65
2	2	270	70	-0.272	0.168	44.1	239.1	54.9	6.38
2	2	270	100	-0.254	0.147	43.8	249.4	70.4	8.98
2	2	270	130	-0.241	0.180	43.1	265.7	38.3	6.84
2	3	0	10	-0.357	0.196	46.2	253.2	34.7	5.23
2	3	0	40	-0.333	0.193	45.3	253.6	38.3	5.45
2	3	0	70	-0.279	0.167	44.8	245.4	49.1	6.80
2	3	0	100	-0.270	0.137	45.1	244.1	68.6	9.94
2	3	0	130	-0.265	0.153	45.0	245.3	35.4	8.07
2	3	90	10	-0.426	0.190	46.7	215.7	36.1	4.06
2	3	90	40	-0.402	0.191	46.3	236.0	36.5	4.78
2	3	90	70	-0.315	0.181	44.6	238.6	52.0	5.48
2	3	90	100	-0.275	0.152	44.3	246.4	57.4	8.28
2	3	90	130	-0.246	0.182	44.0	248.2	45.1	5.85
2	3	180	10	-0.412	0.193	46.9	217.9	31.0	4.00
2	3	180	40	-0.385	0.197	46.2	232.7	39.0	4.39
2	3	180	70	-0.289	0.166	44.9	242.8	39.3	6.71
2	3	180	100	-0.257	0.146	44.5	258.4	56.3	9.83
2	3	180	130	-0.261	0.179	44.8	262.8	36.1	6.77
2	3	270	10	-0.418	0.192	46.4	215.7	41.2	3.96
2	3	270	40	-0.404	0.196	46.3	236.9	37.9	4.60
2	3	270	70	-0.333	0.179	45.6	241.3	54.2	5.69
2	3	270	100	-0.280	0.152	44.4	254.3	60.3	8.80
2	3	270	130	-0.250	0.195	42.1	267.9	43.3	5.91
2	4	0	10	-0.339	0.213	45.5	267.4	28.9	4.95
2	4	0	40	-0.333	0.206	45.5	272.3	46.9	5.48
2	4	0	70	-0.282	0.178	44.7	267.2	60.6	7.11
2	4	0	100	-0.265	0.150	45.0	266.3	65.0	9.94
2	4	0	130	-0.262	0.176	44.9	267.0	39.7	7.21
2	4	90	10	-0.461	0.186	47.6	199.2	38.6	3.59
2	4	90	40	-0.419	0.188	47.1	220.7	43.0	4.31
2	4	90	70	-0.339	0.175	45.9	222.4	46.9	5.06
2	4	90	100	-0.300	0.148	45.2	231.1	70.0	7.67
2	4	90	130	-0.320	0.184	45.4	236.4	37.9	5.20
2	4	180	10	-0.412	0.210	46.5	234.4	35.0	3.93
2	4	180	40	-0.378	0.202	46.3	244.2	34.3	4.60
2	4	180	70	-0.292	0.174	45.1	246.4	51.3	6.33
2	4	180	100	-0.263	0.144	45.0	254.7	58.1	9.80
2	4	180	130	-0.271	0.190	44.8	259.1	31.4	5.85
2	4	270	10	-0.418	0.196	46.4	220.5	41.2	3.99
2	4	270	40	-0.391	0.198	46.0	238.7	43.3	4.55
2	4	270	70	-0.315	0.185	45.1	245.9	47.3	5.56
2	4	270	100	-0.281	0.154	44.7	256.1	65.7	8.65
2	4	270	130	-0.277	0.200	43.8	270.7	40.8	5.75

Crankcase	Cylinder bore	Angle pos. [°]	Liner pos. [mm]	R	η [1/s]	C [°]	d [μm]	PAT [MPa]	α [mm²/s]
2	5	0	10	-0.344	0.217	45.3	263.4	34.7	4.61
2	5	0	40	-0.331	0.203	45.0	261.8	42.6	5.21
2	5	0	70	-0.285	0.183	44.5	263.7	50.5	6.51
2	5	0	100	-0.264	0.149	44.8	266.0	71.5	10.04
2	5	0	130	-0.254	0.171	44.7	265.4	30.3	7.60
2	5	90	10	-0.462	0.185	47.4	205.1	40.8	3.87
2	5	90	40	-0.414	0.194	46.3	221.1	39.3	4.08
2	5	90	70	-0.349	0.181	45.6	231.7	44.4	5.16
2	5	90	100	-0.304	0.151	45.2	238.1	54.9	7.77
2	5	90	130	-0.321	0.183	45.3	243.1	43.0	5.53
2	5	180	10	-0.399	0.188	45.9	210.1	33.9	3.91
2	5	180	40	-0.384	0.192	46.0	221.9	42.6	4.19
2	5	180	70	-0.303	0.164	44.8	229.6	42.2	6.15
2	5	180	100	-0.257	0.141	44.5	239.8	66.1	9.15
2	5	180	130	-0.262	0.180	44.5	250.8	36.8	6.08
2	5	270	10	-0.412	0.215	45.8	246.6	44.4	4.13
2	5	270	40	-0.415	0.215	46.0	247.1	40.4	4.16
2	5	270	70	-0.321	0.190	44.7	248.1	49.8	5.35
2	5	270	100	-0.294	0.153	45.1	259.1	58.1	9.00
2	5	270	130	-0.294	0.186	44.4	272.0	39.7	6.73
2	6	0	10	-0.368	0.197	46.0	244.0	32.5	4.80
2	6	0	40	-0.343	0.199	45.5	261.1	29.6	5.42
2	6	0	70	-0.307	0.180	45.0	259.8	39.7	6.56
2	6	0	100	-0.266	0.147	44.8	255.9	57.0	9.58
2	6	0	130	-0.262	0.171	44.9	254.4	29.6	6.91
2	6	90	10	-0.476	0.207	48.0	223.0	26.7	3.63
2	6	90	40	-0.454	0.201	47.7	229.5	31.0	4.10
2	6	90	70	-0.375	0.189	46.4	234.5	36.8	4.85
2	6	90	100	-0.313	0.148	45.6	237.1	54.5	8.12
2	6	90	130	-0.341	0.182	46.0	240.7	34.3	5.50
2	6	180	10	-0.430	0.221	47.2	236.4	30.0	3.59
2	6	180	40	-0.380	0.203	46.1	237.3	32.1	4.29
2	6	180	70	-0.312	0.172	45.6	234.3	41.9	5.85
2	6	180	100	-0.264	0.139	45.0	239.3	46.2	9.36
2	6	180	130	-0.277	0.185	44.8	246.4	29.6	5.60
2	6	270	10	-0.438	0.216	46.9	236.6	28.9	3.77
2	6	270	40	-0.429	0.211	46.7	237.8	29.2	4.00
2	6	270	70	-0.359	0.186	45.8	245.1	40.1	5.45
2	6	270	100	-0.293	0.154	45.1	255.8	53.1	8.62
2	6	270	130	-0.308	0.201	44.8	260.1	31.0	5.26
3	1	0	10	-0.337	0.197	45.3	252.3	35.4	5.14
3	1	0	40	-0.324	0.194	44.8	255.0	37.5	5.41
3	1	0	70	-0.277	0.155	44.8	243.6	61.4	7.77
3	1	0	100	-0.278	0.140	45.1	241.0	65.0	9.26
3	1	0	130	-0.271	0.162	44.9	239.7	34.7	6.85
3	1	90	10	-0.430	0.211	45.7	227.6	38.3	3.65
3	1	90	40	-0.397	0.204	45.7	243.8	43.3	4.48
3	1	90	70	-0.313	0.175	45.0	250.4	53.8	6.44
3	1	90	100	-0.312	0.165	45.1	262.3	58.5	7.91
3	1	90	130	-0.358	0.217	45.5	266.0	34.7	4.74
3	1	180	10	-0.426	0.208	46.6	232.0	30.0	3.91
3	1	180	40	-0.374	0.207	45.8	257.2	45.8	4.87
3	1	180	70	-0.289	0.177	45.0	259.4	48.4	6.77
3	1	180	100	-0.273	0.163	45.0	275.9	52.7	8.98
3	1	180	130	-0.299	0.206	45.5	286.2	30.3	6.07
3	1	270	10	-0.442	0.200	47.1	225.5	32.5	3.99
3	1	270	40	-0.385	0.195	45.7	236.6	38.6	4.65
3	1	270	70	-0.313	0.164	45.2	237.1	62.8	6.54
3	1	270	100	-0.303	0.152	45.0	247.2	54.5	8.30
3	1	270	130	-0.281	0.201	43.4	253.7	32.9	5.01
3	2	0	10	-0.327	0.192	45.2	247.4	33.9	5.22
3	2	0	40	-0.332	0.186	45.3	252.8	42.6	5.77
3	2	0	70	-0.288	0.161	45.1	248.3	54.2	7.48
3	2	0	100	-0.281	0.136	45.5	244.3	71.5	10.09
3	2	0	130	-0.270	0.163	45.3	243.3	33.2	7.03
3	2	90	10	-0.456	0.194	47.3	223.0	34.3	4.14
3	2	90	40	-0.406	0.197	46.3	241.0	36.5	4.71
3	2	90	70	-0.338	0.176	45.6	247.3	46.6	6.22
3	2	90	100	-0.310	0.160	45.3	254.1	67.9	7.90
3	2	90	130	-0.331	0.216	44.7	256.5	35.0	4.44

Crankcase	Cylinder bore	Angle pos. [°]	Liner pos. [mm]	R	η [1/s]	C [°]	d [μm]	PAT [MPa]	α [mm^2/s]
3	2	180	10	-0.422	0.204	46.9	232.8	32.1	4.10
3	2	180	40	-0.385	0.201	46.3	250.0	35.7	4.85
3	2	180	70	-0.309	0.179	45.2	256.4	45.1	6.41
3	2	180	100	-0.281	0.159	45.1	268.9	57.4	8.94
3	2	180	130	-0.291	0.207	45.3	289.7	31.0	6.12
3	2	270	10	-0.422	0.193	46.8	223.0	35.7	4.19
3	2	270	40	-0.382	0.192	45.8	236.0	43.7	4.76
3	2	270	70	-0.320	0.173	45.2	239.8	41.9	6.02
3	2	270	100	-0.280	0.151	44.5	248.6	63.9	8.52
3	2	270	130	-0.261	0.194	42.7	255.2	36.1	5.46
3	3	0	10	-0.331	0.205	45.1	267.7	32.5	5.34
3	3	0	40	-0.344	0.201	45.5	262.6	41.2	5.39
3	3	0	70	-0.284	0.174	44.7	253.5	57.8	6.66
3	3	0	100	-0.259	0.152	44.5	253.9	47.7	8.71
3	3	0	130	-0.288	0.173	45.3	255.6	33.9	6.88
3	3	90	10	-0.439	0.197	46.3	216.6	32.5	3.80
3	3	90	40	-0.413	0.198	46.1	229.7	41.5	4.24
3	3	90	70	-0.338	0.185	45.3	238.7	39.7	5.22
3	3	90	100	-0.308	0.169	45.1	245.6	44.4	6.62
3	3	90	130	-0.351	0.201	44.4	247.5	36.8	4.76
3	3	180	10	-0.429	0.214	46.7	234.8	33.6	3.77
3	3	180	40	-0.412	0.211	46.6	246.9	39.0	4.31
3	3	180	70	-0.311	0.181	45.1	250.7	37.5	6.05
3	3	180	100	-0.272	0.170	44.7	263.0	41.9	7.50
3	3	180	130	-0.323	0.223	45.4	274.2	34.3	4.75
3	3	270	10	-0.414	0.194	46.1	219.9	34.7	4.03
3	3	270	40	-0.389	0.193	45.9	232.5	37.5	4.58
3	3	270	70	-0.312	0.176	44.8	234.0	41.9	5.56
3	3	270	100	-0.273	0.154	44.1	244.5	46.2	7.96
3	3	270	130	-0.298	0.204	43.7	257.1	36.1	5.00
3	4	0	10	-0.338	0.203	44.9	253.2	32.5	4.88
3	4	0	40	-0.334	0.202	45.3	258.5	37.5	5.16
3	4	0	70	-0.282	0.178	44.8	259.1	51.3	6.69
3	4	0	100	-0.272	0.153	45.1	258.3	47.7	8.95
3	4	0	130	-0.292	0.183	45.1	259.1	37.5	6.32
3	4	90	10	-0.444	0.194	46.8	210.0	36.1	3.68
3	4	90	40	-0.421	0.202	46.0	235.0	43.7	4.27
3	4	90	70	-0.354	0.183	45.8	242.3	48.0	5.49
3	4	90	100	-0.323	0.171	45.6	248.8	37.5	6.63
3	4	90	130	-0.361	0.211	44.9	250.5	35.7	4.41
3	4	180	10	-0.438	0.205	47.0	224.6	34.7	3.78
3	4	180	40	-0.390	0.198	46.1	233.0	37.9	4.37
3	4	180	70	-0.301	0.175	45.0	240.0	36.1	5.89
3	4	180	100	-0.270	0.160	44.8	249.2	40.1	7.61
3	4	180	130	-0.297	0.192	45.0	254.1	34.3	5.50
3	4	270	10	-0.441	0.191	46.7	221.6	35.7	4.22
3	4	270	40	-0.402	0.197	46.0	234.5	36.1	4.47
3	4	270	70	-0.340	0.184	45.7	237.5	43.0	5.24
3	4	270	100	-0.303	0.162	45.2	246.9	40.8	7.34
3	4	270	130	-0.349	0.204	45.7	262.7	35.0	5.20
3	5	0	10	-0.345	0.202	45.4	257.8	25.3	5.11
3	5	0	40	-0.331	0.191	45.4	259.6	36.1	5.82
3	5	0	70	-0.295	0.179	45.1	265.3	31.0	6.93
3	5	0	100	-0.270	0.156	45.1	270.1	45.5	9.44
3	5	0	130	-0.304	0.198	45.4	271.6	30.3	5.90
3	5	90	10	-0.458	0.201	47.4	217.8	37.9	3.67
3	5	90	40	-0.426	0.192	46.9	232.5	38.6	4.59
3	5	90	70	-0.367	0.184	46.2	242.7	46.6	5.46
3	5	90	100	-0.330	0.171	46.0	255.3	43.3	7.01
3	5	90	130	-0.390	0.205	46.2	259.7	38.3	5.06
3	5	180	10	-0.425	0.193	47.3	224.9	35.7	4.26
3	5	180	40	-0.403	0.198	46.8	234.5	37.9	4.43
3	5	180	70	-0.310	0.176	45.3	234.3	40.1	5.56
3	5	180	100	-0.265	0.158	44.8	241.8	35.0	7.39
3	5	180	130	-0.314	0.198	45.5	249.6	33.9	4.97
3	5	270	10	-0.441	0.211	47.1	238.5	41.9	4.03
3	5	270	40	-0.421	0.198	47.1	246.6	39.7	4.87
3	5	270	70	-0.344	0.189	45.7	248.3	36.8	5.44
3	5	270	100	-0.301	0.163	45.2	250.9	40.8	7.47
3	5	270	130	-0.343	0.207	45.6	253.5	33.9	4.70

Crankcase	Cylinder bore	Angle pos. [°]	Liner pos. [mm]	R	η [1/s]	C [°]	d [μm]	PAT [MPa]	α [mm²/s]
3	6	0	10	-0.364	0.207	45.7	251.0	26.0	4.63
3	6	0	40	-0.344	0.213	45.2	268.5	27.4	4.98
3	6	0	70	-0.294	0.184	44.5	266.6	34.7	6.56
3	6	0	100	-0.266	0.157	45.0	271.8	33.9	9.44
3	6	0	130	-0.317	0.195	45.4	272.5	21.7	6.13
3	6	90	10	-0.456	0.220	46.8	232.2	31.8	3.50
3	6	90	40	-0.437	0.214	46.4	249.1	36.1	4.28
3	6	90	70	-0.370	0.189	45.9	255.4	34.7	5.72
3	6	90	100	-0.306	0.168	45.0	258.6	48.4	7.48
3	6	90	130	-0.374	0.222	45.0	261.8	37.9	4.39
3	6	180	10	-0.427	0.236	46.4	249.6	29.6	3.50
3	6	180	40	-0.405	0.211	46.5	250.2	33.9	4.42
3	6	180	70	-0.313	0.181	44.9	246.8	41.5	5.81
3	6	180	100	-0.266	0.155	44.6	245.9	53.8	7.87
3	6	180	130	-0.314	0.193	45.4	251.2	32.1	5.30
3	6	270	10	-0.448	0.218	46.8	229.2	33.6	3.46
3	6	270	40	-0.426	0.209	46.5	237.8	31.4	4.06
3	6	270	70	-0.365	0.188	46.2	238.7	33.2	5.08
3	6	270	100	-0.304	0.155	45.4	244.9	56.0	7.86
3	6	270	130	-0.359	0.199	45.9	251.5	39.7	5.02
4	1	0	10	-0.370	0.190	46.3	235.1	41.9	4.81
4	1	0	40	-0.357	0.190	46.0	249.1	37.5	5.41
4	1	0	70	-0.297	0.154	45.4	243.4	41.9	7.87
4	1	0	100	-0.297	0.139	45.9	235.3	72.2	9.05
4	1	0	130	-0.316	0.173	46.0	233.7	24.5	5.75
4	1	90	10	-0.355	0.170	45.6	207.5	34.7	4.69
4	1	90	40	-0.367	0.184	45.8	232.1	29.6	4.99
4	1	90	70	-0.282	0.148	44.8	231.0	67.9	7.63
4	1	90	100	-0.292	0.149	45.1	238.2	57.0	8.05
4	1	90	130	-0.284	0.166	44.9	246.3	32.5	6.90
4	1	180	10	-0.357	0.181	45.7	219.8	33.2	4.65
4	1	180	40	-0.351	0.195	45.8	247.5	32.5	5.04
4	1	180	70	-0.288	0.157	45.5	251.3	59.9	8.01
4	1	180	100	-0.281	0.154	45.5	260.5	53.4	9.02
4	1	180	130	-0.317	0.194	46.1	265.5	28.9	5.86
4	1	270	10	-0.369	0.187	45.9	225.0	34.7	4.55
4	1	270	40	-0.371	0.195	46.0	246.7	36.8	5.01
4	1	270	70	-0.315	0.167	45.5	247.0	60.6	6.90
4	1	270	100	-0.314	0.159	45.7	253.2	68.6	8.01
4	1	270	130	-0.344	0.199	46.3	258.2	28.9	5.29
4	2	0	10	-0.344	0.183	45.8	236.8	36.1	5.23
4	2	0	40	-0.369	0.190	46.7	246.5	31.0	5.27
4	2	0	70	-0.315	0.162	45.9	246.5	34.7	7.29
4	2	0	100	-0.298	0.140	46.0	241.1	49.8	9.33
4	2	0	130	-0.320	0.177	46.6	239.1	24.5	5.76
4	2	90	10	-0.399	0.174	46.9	209.8	38.3	4.57
4	2	90	40	-0.412	0.184	47.2	222.4	36.8	4.60
4	2	90	70	-0.348	0.160	46.4	227.8	60.6	6.36
4	2	90	100	-0.329	0.150	46.3	227.3	64.3	7.18
4	2	90	130	-0.348	0.168	46.6	225.1	35.4	5.61
4	2	180	10	-0.364	0.181	46.2	224.3	25.3	4.80
4	2	180	40	-0.375	0.194	46.5	240.6	34.7	4.85
4	2	180	70	-0.303	0.161	45.7	247.6	54.9	7.41
4	2	180	100	-0.290	0.150	45.7	255.3	45.5	9.05
4	2	180	130	-0.307	0.189	46.0	255.0	32.5	5.74
4	2	270	10	-0.358	0.174	45.7	213.4	NaN	4.72
4	2	270	40	-0.387	0.188	46.6	232.0	37.5	4.80
4	2	270	70	-0.324	0.165	45.9	239.4	46.9	6.60
4	2	270	100	-0.321	0.156	46.1	247.5	43.3	7.90
4	2	270	130	-0.353	0.197	46.5	250.1	31.8	5.07
4	3	0	10	-0.363	0.202	46.0	259.0	26.7	5.17
4	3	0	40	-0.364	0.198	46.1	260.4	28.9	5.42
4	3	0	70	-0.310	0.169	45.6	257.5	33.9	7.26
4	3	0	100	-0.303	0.148	46.0	251.6	72.2	9.10
4	3	0	130	-0.330	0.184	46.4	250.6	28.2	5.82
4	3	90	10	-0.383	0.175	46.0	197.0	33.2	3.98
4	3	90	40	-0.402	0.185	46.5	227.7	35.4	4.77
4	3	90	70	-0.357	0.167	46.5	229.3	54.2	5.95
4	3	90	100	-0.328	0.154	46.0	229.4	53.4	6.98
4	3	90	130	-0.351	0.176	46.6	233.3	36.8	5.53

Crankcase	Cylinder bore	Angle pos. [°]	Liner pos. [mm]	R	η [1/s]	C [°]	d [μm]	PAT [MPa]	α [mm²/s]
4	3	180	10	-0.350	0.175	45.6	216.3	31.0	4.80
4	3	180	40	-0.366	0.191	46.0	238.8	28.9	4.92
4	3	180	70	-0.303	0.160	45.3	245.2	52.7	7.35
4	3	180	100	-0.286	0.143	45.5	247.7	49.1	9.45
4	3	180	130	-0.320	0.191	46.0	249.7	28.2	5.35
4	3	270	10	-0.362	0.172	45.8	202.4	31.0	4.33
4	3	270	40	-0.380	0.181	46.2	227.6	37.5	4.99
4	3	270	70	-0.334	0.168	46.0	234.3	66.4	6.13
4	3	270	100	-0.315	0.159	45.9	243.1	45.5	7.33
4	3	270	130	-0.357	0.193	46.5	246.2	33.9	5.09
4	4	0	10	-0.354	0.203	45.7	258.9	42.6	5.09
4	4	0	40	-0.356	0.206	45.7	260.6	25.3	5.01
4	4	0	70	-0.307	0.175	45.4	260.9	29.6	7.01
4	4	0	100	-0.293	0.153	45.7	260.0	25.3	9.07
4	4	0	130	-0.336	0.192	46.2	260.7	27.4	5.79
4	4	90	10	-0.404	0.177	46.6	212.7	30.3	4.52
4	4	90	40	-0.397	0.187	46.4	228.5	37.5	4.68
4	4	90	70	-0.336	0.168	45.7	235.0	54.9	6.13
4	4	90	100	-0.325	0.158	46.0	240.5	47.7	7.26
4	4	90	130	-0.353	0.177	46.6	244.7	33.2	6.00
4	4	180	10	-0.337	0.165	45.2	205.0	30.3	4.82
4	4	180	40	-0.361	0.177	46.1	223.9	35.4	5.03
4	4	180	70	-0.303	0.156	45.5	235.3	51.3	7.18
4	4	180	100	-0.284	0.141	45.6	236.4	55.6	8.79
4	4	180	130	-0.330	0.187	46.1	237.2	31.8	5.04
4	4	270	10	-0.353	0.172	45.4	210.0	28.2	4.66
4	4	270	40	-0.372	0.180	46.0	228.6	35.4	5.05
4	4	270	70	-0.328	0.168	45.8	234.4	63.5	6.12
4	4	270	100	-0.312	0.157	45.6	243.9	59.9	7.61
4	4	270	130	-0.353	0.190	46.4	245.1	28.2	5.23
4	5	0	10	-0.362	0.196	46.2	254.6	36.1	5.32
4	5	0	40	-0.356	0.194	46.0	266.0	27.4	5.88
4	5	0	70	-0.319	0.181	45.8	264.2	31.8	6.70
4	5	0	100	-0.296	0.156	46.0	262.1	53.4	8.84
4	5	0	130	-0.346	0.200	46.5	261.2	43.3	5.35
4	5	90	10	-0.396	0.183	46.5	217.0	34.7	4.43
4	5	90	40	-0.405	0.188	46.9	234.8	40.4	4.92
4	5	90	70	-0.349	0.170	46.2	235.4	57.0	6.04
4	5	90	100	-0.341	0.158	46.4	243.9	34.7	7.45
4	5	90	130	-0.365	0.187	46.8	249.1	32.5	5.59
4	5	180	10	-0.365	0.178	46.1	212.9	28.2	4.48
4	5	180	40	-0.370	0.179	46.5	232.5	35.7	5.28
4	5	180	70	-0.324	0.156	46.1	233.5	41.9	7.04
4	5	180	100	-0.295	0.137	46.1	234.7	50.5	9.24
4	5	180	130	-0.347	0.181	46.6	238.0	33.9	5.41
4	5	270	10	-0.350	0.182	45.6	227.9	36.1	4.91
4	5	270	40	-0.371	0.189	46.2	238.9	35.4	5.04
4	5	270	70	-0.334	0.169	45.9	236.6	50.5	6.18
4	5	270	100	-0.302	0.149	45.7	239.7	43.3	8.13
4	5	270	130	-0.358	0.192	46.5	240.1	26.7	4.92
4	6	0	10	-0.378	0.208	46.4	255.3	27.4	4.72
4	6	0	40	-0.365	0.218	46.1	274.6	27.4	4.98
4	6	0	70	-0.320	0.188	45.7	270.7	28.2	6.53
4	6	0	100	-0.294	0.161	45.7	271.8	28.9	8.98
4	6	0	130	-0.374	0.216	46.1	274.6	28.9	5.09
4	6	90	10	-0.405	0.196	46.6	227.9	28.9	4.27
4	6	90	40	-0.416	0.195	46.9	241.4	33.6	4.80
4	6	90	70	-0.364	0.177	46.3	241.4	47.7	5.82
4	6	90	100	-0.324	0.160	46.0	243.5	57.8	7.30
4	6	90	130	-0.359	0.184	46.8	245.9	33.2	5.61
4	6	180	10	-0.364	0.191	45.9	234.6	27.4	4.72
4	6	180	40	-0.366	0.190	46.0	235.6	29.6	4.81
4	6	180	70	-0.312	0.163	45.5	231.7	45.5	6.38
4	6	180	100	-0.295	0.140	45.8	226.0	49.8	8.23
4	6	180	130	-0.333	0.178	46.1	224.2	35.4	4.97
4	6	270	10	-0.361	0.191	45.4	231.7	26.7	4.63
4	6	270	40	-0.378	0.193	45.8	234.7	33.9	4.66
4	6	270	70	-0.342	0.178	45.8	237.8	32.5	5.60
4	6	270	100	-0.308	0.154	45.6	241.1	48.4	7.67
4	6	270	130	-0.367	0.199	46.3	242.1	31.0	4.63